Application of homogenization methods and crystal plasticity to the modeling of heterogeneous materials of technological interest

Von der Fakultät Maschinenbau
der Technischen Universität Dortmund
zur Erlangung des Grades eines
Doktor-Ingenieurs
(Dr.-Ing.)
genehmigte Dissertation

von

Benjamin Klusemann

Dortmund 2010

This research project was supperted by the DFG (Deutsche Forschungsgemeinschaft) within the special research project SFB 708 (TP B6) and under contract Sv 8/8-2. This financial support is gratefully acknowledged.

The commission:

Prof. Dr. rer. nat. Bob Svendsen, supervisor
Prof. Dr.-Ing. Thomas Böhlke (Karlsruhe Institute of Technology)
Jun.-Prof. Dr.-Ing. Swantje Bargmann
Prof. Dr.-Ing. Andreas Menzel, chairman

© by Benjamin Klusemann 2010

Contents

Summary **xi**

1 Comparison of homogenization methods in the context of multi-phase elastic composites with variable shape **1**

1.1 Introduction . . . 1

1.2 Determination of effective elastic properties . . . 4

1.3 Comparison of different homogenization approaches for spherical inclusions . . 8

1.4 Dealing with irregular (non-ellipsoidal) inhomogeneities . . . 15

1.5 Comparison of different homogenization approaches for irregular inhomogeneities 21

1.6 Summary and outlook . . . 28

2 Homogenization modeling of two-phase composites with a layered microstructure **31**

2.1 Introduction . . . 31

2.2 Material model . . . 33

2.3 Model based on phase-wise constant plastic strain . . . 34

2.4 Laminate model . . . 36

2.5 Model behavior . . . 38

2.6 Comparison with other homogenization approaches . . . 43

2.7 The case of variable interface orientation . . . 45

2.8 Discussion and conclusions . . . 47

3 Crystal plastic modeling of the deformation behavior of thin sheets with large grains **51**

3.1 Introduction . . . 51

3.2 Model formulation for single-crystal plasticity . . . 53

3.3 Algorithmic formulation . . . 55

3.4 Model identification . . . 57

3.5 Experimental methods . . . 59

3.6 Finite element model . . . 60

3.7 Results . . . 61

3.8 Conclusion . . . 68

4 Crystal plastic modeling of the development of orientation gradients and geometrically necessary dislocations in thin sheets with large grains 69

4.1 Introduction . . . 69

4.2 Model formulation for single-crystal plasticity . . . 71

4.3 Experimental and simulation methods . . . 73

4.4 Determination of Schmid and Taylor factors . . . 77

4.5 Results . . . 79

4.6 Conclusion . . . 86

5 Identification of the macroscopic material properties for thermal sprayed coatings based on nanoindentation 87

5.1 Introduction . . . 87

5.2 Nanoindentation . . . 89

5.3 Construction of finite element models from real micrographs . . . 93

5.4 Discussion . . . 96

5.5 Summary and outlook . . . 98

A Basics of homogenization 99

A.1 Eshelby solution . . . 99

A.2 Review of some standard homogenization methods . . . 102

B Crystalline Structure 107

B.1 Lattice structures of metals . . . 107

B.2 Crystal defects . . . 109

B.3 Critical resolved shear stress . . . 112

C Basics of continuum mechanics 113

C.1 Flow kinematics . . . 113

C.2 Mechanical balance equation . . . 116

C.3 Concepts in material modeling . . . 119

References 121

Acknowledgements 133

Curriculum Vitae 134

List of Figures

1.1 A schematic overview on different homogenization schemes for estimating the average stress or strain, respectively. 5

1.2 A schematic overview on the ESCS approach (Zheng and Du, 2001). 6

1.3 Prediction of effective Young's modulus E^* with different homogenization methods for $E_\mathrm{M} = 210$ GPa, $E_\mathrm{I} = 430$ GPa and $\nu = 0.25$. (MT = Mori-Tanaka; SCS = self-consistent; HS = Hashin-Shtrikman bounds; IDIM = interpolative double inclusion model) 9

1.4 Prediction of effective Young's modulus E^* with different homogenization methods for $E_\mathrm{M} = 21$ GPa, $E_\mathrm{I} = 210$ GPa and $\nu = 0.25$. (MT = Mori-Tanaka; SCS = self-consistent; HS = Hashin-Shtrikman bounds; IDIM = interpolative double inclusion model) 9

1.5 Prediction of effective Young's modulus E^* of Voigt method for different concentrations c and stiffness ratios $E_\mathrm{I}/E_\mathrm{M}$ 10

1.6 Prediction of effective Young's modulus E^* of Reuss method for different concentrations c and stiffness ratios $E_\mathrm{I}/E_\mathrm{M}$ 10

1.7 Prediction of effective Young's modulus E^* of Hashin-Shtrikman upper bound for different concentrations c and stiffness ratios $E_\mathrm{I}/E_\mathrm{M}$ 10

1.8 Prediction of effective Young's modulus E^* of Hashin-Shtrikman lower bound and Mori-Tanaka estimate, respectively, for different concentrations c and stiffness ratios $E_\mathrm{I}/E_\mathrm{M}$ 10

1.9 Prediction of effective Young's modulus E^* of self-consistent method for different concentrations c and stiffness ratios $E_\mathrm{I}/E_\mathrm{M}$ 10

1.10 Prediction of effective Young's modulus E^* of the interpolative double inclusion model (IDIM) for different concentrations c and stiffness ratios $E_\mathrm{I}/E_\mathrm{M}$ . . 10

1.11 Prediction of effective Young's modulus E^* with different homogenization methods for different stiffness ratios $E_\mathrm{I}/E_\mathrm{M}$ for $c = 0.3$ 11

1.12 Prediction of effective Young's modulus E^* with different homogenization methods for different stiffness ratios $E_\mathrm{I}/E_\mathrm{M}$ for $c = 0.8$ 11

1.13 RVE with randomly distributed spherical inclusions of a volume fraction $c = 0.2$ 12

1.14 RVE with randomly distributed voids of a volume fraction $c = 0.2$ 12

1.15 Comparison of homogenization results for effective Young's modulus E^* with FEM-results for $E_\mathrm{M} = 21$ GPa, $E_\mathrm{I} = 210$ GPa and $\nu = 0.25$. 13

1.16 Comparison of homogenization results for effective Young's modulus E^* with FEM-results for different stiffness ratios $E_\mathrm{I}/E_\mathrm{M}$ for $c = 0.3$ 13

1.17 Comparison of different homogenization results and numerical evaluation for the effective Young's modulus E^* of homogenously distributed spherical voids embedded in an isotropic matrix. 13

1.18 Prediction of effective Young's modulus E^* of ESCS method for different concentrations c and stiffness ratios $E_\mathrm{I}/E_\mathrm{M}$ 13

1.19 Comparison of homogenization results for effective Young's modulus E^* for $E_\mathrm{M} = 21$ GPa, $E_\mathrm{I} = 210$ GPa and $\nu = 0.25$. 14

1.20 Comparison of homogenization results for effective Young's modulus E^* for different stiffness ratios $E_\mathrm{I}/E_\mathrm{M}$ for $c = 0.3$ 14

1.21 Laurent polynomial approximations for describing various shapes. a) circle: $e^(i\,\theta)$, ellipse: $e^{i\,\pi/4}[1.5\,\cos(\theta - \pi/4) + i\,0.5\,\sin(\theta - \pi/4)]$. b) hypocycloid: $e^{i\,\theta} + \lambda e^{(2\,i\,\pi/3)}\,e^{-3\,i\,\theta}$, quasi-rectangular: $e^{i\,\theta} - \frac{1}{8}\,e^{-3\,i\,\theta}$. 17

1.22 a) An exemplary micrograph obtained from a HVOF sprayed 88WC-12Co coating with SEM (Tillmann et al., 2008b). b) FE-mesh on microstructure. 19

1.23 Comparison of homogenization results for effective Young's modulus E^* for $E_\mathrm{M} = 21$ GPa, $E_\mathrm{I} = 210$ GPa and $\nu = 0.3$ for circular inclusions. (HS = Hashin-Shtrikman bounds; IDIM = interpolative double inclusion model) . . . 22

1.24 Comparison of homogenization results for component C^*_{11} from the effective elasticity tensor $\mathcal{C}^*$ for $E_\mathrm{M} = 21$ GPa, $E_\mathrm{I} = 210$ GPa and $\nu = 0.3$ for quadratic inclusions. (RMTM = Mori-Tanaka method with replacement tensor approach Nogales and Böhm (2008); classic MT = results of Mori-Tanaka method for circular inclusion) 22

1.25 Approximated square described by $e^{i\,\theta} - \frac{1}{8}\,e^{-3\,i\,\theta}$ (dotted line) to calculate average Eshelby tensor. 22

1.26 Approximated triangle described by $e^{i\,\theta} + 0.3\,e^{-i\,\theta} + 0.3\,e^{-3\,i\,\theta}$ (dotted line) to calculate average Eshelby tensor. 23

1.27 Comparison of homogenization results for component C^*_{11} from the effective elasticity tensor $\mathcal{C}^*$ for $E_\mathrm{M} = 21$ GPa, $E_\mathrm{I} = 210$ GPa and $\nu = 0.3$ for triangular inclusions. 23

1.28 Comparison of homogenization results for component C^*_{11} from the effective elasticity tensor $\mathcal{C}^*$ for $E_\mathrm{M} = 21$ GPa, $E_\mathrm{I} = 210$ GPa and $\nu = 0.3$ for hexagonal inclusions. 23

1.29 Approximated hexagon described by $e^{i\,\theta} + 0.2\,e^{-i\,\theta} + 0.05\,e^{-5\,i\,\theta}$ (dotted line) to calculate average Eshelby tensor. 24

1.30 Prediction of effective Young's modulus E^* of Voigt method for different concentrations c and stiffness ratios $E_\mathrm{I}/E_\mathrm{M}$ for hexagonal inclusions 24

1.31 Prediction of effective Young's modulus E^* of Reuss method for different concentrations c and stiffness ratios $E_\mathrm{I}/E_\mathrm{M}$ for hexagonal inclusions 24

1.32 Prediction of effective Young's modulus E^* of Hashin-Shtrikman upper bound for different concentrations c and stiffness ratios $E_\mathrm{I}/E_\mathrm{M}$ for hexagonal inclusions 24

1.33 Prediction of effective Young's modulus E^* of Hashin-Shtrikman lower bound, Mori-Tanaka estimate and IDD method, respectively, for different concentrations c and stiffness ratios $E_\mathrm{I}/E_\mathrm{M}$ for hexagonal inclusions 24

1.34 Prediction of effective Young's modulus E^* of double-inclusion method for different concentrations c and stiffness ratios $E_\mathrm{I}/E_\mathrm{M}$ for hexagonal inclusions . 25

1.35 Prediction of effective Young's modulus E^* of ESCS method for different concentrations c and stiffness ratios $E_\mathrm{I}/E_\mathrm{M}$ for hexagonal inclusions 25

1.36 Prediction of effective Young's modulus E^* of RMTM method for different concentrations c and stiffness ratios $E_\mathrm{I}/E_\mathrm{M}$ for hexagonal inclusions 25

1.37 Prediction of effective Young's modulus E^* of Mori-Tanaka estimate for different concentrations c and stiffness ratios $E_\mathrm{I}/E_\mathrm{M}$ for circular inclusions 25

1.38 Prediction of effective Young's modulus C^*_{11} with different homogenization methods for different stiffness ratios $E_\mathrm{I}/E_\mathrm{M}$ for $c = 0.4$ for hexagonal inclusions. 26

1.39 Prediction of effective Young's modulus C^*_{11} with different homogenization methods for different stiffness ratios $E_\mathrm{I}/E_\mathrm{M}$ for $c_\mathrm{hex} = 0.4$, $c_\mathrm{tri} = 0.19$ and $c_\mathrm{square} = 0.18$. (RMS = real microstructure) 27

1.40 Prediction of effective Young's modulus C^*_{11} with different homogenization methods for different stiffness ratios $E_\mathrm{I}/E_\mathrm{M}$ for $c_\mathrm{hex} = 0.2$, $c_\mathrm{tri} = 0.1$ and $c_\mathrm{square} = 0.1$. 27

2.1 Example of a layered microstructure in an arc sprayed WC-FeCSiMn coating which has been thermally sprayed at 700 K onto a steel (Ck45) substrate at room temperature. The original micrograph was processed by an image processing software (Klusemann et al., 2009b). Green and white regions represent Fe- and WC-based alloys, respectively; blue regions signify pores. Note that the normal direction to the interface between layers is on average more or less parallel to the thickness direction of the coating, which corresponds to the vertical direction in the figure. 39

2.2 Deformation conditions for investigation of the composite behavior. 40

2.3 Von Mises stress σ_vM in the composite subject to different normal deformation conditions as a function of F_{11}(compression) or F_{33} (extension) for soft-phase volume fraction of $\lambda = 0.5$. Also shown for comparison is the behavior of the pure hard (solid circles) and pure soft (solid squares) for either extension or compression. 40

2.4 Relative normal deformation $\boldsymbol{h} \cdot \boldsymbol{m}$ across the interface for F_{11}-compression and F_{33}-extension at $\lambda = 0.5$. 40

2.5 Von Mises stress σ_{vM} in the composite subject to different shear deformation conditions as a function of strain in the form of displacement u divided by length l for soft-phase volume fraction of $\lambda = 0.5$. See text for details. 41

2.6 Schematic behavior of laminate model for shear parallel to the laminate, e.g., for F_{21}-shear. 41

2.7 FE-model for laminate with applied loading cases. 41

2.8 Applied boundary conditions and coupling conditions for one-element case. . . 42

2.9 Comparison between the FE model and the laminate model for $\lambda = 0.5$. Both models show the same behavior under the applied loads. 42

2.10 Comparison of von Mises stress distribution in the structure predicted by the FE model (above) and by the laminate model (below) for $w/r = 2$ (left) and $w/r = 10$ (right). Although more inhomogeneous in the FE-case, the stress distribution in both cases is quite similar. As shown, with increasing w/r, better agreement is obtained (red implies $\sigma_{\mathrm{vM}} \geq 1000$ MPa). 43

2.11 Comparison of stress-strain behavior predicted by different homogenization approaches for $\lambda = 0.5$. 44

2.12 Comparison of stress-strain behavior of different homogenization models for $\lambda = 0.6$ and $\lambda = 0.3$. Different homogeneous methods show analogous results as described in Figure 2.11. 44

2.13 Distribution of α_{P} in an ideal composite microstructure with 30% (volume) spherical inclusions after 20% applied strain E_{11}. 45

2.14 Comparison of stress-strain behavior for a metal-matrix composite with spherical inclusion ($\lambda = 0.7$) predicted by the homogenization models considered in this work. For comparison, the corresponding FE results are also shown. 46

2.15 Comparison of stress-strain behavior of homogenization model for fixed $\boldsymbol{m} = \{1\,0\,0\}$ under compression and extension with model with variational $\boldsymbol{m}$ for $\lambda = 0.7$ with $\boldsymbol{m}_{\mathrm{initial}} = \{1\,0\,0\}$. For comparison, the corresponding FE results for spherical inclusions are also shown 46

2.16 Comparison of stress-strain behavior of homogenization model for variable $\boldsymbol{m}$ for different values of the interface resistance $\gamma = \beta\, E_{\mathrm{soft}}$ under compression with $\boldsymbol{m}_0 = \{1\,0\,0\}$ and $\lambda = 0.7$. For comparison, the corresponding results for fixed $\boldsymbol{m} = \{1\,0\,0\}$ are also shown. 47

2.17 Development of the reorientation angle $\alpha = \arccos{(\boldsymbol{m} \cdot \boldsymbol{m}_0)}$ during compression for $\boldsymbol{m}_0 = \{1\,0\,0\}$ and various $\gamma = \beta\, E_{\mathrm{soft}}$ with $\lambda = 0.7$. 47

2.18 von Mises stress σ_{vM} in the composite subject to different normal deformation conditions as a function of F_{11}(compression) or F_{33} (extension) for soft-phase volume fraction of $\lambda = 0.5$. The material parameters of the hard phase are changed to $s_{\mathrm{H}} = -1870$MPa and $c_{\mathrm{H}} = 100$. Also shown for comparison is the behavior of the pure hard (solid circles), modeled with softening behavior and pure soft (solid squares) for either extension or compression. 48

3.1 Experimental results of the deformation field and orientation gradient (Henning and Vehoff, 2005). Approximation of grain boundaries shown as red lines. . . . 60

3.2 FE mesh used for simulations with grains numbered. 61

3.3 a) Light-optical micrograph of the tensile test sample. b)-e) In the left column the plastic strain component in tensile direction of the least square fit strain tensor for each grain for $\alpha_\mathrm{P} \approx \{1.5\%, 4\%, 10\%, 19.5\%\}$ Henning and Vehoff (2005) is shown. The other columns show the accumulated crystallographic slip for all glide systems in the simulation for active glide system class $\{110\}\langle 111\rangle$ or $\{112\}\langle 111\rangle$ or $\{112\}\langle 111\rangle$ and $\{110\}\langle 111\rangle$. The scale is according to the experimental ones. The shape change of the grains is not reflected. 62

3.4 a)-d) Comparison between observed experimental deformation (red thinner lines) for $\alpha_\mathrm{P} \approx \{1.5\%, 4\%, 10\%, 19.5\%\}$ to simulation results (black thicker lines) for different active glide system classes ($\{110\}\langle 111\rangle$(left), $\{112\}\langle 111\rangle$(middle), $\{110\}\langle 111\rangle$ and $\{112\}\langle 111\rangle$(right)) without hardening. 63

3.5 Optical photograph of the sample at $\alpha_\mathrm{P} \approx 40\%$ Henning and Vehoff (2005). . . 64

3.6 Reorientation field β for $\alpha_\mathrm{P} \approx \{1.5\%, 4\%, 10\%, 19.5\%\}$ for active glide systems $\{112\}$+$\{110\}$(left) or $\{112\}$ (middle) alone or $\{110\}$(right) alone, respectively, without hardening. 65

3.7 Stress distribution at $\alpha_\mathrm{P} \approx 40\%$ with distorted finite element mesh 65

3.8 Comparison between observed experimental deformation (red thinner lines) Henning and Vehoff (2005) for $\alpha_\mathrm{P} \approx \{1.5\%, 4\%, 10\%, 19.5\%\}$ to simulation results (black thicker lines) for glide system classes $\{110\}\langle 111\rangle$ and $\{112\}\langle 111\rangle$ separately and simultaneously active with included hardening. 66

3.9 Reorientation field β for $\alpha_\mathrm{P} \approx \{1.5\%, 4\%, 10\%, 19.5\%\}$ for glide system classes $\{110\}\langle 111\rangle$ and $\{112\}\langle 111\rangle$ separately and simultaneously active with included hardening. 68

4.1 Decomposition of the total deformation gradient 71

4.2 (a)(e) Orientation gradient max(θ_x,θ_y) in (°) for $\alpha_\mathrm{P} \approx \{0\%, 1.5\%, 4\%, 10\%, 19.5\%\}$. The regions in black indicate failure of automatic orientation estimation. (Henning and Vehoff, 2005). 74

4.3 FE mesh used for simulations with grains numbered (Henning, 2008). 75

4.4 Averaged Schmid-factor $S_\mathrm{fac,avg}$ in the single grains for a) $\{110\}\langle 111\rangle$ and b) $\{123\}\langle 111\rangle$ glide system for a test-loading in $[010]$ direction for the initial specimen. The same qualitative results as for $\{110\}\langle 111\rangle$ are obtained for $\{112\}\langle 111\rangle$ glide systems 78

4.5 Taylor-factor T in the single grains for a) $\{110\}\langle 111\rangle$, b) $\{112\}\langle 111\rangle$ and c) $\{110\}\langle 111\rangle$ and $\{112\}\langle 111\rangle$ glide systems for a test-loading in $[010]$ direction. 78

4.6 Simulation results without hardening for $\|\mathrm{mag}(\boldsymbol{L}_\mathrm{P})\|$ for $\alpha_\mathrm{P} \approx \{1.5\%, 4\%, 10\%, 19.5\%\}$ for active glide system $\{112\}$+$\{110\}$(left) or $\{112\}$(middle) alone or $\{110\}$(right) alone, respectively. The legend is constant for all deformation stages. (red=$10^{-6}s^{-1}$, blue=$0s^{-1}$) . . . 79

4.7 Sum of GND densities $\sum_a \varrho_a$ of all systems without hardening for $\alpha_\mathrm{P} \approx \{1.5\%, 4\%, 10\%, 19.5\%\}$ for active glide systems $\{112\}$+$\{110\}$(left) or $\{112\}$(middle) alone or $\{110\}$(right) alone, respectively. . . . 80

4.8 Orientation gradient for $\Delta\theta_\infty$ in ° for $\alpha_\mathrm{P} \approx \{1.5\%, 4\%, 10\% \, 19.5\%\}$ for active glide systems $\{112\}$ and $\{110\}$ without hardening. . . . 81

4.9 Reorientation field β in ° for $\alpha_\mathrm{P} \approx \{1.5\%, 4\%, 10\%, 19.5\%\}$ for active glide systems $\{112\}$+$\{110\}$(left) or $\{112\}$(middle) alone or $\{110\}$(right) alone, respectively, without hardening. . . . 82

4.10 Simulation results for $\|\mathrm{mag}(\boldsymbol{L}_\mathrm{P})\|$ for $\alpha_\mathrm{P} \approx \{1.5\%, 4\%, 10\%, 19.5\%\}$ for glide systems $\{112\}$ and $\{110\}$ simultaneously and separately active with included hardening. The legend is constant for all deformation stages. (red=$10^{-6}s^{-1}$, blue=$0s^{-1}$) . . . 83

4.11 Orientation gradient for $\Delta\theta_\infty$ in ° for $\alpha_\mathrm{P} \approx \{1.5\%, 4\%, 10\% \, 19.5\%\}$ for active glide systems $\{112\}$ and $\{110\}$ with included hardening. . . . 83

4.12 Sum of GND densities $\sum_a \varrho_a$ of all systems for $\alpha_\mathrm{P} \approx \{1.5\%, 4\%, 10\% \, 19.5\%\}$ for active glide systems $\{112\}$ and $\{110\}$ with included hardening. . . . 84

4.13 Reorientation field β in ° for $\alpha_\mathrm{P} \approx \{1.5\%, 4\%, 10\%, 19.5\%\}$ for glide system classes $\{110\}\langle 111\rangle$ and $\{112\}\langle 111\rangle$ separately and simultaneously active with included hardening. . . . 85

5.1 Overview of indentations for a depth of 100 nm - TWAS WC-FeCSiMn coating. 90

5.2 Detail view of analyzed point of indentation into FTC for a depth of 100nm and corresponding EDX analysis. . . . 90

5.3 Detail view of analyzed point of indentation into FeCSiMn for a depth of 100 nm and corresponding EDX analysis. . . . 91

5.4 Finite element mesh of indenter and coating. . . . 92

5.5 Comparison between experimental and simulation data for indentation into FTC and an indentation depth of 100nm. . . . 92

5.6 a) An exemplary micrograph obtained from a wire (AS-850) arc-sprayed coating with SEM. b) Distinguished material phases. c) Cleaned Image. d) FE-mesh on microstructure. . . . 95

5.7 Predicted effective Young's modulus calculated from real microstructures compared (HD = parallel to lamellar structure, ND= perpendicular to lamellar structure) with results from different homogenization techniques. (HS+ = upper Hashin-Shtrinkman bound, HS- = lower Hashin-Shtrinkman bound). . . . 97

A.1 The inclusion has undergone a stress-free transformation, eigenstrain $\boldsymbol{E}^*$, and has been placed back in the matrix. The matrix constrains the inclusion forcing it to assume a final strain $\boldsymbol{E}$, which can be related to $\boldsymbol{E}^*$ using the Eshelby tensor $\mathcal{S}$ (dark area represents embedded inclusion). 100
A.2 The inclusion and matrix consists of two different materials. The eigenstrain can occur due to a change in temperature or a phase transformation, etc.. The equivalent imaginary problem is constructed in the way that the inclusion and matrix have identical material properties so that the Eshelby formula can be applied, as shown on the right. 100
A.3 a) Ellipsoidal inclusion embedded in a matrix. b) Homogeneous material with eigenstrain subjected to an applied external load 101
A.4 Principle of homogenization and different length scales 102
A.5 Micro fluctuation fields on the RVE boundary and their average. 103

B.1 The most important lattice structures of metals (bcc, hcp, fcc) (Bauser et al., 2001). 107
B.2 Miller indices (Bauser et al., 2001). 108
B.3 Different types of point defects 109
B.4 Different types of line defects: a) edge dislocation b) screw dislocation (Bauser et al., 2001). 110
B.5 Different types of grain boundaries: a) low angle grain boundary ($\alpha < 15°$) b) high angle grain boundary (Bauser et al., 2001). 110
B.6 Different deformation behavior when applying shear stress: a) elastic deformation b) plastic deformation (Bauser et al., 2001). 111
B.7 Frank-Read mechanism (Bauser et al., 2001). 111
B.8 Determining the Schmid-factor (Shackelford and Sullivan, 2005). 112

C.1 Kinematics: Deformation map ϕ maps the reference configuration $\mathcal{B}_{\text{ref}}$ to the current configuration $\mathcal{B}_{\text{cur}}$ and the deformation map Φ maps vice versa. 114
C.2 Decomposition of the total deformation gradient. 115

List of Tables

2.1 Material properties of the two phases in the model microstructure. $\sigma_{\mathrm{D}} = 100\mathrm{MPa}$ and $\dot{\alpha}_{\mathrm{r}} = 0.001 s^{-1}$ are for both phases the same. 38

3.1 Material properties of Fe-3%Si (BCC) (Routbort et al., 1971). 58

3.2 Material properties of hardening of Fe-3%Si (BCC) fitted to the experimental results of Hull (1963). 59

4.1 Material properties of Fe-3%Si (BCC) (Routbort et al., 1971). 75

4.2 Material properties of hardening of Fe-3%Si (BCC) fitted to the experimental results of Hull (1963). 75

5.1 Identified mechanical properties of single chemical composition for AS-850. . . 93

5.2 WC-FeCSiMn Youngs moduli for compression stresses. 94

Summary

In the first part of this work homogenization methods in the context of linear elasticity are considered. Classical homogenization methods are compared on the basis of the contrast in the elastic properties of the constituents for spherical inclusion. It is shown that this has a significant influence on the accuracy of the homogenization methods. In the following three strategies for dealing with irregular shaped inclusions in the context of homogenization methods are investigated, namely homogenization methods using an analytical description for the Eshelby tensor, the Mori-Tanaka method with replacement tensor approach (RMTM) and the direct discretization of a real microstructure. The study shows that the RMTM method is very good agreement with FE-results whereas the analytical description did not predict the correct behavior for all shapes. For a real microstructure the direct discretization is the best strategy.

In the second part a homogenization method for the material behavior of two-phase composites characterized by a thin-layer-type microstructure is introduced. The basic idea here is to idealize the thin-layered microstructure as a first-order laminate. Comparison of the method with existing homogenization schemes as well as with the reference finite-element model for idealized composites demonstrates the advantage of the current approach for such microstructures. Further a first extension to a variable interface orientation is given.

The third and fourth part deal with the application of a crystal plasticity material model to a thin sheet metal specimen with large grains subjected to a tensile test. To this end an explicit finite-element-, crystal-plasticity-based model is developed for each grain, the grain morphology, and the thin sheet specimen as a whole. In particular, the crystal plasticity model is rate-dependent and accounts for (local) dissipative hardening effects. The predictions of the model are compared with experimental results of Henning and Vehoff (2005) for the deformation behavior of thin sheets of Fe-3%Si loaded incrementally in tension as well as for further properties like the orientation gradient. To this end attention is restricted to the two slip families $\{110\}$ and $\{112\}$. At the beginning all hardening is neglected. Even for this oversimplified case a good correlation with the experimental results is obtained. Even better agreement is obtained with experiment when hardening is included. Results for GNDs, OGM and local orientation changes are investigated and discussed.

The last part of this work deals with the characterization and parameter identification of single constituents in thermal sprayed coatings as well as for whole coatings. Based on results in nanoindentation tests the Youngs modulus as well as further mechanical properties are identified for each constituent. A general procedure is presented to predict the effective mechanical properties based on the microstructure, porosity, chemical composition and properties of the coating after thermal spraying.

Zusammenfassung

Im ersten Kapitel der Arbeit werden Homogenisierungsmethoden im Kontext linearer Elastizität betrachtet. Klassische Homogenisierungsmethoden werden untersucht und für sphär-ische Einschlüsse in Hinblick auf den Unterschied in den elastischen Eigenschaften der einzelnen Materialphasen verglichen. Es wird gezeigt, dass dieser einen entscheidenden Einfluss auf die Genauigkeit der Homogenisierungsmethoden hat. Im Folgenden werden drei Strategien für den Einsatz von Homogenisierungsmethoden für nicht-ellipsoide Einschlüsse diskutiert und untersucht. Zum Einen wird eine analytische Vorgehensweise für die Ermittlung des Eshelby-Tensors, zum Zweiten die Mori-Tanaka Methode mit einem Ersatztensoransatz (RMTM) und zum Schluss eine direkte Diskretisierung anhand der realen Mikrostruktur diskutiert. Die Studie zeigte, dass die RMTM die beste Vorhersage gegenüber den FE-Resultaten liefert. Die analytische Vorgehensweise lieferte für einige Einschlusstypen nicht sehr brauchbare Ergebnisse. Für eine reale Mikrostruktur ist die direkte Diskretisierung als beste Strategie anzusehen.

Im zweiten Kapitel der Arbeit wird eine Homogenisierungsmethode für einen zweiphasigen Verbundwerkstoff vorgestellt, welcher durch eine dünne schichtartige Mikrostruktur gekennzeichnet ist. Die grundsätzliche Idee ist die Idealisierung dieser Mikrostruktur mittels erster-Ordnung Laminate. Vergleiche mit existierenden Homogenisierungsmethoden sowie einem RVE für solche Mikrostrukturen zeigen die Vorteile der vorgestellten Modellierung. Des Weiteren ist eine erste Erweiterung für variable Interfacerichtungen gegeben.

Das dritte und vierte Kapitel dieser Arbeit behandeln die Anwendung eines Kristallplastizitätsmodells auf einen Zugversuch von dünnen Blechproben mit großen Körnern. Zu diesem Zweck ist ein explizites Finite-Element-Modell, basierend auf Kristallplastizität, entwickelt worden. Im Besonderen, ist das Kristallplastizitätsmodell dehnratenabhängig und berücksichtigt lokale dissipative Verfestigungsaspekte. Die Simulationsergebnisse werden mit experimentellen Ergebnissen von Henning and Vehoff (2005) bzgl. des Deformationsverhaltens von Blechen aus Fe-3%Si, welche durch inkrementellen Zug belastet worden sind, verglichen. Hierbei werden nur die zwei Gleitsystemfamilien $\{110\}$ und $\{112\}$ betrachtet. Zu Beginn wird keine Verfestigung berücksichtigt. Schon für diesen vereinfachten Fall wird eine gute Übereinstimmung mit den experimentellen Ergebnissen bzgl. des Deformationsverhaltens erzielt. Eine noch bessere Übereinstimmung zeigen die Resultate mit aktiver Verfestigung. Ergebnisse bzgl. geometrisch notwendiger Versetzungen, dem Orientierungsgradienten sowie lokalen Orientierungsänderungen werden untersucht und diskutiert.

Das letzte Kapitel der Arbeit behandelt die Charakterisierung und Parameteridentifikation von einzelnen Materialbestandteilen in thermisch gespritzten Schichten. Basierend auf den Ergebnissen aus Nanoindentation werden der E-Modul sowie weitere Materialeigenschaften für jeden Bestandteil identifiziert. Eine Methode, die effektiven Eigenschaften der Beschichtung, basierend auf ihrer Mikrostruktur, Porosität und chemischer Zusammensetzung zu ermitteln, wird vorgestellt.

Chapter 1

Comparison of homogenization methods in the context of multi-phase elastic composites with variable shape [*]

Abstract– In this chapter homogenization methods in the framework of linear elasticity are discussed. Classical homogenization methods are recalled and compared on the basis of the contrast in the elastic properties of the constituents for spherical inclusions. It is shown that this contrast has a significant influence on the accuracy of the homogenization methods. Furthermore two recently developed approaches, the ESCS and IDD method, are compared to standard homogenization schemes as well as corresponding finite element results. In the following three strategies for the homogenization of materials with irregularly shaped inclusions are investigated. Homogenization approaches are used in combination with an analytical expression for the Eshelby tensor based on its irreducible decomposition. The second strategy to be investigated is the Mori-Tanaka method with replacement tensor approach which is based on the result of a calculation of a dilute inclusion embedded in an infinite matrix. Subsequently the third approach, namely the direct discretization of a real microstructure via finite-elements, is discussed. Numerous comparisons are carried out in order to compare the different strategies mentioned above appropriately.

1.1 Introduction

The prediction of the macroscopic stress-strain response of composite materials is related to the description of their complex microstructural behavior exemplified by the interaction between the constituents. In this context, the microstructure of the material under consideration is basically taken into account by representative volume elements (RVE). In previous decades and especially in the absence of computers, analytical and semi-analytical approximations based on RVEs and mean-field homogenization schemes were developed. Mean-field homogenization methods were first developed in the framework of linear elasticity and are now well-established. These schemes provide efficient and straight forward algorithms for the prediction of, among other properties, the elastic constants. These include for example the Mori-Tanaka method (Mori and Tanaka, 1973) and the interpolative double inclusion method (IDIM) (Pierard et al., 2004). For elastic-plastic behavior, there is for example the self consistent scheme (Mercier and Molinari, 2009; Molinari et al., 1987). Moreover, the results obtained can be shown to be upper or lower bounds to the true solution of the underlying problem in most cases (e.g., Voigt-Reuss,

---

[*] results partly published in Klusemann and Svendsen (2010)

Hashin-Shtrikman bounds, see Gross and Seelig, 2001; Nemat-Nasser and Hori, 1999). All these methods are based on two steps to predict the macroscopic response. In a first step, a local problem for a single inclusion is solved in order to obtain approximations for the local field behavior as outlined by Eshelby for elastic fields of an ellipsoidal inclusion (Eshelby, 1957). The second step consists of averaging the local fields to obtain the global ones (e.g. Mercier and Molinari, 2009).

In this context, the main requirements on homogenization methods for predicting the effective properties, according to Zheng and Du (2001) are

a) a simple structure which can be solved explicitly, such that a physical interpretation for the behavior of all the components involved is possible;

b) a valid structure for multiphase composites with various inclusion geometries, isotropy and anisotropy;

c) an accurate model for the influence of various inclusion distributions and interactions between inclusions and their immediate surrounding matrix.

However, none of the aforementioned methods is actually able to fulfill these requirements completely. The major disadvantages of these methods are exemplified by the fact that inclusion distributions are unaccounted for and that the properties of the surrounding matrix material do not enter these methods directly. An interesting approach was presented by Guinovart-Díaz et al. (2005), namely the recursive asymptotic homogenization scheme (RAHS), which takes the variation of properties around cylindrical fibers into account by using multi-phase fibrous elastic composites, wherein the constituents exhibit transverse isotropy.

A new micromechanical model has been proposed by Zheng and Du (2001), namely the so-called effective self-consistent scheme (ESCS), which is based on the three-phase model which corresponds to the generalized self-consistent scheme (GSCS) (see Christensen, 1990). In the three-phase model, the inclusion is embedded in a matrix which itself is embedded in an unbound, initially unknown effective medium. This GSCS method fulfills requirements b) and c) but is still rather complicated in terms of its application due to its implicit structure and furthermore restricted to spherical or cylindrical inclusion. The ESCS overcomes the restriction of spherical and cylindrical inclusions and still fulfills requirements b) and c) from above. However, its structure is as well rather complicated. A simplified and explicit version of the ESCS method, which is referred to as the Interaction Direct Derivative (IDD) estimate, was proposed satisfying all three requirements Zheng and Du (2001). This method has a simple structure with physical meaning of the single constituent parts. Du and Zheng (2002); Zheng and Du (2001) show results for void distribution, although the formulation is also valid for spherical inclusions. This encourages a first discussion of this method regarding the inclusion as well as its comparison to classical homogenization schemes presented in this chapter.

A key point for the determination of the effective elastic properties of heterogeneous materials is the investigation of the influence of single inclusions on the macroscopic stiffness. In materials science applications, inhomogeneities may have irregular non-ellipsoidal shapes which invalidate the analytical solution based on on the work of Eshelby (1957). The remarkable result found by Eshelby was that the Eshelby tensor field $\mathcal{S}^{\omega}(\boldsymbol{x})$ is uniform inside a 2D ellipse or 3D ellipsoidal domain ω embedded into an isotropic medium. In Gavazzi and Lagoudas (1990) a numerical scheme was presented for an ellipsoidal inclusion embedded into an anisotropic matrix. For the case of irregular inclusions embedded into an isotropic matrix Rodin (1996) proved the impossibility of Eshelby's uniformity result for any domain with corners and Markenscoff (1997) proved it for domains with flat surface segments. Recently Kang and Milton (2008) and Liu (2008) proved this result for any irregular inclusion. In general three approaches can be found in the literature for solving the problem of irregular inhomogeneities which can generally be classified as follows:

- Analytical procedures for estimating the Eshelby tensor.

  Rodin (1996) presented an algorithmic closed-form solution to a problem of classical elasticity for an infinite homogeneous body that contains a polyhedral subdomain subject to a uniform transformation strain. In this work the Eshelby tensor was derived by a double or triple integral which was evaluated by dividing the inclusions into two- or three dimensional rectangular simplexes. Nozaki and Taya (1997, 2001) proposed a procedure for phase averaging the Eshelby tensor for inclusions with fluctuating microfields. A complex variable approach to the Eshelby problem is described in Tsukrov and Novak (2001, 2004), Kawashita and Nozaki (2001) and Ru (1999).

- Direct computation of the effective elastic properties for a given microstructure by discretizing the domain and using FEM.

  Arns et al. (2002) presented a comparison between results for the elastic property-porosity relationship derived directly from microtomographic images with analytical results. A similar approach was applied by Tillmann et al. (2010a) and Klusemann et al. (2009a) for evaluating the elastic properties in thermal sprayed coatings.

- Computation of the contribution of one isolated inclusion into an infinite matrix material and application to the effective behavior.

  Such an approach is used in combination with the Mori-Tanaka method to predict the thermal conductivity of diamond reinforced composites by Nogales and Böhm (2008). This method is an alternative approach to the compliance contribution formalism of Kachanov et al. (1994). Sevostianov et al. (2008) discussed the evaluation of the effective stiffness as a function of the shape factor concavity-convexity in this context.

The outline of this chapter is as follows: First the basic idea of homogenization methods is discussed followed by an overview on the ESCS and IDD approach. A comparison of different homogenization schemes with FE-results for different volume fractions of spherical inclusions as well as different stiffness ratios are provided in section 1.3. In section 1.4 three approaches for dealing with irregular shaped inclusions, one based on an analytical evaluation of the Eshelby tensor, one based on calculating the contribution of one isolated inclusion into an infinite matrix and one method to discretize the microstructure directly, are described. A comparison of these methods for different inclusion shapes with FE results is given in the following. The chapter concludes with a summary and outlook.

Before we begin, a short word to notation. Use will be made of the dyadic or tensor product $(\boldsymbol{a} \otimes \boldsymbol{b})\boldsymbol{c} := (\boldsymbol{b} \cdot \boldsymbol{c})\boldsymbol{a}$ of any non-zero Euclidean vector $\boldsymbol{a}$. Basic operations on second-order Euclidean tensors $\boldsymbol{A}$ used here includes symmetrization $\mathrm{sym}(\boldsymbol{A}) := \frac{1}{2}(\boldsymbol{A} + \boldsymbol{A}^{\mathrm{T}})$. The orthogonal additive split $\boldsymbol{A} := \mathrm{sph}(\boldsymbol{A}) + \mathrm{dev}(\boldsymbol{A})$ of any $\boldsymbol{A}$ into spherical $\mathrm{sph}(\boldsymbol{A}) := \frac{1}{3}\mathrm{tr}(\boldsymbol{A})\boldsymbol{I}$ and deviatoric $\mathrm{dev}(\boldsymbol{A}) := \boldsymbol{A} - \frac{1}{3}\mathrm{tr}(\boldsymbol{A})\,\boldsymbol{I}$ parts is used.

1.2 Determination of effective elastic properties

Basically, a macroscopic material point at a position $\boldsymbol{X}$ in a fixed Cartesian frame is considered next. In linear elasticity the macroscopic stresses $\boldsymbol{T}^{\mathrm{macro}}$ and strains $\boldsymbol{E}^{\mathrm{macro}}$ are related via the macroscopic elasticity tensor $\mathcal{C}_{\mathrm{macro}}$ with

$$\boldsymbol{T}^{\mathrm{macro}} = \mathcal{C}_{\mathrm{macro}}\boldsymbol{E}^{\mathrm{macro}}. \tag{1.1}$$

Homogenization procedures are mainly based on the definition of a local surrounding of a macroscopic material point with microscopic volume V and the boundary ∂V. This volume V represents a characteristic part of the material in terms of its structure and behavior, respectively. This implies that the size of heterogeneities at the microlevel is at least one order of magnitude smaller than the size of the volume V of the macropoint. As it is shown by Nemat-Nasser and Hori (1999) and Gross and Seelig (2001) the Hill-Mandel condition is fulfilled by applying linear displacement, periodic, uniform traction or mixed boundary conditions (Pahr and Zysset, 2008) on ∂V.

The previous explanation emphasizes that the macro elasticity tensor $\mathcal{C}_{\mathrm{macro}}$ averages out the heterogeneities on the microlevel and characterizes a homogenous behavior at the macroscopic level. The constitutive law from the microlevel

$$\boldsymbol{T}(\boldsymbol{x}) = \mathcal{C}(\boldsymbol{x})\,\boldsymbol{E}(\boldsymbol{x}) \tag{1.2}$$

can be rewritten to the macroscale

$$\langle \boldsymbol{T} \rangle = \mathcal{C}^*\,\langle \boldsymbol{E} \rangle \tag{1.3}$$

with the effective elasticity tensor $\mathcal{C}^* = \mathcal{C}_{\mathrm{macro}}$ for a multiphase composite consisting of n phases, $c_\alpha = V_\alpha/V$ denotes the volume fraction of each phase α with respect to the total volume V of the RVE, which are subjected to the restriction $\sum_{\alpha=1}^{n} c_\alpha = 1$. The effective elasticity tensor has to be approximated for what often mean-field methods are used. These methods provide relatively simple models to approximate the overall behavior of the composites where the fields on the microscale entering these methods by their phase averages. Most of the used mean-field homogenization methods are shown schematically in Figure 1.1. The exact formulation of the more standart methods can be taken from the literature (Gross and Seelig, 2001; Nemat-Nasser and Hori, 1999; Pierard et al., 2004) or can also be found in A.2. The following provides an overview on the recently developed ESCS and IDD approach by Zheng and Du (2001).

1.2.1 ESCS and IDD approach

Effective self-consistent scheme (ESCS)

The effective self-consistent scheme (ESCS), proposed by Zheng and Du (2001) is based on the three-phase model. In the three-phase model the average stress $\langle \boldsymbol{T} \rangle_i$ over all type-i in-

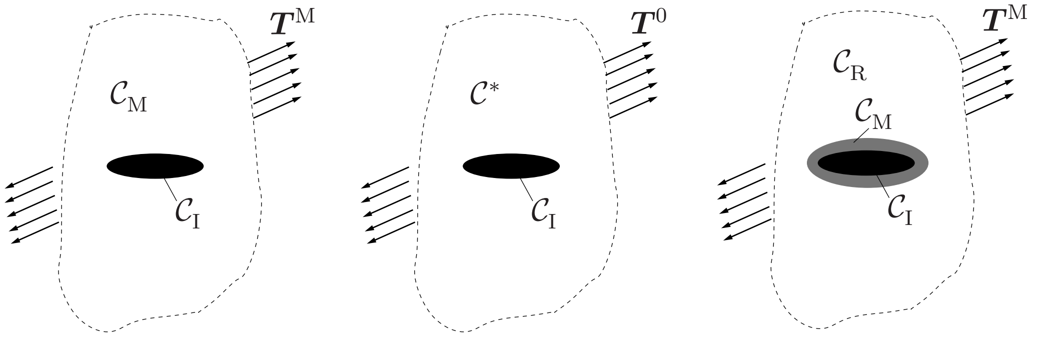
$\boldsymbol{T}^{\mathrm{M}}$
$\mathcal{C}_{\mathrm{M}}$
$\mathcal{C}_{\mathrm{I}}$
$\boldsymbol{T}^{0}$
$\mathcal{C}^{*}$
$\mathcal{C}_{\mathrm{I}}$
$\boldsymbol{T}^{\mathrm{M}}$
$\mathcal{C}_{\mathrm{R}}$
$\mathcal{C}_{\mathrm{M}}$
$\mathcal{C}_{\mathrm{I}}$

a) Mori-Tanaka b) Self-consistent c) IDIM: $\mathcal{C}_{\mathrm{R},1} = \mathcal{C}_{\mathrm{M}}$; $\mathcal{C}_{\mathrm{R},2} = \mathcal{C}_{\mathrm{I}}$

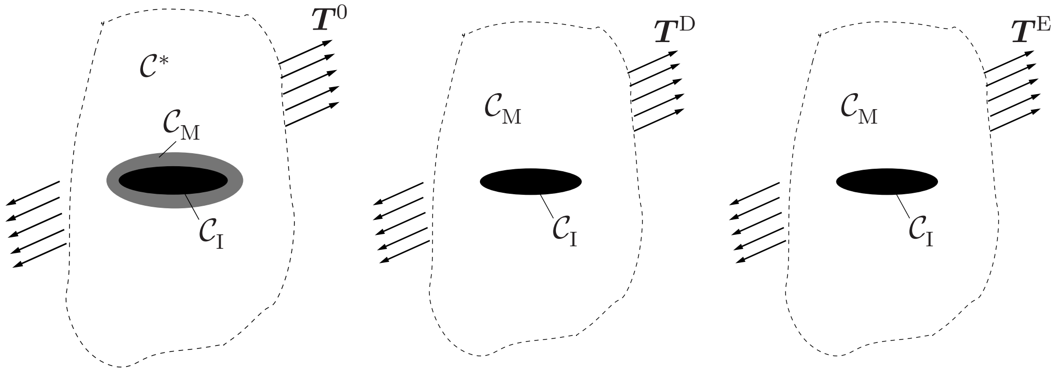
$\boldsymbol{T}^{0}$
$\mathcal{C}^{*}$
$\mathcal{C}_{\mathrm{M}}$
$\mathcal{C}_{\mathrm{I}}$
$\boldsymbol{T}^{\mathrm{D}}$
$\mathcal{C}_{\mathrm{M}}$
$\mathcal{C}_{\mathrm{I}}$
$\boldsymbol{T}^{\mathrm{E}}$
$\mathcal{C}_{\mathrm{M}}$
$\mathcal{C}_{\mathrm{I}}$

d) three phase model (GSCS) e) ESCS f) IDD

Figure 1.1: A schematic overview on different homogenization schemes for estimating the average stress or strain, respectively.

clusions is estimated by embedding a single inclusion i in a finite matrix material, the matrix atmosphere, which is in turn embedded in the unbounded unknown effective medium, shown in Figure 1.2 a). In the following the inclusion together with its matrix atmosphere will be called inclusion-matrix cell and will be denoted by a subscript 'D', which implies that this cell has to be representative for an inclusion distribution.

Shortly recall the assumptions made in order to obtain the effective elasticity tensor for this method. For a more detailed description see Du and Zheng (2002). The volume V is subjected to the uniform stress distribution $\boldsymbol{T}^{0}$. In the first step it is assumed that the inclusion-matrix cell only consists of the matrix material, leading to stress and strain being uniform according to the Eshelby theorem and taking the form

$$\boldsymbol{E}_i^{\mathrm{D}} = \mathcal{C}_{\mathrm{M}}^{-1} \boldsymbol{T}_i^{\mathrm{D}}, \qquad \boldsymbol{T}_i^{\mathrm{D}} = \left(\mathcal{I} - \Omega_{\mathrm{D}i} \mathcal{H}\right)^{-1} \boldsymbol{T}^{0} \tag{1.4}$$

where $\Omega_{\mathrm{D}i}$ is the eigenstiffness tensor of the cell with respect to the unknown effective medium which is also often referred as dual of the polarization factor tensor, and $\mathcal{H}$ describes the compliance increment, defined by

$$\mathcal{H} = \mathcal{C}^{*-1} - \mathcal{C}_{\mathrm{M}}^{-1}. \tag{1.5}$$

$\Omega_{\mathrm{D}i}$ is calculated by

$$\Omega_{\mathrm{D}i} = \mathcal{C}^{*} (\mathcal{I} - \mathcal{S}_i^{*}) \tag{1.6}$$

where $\mathcal{S}_i^{*}$ denotes the Eshelby tensor for the cell embedded into the unknown effective material.

In the next step the uniform strain $\boldsymbol{E}_i^{\mathrm{D}}$ has to be incorporated in the original three-phase model problem, by applying extra tractions $\boldsymbol{\tau}_i^{\mathrm{D}}\boldsymbol{n}$, with the outward normal $\boldsymbol{n}$ on the inclusion boundary. This additional stress contribution is calculated by

$$\boldsymbol{\tau}_i^{\mathrm{D}} = (\mathcal{C}_{\mathrm{I},i} - \mathcal{C}_{\mathrm{M}})\boldsymbol{E}_i^{\mathrm{D}}. \tag{1.7}$$

As depicted in Figure 1.2 b) and c) the solution for the original problem is thus obtained by

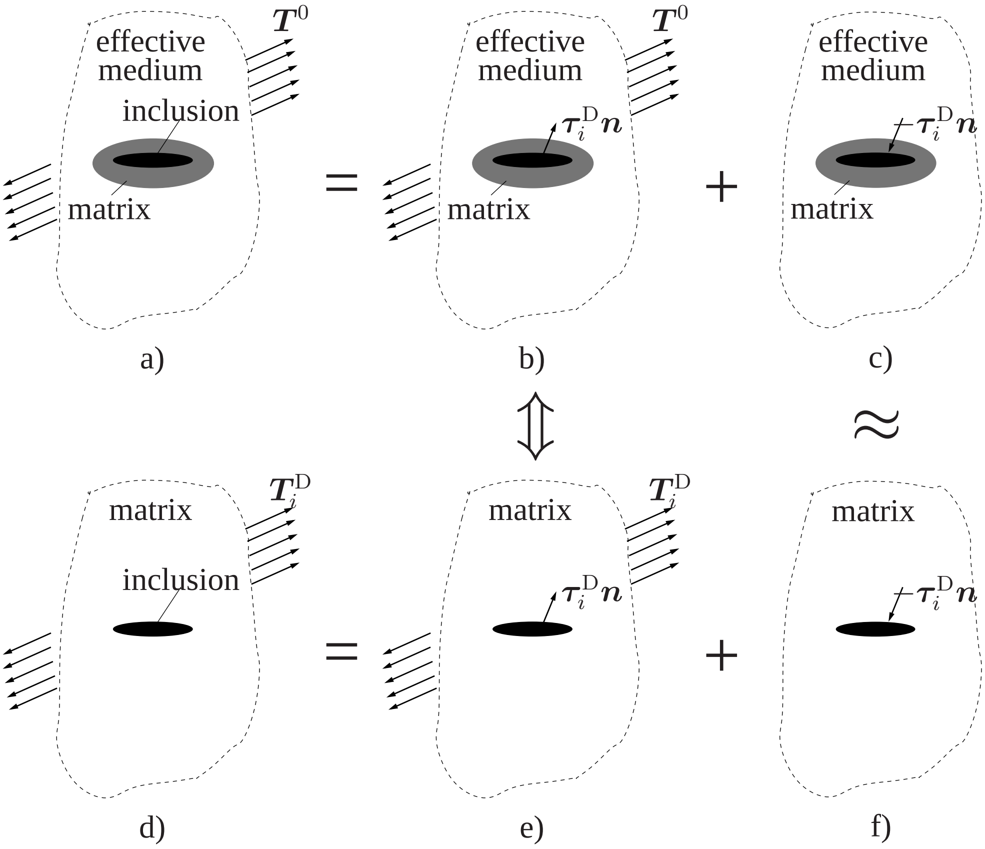
$\boldsymbol{T}^0$
effective medium
inclusion
matrix
=
$\boldsymbol{T}^0$
effective medium
$\boldsymbol{\tau}_i^{\mathrm{D}}\boldsymbol{n}$
matrix
+
effective medium
$\boldsymbol{\tau}_i^{\mathrm{D}}\boldsymbol{n}$
matrix
a)
b)
c)
⇕
≈
matrix
$\boldsymbol{T}_i^{\mathrm{D}}$
inclusion
=
matrix
$\boldsymbol{T}_i^{\mathrm{D}}$
$\boldsymbol{\tau}_i^{\mathrm{D}}\boldsymbol{n}$
+
matrix
$\boldsymbol{\tau}_i^{\mathrm{D}}\boldsymbol{n}$
d)
e)
f)

Figure 1.2: A schematic overview on the ESCS approach (Zheng and Du, 2001).

the superposition of two separate problems. A key ingredient in order to establish the ESCS estimate is the approximation of the average stress, denoted by $\boldsymbol{T}_i^*$ within the inclusion for the decomposed problem as shown in Figure 1.2 c). In Du and Zheng (2002) it has been shown, that this average stress $\boldsymbol{T}_i^*$ can be approximated by an average stress, denoted by $\boldsymbol{T}_i^{'}$, which occurs in a two-phase reference problem where the effective medium is replaced by the matrix material as shown in Figure 1.2 f). The error due to this approximation is in the second order in c.

By definition, the stress and strain are uniform in the matrix atmosphere in Figure 1.2 b) and equal to $\boldsymbol{T}_i^{\mathrm{D}}$ and $\boldsymbol{E}_i^{\mathrm{D}}$. Therefore a two-phase model with a single inclusion embedded in the unbounded matrix material is considered, which is subjected to a uniform stress field $\boldsymbol{T}_i^{\mathrm{D}}$ and $\boldsymbol{\tau}_i^{\mathrm{D}}\boldsymbol{n}$ on the boundary of the inclusion. The obtained strain field is constant and equal to $\boldsymbol{E}_i^{\mathrm{D}}$. Therefore the problems in Figure 1.2 b) and e) are completely equivalent. Next the superposition of the two problems illustrated in Figure 1.2 e) and f) leads to a much simpler problem of the matrix-inclusion problem. The average stress over the inclusion results in

$$\langle \boldsymbol{T} \rangle_i^{\mathrm{escs}} = \left(\mathcal{I} + \Omega_i^{\mathrm{M}} \mathcal{H}_i\right)^{-1} \left(\mathcal{I} - \Omega_{\mathrm{D}i} \mathcal{H}\right)^{-1} \boldsymbol{T}^0. \tag{1.8}$$

As mentioned before, the substitution of the problem in Figure 1.2 c) by e) leads to an error of $O(c^2)$ compared to $\langle \boldsymbol{T} \rangle_i^{\mathrm{escs}}$ and the exact average stress $\langle \boldsymbol{T} \rangle_i$ in the inclusion for the whole estimate. Therefore $\langle \boldsymbol{T} \rangle_i$ can be replaced by $\langle \boldsymbol{T} \rangle_i^{\mathrm{escs}}$. The average strain tensor $\langle \boldsymbol{E} \rangle$ can be expressed by (see Nemat-Nasser and Hori (1993))

$$\langle \boldsymbol{E} \rangle = \mathcal{C}_{\mathrm{M}}^{-1} \boldsymbol{T}^0 + \sum_i c_i (\mathcal{C}_i^{-1} - \mathcal{C}_{\mathrm{M}}) \langle \boldsymbol{T} \rangle_i. \tag{1.9}$$

Adopting the strain-equivalence $\langle \boldsymbol{E} \rangle = \mathcal{C}^{*-1} \boldsymbol{T}^0$ yields to the relation

$$\mathcal{H} \boldsymbol{T}^0 = \sum_i \mathcal{H}_i \langle \boldsymbol{E} \rangle_i, \tag{1.10}$$

where $\mathcal{H}_i$ are defined as the compliance fluctuations

$$\mathcal{H}_i = \mathcal{C}_i^{-1} - \mathcal{C}_{\mathrm{M}}. \tag{1.11}$$

Using (1.11) together with (1.4) leads to an implicit equation for the compliance increment represented by

$$\mathcal{H} = \mathcal{H}_i^{\mathrm{d}} \left(\mathcal{I} - \Omega_{\mathrm{D}i} \mathcal{H}\right)^{-1} \tag{1.12}$$

which results in an error of third order dependent of c. $\mathcal{H}_i^{\mathrm{d}}$ can be interpreted as the dilute estimate and is calculated by

$$\mathcal{H}_i^{\mathrm{d}} = \sum_i c_i \left(\mathcal{H}_i^{-1} + \Omega_i^0\right)^{-1}. \tag{1.13}$$

This relation can therefore be used to determine the effective elasticity tensor $\mathcal{C}^*$, thereby obtaining the relation

$$\mathcal{C}^*_{(\mathrm{ESCS})} = \left(\mathcal{H} + \mathcal{C}_{\mathrm{M}}\right)^{-1}. \tag{1.14}$$

Zheng and Du (2001) showed that in the case that all $\Omega_{\mathrm{D},i}$ are identical, denoted by Ω_{D}, the solution of the ESCS method coincides with an effective stress model for the estimation of the average stress over any inclusion, which is embedded in the unbounded matrix material which is subjected to a modified uniform far-field stress $\boldsymbol{T}^{\mathrm{D}}$ given by

$$\boldsymbol{T}^{\mathrm{D}} = \left(\mathcal{I} - \Omega_{\mathrm{D}} \mathcal{H}\right)^{-1} \boldsymbol{T}^0 \tag{1.15}$$

rather than the real stress $\boldsymbol{T}^0$ which is also the physical explanation for the name prefix *effective* in the term of ESCS.

Interaction direct derivative (IDD)

Zheng and Du (2001) derived an explicit version for estimating $\mathcal{C}^*$ instead of an implicit equation like (1.14), namely the interaction direct derivative (IDD) estimate. First the right side of (1.12) is expanded to

$$\mathcal{H} = \mathcal{H}^{\mathrm{d}} + \sum_i \mathcal{H}_i^{\mathrm{d}} \Omega_{\mathrm{D}i} \mathcal{H}, \tag{1.16}$$

where $\mathcal{H}^{\mathrm{d}} = \sum_i \mathcal{H}_i^{\mathrm{d}}$. This yields to an error of third order in c. Due to the fact that $\Omega_{\mathrm{D}i}^{\mathrm{M}}$ is an approximation of $\Omega_{\mathrm{D}i}$ with an error of first order in c, this yields to the approximate solution

$$\mathcal{H}^{\mathrm{idd}} = \left(\mathcal{I} - \sum_i \mathcal{H}_i^{\mathrm{d}} \Omega_{\mathrm{D}i}^{\mathrm{M}} \right)^{-1} \mathcal{H}^{\mathrm{d}} \tag{1.17}$$

and the effective elasticity tensor

$$\mathcal{C}_{(\mathrm{idd})}^{*} = \left(\mathcal{H}^{\mathrm{idd}} + \mathcal{C}_{\mathrm{M}} \right)^{-1}. \tag{1.18}$$

This solution is called interactive direct derivative estimate for the effective elasticity tensor $\mathcal{C}_{(\mathrm{idd})}^{*}$. To estimate the average stress and strain, respectively, of any inclusion, this inclusion is embedded in the matrix material which is subjected to a modified remote boundary traction $\boldsymbol{T}^{\mathrm{E}}\boldsymbol{n}$ with

$$\boldsymbol{T}^{\mathrm{E}} = \left(\mathcal{I} - \sum_i \Omega_{\mathrm{D}i}^{\mathrm{M}} \mathcal{H}_i^{\mathrm{d}} \right)^{-1} \boldsymbol{T}^{0} \tag{1.19}$$

called the effective stress. As can be seen the IDD estimate $\mathcal{C}_{(\mathrm{idd})}^{*}$ has always an explicit structure, which only involves physical and quantitatively well-defined quantities due to its derivation. The IDD method is valid for any physically possible high concentration of inclusions and is also capable of taking any inclusion distribution into account. If the inclusions are of the same type a much easier form can be obtained (see Zheng and Du (2001)). In this case it can also be shown that the IDD and Mori-Tanaka estimate coincide with each other in the sense of energy-equivalence. Note that

$$\boldsymbol{T}^{\mathrm{M}} = \left(\mathcal{I} - \sum_i \Omega_i^{\mathrm{M}} \mathcal{H}_i^{\mathrm{d}} \right)^{-1} \boldsymbol{T}^{0} \tag{1.20}$$

represents the analogous expression to (1.19) in the context of the Mori-Tanaka method.

1.3 Comparison of different homogenization approaches for two-phase composites with spherical inclusions

Throughout this section we assume that the matrix and inclusion are isotropic and only two-phase composites in isothermal linear elasticity are considered. We compare the prediction of the macroscopic behavior of different classical mean-field homogenization methods with FE results obtained from a RVE. Furthermore we will investigate the prediction of these methods concerning different stiffness ratios of the inclusion-matrix pair. Finally a comparison is made regarding the ESCS and IDD method. Firstly the well-known mean field homogenization methods for two different stiffness ratios over the inclusion concentration are investigated. Figure 1.3 shows the predicted macroscopic elastic modulus E^* for a combination of $E_{\mathrm{M}} = 210$ GPa and $E_{\mathrm{I}} = 430$ GPa, where the subscript M is the matrix material and I the inclusion. In the following the Poisson ratio is assumed to be $\nu = 0.25$ for all phases. The concentration c describes the volume fraction of the inclusion. Figure 1.4 shows the predicted macroscopic elastic modulus E^* for a combination of $E_{\mathrm{M}} = 21$ GPa and $E_{\mathrm{I}} = 210$ GPa.

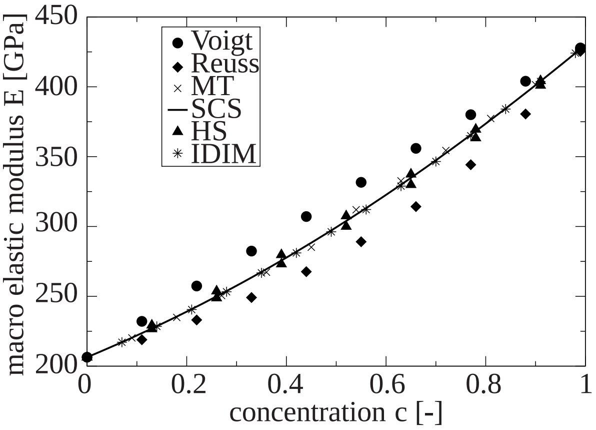

Figure 1.3: Prediction of effective Young's modulus E^* with different homogenization methods for $E_\mathrm{M} = 210$ GPa, $E_\mathrm{I} = 430$ GPa and $\nu = 0.25$. (MT = Mori-Tanaka; SCS = self-consistent; HS = Hashin-Shtrikman bounds; IDIM = interpolative double inclusion model)

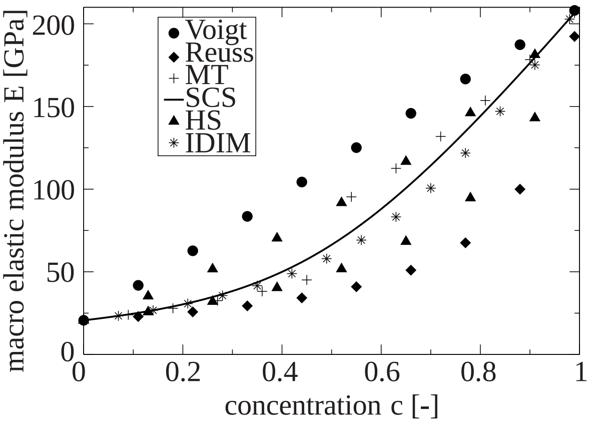

Figure 1.4: Prediction of effective Young's modulus E^* with different homogenization methods for $E_\mathrm{M} = 21$ GPa, $E_\mathrm{I} = 210$ GPa and $\nu = 0.25$. (MT = Mori-Tanaka; SCS = self-consistent; HS = Hashin-Shtrikman bounds; IDIM = interpolative double inclusion model)

As expected the different methods deviate distinctly from each other for a higher contrast in the material properties of the matrix and inclusion. For a small contrast, as shown in Figure 1.3 for a ratio of $\sim$2, only small differences in the prediction of the elastic modulus using the different methods can be seen. In this context we would like to emphasize the well-known fact, that the Voigt-bound represents the maximum upper bound whereas the Reuss-bound defines the minimum lower bound of the stiffness. Voigt and Reuss method predict in general a distinct different Young's modulus, which can already been seen for a small stiffness ratio. Numerous narrow bounds are provided by the Hashin-Shtrikman bounds where all other predictions are located. To be able to distinguish better between the different homogenization methods, we investigate the different methods on Figure 1.4 where the predictions are done for a stiffness ratio of 10. Here the difference between the methods is more clearly visible over the volume fraction. In this case the Hashin-Shtrikman bounds are also quite far from each other. The Mori-Tanaka method shows a jump in the predicted elastic modulus for concentrations around 50 % which results from the fact that in the Mori-Tanaka scheme the matrix material is defined as the material having the higher concentration. This shows that, depending on which material is considered to be the matrix material, the Mori-Tanaka estimate coincides with the lower (for matrix = softer material) or the upper (for matrix = harder material) Hashin-Shtrikman bound. For a small volume fraction of inclusions up to 30% the Mori-Tanaka, self-consistent and IDIM estimate nearly coincide with each other. However, with increasing volume fraction the difference in the predictions is rather pronounced. The reason for this is the different approximation of the effective properties which leads to errors from the first order upwards in c. This leads to wrong predictions for high volume fractions. Physically it is not possible to realize volume fractions higher than 74%, as known for face-centered cubic crystal structure, for equal spherical inclusions without letting the inclusion spheres intersect each other. In Castaneda and Willis (1995)

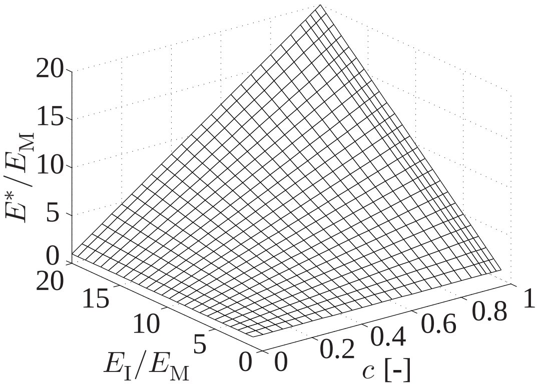

Figure 1.5: Prediction of effective Young's modulus E^* of Voigt method for different concentrations c and stiffness ratios $E_\mathrm{I}/E_\mathrm{M}$

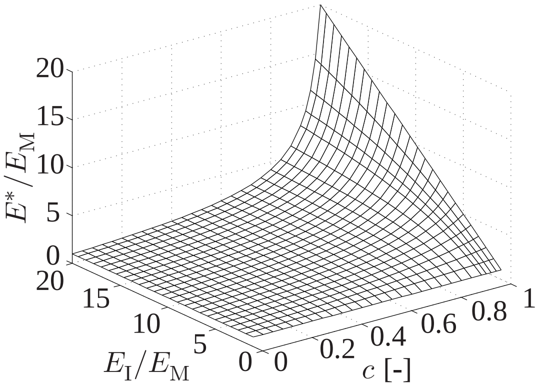

Figure 1.6: Prediction of effective Young's modulus E^* of Reuss method for different concentrations c and stiffness ratios $E_\mathrm{I}/E_\mathrm{M}$

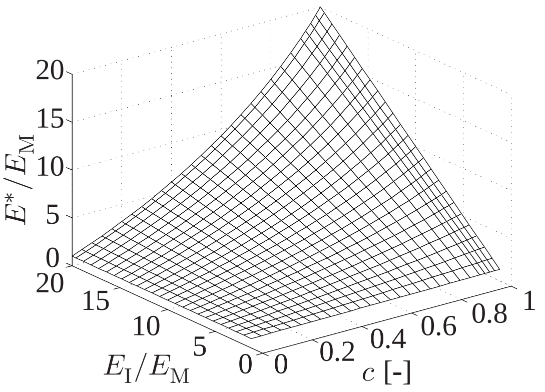

Figure 1.7: Prediction of effective Young's modulus E^* of Hashin-Shtrikman upper bound for different concentrations c and stiffness ratios $E_\mathrm{I}/E_\mathrm{M}$

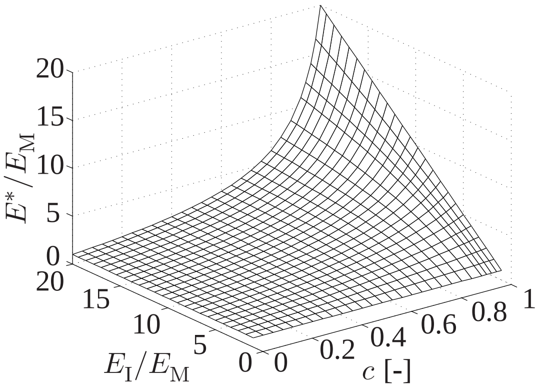

Figure 1.8: Prediction of effective Young's modulus E^* of Hashin-Shtrikman lower bound and Mori-Tanaka estimate, respectively, for different concentrations c and stiffness ratios $E_\mathrm{I}/E_\mathrm{M}$

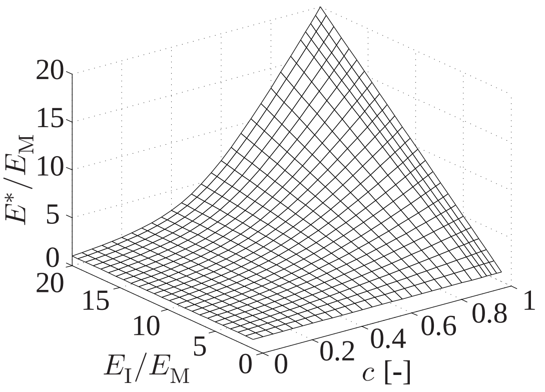

Figure 1.9: Prediction of effective Young's modulus E^* of self-consistent method for different concentrations c and stiffness ratios $E_\mathrm{I}/E_\mathrm{M}$

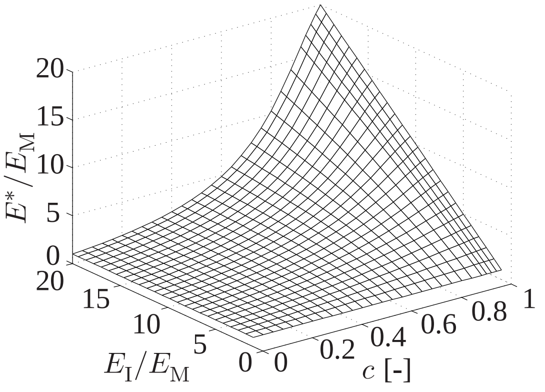

Figure 1.10: Prediction of effective Young's modulus E^* of the interpolative double inclusion model (IDIM) for different concentrations c and stiffness ratios $E_\mathrm{I}/E_\mathrm{M}$

it has been proven that the Mori-Tanaka method is generally incorrect for higher concentrations of inclusions. But it is hard to decide whether the IDIM estimate or the self-consistent scheme provide better results for higher volume fractions. A comparison with the obtained FE-results of ideal spherical inclusion for volume fractions up to 30% will be provided later in this section.

Further analyses of these homogenization methods for different stiffness ratios and concentrations are presented in the following. Figure 1.5 to 1.10 provide 3D-surface plots of the prediction for the different methods for stiffness ratios up to 20. Due to the fact that it is not possible to compare the behavior over different stiffness ratios by plotting the surfaces above each other, in Figure 1.11 and 1.12 the resulting effective elastic modulus E^* normalized by E_M over the stiffness ratio of inclusion and matrix material is shown. As can be seen from the surface plots, the behavior of the homogenization methods over different stiffness ratios is changed for different concentrations of the inclusion volume fraction c, however, the general behavior remains the same. The Voigt estimate shows a linear dependence of the effective elastic modulus with respect to the volume fraction of the inclusion representing an upper bound as mentioned before. The Reuss estimate is the lower bound which only shows an increase of the effective elastic modulus in the end. Afore it remains at a nearly constant level. The same behavior can be observed for the upper and lower Hashin-Shrikman bounds only at a higher or lower level, respectively. For a relatively low volume fraction of inclusion the IDIM and self-consistent estimate coincide, result in curves showing only small increase of E^*/E_M with respect to $E_\mathrm{I}/E_\mathrm{M}$. For a large amount of inclusions ($c = 0.8$) both methods deviate from each other, where the self-consistent shows a nearly linear behavior with increasing stiffness ratio, whereas the IDIM estimate shows a more quadratic behavior. Both are quite close to the Hashin-Shtrikman bounds which is depicted for high concentration c of inclusions in Figure 1.4. As can be seen by interpretation of Figure 1.12, the stiffness ratio has an immense effect on the effective properties, especially at high volume fractions of inclusion, and therefore the homogenization methods should also be checked for their behavior for high stiffness ratios as done here, instead of solely investigating their behavior at different volume fractions.

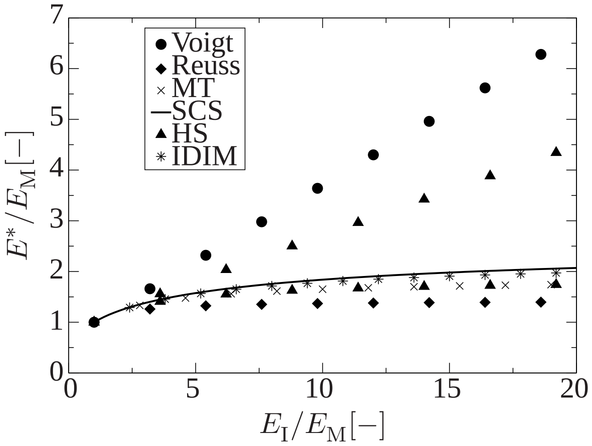

Figure 1.11: Prediction of effective Young's modulus E^* with different homogenization methods for different stiffness ratios $E_\mathrm{I}/E_\mathrm{M}$ for $c = 0.3$

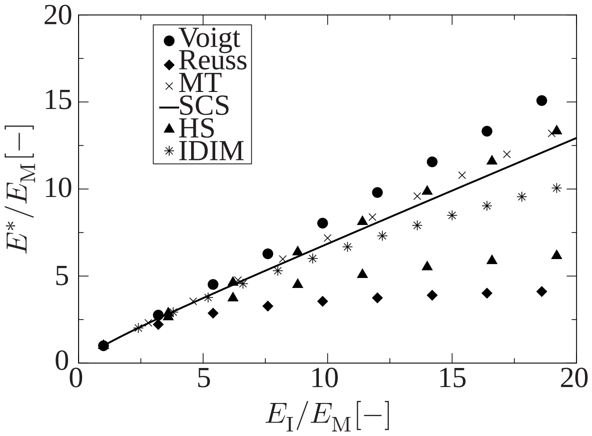

Figure 1.12: Prediction of effective Young's modulus E^* with different homogenization methods for different stiffness ratios $E_\mathrm{I}/E_\mathrm{M}$ for $c = 0.8$

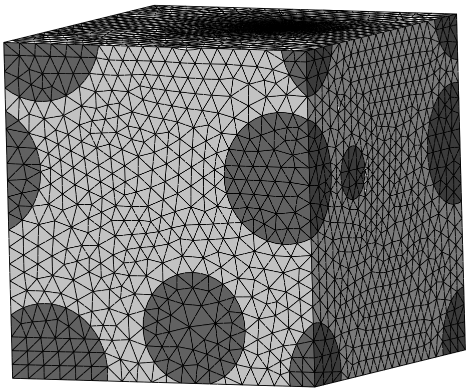

Figure 1.13: RVE with randomly distributed spherical inclusions of a volume fraction $c = 0.2$

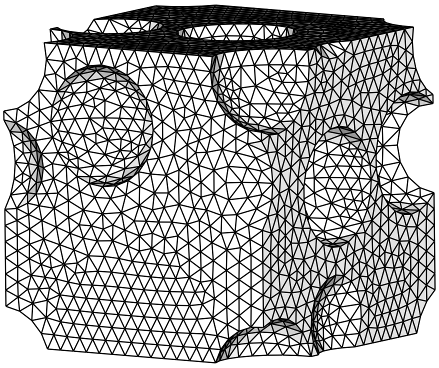

Figure 1.14: RVE with randomly distributed voids of a volume fraction $c = 0.2$

1.3.1 Comparison with FE-results

Before we compare these well-known homogenization methods with the ESCS and IDD estimate, first the results obtained so far are compared with Finite-Element simulations. For this purpose RVEs with randomly distributed inclusions are generated for different volume fractions using the software DIGIMAT. The model is generated by successively placing randomly distributed equally sized spheres into the matrix material until the desired volume fraction with the desired number of spheres or voids is reached. If a randomly placed sphere intersects another already placed sphere, it is attempted to place that particular sphere differently using yet another random generator. The resulting models with spherical inclusion are shown in Figure 1.13 and with spherical voids in Figure 1.14. The FE simulations were done with the software ABAQUS/Standard applying linear displacement boundary conditions to three faces of the model so that these are fixed in their respective normal direction so that every degree of freedom is fixed on one single face. The displacement is applied on a further face in its normal direction.

In Figure 1.15 the results of the different homogenization methods are compared for a stiffness ratio $E_{\mathrm{I}}/E_{\mathrm{M}} = 10$ with the obtained results from the FE-simulation up to an inclusion volume fraction of $c = 0.35$. It can be stated that for the case of spherical isotropic inclusion the IDIM shows the best agreement for higher inclusion volume fractions found earlier by Pierard et al. (2004). However, as seen in Figure 1.16 with increasing stiffness ratio $E_{\mathrm{I}}/E_{\mathrm{M}}$, the FEM-results yield to a softer behavior as the IDIM but which still predicts the best agreement compared to the other methods.

1.3.2 Investigation of ESCS and IDD approach in the context of spherical inclusions

Now we are investigating the ESCS and IDD method, in order to verify the implementation of both approaches. Therefore the effective Young's modulus E^* is calculated for an isotropic matrix containing spherical holes, to compare these results with results obtained by Zheng and

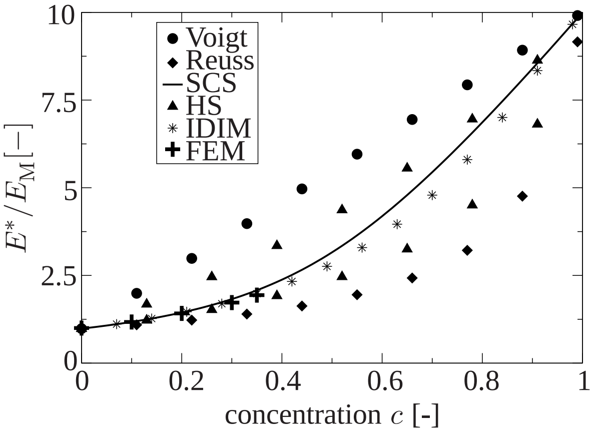

Figure 1.15: Comparison of homogenization results for effective Young's modulus E^* with FEM-results for $E_\mathrm{M} = 21$ GPa, $E_\mathrm{I} = 210$ GPa and $\nu = 0.25$.

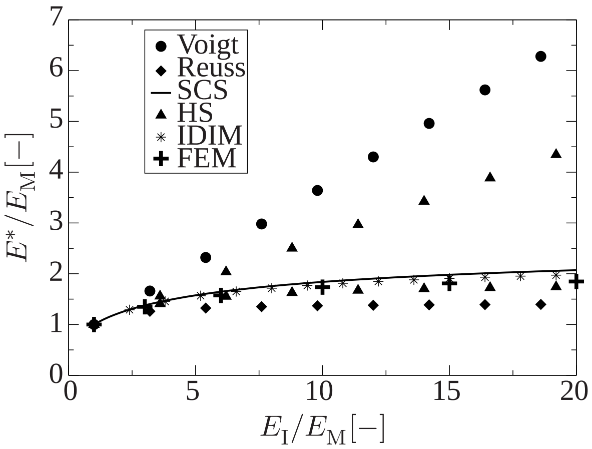

Figure 1.16: Comparison of homogenization results for effective Young's modulus E^* with FEM-results for different stiffness ratios $E_\mathrm{I}/E_\mathrm{M}$ for $c = 0.3$

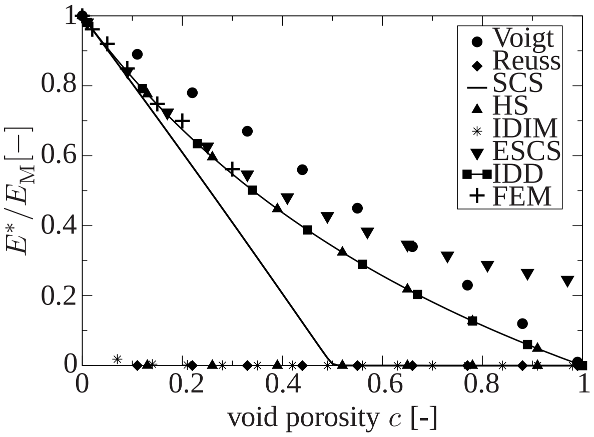

Figure 1.17: Comparison of different homogenization results and numerical evaluation for the effective Young's modulus E^* of homogenously distributed spherical voids embedded in an isotropic matrix.

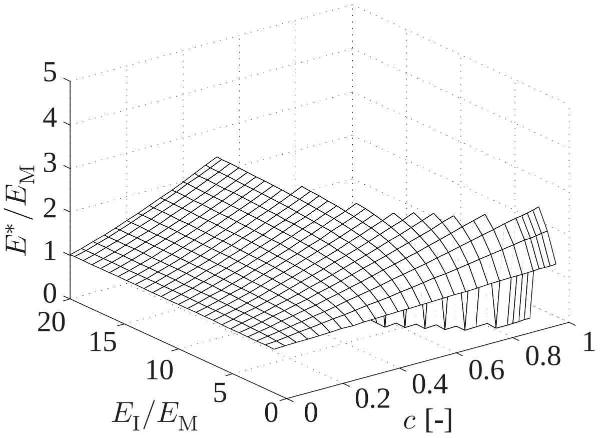

Figure 1.18: Prediction of effective Young's modulus E^* of ESCS method for different concentrations c and stiffness ratios $E_\mathrm{I}/E_\mathrm{M}$

Du (2001). Figure 1.17 shows the resulting effective Young's modulus E^* over the void porosity c for $\nu = 0$. For comparison, we also plot the corresponding self-consistent scheme, IDIM, Hashin-Shtrikman, Voigt and Reuss bounds as well as the numerical results obtained from FEM-simulations. The Reuss bound as well as the Hashin-Shtrikman lower bound and IDIM provide inappropriate results, meaning they are not appropriate for vanishing stiffness of one phase. The self-consistent scheme also predicts a very soft behavior, where the maximum permitted porosity is $c = 0.5$. The ESCS method does not predict a complete loss of stiffness at $c = 1$ which is of course inappropriate. Here it becomes clear that this method is only valid for small void porosity c. It can be seen that the IDD method agrees perfectly with the Mori-Tanaka method or Hashin-Shtrikman upper bound, respectively. Zheng and Du (2001) showed that the IDD method provides the best agreement for most materials with numerical simulations, especially for $c \to 1$. The here presented results agree agree with their reported results for voids.

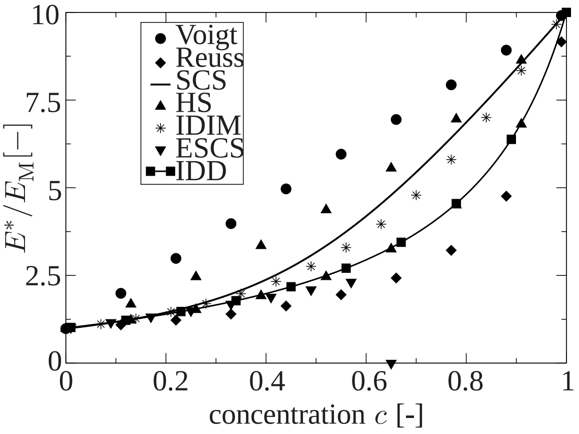

Figure 1.19: Comparison of homogenization results for effective Young's modulus E^* for $E_\mathrm{M} = 21$ GPa, $E_\mathrm{I} = 210$ GPa and $\nu = 0.25$.

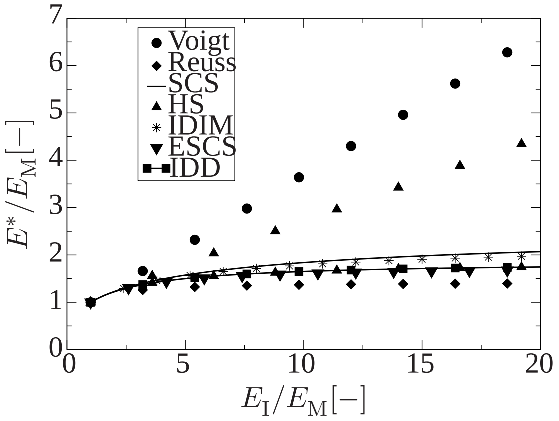

Figure 1.20: Comparison of homogenization results for effective Young's modulus E^* for different stiffness ratios $E_\mathrm{I}/E_\mathrm{M}$ for $c = 0.3$

In the following the behavior of the ESCS and IDD method is investigated regarding isotropic homogeneously distributed spherical inclusions embedded in an isotropic matrix for different stiffness ratios. In Figure 1.19 the predicted effective Young's modulus E^* is shown over the inclusion volume fraction c for a stiffness ratio $E_\mathrm{I}/E_\mathrm{M} = 10$. As can be seen for the case of voids, the IDD method agrees with the Mori-Tanaka estimate. The ESCS predicts a lower effective stiffness ratio E^* than the IDD method. Although both methods predict for $c = 0.3$ and a stiffness ratio $E_\mathrm{I}/E_\mathrm{M} = 10$ a similar effective Young's modulus, with increasing stiffness ratio the ESCS methods predicts a slightly lower result as shown in Figure 1.20. Furthermore the ESCS method has its numerical limits in predicting the effective behavior. Investigating the behavior in Figure 1.18 shows that this limit depends on both factors, inclusion volume fraction and stiffness ratio. Therefore this method provides good results only for low stiffness ratios and low volume fractions, moreover this method is more complex than the IDD method. The results found here from numerical analysis confirm the results analytically done by Du and Zheng (2002) where the effective elasticity tensor, here exemplary for the Young's modulus E, fulfills the following conditions:

$$\begin{aligned} E_\mathrm{SCS} \leq E^* \leq E_\mathrm{idd} \leq E_\mathrm{ESCS} \quad &\mathrm{as} \quad E_\mathrm{I} \leq E_\mathrm{M} \\ E_\mathrm{ESCS} \leq E_\mathrm{idd} \leq E^* \leq E_\mathrm{SCS} \quad &\mathrm{as} \quad E_\mathrm{M} \leq E_\mathrm{I} \end{aligned} \tag{1.21}$$

It should also be mentioned that the Ponte Castañeda-Willis (PW) estimate (cf. Castaneda and Willis (1995)) coincides with the IDD-method if all inclusion-matrix cells have identical shape and orientation for identical inclusion-interaction distribution, however, the PW does not have an explicit form in all cases which makes the IDD estimate more favorable.

1.4 Dealing with irregular (non-ellipsoidal) inhomogeneities

1.4.1 Eshelby tensor field

Zheng et al. (2006) established the following irreducible decomposition

$$\mathcal{S}^{\omega}(\boldsymbol{x}) = \mathcal{S}^{0}\,\chi^{\omega} + \mathcal{Q}^{\omega}(\boldsymbol{x}) \tag{1.22}$$

for the Eshelby tensor field $\mathcal{S}^{\omega}(\boldsymbol{x})$. $\mathcal{S}^{0}$ describes the isotropic part of $\mathcal{S}^{\omega}$ for an arbitrary domain ω. For isotropic elasticity this part vanishes outside of ω and is uniform inside ω. $\mathcal{S}^{0}$ is identical to the Eshelby tensor for spherical inclusions in 3D and circular inclusions in 2D. Due to the minor symmetry of the Eshelby tensor, $\mathcal{S}^{\omega}$ might have a maximum of nine independent components in two dimensions. For the special case of a elliptical inclusion for plain strain and isotropic material the Eshelby tensor $\mathcal{S}^{\omega}$ can be calculated and written in matrix notation as a second order tensor $\boldsymbol{S}^{\omega}$ as

$$\boldsymbol{S}^{\omega} = \frac{1}{8(1-\nu)} \begin{bmatrix} 5-4\nu & 4\nu-1 & 0 \\ 4\nu-1 & 5-4\nu & 0 \\ 0 & 0 & 3-4\nu \end{bmatrix}, \tag{1.23}$$

where ν denotes the Poisson ratio. The part $\mathcal{Q}^{\omega}(\boldsymbol{x})$ describes the anisotropic part of $\mathcal{S}^{\omega}$. The formalism (1.22) is valid for arbitrary inclusion ω in a two- or three- dimensional isotropic medium which is a deviatoric fourth- or second-order tensor and independent of the material symmetry. Therefore $\mathcal{Q}^{\omega}$ has a maximum of fourteen or four independent components in the 3D and 2D case. In the two-dimensional plane strain problem $\mathcal{Q}^{\omega}$ results in

$$\boldsymbol{Q}^{\omega}(\boldsymbol{x}) = \frac{1-2\nu}{2(1-\nu)}\boldsymbol{i}\otimes\boldsymbol{d} + \frac{1}{2(1-\nu)}\boldsymbol{d}\otimes\boldsymbol{i} + \frac{1}{1-\nu}\boldsymbol{D}, \tag{1.24}$$

with

$$\boldsymbol{d}(\boldsymbol{x}) = -\frac{1}{2\pi}\operatorname{sym}\operatorname{dev}\int_{\omega}\partial_{\boldsymbol{z}}(\ln\frac{1}{|\boldsymbol{z}|})\mathrm{d}\boldsymbol{y} \tag{1.25}$$

$$\boldsymbol{D}(\boldsymbol{x}) = -\frac{2}{\pi}\operatorname{sym}\operatorname{dev}\int_{\omega}\frac{\boldsymbol{z}\otimes\boldsymbol{z}\otimes\boldsymbol{z}\otimes\boldsymbol{z}}{|\boldsymbol{z}|^{6}}\mathrm{d}\boldsymbol{y}, \tag{1.26}$$

where $\boldsymbol{z} \equiv \boldsymbol{y} - \boldsymbol{x}$ and $\operatorname{sym}\operatorname{dev}$ denotes the operation of taking the symmetric deviatoric part. $\boldsymbol{d}$ and $\boldsymbol{D}$ are material-independent and they have at maximum two independent components (Zou et al., 2010). Following the definition in Zou et al. (2010) we are using $\boldsymbol{d} = d_{ij}$ and $\boldsymbol{D} = D_{ijkl}$ and the following definitions

$$p_2 \equiv d_{11}, \quad q_2 \equiv d_{12}, \quad p_4 \equiv D_{1111}, \quad q_4 \equiv D_{1112}. \tag{1.27}$$

The matrix representation of $\boldsymbol{Q}^\omega$ is given by

$$\boldsymbol{Q}^\omega = \frac{1}{1-\nu}\begin{bmatrix} (1-\nu)p_2 + p_4 & \nu p_2 - p_4 & \frac{1-2\nu}{2}q_2 + q_4 \\ -\nu p_2 - p_4 & -(1-\nu)p_2 + p_4 & \frac{1-2\nu}{2}q_2 + q_4 \\ \frac{1}{2}q_2 + q_4 & \nu\frac{1}{2}q_2 - q_4 & -p_4 \end{bmatrix}. \tag{1.28}$$

Zou et al. (2010) derived the following complex-variable integral expression

$$\begin{aligned} \gamma_2(x) &\equiv p_2(x) + iq_2(x) = \tfrac{1}{4\pi i}\oint_{\partial\omega}\tfrac{\mathrm{dy}}{\bar{z}}, \\ \gamma_4(x) &\equiv p_4(x) + iq_4(x) = \tfrac{1}{16\pi i}\oint_{\partial\omega}\tfrac{z\mathrm{dy}}{\bar{z}^2}, \end{aligned} \tag{1.29}$$

from which the entries in (1.28) can be identified. Here $i = \sqrt{-1}$ is the imaginary unit and the overbar describes the complex conjugated. For the averaged values of γ_2 and γ_4 over the inclusion ω Zou et al. (2010) obtained

$$\begin{aligned} \langle\gamma_2\rangle &\equiv \langle p_2\rangle + i\langle q_2\rangle = -\tfrac{1}{8\pi\omega}\oint_{\partial\omega}\oint_{\partial\omega}\tfrac{z}{\bar{z}}\mathrm{dyd\bar{x}}, \\ \langle\gamma_4\rangle &\equiv \langle p_4\rangle + i\langle q_4\rangle = -\tfrac{1}{32\pi\omega}\oint_{\partial\omega}\oint_{\partial\omega}\tfrac{z}{\bar{z}}\mathrm{dydx}. \end{aligned} \tag{1.30}$$

The decomposition

$$\langle\boldsymbol{S}^\omega\rangle = \boldsymbol{S}^0 + \langle\boldsymbol{Q}^\omega\rangle \tag{1.31}$$

can be done similar to (1.22) for the average Eshelby tensor $\langle\boldsymbol{S}^\omega\rangle$ in two dimension.

1.4.2 Averaged Eshelby tensor characerized by Laurent polynomials

In complex analysis, it is known that the Riemann mapping theorem states that for an arbitrarily given simple-closed curve $\partial\omega$, there exists a biholomorphic mapping from the outer domain of the unit disk I onto the outer domain of $\partial\omega$ (Henrici, 1974; Riemann, 1851). This mapping can be expressed in terms of the Laurent series

$$f(w) = f_0 + a\left(w + \sum_{k=1}^{\infty} b_k\, w^{-k}\right), \quad |w| \geq 1, \tag{1.32}$$

where f_0 is a unique inner point of the domain ω, a is a positive real number and every complex coefficient b_k satisfies $|b_k| < 1/k$ (Zou et al., 2010). Without loss of generality, it is possible to set $f_0 = 0$ and $a = 1$ which leads to the following expression

$$f(\theta) = e^{i\theta} + \sum_{k=1}^{\infty} b_k e^{-k\,i\theta}, \quad 0 \leq \theta \leq 2\pi. \tag{1.33}$$

This expression can be used to approximate various 2D shapes. Examples for such approximations are shown in Figure 1.21 with the associated polynomial. Zheng et al. (2006) and Zou et al. (2010) showed a solution procedure to obtain the average Eshelby tensor based on (1.30) and using the residue theorem for various inclusions characterized by Laurent polynomials. The

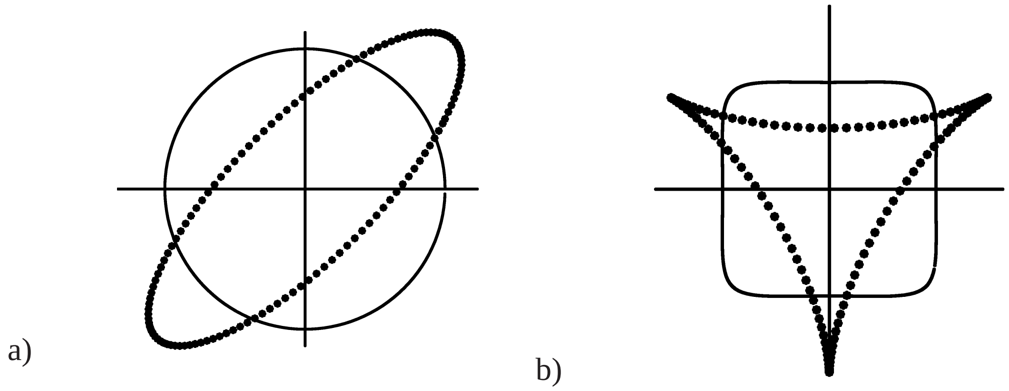

Figure 1.21: Laurent polynomial approximations for describing various shapes. a) circle: $e^{(}i\,\theta)$, ellipse: $e^{i\,\pi/4}[1.5\,\cos(\theta-\pi/4)+i\,0.5\,\sin(\theta-\pi/4)]$. b) hypocycloid: $e^{i\,\theta}+\lambda e^{(2\,i\,\pi/3)}\,e^{-3\,i\,\theta}$, quasi-rectangular: $e^{i\,\theta}-\frac{1}{8}\,e^{-3\,i\,\theta}$.

detailed solution procedure can be taken from there. Here we shortly recall the basic solution for inclusion characterized by the following Laurent polynomial

$$f(\theta)=e^{i\theta}+b_1e^{-i\,\theta}+b_ne^{-i\,n\,\theta} \tag{1.34}$$

by which the shown shapes in Figure 1.21 can all be approximated. The solution has the following explicit expression for $\langle\gamma_2\rangle$ and $\langle\gamma_4\rangle$. (Zou et al., 2010)

- n=even number ≥ 2

$$\begin{aligned}\tfrac{2\omega}{\pi}\langle\gamma_2\rangle &= -b_1\,(1-|b_1|^2-2n\,|b_n|^2)+n\,b_n^2\,\bar{b}_1^n\\ \tfrac{8\omega}{\pi}\langle\gamma_4\rangle &= -b_1^2\,(1-|b_1|^2-3n\,|b_n|^2)\\ &\quad -n\,b_n^2\,\bar{b}_1^{n-1}[n-(n+2)|b_1|^2-n^3\,|b_n|^2]\end{aligned} \tag{1.35}$$

- n=odd number ($n=2k+1$) ≥ 3

$$\begin{aligned}\tfrac{2\omega}{\pi}\langle\gamma_2\rangle &= -b_1\,(1-|b_1|^2-2n\,|b_n|^2)+n\,b_n^2\,\bar{b}_1^n\\ &\quad +n^2\,|b_n|^2\,b_2\,|b_1|^k\\ \tfrac{8\omega}{\pi}\langle\gamma_4\rangle &= -b_1^2\,(1-|b_1|^2-3n\,|b_n|^2)\\ &\quad -n\,b_n^2\,\bar{b}_1^{n-1}[n-(n+2)|b_1|^2-n^3\,|b_n|^2]\\ &\quad +n^2\,b_n^3\,\bar{b}_1^{3k+1}+b_n\,\bar{b}_1^{k-1}\,(1-2|b_1|^2\\ &\quad -\tfrac{n-1}{2}n^2\,|b_n|^2+\tfrac{n+1}{2}n^2\,|b_1|^2\,|b_n|^2+|b_1|^4\Big)\\ &\quad -\tfrac{n}{2}|b_n|^2\,b_n\,\bar{b}_1^{k-1}\,((n-1)^2-(n+1)^2\,|b_n|^2\\ &\quad -\tfrac{(3n^2+1)(n^2-1)n}{16}|b_n|^2\Big)\,.\end{aligned} \tag{1.36}$$

1.4.3 Mori-Tanaka method with replacement tensor approach (RMTM)

The Mori-Tanaka method approximates the interaction between the phases by assuming that each inclusion I is embedded, in turn, in an infinite matrix that is remotely loaded by the average matrix strain $\boldsymbol{E}_{\mathrm{M}}$ or average matrix stress $\boldsymbol{T}_{\mathrm{M}}$, respectively. This implies that the Mori-Tanaka method estimates the behavior of the composite for a non-dilute volume fraction of inclusions via dilute inclusions that are subjected to the effective or averaged matrix strain $\boldsymbol{E}_{\mathrm{M}}$ or stress $\boldsymbol{T}_{\mathrm{M}}$, respectively (Mori and Tanaka, 1973).

$$\boldsymbol{E}^{\mathrm{I}} = \mathcal{A}^0_{\mathrm{I}} \boldsymbol{E}^{\mathrm{M}} = \mathcal{A}_{\mathrm{I\,(MT)}}\, \boldsymbol{E}^0, \tag{1.37}$$

where $\mathcal{A}^0_{\mathrm{I}}$ denotes the dilute strain concentration tensor (influence tensor) of the inclusion, $\mathcal{A}_{\mathrm{I\,(MT)}}$ the Mori-Tanaka strain concentration tensor of the inclusion and $\boldsymbol{E}^0$ the macroscopic strain. The expression for $\mathcal{A}^0_{\mathrm{I}}$ is given by Hill (1965) to be

$$\mathcal{A}^0_{\mathrm{I}} = \left[\mathcal{I} + \mathcal{S}^0 \mathcal{C}^{-1}_{\mathrm{M}} (\mathcal{C}_{\mathrm{I}} - \mathcal{C}_{\mathrm{M}})\right]^{-1}. \tag{1.38}$$

In Benveniste (1987) the method is interpreted in the sense that ”each inclusion behaves like an isolated inclusion in the matrix seeing $\boldsymbol{E}_{\mathrm{M}}$ as a far-field strain”.

The effective elasticity tensor can be obtained via

$$\mathcal{C}^*_{\mathrm{(MT)}} = \mathcal{C}_{\mathrm{M}} + c_{\mathrm{I}}(\mathcal{C}_{\mathrm{I}} - \mathcal{C}_{\mathrm{M}})\mathcal{A}_{\mathrm{I(MT)}}. \tag{1.39}$$

The Mori-Tanaka gradient concentration tensors of the inclusion $\mathcal{A}_{\mathrm{I(MT)}}$ can be written for spherical inclusion as

$$\mathcal{A}_{\mathrm{I(MT)}} = \left[c_{\mathrm{I}}\mathcal{I} + c_{\mathrm{M}}(\mathcal{A}^0_{\mathrm{I}})^{-1}\right]^{-1}. \tag{1.40}$$

Nogales and Böhm (2008) presented a framework how to extend the standard Mori-Tanaka scheme to inclusions with non-ellipsoidal shape which was done firstly by Duschlbauer (2004). Although Nogales and Böhm (2008) focuses mainly on thermal problems their approach can be applied analogously for elasticity. Therefore a phase averaged dilute ”replacement” elasticity tensor $\mathcal{C}^{\mathrm{red}}_{\mathrm{I}}$ and the dilute ”replacement” inclusion gradient tensor $\mathcal{A}^{0,\mathrm{red}}_{\mathrm{I}}$ have to be introduced. These replacement tensors have to fulfill the consistency condition

$$\mathcal{C}^{\mathrm{red}}_{\mathrm{I}} = \mathcal{C}_{\mathrm{M}} + \frac{1}{c_{\mathrm{I},0}}(\mathcal{C}^*_0 - \mathcal{C}_{\mathrm{M}})(\mathcal{A}^{0,\mathrm{red}}_{\mathrm{I}})^{-1}, \tag{1.41}$$

where $c_{\mathrm{I},0}$ describes the volume fraction and $\mathcal{C}^*_0$ the effective stiffness tensor in the inclusion in the dilute case. The name RMTM results from the introduction of these replacement tensors in the classical Mori-Tanaka scheme. This leads to the following Mori-Tanaka concentration gradient tensor

$$\mathcal{A}_{\mathrm{I(RMTM)}} = \left[c_{\mathrm{I}}\mathcal{I} + c_{\mathrm{M}}(\mathcal{A}^{0,\mathrm{red}}_{\mathrm{I}})^{-1}\right]^{-1} \tag{1.42}$$

and to the resulting effective elasticity tensor

$$\mathcal{C}^*_{\mathrm{(RMTM)}} = \mathcal{C}_{\mathrm{M}} + c_{\mathrm{I}}(\mathcal{C}^{\mathrm{red}}_{\mathrm{I}} - \mathcal{C}_{\mathrm{M}})\mathcal{A}_{\mathrm{I(RMTM)}}. \tag{1.43}$$

For non-spherical inclusions $\mathcal{A}^{0,\mathrm{red}}_{\mathrm{I}}$ and $\mathcal{C}^*_0$ have to be obtained numerically, e.g. with help of the finite element simulation of a single inclusion of appropriate shape and properties embedded into an infinite matrix. For ideal interfaces $\mathcal{A}^{0,\mathrm{red}}_{\mathrm{I}}$ can be obtained from volume averages over the inclusion. Therefore the 2D model is subjected to three linearly independent load cases,

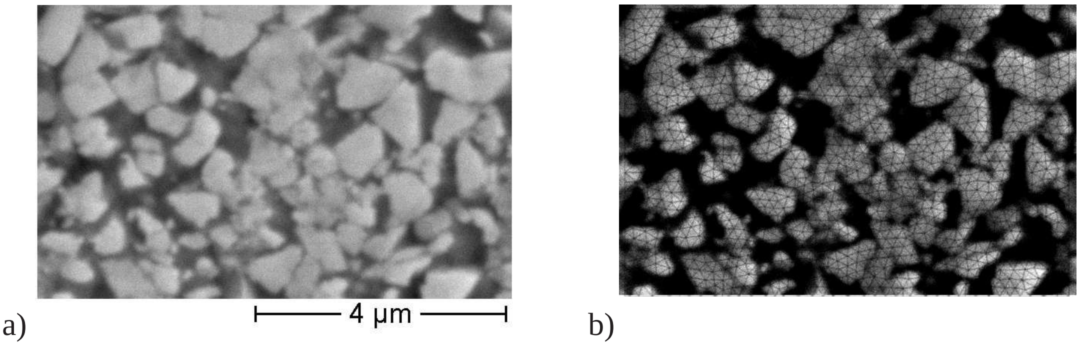

Figure 1.22: a) An exemplary micrograph obtained from a HVOF sprayed 88WC-12Co coating with SEM (Tillmann et al., 2008b). b) FE-mesh on microstructure.

namely tension in x-, y-direction and one case of simple shear, all applied as linear displacement boundary conditions. The volume fraction for the inclusion was for all presented cases between $0.4 - 0.8\%$ of the total volume. The proposed results in Nogales and Böhm (2008) stating that the replacement tensor were found to be largely independent of the inclusion volume fraction could be confirmed in this study.

In the end of this work we will analyze a combination of inclusions shapes. Therefore we extended the presented framework slightly to a multiphase composite. The Mori-Tanaka concentration tensor for each inclusion i is then given by

$$\mathcal{A}_{\mathrm{I(RMTM)},i} = \left[c_i \mathcal{I} + c_{\mathrm{M}} (\mathcal{A}_{\mathrm{I},i}^{0,\mathrm{red}})^{-1} + \sum_j c_j \mathcal{A}_{\mathrm{I},j}^{0,\mathrm{red}} (\mathcal{A}_{\mathrm{I},i}^{0,\mathrm{red}})^{-1} \right]^{-1}, \tag{1.44}$$

which results in the effective elasticity tensor

$$\mathcal{C}^*_{\mathrm{(RMTM)}} = \mathcal{C}_{\mathrm{M}} + \sum_i c_i (\mathcal{C}_{\mathrm{I},i}^{\mathrm{red}} - \mathcal{C}_{\mathrm{M}}) \mathcal{A}_{\mathrm{I(RMTM)},i}. \tag{1.45}$$

1.4.4 Construction of Finite Element Models from Real Micrographs

The investigated microstructure is manufactured by an HVOF thermal spray process of sub-micron WC-Co powders. In thermal spraying metallic and non-metallic surface coatings are manufactured by melting the coating materials in the form of powders or wires in an oxy-fuel gas flame, a plasma jet or an electrical arc and accelerating them towards the surface to be coated by means of the expanding combustion gases or a separate carrier gas. On the surface the impacting particles flatten, cool and solidify and thereby form a coating on the workpiece.

To perform analysis of real microstructures, micrographs obtained with the Scanning Electron Micrographs (SEM) are used. These micrographs provide the possibility to distinguish between the phases which is possible due to their different brightness in the micrograph caused by regions of atoms with different atomic numbers. Correlating to the huge difference in the relative atomic weight of tungsten (183.84 g/mol) and cobalt (58.933 g/mol) the phases of the sprayed WC-Co feature a good contrast. Figure 1.22a) shows an exemplary micrograph obtained from the coating. An image processing tool is used which now identifies the phases and generates an image consisting of Co- and WC-based alloys only. The differentiation between the phases is carried out by finding optimal thresholds based on the color distribution, from which the different phases are separated.

To generate a FE-mesh from such an image the software Object Oriented Finite Element 2 (OOF2), from the United States National Institute of Standards and Technology (NIST), is used. This software was developed to investigate the behavior of microstructures. OOF2 takes a non-reductionist approach to build a data structure on the digitized image of the microstructure whereby it gets connected to the associated material properties. At the end OOF2 creates a FE-mesh which reflects the shape of the different phases in the microstructure with the associated material parameters. The mesh is generated by minimizing an energy functional which is composed of a homogeneity part of the mesh and a shape part of the elements via

$$E = \alpha E_{\mathrm{hom}} + (1-\alpha) E_{\mathrm{shape}} \tag{1.46}$$

where α is an adjustable parameter, enabling the user to control if the mesh should be highly accurate to the image with bad shaped elements ($\alpha = 1$) or if the elements are well shaped but with less accuracy to the shape of the phases in the micrograph ($\alpha = 0$). Choosing a middle value will lead to an optimal choice. The homogeneity energy for triangle elements can be calculated by

$$E_{hom} = \sum_t \prod_{i=1}^{N} \left(\frac{1-\alpha_i(t)}{1-1\backslash N} \right) \tag{1.47}$$

in which the pixels are separated into N categories where all the pixels belong to one material group. For each mesh element t, $\alpha_i(t)$ describes the percentage of its area that overlies pixels in category i. When the element lies on only one material $\alpha_i(t) = 1$ so that it is minimized if an element is completely homogeneous. The shape term E_{shape} is defined by

$$E_{shape} = \sum_t \left(1 - \frac{36}{\sqrt{3}} \frac{A_t}{L_t^2} \right) \tag{1.48}$$

in which A_t corresponds to the area of the element t and L_t describes the perimeter. This term is zero for equilateral triangular elements and one for degenerated ones. For further details and the features of the program OOF2 the readers are referred to Langer et al. (2001) and Reid et al. (2008). The resulting mesh can be seen in Fig. 1.22b) which includes $\approx 77\mathrm{vol.}\%$ WC particles. It is assumed that the phases are perfectly bonded. To obtain information about the microstructural behavior and macroscopic properties tension tests are done with plane strain conditions.

At this point it is assumed that the micrograph fulfills the requirements for a Representative Volume Element. This is a crucial assumption in order to compare the obtained results with those from the homogenization methods. The elastic constants of the microstructure are obtained by evaluating the reaction forces at the boundaries and the displacement at the free lateral sides.

1.5 Comparison of different homogenization approaches for irregular (non-ellipsoidal) inhomogeneities

Throughout this section we assume that the matrix and inclusion are isotropic and only two-phase composites in isothermal linear elasticity are considered. We restrict our analysis to the case of plain strain. We compare the prediction of the macroscopic behavior of different classical mean-field homogenization methods (Voigt, Reuss, Hashin-Shtrikman, Mori-Tanaka, interpolative double inclusion model) and more recent methods (ESCS and IDD) with FE results obtained from a RVE. Furthermore we will investigate the prediction of these methods concerning different stiffness ratios of the inclusion-matrix pair and different shapes of the inclusion. In the following we will use the Mori-Tanaka scheme with the matrix material as the softer material instead of defining it over the higher volume fraction. Therefore the MT scheme coincides with the lower Hashin-Shtrikman bound for all volume fractions. For irregular inclusions the averaged Eshelby tensor by Zou et al. (2010) will be used in these methods and the results will be further compared to the RMTM method. A detailed analysis for spherical inclusions concerning different stiffness ratios can be found in Klusemann and Svendsen (2010).

A comparison of the classical homogenization methods with the ESCS and IDD method and FEM results for circular inclusions for a stiffness ratio $\frac{E_{\mathrm{I}}}{E_{\mathrm{M}}} = 10$ is shown in Figure 1.23 for C^*_{11}. The FEM results are obtained for randomly distributed circular inclusions of equal size ($V_{\mathrm{I}} \approx 1.5\% V$) applying linear displacement boundary conditions. It has to be considered that in the plain strain context the resulting elasticity tensor is anisotropic also called ”geometric anisotropy” (Bartel, 2009). This results in an uncoupled evolution between tension and shear components in the elasticity tensor. However, the homogenization results in a similar behavior of the single components in the elasticity tensor therefore in the following we will concentrate in a first step on C^*_{11} to analyze the behavior of the different methods.

It can be seen that the IDIM method provides the best fit to the FEM results. Further the IDD method agrees perfectly with the Mori-Tanaka method or Hashin-Shtrikman lower bound, respectively. The ESCS method predicts until $c = 0.5$ sensible results but afterwards the results are unstable and inappropriate.

1.5.1 Square

As a first irregular shape we investigate a square as shown in Figure 1.25. For the calculation of the average Eshelby tensor as described in section 1.4.2 the Laurant polynom $f_{\mathrm{square}}(\theta) = e^{i\,\theta} - \frac{1}{8}\,e^{-3\,i\,\theta}$ is used as an approximation of the displayed square.

Figure 1.24 shows the results for C^*_{11} for $\frac{E_{\mathrm{I}}}{E_{\mathrm{M}}} = 10$ with the different homogenization approaches. Here the shown FEM results were obtained for randomly distributed square inclusions of equal size ($V_{\mathrm{I}} \approx 2\% V$) without interpretation of each other. Linear displacement boundary conditions were applied. The FEM results for $c = 0.8$ were obtained by aligning the inclusions perfectly. The prediction with Voigt and Reuss are the same as for circular inclusions due to the independence of the shape of the inclusion in the formulation. The analysis shows that the calculated Eshelby tensor for a square is only slightly different compared to a circular inclusion. Therefore the prediction is only slightly different as shown by the comparison between the results of the Mori-Tanaka method for square and circular inclusions. As previously

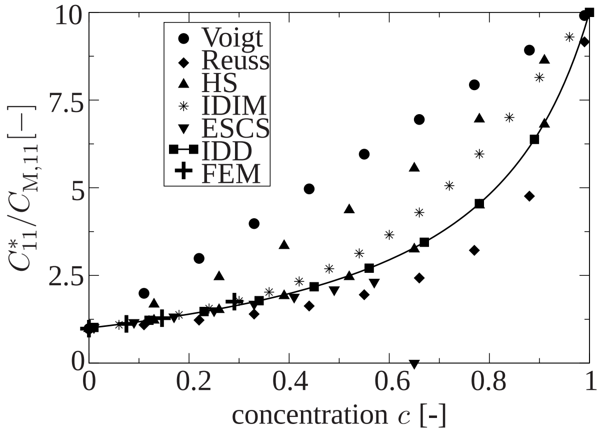

Figure 1.23: Comparison of homogenization results for effective Young's modulus E^* for $E_\mathrm{M} = 21$ GPa, $E_\mathrm{I} = 210$ GPa and $\nu = 0.3$ for circular inclusions. (HS = Hashin-Shtrikman bounds; IDIM = interpolative double inclusion model)

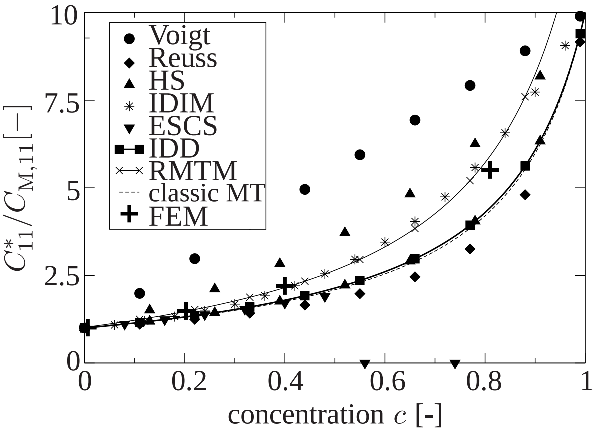

Figure 1.24: Comparison of homogenization results for component C^*_{11} from the effective elasticity tensor $\mathcal{C}^*$ for $E_\mathrm{M} = 21$ GPa, $E_\mathrm{I} = 210$ GPa and $\nu = 0.3$ for quadratic inclusions. (RMTM = Mori-Tanaka method with replacement tensor approach Nogales and Böhm (2008); classic MT = results of Mori-Tanaka method for circular inclusion)

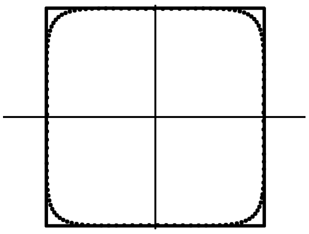

Figure 1.25: Approximated square described by $e^{i\theta} - \frac{1}{8}\,e^{-3i\theta}$ (dotted line) to calculate average Eshelby tensor.

seen the IDIM method shows a very good prediction of the effective behavior as calculated via FEM. However, for smaller volume fractions $c \leq 0.8$ the RMTM method seems to give the best prediction of the effective behavior. For larger volume fractions $c \geq 0.9$ this method produces insensible results. The reason for this is the fact that the RMTM converges for $c \to 1$ to $\mathcal{C}^{\mathrm{red}}_{\mathrm{I}}$ rather than to $\mathcal{C}_\mathrm{I}$ which is of course a certain limitation of the RMTM. The IDD method coincides with the lower Hashin-Shtrikman bound in this case and the ESCS predicts lower values for C^*_{11} as the Hashin-Shtrikman bound and unreasonable results for $c \geq 0.4$.

1.5.2 Triangle

Secondly we investigate an acute-angled triangle as shown in Figure 1.26. For the calculation of the average Eshelby tensor the Laurant polynom $f_{\mathrm{triangle}}(\theta) = e^{i\theta} + 0.3\,e^{-i\theta} + 0.3\,e^{-3i\theta}$ is used as an approximation of the displayed triangle. Figure 1.27 shows the results for C^*_{11} for

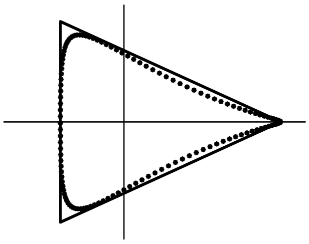

Figure 1.26: Approximated triangle described by $e^{i\,\theta} + 0.3\,e^{-i\,\theta} + 0.3\,e^{-3\,i\,\theta}$ (dotted line) to calculate average Eshelby tensor.

$\frac{E_{\mathrm{I}}}{E_{\mathrm{M}}} = 10$ for triangular inclusions. The calculated averaged Eshelby tensor strongly deviates from the Eshelby tensor for circular inclusions which results in different homogenization results compared to circular inclusion as can be seen by comparison of the curves for the classical MT and lower HS bound. However, the general predicted behavior especially in comparison to the RMTM is the same. Again the limitation for $c \rightarrow 1$ can clearly be seen. The performed representative FE results predict a higher value for C^*_{11} as most of the methods in which the upper HS bound shows the closest prediction. This shows the difficulty of the prediction for inclusions which introduce a high anisotropy due to their shapes.

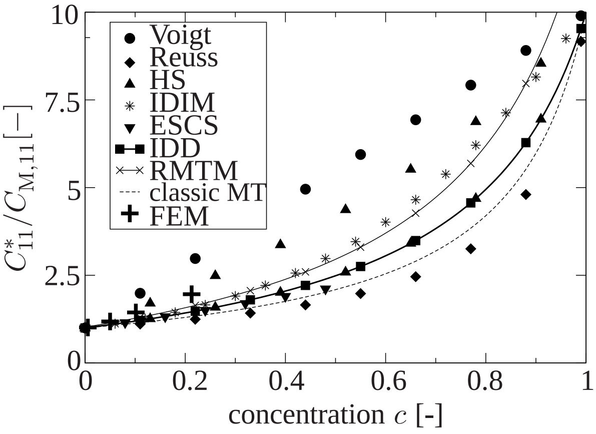

Figure 1.27: Comparison of homogenization results for component C^*_{11} from the effective elasticity tensor $\mathcal{C}^*$ for $E_{\mathrm{M}} = 21$ GPa, $E_{\mathrm{I}} = 210$ GPa and $\nu = 0.3$ for triangular inclusions.

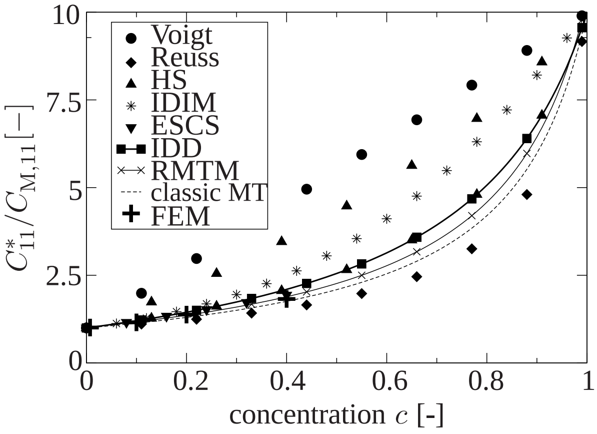

Figure 1.28: Comparison of homogenization results for component C^*_{11} from the effective elasticity tensor $\mathcal{C}^*$ for $E_{\mathrm{M}} = 21$ GPa, $E_{\mathrm{I}} = 210$ GPa and $\nu = 0.3$ for hexagonal inclusions.

1.5.3 Hexagon

Lastly we investigate a compressed hexagon as shown in Figure 1.29 as a kind of combination of the previously discussed triangle and square. For the calculation of the average Eshelby tensor the Laurant polynom $f_{\mathrm{hex}}(\theta) = e^{i\,\theta} + 0.2\,e^{-i\,\theta} + 0.05\,e^{-5\,i\,\theta}$ is used as an approximation of the displayed hexagon. The results for C^*_{11} for $\frac{E_{\mathrm{I}}}{E_{\mathrm{M}}} = 10$ for hexagonal inclusions are shown in Figure 1.28. The averaged Eshelby tensor shows a similar form as for the triangular case. Therefore the predictions also look quite equivalent. In contrast the RMTM method shows a completely different behavior as in the previous case. The RMTM predicts a lower value for

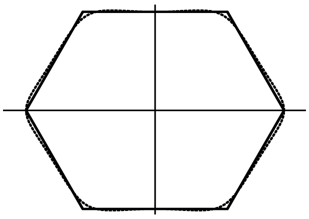

Figure 1.29: Approximated hexagon described by $e^{i\theta} + 0.2\,e^{-i\theta} + 0.05\,e^{-5i\theta}$ (dotted line) to calculate average Eshelby tensor.

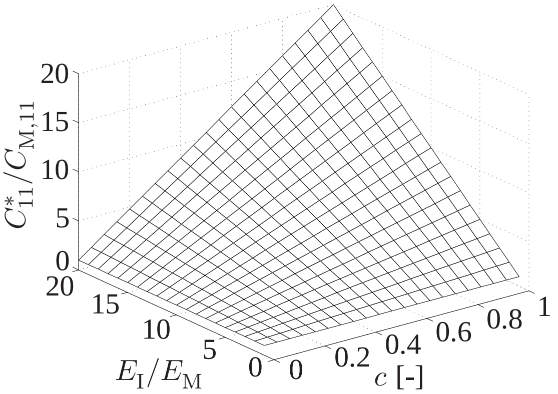

Figure 1.30: Prediction of effective Young's modulus E^* of Voigt method for different concentrations c and stiffness ratios $E_\mathrm{I}/E_\mathrm{M}$ for hexagonal inclusions

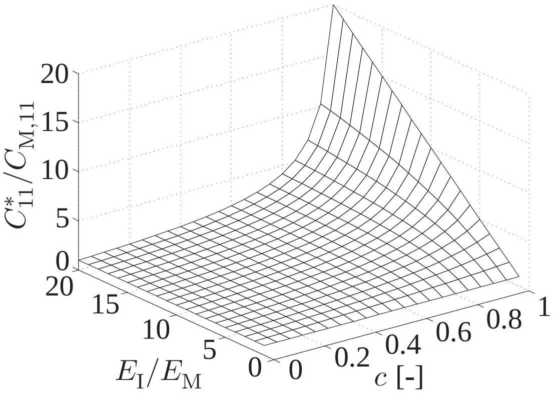

Figure 1.31: Prediction of effective Young's modulus E^* of Reuss method for different concentrations c and stiffness ratios $E_\mathrm{I}/E_\mathrm{M}$ for hexagonal inclusions

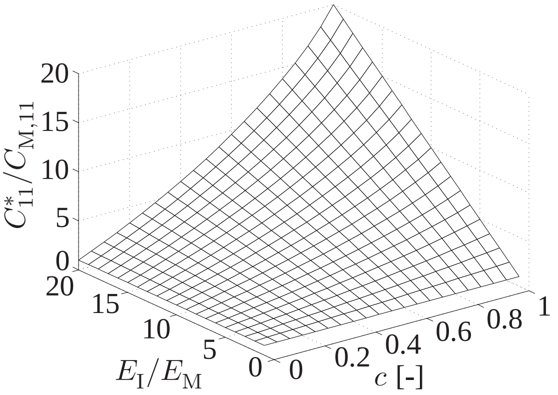

Figure 1.32: Prediction of effective Young's modulus E^* of Hashin-Shtrikman upper bound for different concentrations c and stiffness ratios $E_\mathrm{I}/E_\mathrm{M}$ for hexagonal inclusions

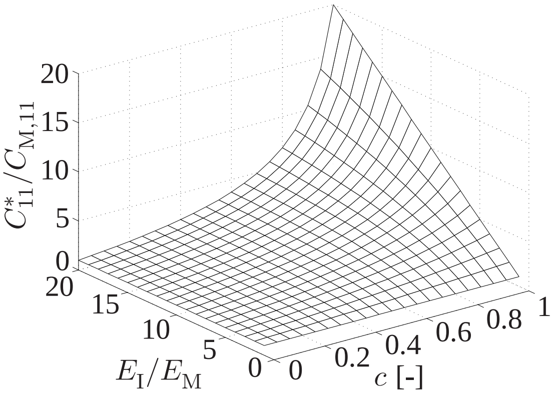

Figure 1.33: Prediction of effective Young's modulus E^* of Hashin-Shtrikman lower bound, Mori-Tanaka estimate and IDD method, respectively, for different concentrations c and stiffness ratios $E_\mathrm{I}/E_\mathrm{M}$ for hexagonal inclusions

C^*_{11} as the lower HS bound. In general the HS bounds provides the narrowest known bounds between which the true value has to be. For this inclusion this is not the case as the FEM results show. The results of the RMTM are in very good agreement with the calculated FEM results. Further analyses of these homogenization methods concerning hexagonal inclusions for different stiffness ratios and concentrations are presented in the following. Figure 1.30 to 1.37 provide 3D-surface plots of the prediction for the different methods for stiffness ratios up to 20. Due to the fact that it is not possible to compare the behavior over different stiffness ratios by plotting the surfaces above each other, in Figure 1.38 the resulting effective entry C^*_{11} normalized by $C_{\mathrm{M},11}$ over the stiffness ratio of inclusion and matrix material is shown. As can be seen from the surface plots, the behavior of the homogenization methods over different stiffness ratios is changed for different concentrations of the inclusion volume fraction c, however, the general behavior remains the same. The Voigt estimate shows a linear dependence of the effective elastic modulus with respect to the volume fraction of the inclusion representing an upper bound as mentioned before. The Reuss estimate is the lower bound which only shows an

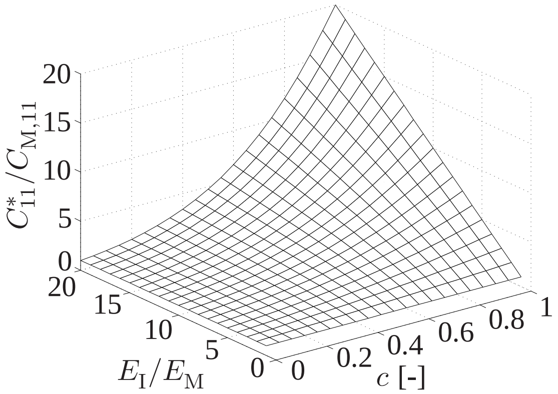

Figure 1.34: Prediction of effective Young's modulus E^* of double-inclusion method for different concentrations c and stiffness ratios $E_\mathrm{I}/E_\mathrm{M}$ for hexagonal inclusions

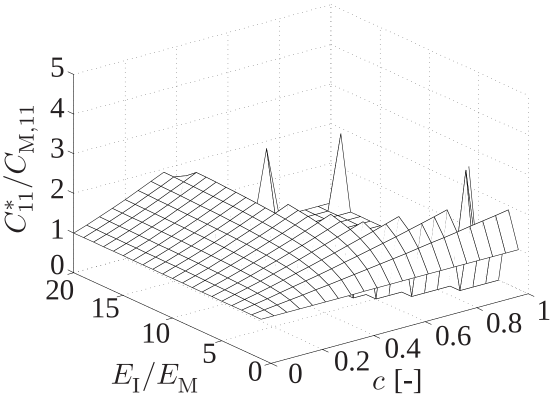

Figure 1.35: Prediction of effective Young's modulus E^* of ESCS method for different concentrations c and stiffness ratios $E_\mathrm{I}/E_\mathrm{M}$ for hexagonal inclusions

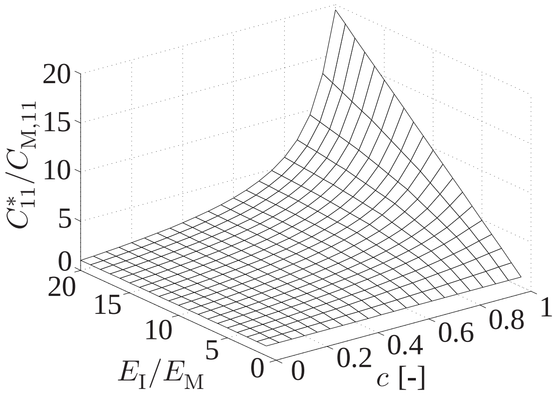

Figure 1.36: Prediction of effective Young's modulus E^* of RMTM method for different concentrations c and stiffness ratios $E_\mathrm{I}/E_\mathrm{M}$ for hexagonal inclusions

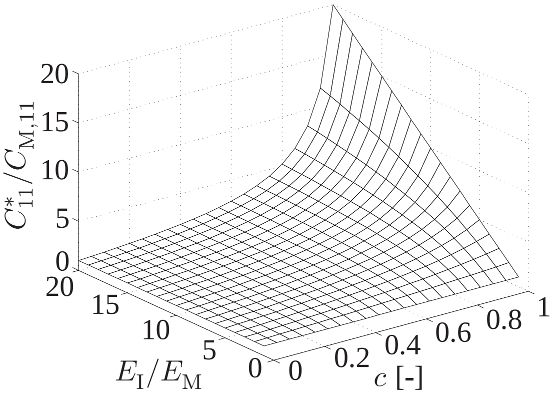

Figure 1.37: Prediction of effective Young's modulus E^* of Mori-Tanaka estimate for different concentrations c and stiffness ratios $E_\mathrm{I}/E_\mathrm{M}$ for circular inclusions

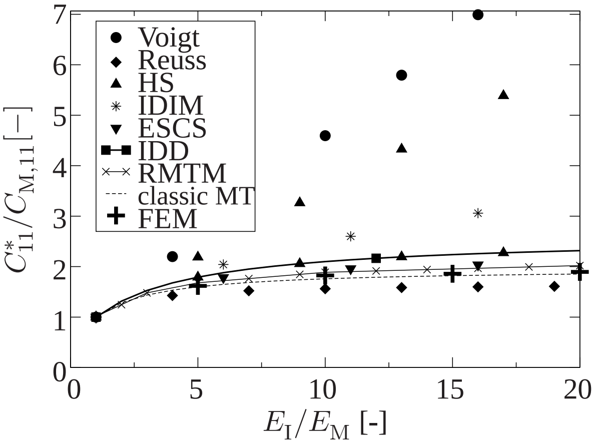

Figure 1.38: Prediction of effective Young's modulus C^*_{11} with different homogenization methods for different stiffness ratios $E_\mathrm{I}/E_\mathrm{M}$ for $c = 0.4$ for hexagonal inclusions.

increase of the effective elastic modulus in the end. Afore it remains at a nearly constant level. The same behavior can be observed for the upper and lower Hashin-Shtrikman bounds only at a higher or lower level, respectively. As mentioned previously the results for the IDD method and the Mori-Tanaka method coincide with the lower Hashin-Shtrikman bound. The interpolative double inclusion model shows a behavior between the lower and upper Hashin-Shtrikman bounds. In the beginning the IDIM shows a similar behavior as the lower HS bound but with increasing volume fraction the behavior of the upper HS bound has an increasing influence on the behavior. It can be seen that the ESCS has a very unstable behavior which depends strongly on the stiffness ratio. By comparing the results from RMTM for hexagonal inclusions with the results from the MT scheme for circular inclusions the general behavior is similar, however, the values are in certain regions of the volume fraction and the stiffness ratio quite different.

As can be seen by interpretation of these surface plots and Figure 1.38, the stiffness ratio has an immense effect on the effective properties, especially at high volume fractions of inclusion. The gradient in the effective stiffness component C^*_{11} between different stiffness ratios is decreasing with increasing volume fraction, however, the range over the stiffness ratio where a gradient is existent is increasing with increasing volume fraction. E.g., the RMTM shows for $c = 0.4$ nearly no gradient after a stiffness ratio of five but for smaller stiffness ratios a quite high gradient. For $c = 0.8$ this gradient is very small between the single ratios but still existent until high ratios. As Figure 1.38 shows, the different homogenization methods behave very differently over different stiffness ratios which is also visible in the surface plots.

Therefore the homogenization methods should also be checked for their behavior for different stiffness ratios, as done here, instead of solely investigating their behavior at different volume fractions. It was shown that the IDD method coincides with the Mori-Tanaka estimate for all investigated inclusion shapes if the material is isotropic. Anisotropic material behavior will be investigated in future work. The ESCS shows no sensible results in this study and therefore will not be considered further. However, it has to be reconsidered in how far the IDD method is valid due to the fact that this method is derived from the ESCS. The analytical solution for the Eshelby tensor is quite simple to evaluate due to its explicit form and shows quite good results for the triangular and square shaped inclusion, however, for the hexagonal inclusion the prediction was wrong. It is to be expected that the results for non-convex shaped inclusions would lead to larger errors as seen for the convex hexagonal inclusion. This implies that the analytical solution for the Eshelby tensor for non-ellipsoidal inclusions cannot directly be applied without considering that the prediction is valid. The investigated RMTM show a very good agreement for the presented inclusion shapes. Only for very high volume fraction this method predicts unreasonable results. However, the potential of this method is promising and could be combined with a database approach (e.g., Temizer and Wriggers, 2007; Temizer and Zohdi, 2007) to obtain the elastic behavior for a distribution of different irregular shaped inclusions. In general the homogenization schemes predicted acceptable results for non-ellipsoidal inclusions where the RMTM gave the best prediction. Also the IDIM showed good results for triangular and square inclusions, however, the quality depends on the validity of the analytic approximated Eshelby tensor.

1.5.4 Distribution of shapes

In this section the effective elasticity tensor for a distribution of inclusion shapes is calculated with the previously compared methods. Further these results are compared with results obtained from a discretized exemplary microstructure. It is assumed that the analyzed microstructure can be representatively described via the previously three analyzed shapes. The amount of each inclusion shape is anticipated due to the fact that we do not have a software which can do this automatically. Therefore the following shape distribution is assumed: $c_{\text{hex}} = 0.4$, $c_{\text{tri}} = 0.19$ and $c_{\text{square}} = 0.18$. Figure 1.39 shows the corresponding results. It can be seen that the RMTM method predicts the same values for higher stiffness ratios as the IDD method with analytical Eshelby tensor. However, both do not predict the correct behavior of the microstructure. The

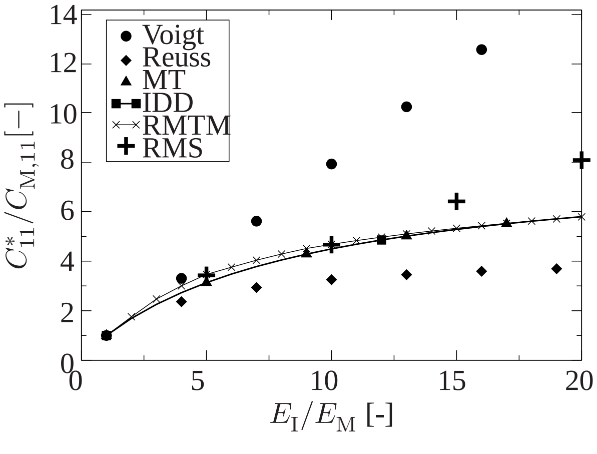

Figure 1.39: Prediction of effective Young's modulus C^*_{11} with different homogenization methods for different stiffness ratios $E_\mathrm{I}/E_\mathrm{M}$ for $c_{\text{hex}} = 0.4$, $c_{\text{tri}} = 0.19$ and $c_{\text{square}} = 0.18$. (RMS = real microstructure)

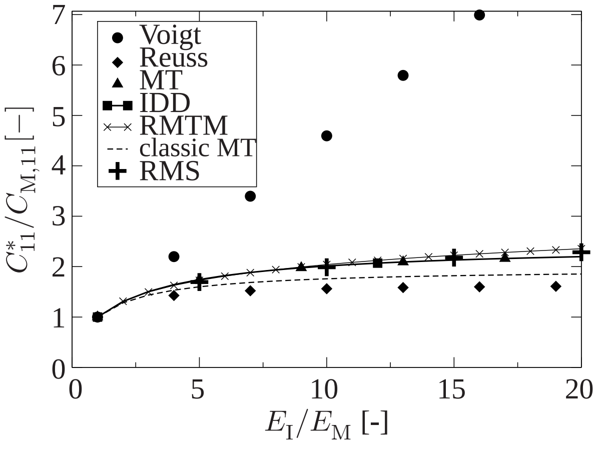

Figure 1.40: Prediction of effective Young's modulus C^*_{11} with different homogenization methods for different stiffness ratios $E_\mathrm{I}/E_\mathrm{M}$ for $c_{\text{hex}} = 0.2$, $c_{\text{tri}} = 0.1$ and $c_{\text{square}} = 0.1$.

main reason for this is that the three shapes are not sufficient and also the orientation of the inclusion has to be taken into consideration. With a detailed characterization it would be possible to determine this information, however, a lot of work has to be done which results in the fact that it is ”cheaper” to discretize directly the microstructure.

In Figure 1.40 another comparison for a distribution with lower volume fraction is shown. The presented FEM results are obtained from an ideal microstructure where the inclusions are randomly distributed. As it can be seen the RMTM predicts best the FEM results for all stiffness ratios. Also the MT and IDD method with analytical Eshelby tensor predict the FEM results more accurately compared to the results with the classic MT scheme for circular inclusions. Generally this shows that also the effective properties for a distribution of irregular inclusion shapes can be calculated via RMTM and also with the homogenization methods which use an analytical expression of the Eshelby tensor for each irregular inclusion.

1.6 Summary and outlook

In this paper, a number of standard homogenization methods are reviewed and their behavior is compared. The comparison was performed with regard to the inclusion volume fraction, which can usually be found in the literature, but also regarding the contrast in the elastic constituents. It was shown that the contrast has a significant influence on the estimates of these methods and therefore has to be taken into consideration. Results obtained from FEM were compared with these predictions. It was shown that especially the IDIM agrees quite well with the FEM results. Furthermore two relatively new approaches, the ESCS and IDD method, were recalled and compared to the classical homogenization results. The results obtained show that a further analysis of the IDD method especially in comparison to the Mori-Tanaka estimate, is reasonable due to its formulation. The IDD estimate has an explicit structure, with a physical explanation of the involved components and it is valid for multiphase composites. It also takes into account the influence of the interaction between inclusions and their surrounding matrix. Formally the method has a universally applicable form to various inclusion distributions. Therefore this method fulfills the main requirements on homogenization methods as mentioned before.

Further three strategies have been evaluated to determine the effective properties of elastic media with irregular shaped inclusions. An analytical procedure for determining the Eshelby tensor based on the irreducible decomposition of the Eshelby tensor (Zheng et al., 2006) was implemented and used in classical homogenization schemes and compared with results obtained via the Mori-Tanaka method with replacement tensor approach. This method is based on the computation of the contribution of a dilute volume fraction of one inclusion into an infinite matrix material. These comparisons were carried out for three different irregular shaped inclusions. Further these methods were also applied to a distribution of different irregular inclusion shapes and the results were compared with a discretized real microstructure and a discretized ideal microstructure. All investigations were not limited to the volume fraction but rather to different stiffness ratios between matrix and inclusion which has an immense influence on the results of the homogenization schemes.

It was shown that the IDD method coincides with the Mori-Tanaka estimate for all investigated inclusion shapes if the material is isotropic. Anisotropic material behavior will be investigated in future work and it will be checked if a case can be obtained in which both methods do not agree. Due to the structure of the IDD method, with a physical explanation of the involved components, this method will be considered in further work. The ESCS shows no sensible results in this study and therefore can not be recommended in further studies. This study has shown that the RMTM gives the best prediction of the effective properties as long as the volume fractions do not reach values of 80% or higher. However, the evaluation is quite time consuming. In our opinion this could be decreased by using this method in combination with a database approach which would make the method really applicable to distribution of inclusion shapes. Also the homogenization methods using an analytical expression for the Eshelby tensor show for most inclusion shapes good results. Also for a combination of different inclusion shapes these method show acceptable results. However, for every shape it has to be checked if the solution is valid or not.

A procedure for discretizing a real micrograph was presented and the results were compared with the previous mentioned method. It was not possible to determine the exact distribution of shapes and therefore the results of the comparison were rather poor. To determine the elastic properties of a real microstructure it is recommended to use a discretization instead of using another method. For ideal microstructures these homogenization methods show valid results.

Chapter 2

Homogenization modeling of two-phase composites with a layered microstructure

Abstract– The purpose of this chapter is to introduce a homogenization method for the material behavior of two-phase composites characterized by a thin-layer-type microstructure. Such microstructures can be found for example in thermally-sprayed coating materials like WC/Fe in which the phase morphology takes the form of interpenetrating layers. The basic idea here is to idealize the thin-layered microstructure as a first-order laminate. Comparison of the methods with existing homogenization schemes as well as with the reference finite-element model for idealized composites demonstrates the advantage of the current approach for such microstructures. For completeness, the current method is also applied to the classical case of two-phase microstructure with spherical inclusions, which demonstrates clearly the limits of the approach. Further a first extension to a variable interface orientation is presented.

2.1 Introduction

The modeling of the material behavior of composites is generally based on a model for the behavior of each constituent or phase of the composite together with one for the interaction of the phases. Traditionally, highly-idealized analytical and semi-analytical models were developed for this purpose with the help of volume-averaging or homogenization methods (e.g., Reuss, Voigt, Hashin-Shriktmann, and so on (see Nemat-Nasser and Hori, 1999), and are limited to linear thermoelasticity. More recently, methods for this purpose based on the assumption of scale-separation and the concept of representative volume element (RVE) have been developed and applied (e.g., the Mori-Tanaka method (e.g., Benveniste, 1987), the double inclusion model (e.g., Pierard et al., 2004), Interaction Direct Derivative (IDD) method (Du and Zheng, 2002; Zheng and Du, 2001), or self-consistent schemes such as Molinari et al. (1987) or Mercier and Molinari (2009), for a further overview and details see Gross and Seelig (2001); Nemat-Nasser and Hori (1993, 1999). Generally-speaking, these latter methods consist of two steps. In the first step, a local problem for a single inclusion is solved in order to obtain a model for the material behavior at the RVE-level. The prototype here is the approach of Eshelby (1957) for the case of an ellipsoidal elastic inclusion in an infinite matrix. The second step consists of averaging the RVE-fields to obtain those for the composite as a whole (e.g., Mercier and Molinari, 2009). As before, the focus here has been on linear thermoelasticity, also in order to exploit linearity in the mathematical formulation. By analogy, extensions of these methods to the inelastic case are generally based on linearized incremental formulations (e.g., Ponte Castaneda and Suquet, 1998) pertaining mainly to metal inelasticity. As discussed by, e.g., Molinari et al. (1997), many of these neglect the interactions between the phases, something which results in too stiff behavior. Because of this, more recent models take phase interaction into account in some fashion (e.g., Lebensohn and Tome, 1993; Molinari et al., 1987). As in the classical case of Eshelby, many of these are based on particular assumptions about the morphology of the microstructural phases. This leads sometimes to limited use of the presented methods. If the size of the RVE is very small, size effects can occur, which are not accounted for at the macroscale. Furthermore, large spatial gradients at the macro-scale cannot be resolved by these methods and they are in general restricted to standard continuum mechanics theory. Full extension to second-order to incorporate size-effects of the underlying microstructure can be found by several authors (e.g., Geers et al., 2010; Jänicke et al., 2009; Kouznetsova et al., 2004). Describing local deformation state of microstructured materials by extended continuum theories is done (, e.g., Forest, 2008; Jänicke et al., 2009). In other cases, e.g., in Böhlke et al. (2008) texture related microstructural effects are accounted for by using orientation distribution functions and texture coefficients to predict the resulting anisotropy in sheet metals and the path-dependent mechanical properties.

The purpose of the current work is to introduce a homogenization approach for two-phase composites whose microstructure is characterized by being layer- or lamellar-like. Such microstructures are present for example in thermally-sprayed coatings. The layered phase morphology arising here is determined among other things by the nature of the manufacturing process. The current homogenization strategy is based on the idealization of such microstructure as first-order laminate (e.g., Silhavy (1997)). Although well-known as a model for the transformation interface between, e.g., austenite and martensite in the realm of phase transformations (e.g., Kouznetsova et al., 2009), its application in the current context of structural two-phase composites is novel.

The paper begins in section 2.2 with a brief summary of the viscoplastic material model for each phase of the two-phase composite under consideration. For comparison with the current approach, existing homogenization methods, in particular that based on the assumption of phase-wise constant plastic strain, are briefly reviewed in section 2.3. The current approach as based on first-order laminate theory is introduced in section 2.4. After investigating the behavior of this model with the help of simple deformation cases in section 2.5, a comparison of results from the laminate model with analogous ones from selected existing homogenization models (e.g., Taylor, phase-wise constant plastic deformation) is given in section 2.6 together with corresponding FE results for layered composites. As discussed for example in Pierard et al. (2007), most of the available results for viscoplastic composites focus on composites containing spherical particles which are periodically distributed within the matrix. To demonstrate the limits of the current approach, it is applied as well to this case, i.e., the “canonical” case of a two-phase composite with spherical inclusions. Followed by a discussion of a variable interface direction in section 2.7. The work ends (section 2.8) with a summary and conclusions. For simplicity, the current work is restricted to small deformation. In work in progress, the method is being extended to large deformation.

2.2 Material model

In the current work, material models are formulated in the context of continuum thermodynamics. In this context, the material behavior is related to energetic and dissipative processes. As usual, the energetic part is determined by the free energy density ψ. For simplicity, attention is restricted here to quasi-static conditions and metallic materials exhibiting small deformation and Voce (i.e., saturation) isotropic hardening. In this case, the additive form

$$\psi(\boldsymbol{E}_{\mathrm{E}},\alpha_{\mathrm{P}}) = \frac{1}{2}\,\boldsymbol{E}_{\mathrm{E}}\cdot\mathcal{C}_{\mathrm{E}}\boldsymbol{E}_{\mathrm{E}} + s_{\mathrm{H}}\left\{\alpha_{\mathrm{P}} + \frac{1}{c_{\mathrm{H}}}\left(e^{-c_{\mathrm{H}}\alpha_{\mathrm{P}}} - 1\right)\right\} \tag{2.1}$$

of ψ into elastic and hardening contributions, respectively, is assumed. In particular, the former depends on the elastic strain

$$\boldsymbol{E}_{\mathrm{E}} = \boldsymbol{E} - \boldsymbol{E}_{\mathrm{P}}\ , \tag{2.2}$$

corresponding inelastic strain $\boldsymbol{E}_{\mathrm{P}}$, and total (small) strain $\boldsymbol{E} = \mathrm{sym}(\boldsymbol{F} - \boldsymbol{I})$, with $\boldsymbol{F}$ the deformation gradient. Here, $\mathrm{sym}(\boldsymbol{A}) := \frac{1}{2}(\boldsymbol{A} + \boldsymbol{A}^{\mathrm{T}})$, represents the symmetric part of any second-order tensor $\boldsymbol{A}$. The evolution of $\boldsymbol{E}_{\mathrm{P}}$ depends on that of the accumulated equivalent inelastic deformation α_{P}, as shown in (2.6) below. Material properties here include the elastic stiffness tensor $\mathcal{C}_{\mathrm{E}}$, the difference s_{H} between the initial and saturated values of the yield stress, and the rate c_{H} of hardening saturation. As usual, the free energy determines in particular the stress

$$\boldsymbol{T} = \partial_{\boldsymbol{E}_{\mathrm{E}}}\psi\ . \tag{2.3}$$

Assuming dislocation glide as the dominant mechanism of inelastic deformation, the inelastic behavior is determined by an inelastic potential ϕ_{P} modeled by the simple viscoplastic form

$$\phi_{\mathrm{P}}(\varsigma_{\mathrm{P}}) = \sigma_{\mathrm{D}}\,\dot{\alpha}_{\mathrm{r}}\left\{\exp\left(\frac{\langle\varsigma_{\mathrm{P}} - \sigma_{\mathrm{A}}\rangle_{+}}{\sigma_{\mathrm{D}}}\right) - \frac{\langle\varsigma_{\mathrm{P}} - \sigma_{\mathrm{A}}\rangle_{+}}{\sigma_{\mathrm{D}}}\right\} \tag{2.4}$$

for the activation of dislocation motion and inelastic deformation. Here, $\langle f\rangle_{+} := \frac{1}{2}(f + |f|)$ represents the ramp function. In particular, this potential determines the flow rule

$$\dot{\alpha}_{\mathrm{P}} = \partial_{\langle\varsigma_{\mathrm{P}}-\sigma_{\mathrm{A}}\rangle_{+}}\phi_{\mathrm{P}} \tag{2.5}$$

for α_{P}. Here, σ_{A} is the initial activation (yield) stress, σ_{D} represents the drag stress, and $\dot{\alpha}_{\mathrm{r}}$ is the characteristic deformation rate associated with dislocation motion. In addition, $\varsigma_{\mathrm{P}} = \sigma_{\mathrm{vM}} - \partial_{\alpha_{\mathrm{P}}}\psi$ is the thermodynamic conjugate to α_{P} for the current model, where $\sigma_{\mathrm{vM}}(\boldsymbol{T}) = \sqrt{3\,\mathrm{dev}(\boldsymbol{T})\cdot\mathrm{dev}(\boldsymbol{T})/2}$ represents the von Mises equivalent stress measure. Here, $\mathrm{dev}(\boldsymbol{A}) := \boldsymbol{A} - \frac{1}{3}\mathrm{tr}(\boldsymbol{A})\,\boldsymbol{I}$ represents the deviatoric part, and $\mathrm{tr}(\boldsymbol{A})$ the trace, of any second-order tensor $\boldsymbol{A}$. The evolution of $\boldsymbol{E}_{\mathrm{P}}$ is assumed to be activated by that of α_{P}. Consider in this regard the constitutive relation

$$\dot{\boldsymbol{E}}_{\mathrm{P}} = \dot{\alpha}_{\mathrm{P}}\,\boldsymbol{N}_{\mathrm{P}} \tag{2.6}$$

for the evolution of $\boldsymbol{E}_{\mathrm{P}}$ quasi-linear in $\dot{\alpha}_{\mathrm{P}}$, with $\boldsymbol{N}_{\mathrm{P}} = \partial_{\boldsymbol{T}}\sigma_{\mathrm{vM}}(\boldsymbol{T})$ the flow direction. Here we have assumed that the deformation is small enough so that no significant grain rotation and no texture development takes place.

For simplicity, the inelastic homogenization models to be considered in what follows are based on the following explicit algorithm. This is formulated on an arbitrary time interval $[t_n, t_{n+1}]$ of duration $t_{n+1,n} := t_{n+1} - t_n$. The algorithm begins with the forward-Euler update

$$\alpha_{\mathrm{P}\,n+1,n} = \begin{cases} 0 & \varsigma_{\mathrm{P}\,n} \leqslant \sigma_{\mathrm{A}} \\ t_{n+1,n}\,\dot{\alpha}_{\mathrm{r}} \left\{ \exp\left(\dfrac{\varsigma_{\mathrm{P}\,n} - \sigma_{\mathrm{A}}}{\sigma_{\mathrm{D}}} \right) - 1 \right\} & \varsigma_{\mathrm{P}\,n} > \sigma_{\mathrm{A}} \end{cases} \tag{2.7}$$

for α_{P} from (2.5), with $\alpha_{\mathrm{P}\,n+1,n} := \alpha_{\mathrm{P}\,n+1} - \alpha_{\mathrm{P}\,n}$. In turn, this induces the update

$$\boldsymbol{E}_{\mathrm{E}\,n+1} = \boldsymbol{E}_{n+1} - \boldsymbol{E}_{\mathrm{P}\,n+1} = \boldsymbol{E}_{n+1} - \boldsymbol{E}_{\mathrm{P}\,n} - \alpha_{\mathrm{P}\,n+1,n}\,\boldsymbol{N}_{\mathrm{P}\,n} \tag{2.8}$$

of the elastic strain, and so that

$$\boldsymbol{T}_{n+1} = \mathcal{C}_{\mathrm{E}}[\boldsymbol{E}_{\mathrm{E}\,n+1}] \tag{2.9}$$

of the stress. Consequently, the history variables for each phase include α_{P} and $\boldsymbol{E}_{\mathrm{P}}$ here.

The above model contains the material properties $\mathcal{C}_{\mathrm{E}}$, s_{H}, c_{H}, σ_{A}, σ_{D}, and $\dot{\alpha}_{\mathrm{r}}$, which are to be specified for each phase in what follows. This completes the short summary of the material model for each phase. Now we turn to the homogenization schemes of interest in this work.

2.3 Model based on phase-wise constant plastic strain

The homogenization approaches to be discussed in what follows are all based as usual on the assumption of scale separation, which lies at the heart of the RVE concept. From the numerical point of view, this facilitates the restriction of microstructural effects on the material behavior to the integration-point level of a corresponding finite-element simulation. In the current purely mechanical incremental inelastic context, this involves as usual the specification of deformation gradients $\boldsymbol{F}_n$ and $\boldsymbol{F}_{n+1}$ at the beginning ($t = t_n$) and end ($t = t_{n+1}$) of the current time interval $[t_n, t_{n+1}]$, as well as the values $\alpha_{\mathrm{P}\,n}$ and $\boldsymbol{E}_{\mathrm{P}\,n}$ of the internal variables at the beginning of this interval. In this case, the total strain $\boldsymbol{E}_n = \mathrm{sym}(\boldsymbol{F}_n - \boldsymbol{I})$ and $\boldsymbol{E}_{n+1} = \mathrm{sym}(\boldsymbol{F}_{n+1} - \boldsymbol{I})$ at the beginning and end of this interval, respectively, are specified.

The assumption of phase-wise constant plastic strain is a special case of the so-called Transformation Field Analysis (TFA) proposed by Dvorak (1992). TFA offers an interesting way of reducing the number of macroscopic internal variables by assuming that phase fields are phase-wise constant. In particular, this assumption is reasonable for microstructures consisting of plastically-homogeneous domains. In general, however, it results in a model for the effective behavior of the composite which is too stiff. Indeed, this method prohibits the localization of inelastic deformation at phase boundaries as a means of stress relaxation, resulting in unrealistic stress concentration there and generally higher stresses. On the other hand, in special cases, e.g., the current one of thin layer-like composites, the relative uniformity of the stress and strain fields almost everywhere may minimize this error and lead to reasonable results.

To begin, consider an elastic problem with the same boundary conditions as the inelastic case. The kinematically allowable fields are given by

$$\begin{aligned} \boldsymbol{u}(\boldsymbol{x}) &= \boldsymbol{E}_0\,\boldsymbol{x}\ , \\ \tilde{\boldsymbol{E}}(\boldsymbol{x}) &= \mathcal{A}(\boldsymbol{x})\,\boldsymbol{E}_0\ , \\ \langle\tilde{\boldsymbol{E}}\rangle &= \boldsymbol{E}_0\ . \end{aligned} \tag{2.10}$$

Here, $\tilde{\boldsymbol{E}}(\boldsymbol{x})$ is the strain field of the elastic problem with uniform displacement boundary condition $\boldsymbol{u}$, and $\langle f\rangle$ represents the volume average of f. Further, $\boldsymbol{E}_0$ is the applied strain at the boundary, and $\mathcal{A}$ represents the influence tensor whose form is determined by solution of the boundary value problem (e.g., Gross and Seelig, 2001). Scalar multiplication of the stress-strain relation $\boldsymbol{T} = \mathcal{C}_{\mathrm{E}}[\boldsymbol{E} - \boldsymbol{E}_{\mathrm{P}}]$ from (2.2) and (2.3) in terms of $\boldsymbol{E}_{\mathrm{P}}$ with $\tilde{\boldsymbol{E}}$ and averaging yields

$$\begin{aligned} \langle\boldsymbol{T}\cdot\tilde{\boldsymbol{E}}\rangle &= \langle(\mathcal{A}^{\mathrm{T}}\mathcal{C}_{\mathrm{E}})\tilde{\boldsymbol{E}}\rangle\cdot\boldsymbol{E}_0 - \langle(\mathcal{A}^{\mathrm{T}}\mathcal{C}_{\mathrm{E}})\boldsymbol{E}_{\mathrm{P}}\rangle\cdot\boldsymbol{E}_0\ , \\ &= \mathcal{C}_{\mathrm{E}*}[\langle\tilde{\boldsymbol{E}}\rangle - \bar{\boldsymbol{E}}_{\mathrm{P}}]\cdot\boldsymbol{E}_0\ , \end{aligned} \tag{2.11}$$

where

$$\mathcal{C}_{\mathrm{E}\,*}\langle\tilde{\boldsymbol{E}}\rangle := \langle(\mathcal{A}^{\mathrm{T}}\mathcal{C}_{\mathrm{E}})\tilde{\boldsymbol{E}}\rangle \tag{2.12}$$

“defines” the effective elasticity tensor $\mathcal{C}_{\mathrm{E}\,*}$ of the composite, and

$$\bar{\boldsymbol{E}}_{\mathrm{P}} := \mathcal{C}_{\mathrm{E}\,*}^{-1}\langle(\mathcal{A}^{\mathrm{T}}\mathcal{C}_{\mathrm{E}})\boldsymbol{E}_{\mathrm{P}}\rangle \tag{2.13}$$

represents the effective inelastic strain tensor. In particular, for the current case of a two-phase material with constant plastic deformation in every phase, i.e.,

$$\langle\boldsymbol{E}_{\mathrm{P}}\rangle = \begin{cases} \boldsymbol{E}_{\mathrm{P}\,1} & \text{in } P_1 \\ \boldsymbol{E}_{\mathrm{P}\,2} & \text{in } P_2 \end{cases} \tag{2.14}$$

one obtains

$$\bar{\boldsymbol{E}}_{\mathrm{P}} = \mathcal{C}_{\mathrm{E}*}^{-1}\sum\nolimits_{\omega=1}^{2}\lambda_\omega\,(\mathcal{A}_\omega^{\mathrm{T}}\mathcal{C}_{\mathrm{E}\,\omega})\boldsymbol{E}_{\mathrm{P}\,\omega} \tag{2.15}$$

for this tensor in terms of the phase properties and the volume fraction $\lambda_1 \equiv \lambda$ of phase 1 and $\lambda_2 \equiv 1 - \lambda_1$ of phase 2 in the composite. Via the Hill-Mandel condition $\langle\boldsymbol{T}\cdot\tilde{\boldsymbol{E}}\rangle = \langle\boldsymbol{T}\rangle\cdot\langle\tilde{\boldsymbol{E}}\rangle = \langle\boldsymbol{T}\rangle\cdot\boldsymbol{E}_0$, the arbitrariness of $\boldsymbol{E}_0$ in (2.11) then implies

$$\langle\boldsymbol{T}\rangle = \mathcal{C}_{\mathrm{E}\,*}[\langle\tilde{\boldsymbol{E}}\rangle - \bar{\boldsymbol{E}}_{\mathrm{P}}] \tag{2.16}$$

for the effective stress-strain relation of the inelastic composite. Identifying then the composite (mixture) stress $\boldsymbol{T}$ with $\langle\boldsymbol{T}\rangle$, the composite (mixture) strain $\boldsymbol{E}$ with $\langle\tilde{\boldsymbol{E}}\rangle$, and the composite (mixture) inelastic strain $\boldsymbol{E}_{\mathrm{P}}$ with $\bar{\boldsymbol{E}}_{\mathrm{P}}$, the form

$$\boldsymbol{T} = \mathcal{C}_{\mathrm{E}\,*}[\boldsymbol{E} - \boldsymbol{E}_{\mathrm{P}}] \tag{2.17}$$

follows for the effective stress of the composite depending on the effective elasticity tensor $\mathcal{C}_{\mathrm{E}\,*}$.

Consider next the relations

$$\boldsymbol{E} = \sum\nolimits_{\omega=1}^{2}\lambda_\omega\,\boldsymbol{E}_\omega \tag{2.18}$$

and

$$\boldsymbol{T} = \sum\nolimits_{\omega=1}^{2} \lambda_\omega \, \boldsymbol{T}_\omega = \sum\nolimits_{\omega=1}^{2} \lambda_\omega \, \mathcal{C}_{\mathrm{E}\,\omega}[\boldsymbol{E}_\omega - \boldsymbol{E}_{\mathrm{P}\,\omega}] \tag{2.19}$$

for the mixture strain and stress, respectively, the latter via (2.3). Enforcing equality between (2.17) and (2.19) then results in the algorithmic system

$$\begin{aligned} \boldsymbol{R}_{\boldsymbol{E}} &= \sum\nolimits_{\omega=1}^{2} \lambda_\omega \, \boldsymbol{E}_\omega - \boldsymbol{E} \, , \\ \boldsymbol{R}_{\boldsymbol{T}} &= \sum\nolimits_{\omega=1}^{2} \lambda_\omega \, \mathcal{C}_{\mathrm{E}\,\omega}[\boldsymbol{E}_\omega - \boldsymbol{E}_{\mathrm{P}\,\omega}] - \mathcal{C}_{\mathrm{E}\,*}[\boldsymbol{E} - \boldsymbol{E}_{\mathrm{P}}] \end{aligned} \tag{2.20}$$

to solve for the $\boldsymbol{E}_1$ and $\boldsymbol{E}_2$. Given or known here are the total strain $\boldsymbol{E}$, the volume fractions λ_1 and λ_2, as well as the material properties $\mathcal{C}_{\mathrm{E}\,1}$ and $\mathcal{C}_{\mathrm{E}\,2}$ of each phase. As discussed above, the effective composite elasticity tensor $\mathcal{C}_{\mathrm{E}\,*}$ is determined via analytical solution of the corresponding elastic homogenization problem using for example the Mori-Tanaka method (e.g., Nemat-Nasser and Hori (1999)).

Algorithmically the solution is obtained as follows. For the current time step $\boldsymbol{E}_n$ and $\boldsymbol{E}_{n+1}$ are known. The constant plastic strains $\boldsymbol{E}^{\mathrm{tr}}_{\mathrm{P}\,1}$ and $\boldsymbol{E}^{\mathrm{tr}}_{\mathrm{P}\,2}$ are calculated via trial values for $\boldsymbol{E}^{\mathrm{tr}}_{1\,n+1}$ and $\boldsymbol{E}^{\mathrm{tr}}_{2\,n+1}$. $\boldsymbol{E}^{\mathrm{tr}}_{\mathrm{P}}$ can be found with (2.15). With help of the Newton-Raphson algorithm, the algorithmic system (2.20) can be solved

$$\begin{pmatrix} \partial_{\boldsymbol{E}_1} \boldsymbol{R}_{\boldsymbol{E}} & \partial_{\boldsymbol{E}_2} \boldsymbol{R}_{\boldsymbol{E}} \\ \partial_{\boldsymbol{E}_1} \boldsymbol{R}_{\boldsymbol{T}} & \partial_{\boldsymbol{E}_2} \boldsymbol{R}_{\boldsymbol{T}} \end{pmatrix}^{(k)}_{n+1} \begin{pmatrix} \boldsymbol{E}^{(k+1)}_1 - \boldsymbol{E}^{(k)}_1 \\ \boldsymbol{E}^{(k+1)}_2 - \boldsymbol{E}^{(k)}_2 \end{pmatrix}_{n+1} = - \begin{pmatrix} \boldsymbol{R}_{\boldsymbol{E}} \\ \boldsymbol{R}_{\boldsymbol{T}} \end{pmatrix}^{(k)}_{n+1} \tag{2.21}$$

for $\boldsymbol{E}^{(k+1)}_{1\,n+1}$ and $\boldsymbol{E}^{(k+1)}_{2\,n+1}$, which are used to calculate the new $\boldsymbol{E}^{(k+1)}_{\mathrm{P}\,n+1}$, $\boldsymbol{E}^{(k+1)}_{\mathrm{P}\,1\,n+1}$ and $\boldsymbol{E}^{(k+1)}_{\mathrm{P}\,2\,n+1}$. This algorithmic system is iteratively solved until $|\boldsymbol{R}_{\boldsymbol{E}}|$ and $|\boldsymbol{R}_{\boldsymbol{T}}|$ are smaller than 10^{-9}. Using the converged results, one can then calculate

$$\boldsymbol{T}_{\omega\,n+1} = \mathcal{C}_{\mathrm{E}\,\omega}[\boldsymbol{E}_\omega - \boldsymbol{E}_{\mathrm{P}\,\omega}] \tag{2.22}$$

and the total stress via (2.19). The corresponding stress tangent

$$\partial_{\boldsymbol{E}_{n+1}} \boldsymbol{T}_{n+1} = \sum\nolimits_{\omega=1}^{2} \lambda_\omega \, \partial_{\boldsymbol{E}_{n+1}} \boldsymbol{T}_{\omega\,n+1} \tag{2.23}$$

results from a simple mixture of the stress tangents of the single materials. Note that the iterative solution is particularly efficient in this case due to the fact that the plastic strain is constant.

2.4 Laminate model

As discussed in the introduction, layer or laminate-like microstructures arise in technological processes such as thermal spray coating. Both from this point of view, and as an alternative means to model the interaction of the phases in a composite with the corresponding morphology, it is interesting to formulate the corresponding homogenization model and compare it with selected existing ones for the inelastic case. For simplicity, attention is restricted here as in the previous section to the case of small deformation. For the case of micron-thick thermal spray coatings, for example, this assumption is certainly reasonable. In this case, the kinematics of the two-phase system is determined by the mixture relation

$$\boldsymbol{F} = \lambda \boldsymbol{F}_1 + (1-\lambda)\,\boldsymbol{F}_2 = \boldsymbol{F}_2 + \lambda\,[\![\boldsymbol{F}]\!] \tag{2.24}$$

for the deformation gradient $\boldsymbol{F}$, where $[\![f]\!] = f_1 - f_2$ represents the ”jump” of f across the phase interface. In particular, in the laminate context (e.g. Silhavy, 1997), the jump $[\![\boldsymbol{F}]\!]$ in deformation state across the phase interface is modeled constitutively via the rank-one connection

$$[\![\boldsymbol{F}]\!] = \boldsymbol{h} \otimes \boldsymbol{m} \tag{2.25}$$

determined by the interface deformation vector $\boldsymbol{h}$ and interface unit normal $\boldsymbol{m}$. In this case, note that $\boldsymbol{h} = [\![\boldsymbol{F}]\!]\boldsymbol{m}$ and $[\![\boldsymbol{F}]\!]\,(\boldsymbol{I} - \boldsymbol{m} \otimes \boldsymbol{m}) = \boldsymbol{0}$ hold at the interface. Solving (2.24) and (2.25) for $\boldsymbol{H}_i = \boldsymbol{F}_i - \boldsymbol{I}$, $i = 1, 2$, we obtain

$$\begin{aligned} \boldsymbol{H}_1(\boldsymbol{H}, \lambda, \boldsymbol{h}, \boldsymbol{m}) &= \boldsymbol{H} + (1-\lambda)\,\boldsymbol{h} \otimes \boldsymbol{m}\ , \\ \boldsymbol{H}_2(\boldsymbol{H}, \lambda, \boldsymbol{h}, \boldsymbol{m}) &= \boldsymbol{H} - \lambda\,\boldsymbol{h} \otimes \boldsymbol{m}\ . \end{aligned} \tag{2.26}$$

In turn, these yield the corresponding strains

$$\begin{aligned} \boldsymbol{E}_1(\boldsymbol{E}, \lambda, \boldsymbol{h}, \boldsymbol{m}) &= \boldsymbol{E} + (1-\lambda)\,\mathrm{sym}(\boldsymbol{h} \otimes \boldsymbol{m})\ , \\ \boldsymbol{E}_2(\boldsymbol{E}, \lambda, \boldsymbol{h}, \boldsymbol{m}) &= \boldsymbol{E} - \lambda\,\mathrm{sym}(\boldsymbol{h} \otimes \boldsymbol{m})\ , \end{aligned} \tag{2.27}$$

as functions of the mixture strain $\boldsymbol{E}$, the volume fraction λ of phase 1, and the interface properties $\boldsymbol{h}$ and $\boldsymbol{m}$. Like the deformation and strain, the free energy density of the mixture is modeled as a volume-fraction-weighted convex combination

$$\begin{aligned} &\psi(\boldsymbol{E}, \lambda, \boldsymbol{h}, \boldsymbol{m}, \boldsymbol{E}_{\mathrm{P}\,1}, \alpha_{\mathrm{P}\,1}, \boldsymbol{E}_{\mathrm{P}\,2}, \alpha_{\mathrm{P}\,2}) \\ &= \lambda\,\psi(\boldsymbol{E}_1(\boldsymbol{E}, \lambda, \boldsymbol{h}, \boldsymbol{m}) - \boldsymbol{E}_{\mathrm{P}\,1}, \alpha_{\mathrm{P}\,1}) \\ &+ (1-\lambda)\,\psi(\boldsymbol{E}_2(\boldsymbol{E}, \lambda, \boldsymbol{h}, \boldsymbol{m}) - \boldsymbol{E}_{\mathrm{P}\,2}, \alpha_{\mathrm{P}\,2}) \end{aligned} \tag{2.28}$$

of the corresponding phase quantities, with ψ given by (2.1). In this case, we neglect any additional possible contributions, e.g., coming from the interface itself. In these relations, the total strain $\boldsymbol{E}$ is given, and the phase quantities $\boldsymbol{E}_{\mathrm{P}\,1,2}$ and $\alpha_{\mathrm{P}\,1,2}$ are determined by the evolution-constitutive relations (2.5) and (2.6), respectively. This leaves λ, $\boldsymbol{h}$ and $\boldsymbol{m}$ as independent constitutive variables in the model yet to be determined. In particular, since λ is basically determined by the technological process and known, we model it as constant here. In addition, we begin by assuming that the orientation $\boldsymbol{m}$ of the laminate interface is fixed and parallel to the thickness direction of the coating / composite. To determine $\boldsymbol{h}$, we assume that it is purely energetic in nature and require its value to satisfy mechanical equilibrium

$$\boldsymbol{0} = \partial_{\boldsymbol{h}}\psi = \lambda\,(1-\lambda)[\![\boldsymbol{T}]\!]\boldsymbol{m} \tag{2.29}$$

at the interface ($\lambda \neq 0$). This yields an implicit equation for $\boldsymbol{h}$.

On this basis, we can use the following algorithm to solve the model relations formulated as follows. As already stated above, for the current time-step, $\boldsymbol{E}_n = \mathrm{sym}(\boldsymbol{F}_{n+1} - \boldsymbol{I})$ and $\boldsymbol{E}_{n+1} = \mathrm{sym}(\boldsymbol{F}_{n+1} - \boldsymbol{I})$ are known. In addition, $\boldsymbol{h}_n$, $\boldsymbol{E}_{\mathrm{P}\,1\,n}$, $\alpha_{\mathrm{P}\,1\,n}$, $\boldsymbol{E}_{\mathrm{P}\,2\,n}$, and $\alpha_{\mathrm{P}\,2\,n}$ are known. From the explicit update of the inelastic phase variables outlined in section 2.2, we then have $\alpha_{\mathrm{P}\,\omega\,n+1}$ and $\boldsymbol{E}_{\mathrm{P}\,\omega\,n+1}$. Using these, one can then calculate

$$\begin{aligned} \boldsymbol{E}_{\mathrm{E}\,\omega\,n+1}(\boldsymbol{h}) &= \boldsymbol{E}_{\omega\,n+1}(\boldsymbol{E}_{n+1}, \boldsymbol{h}) - \boldsymbol{E}^{\omega}_{\mathrm{P}\,n+1} \,, \\ \boldsymbol{T}_{\omega\,n+1}(\boldsymbol{h}) &= \mathcal{C}_{\mathrm{E}\,\omega} \boldsymbol{E}_{\mathrm{E}\,\omega\,n+1}(\boldsymbol{h}) \,, \end{aligned} \tag{2.30}$$

and so solve (2.29) for $\boldsymbol{h}_{n+1}$. A convergence study for the number of iteration steps for the solution of $\boldsymbol{h}$ was carried out. The exact solution was defined for a deviation of 10^{-12} between $\boldsymbol{h}_{\mathrm{n+1}}$ and $\boldsymbol{h}_{\mathrm{n}}$. It was found that after one iteration step the deviation between this value and the exact solution is less than 0.1%. Therefore only one iteration step is necessary. Given $\boldsymbol{h}_{n+1}$ and the corresponding current phase stresses $\boldsymbol{T}_{1\,n+1}$ and $\boldsymbol{T}_{2\,n+1}$, (2.19) determines the current composite stress, and

$$\begin{aligned} \partial^{\mathrm{a}}_{\boldsymbol{E}_{n+1}} \boldsymbol{T}_{n+1} &= \lambda\, \partial^{\mathrm{a}}_{\boldsymbol{E}_{n+1}} \boldsymbol{T}_{1\,n+1} + (1-\lambda)\, \partial^{\mathrm{a}}_{\boldsymbol{E}_{n+1}} \boldsymbol{T}_{2\,n+1} \\ &= \lambda\, \{\partial_{\boldsymbol{E}_{n+1}} \boldsymbol{T}_{1\,n+1} + (\partial_{\boldsymbol{h}_{n+1}} \boldsymbol{T}_{1\,n+1})(\partial^{\mathrm{a}}_{\boldsymbol{E}_{n+1}} \boldsymbol{h}_{n+1})\} \\ &+ (1-\lambda)\, \{\partial_{\boldsymbol{E}_{n+1}} \boldsymbol{T}_{2\,n+1} + (\partial_{\boldsymbol{h}_{n+1}} \boldsymbol{T}_{2\,n+1})(\partial^{\mathrm{a}}_{\boldsymbol{E}_{n+1}} \boldsymbol{h}_{n+1})\} \,, \end{aligned} \tag{2.31}$$

the corresponding stress tangent.

2.5 Model behavior

To apply the laminate model to a given microstructure, the volume fraction λ of phase 1 and normal direction $\boldsymbol{m}$, which are considered fixed and known here in the case of manufactured composites, have to be chosen. In general, these could be chosen arbitrarily. On the other hand, in the case of thin coatings, the layered microstructure has a normal direction approximately parallel to the thickness direction of the coating, as shown in Figure 2.1. As discussed in section 2.2, we investigate the laminate model for a composite consisting of isotropic, thermoelastic, viscoplastic phases, one being soft and the other hard. This is roughly analogous to the case of WC-FeCSiMn coatings shown in Figure 2.1. The parameter values chosen for the two phases are given in Table 2.1. In addition, $\dot{\alpha}_{\mathrm{r}}$ is fixed at 10^{-3} s^{-1}, corresponding to quasi-static loading conditions.

material	E [GPa]	ν [-]	σ_{A} [MPa]	s_{H} [MPa]	c_{H} [-]
soft	210	0.3	130	240	10
hard	430	0.19	2000	0	0

Table 2.1: Material properties of the two phases in the model microstructure. $\sigma_{\mathrm{D}} = 100\mathrm{MPa}$ and $\dot{\alpha}_{\mathrm{r}} = 0.001 s^{-1}$ are for both phases the same.

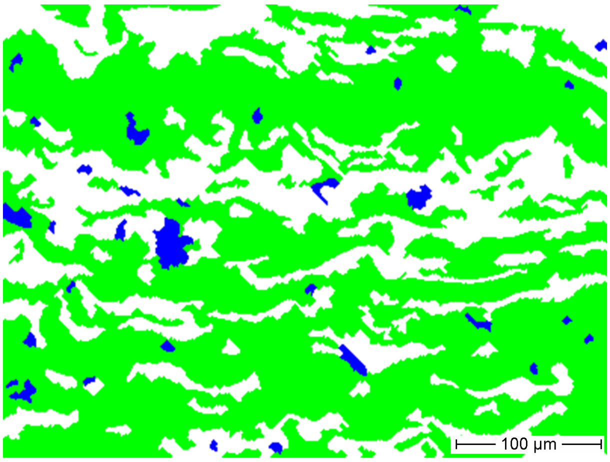

Figure 2.1: Example of a layered microstructure in an arc sprayed WC-FeCSiMn coating which has been thermally sprayed at 700 K onto a steel (Ck45) substrate at room temperature. The original micrograph was processed by an image processing software (Klusemann et al., 2009b). Green and white regions represent Fe- and WC-based alloys, respectively; blue regions signify pores. Note that the normal direction to the interface between layers is on average more or less parallel to the thickness direction of the coating, which corresponds to the vertical direction in the figure.

Realistically speaking, we should model a hard ceramic phase like WC as thermoelastic and brittle. For simplicity, however, we restrict attention to a model microstructure in which the hard phase is modeled as being thermoelastic and ideal viscoplastic. In particular, for lack of more specific information, the value of $\sigma_{\rm A}$ for the hard phase was set equal to the maximum strength of WC/Co at low cobalt content (e.g., Han and Jr, 1990; Okamoto et al., 2005).

Consider next the behavior of the model for this microstructure with the help of the following four deformation conditions: (i) F_{33}-extension parallel to the layers, (ii) F_{11}-compression parallel to $\boldsymbol{m}$, (iii) F_{21}-shear parallel to the layers, and (iv) F_{23}-shear of both phases parallel to the interface. These are shown schematically in Figure 2.2. Below, we will investigate the stress-strain response of the composite subject to these four deformation conditions predicted by different homogenization methods, including the current laminate-based one. Before doing this, we first investigate the behavior of the laminate model using single-element calculations. To this end, uniform displacement boundary conditions are applied to one face in the normal direction while the three other faces are fixed in their respective normal directions.

We begin with cases (i) and (ii), i.e., F_{33}-extension parallel to the layers, and F_{11}-compression parallel to $\boldsymbol{m}$, respectively. The corresponding results are shown in Figure 2.3. As shown here, the soft phase (solid squares) is almost immediately inelastic, whereas the hard phase (solid circles) has a more pronounced elastic range. Note that the elastic-inelastic transition for F_{33}-extension takes place in the composite almost at the same deformation state as in the hard phase alone, numerically 4% later. On the other hand, this transition is displaced to more than 15% larger deformation in the F_{11}-compression case. As deformation proceeds in the inelastic range, the stress-strain response of the composite for these two cases converges. Mechanical equilibrium requires the normal traction at the interface to be continuous. Because of this, the elastic and inelastic strengthening effect of the hard phase is slightly more pronounced in the

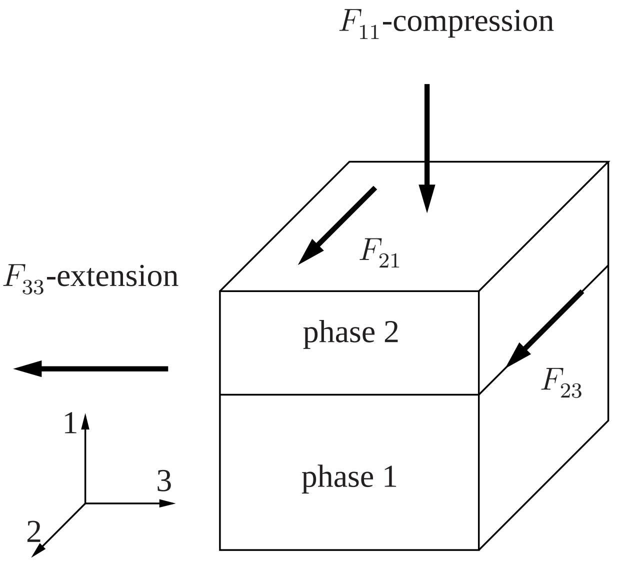

Figure 2.2: Deformation conditions for investigation of the composite behavior.

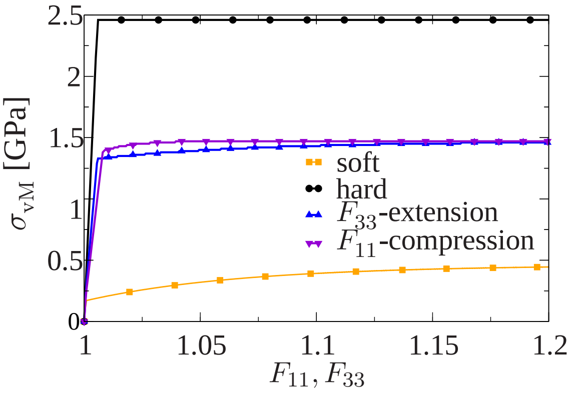

Figure 2.3: Von Mises stress σ_{vM} in the composite subject to different normal deformation conditions as a function of F_{11}(compression) or F_{33} (extension) for soft-phase volume fraction of $\lambda = 0.5$. Also shown for comparison is the behavior of the pure hard (solid circles) and pure soft (solid squares) for either extension or compression.

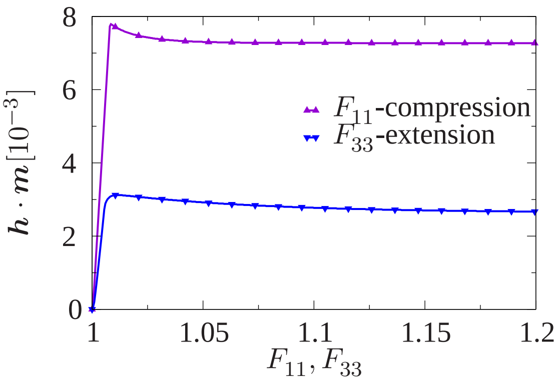

Figure 2.4: Relative normal deformation $\boldsymbol{h} \cdot \boldsymbol{m}$ across the interface for F_{11}-compression and F_{33}-extension at $\lambda = 0.5$.

F_{11}-compression perpendicular to the interface than in F_{33}-extension parallel to the interface.

Consider next the development of the normal $(\boldsymbol{h} \cdot \boldsymbol{m})\,\boldsymbol{m}$ component of $\boldsymbol{h}$ at the interface during extension and compression deformation as shown in Figure 2.4. Relative to the coordinate system in Figure 2.2, note that $\boldsymbol{h} \cdot \boldsymbol{m} = [\![F_{11}]\!]$ holds. In addition, note that $[\![F_{22}]\!] = -[\![F_{33}]\!]$ follows from continuity of the tangential deformation state at the interface. Consequently, as exhibited in Figure 2.4, $\boldsymbol{h} \cdot \boldsymbol{m}$ is much larger in F_{11}- than in F_{33}-compression. After transition to the inelastic regime, $\boldsymbol{h} \cdot \boldsymbol{m}$ decreases slightly due to hardening in the soft phase.

The behavior in the case of shear is different than for extension-compression. In particular, for the F_{23}-shear case, the results seem to be quite similar to those observed in the extension-compression case. In this case, the interface lies in the shear plane, and both phases are loaded equally. Because of this, the resulting behavior is quite similar to the behavior of the Taylor model (Taylor, 1938). On the other hand, in F_{21}-shear case, the laminate model shows completely different behavior. As shown in Figure 2.5, F_{21}-shear is dominated by the behavior of the soft phase. The stress-strain curve of the composite is nearly coincident with the curve for the soft material. This result is quite similar to the behavior of the Sachs model (Sachs, 1928). This behavior can be understood schematically as shown in Figure 2.6.

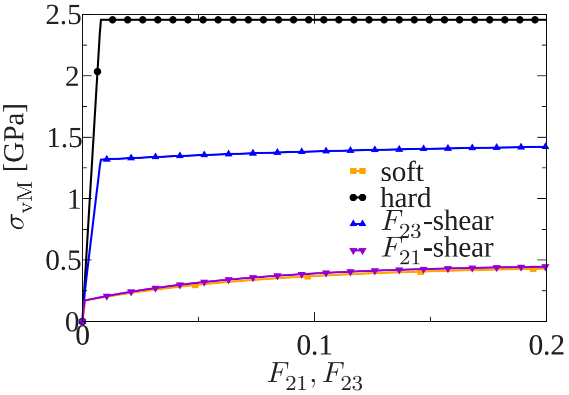

Figure 2.5: Von Mises stress σ_{vM} in the composite subject to different shear deformation conditions as a function of strain in the form of displacement u divided by length l for soft-phase volume fraction of $\lambda = 0.5$. See text for details.

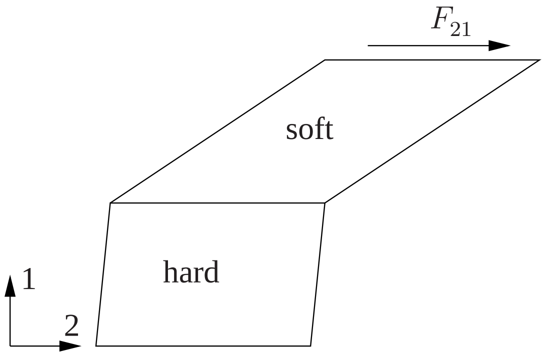

Figure 2.6: Schematic behavior of laminate model for shear parallel to the laminate, e.g., for F_{21}-shear.

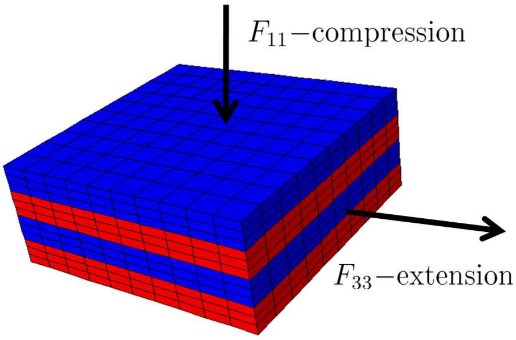

Figure 2.7: FE-model for laminate with applied loading cases.

The externally applied strain leads to large deformation of the softer phase while the hard phase undergoes only small deformation due to a nearly-uniform stress distribution. Before comparing different homogenization approaches below, a verification of the laminate model will be carried out with the help of the FE-model shown in Figure 2.7. The FE model consists of layers of hexahedral finite elements of the type C3D8 with 8 integration points where the different layers are tied together. To verify that the response of the structural model is not influenced by boundary effects the comparison between both models is done on the structural model. In this regard, the results for the laminate model are obtained from the structural model by applying the same material parameters in both layers. The finite material model used for the structural laminate model can be seen in section 2.2.

In contrast to the single element test, displacement boundary conditions are applied in such a fashion that material flow which would otherwise lead to formation of bulges at the faces is prevented. This reflects that in a real compression experiment, e.g. formation of a bulge due to material flow would be prevented for interior regions by surrounded material. Therefore the faces of the different layers are coupled for every side via coupling equations for example in order to couple the displacement into 1-direction on the side with their normal parallel to 1-direction the following equation hold

$$\begin{aligned} \boldsymbol{u}_1^{l1} - \boldsymbol{u}_{\mathrm{RP}_1} &= 0 \\ \boldsymbol{u}_1^{l2} - \boldsymbol{u}_{\mathrm{RP}_1} &= 0 \end{aligned} \tag{2.32}$$

where $\boldsymbol{u}_1^{l1}$ describes the displacement of layer 1($l1$) and $\boldsymbol{u}_1^{l1}$ the displacement of layer 2($l2$) into 1-direction as shown in Figure 2.8. RP_1 describes a reference point which facilitates a displacement in the 1-direction equal at the faces of layer 1 and layer 2 on the corresponding side. These boundary conditions guarantee that the deformation conditions considered lead to homogeneous deformation in every phase. Figure 2.9 shows the resulting stress-strain curves for the FE-model and homogenized laminate model. It can be seen that their behavior agrees quite well, i.e., in the case of homogeneous deformation.

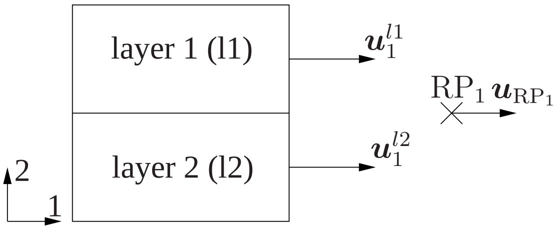

Figure 2.8: Applied boundary conditions and coupling conditions for one-element case.

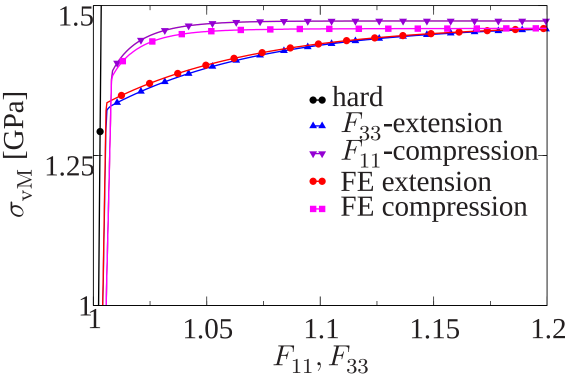

Figure 2.9: Comparison between the FE model and the laminate model for $\lambda = 0.5$. Both models show the same behavior under the applied loads.

Consider next inhomogeneous conditions. These are relevant for example to the technological case of compaction of the coating via incremental forming methods. Related to this is the material testing of such coatings with the help of indentor tests. Consequently, consider the indentation of the coating using a spherical indentor. Since we expect ideal RVE-related boundary conditions being employed in this work not to be completely correct in this case, the relation of the microstructural size to the indentor radius is examined here. In particular, we examine the dependence of the results on the ratio w/r of the width w of the structure to the radius r of the indentor. As this ratio increases, the boundaries are farther away from the region of loading. Consequently, the difference in the stresses predicted by the homogenization model and the FE model should decrease as this ratio increases.

The results of the indenter test are shown in Figure 2.10. It is clear that the stress distribution

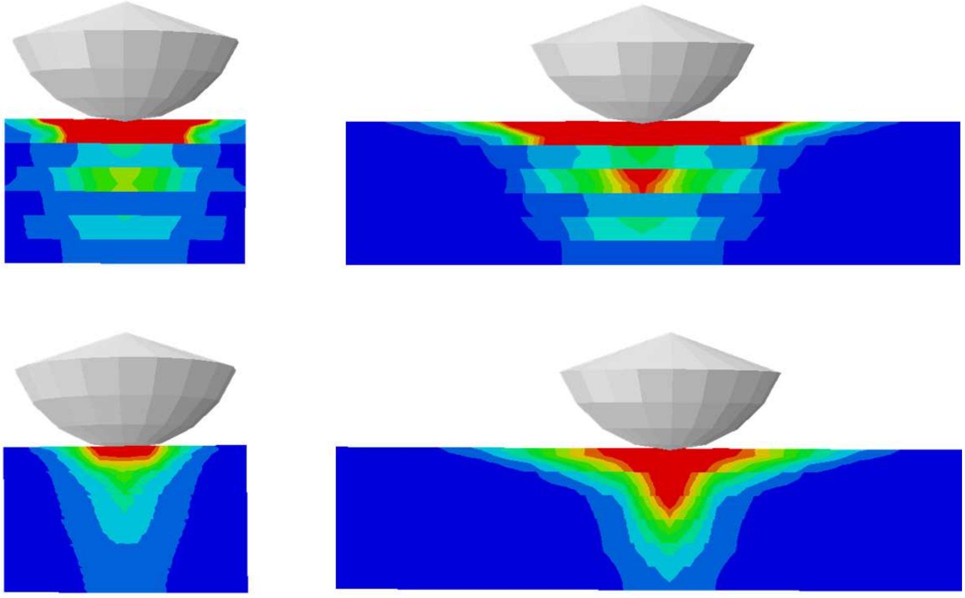

Figure 2.10: Comparison of von Mises stress distribution in the structure predicted by the FE model (above) and by the laminate model (below) for $w/r = 2$ (left) and $w/r = 10$ (right). Although more inhomogeneous in the FE-case, the stress distribution in both cases is quite similar. As shown, with increasing w/r, better agreement is obtained (red implies $\sigma_{\mathrm{vM}} \geq 1000$ MPa).

is more homogeneous for the homogenized laminate model due to the fact that in the FE-model there is a sharp transition at the interface between the layers due to the contrast in material properties. In addition, the results as a function of w/r clearly show the decrease of boundary effects (especially near the indentor at the top) on the vertical stress distribution. As shown and as expected, the agreement improves the boundary influence decreases, i.e., as w/r increases. Except for the differences due to such boundary effects, then, we are justified in concluding that the laminate homogenization model is a reasonable “mean-field” approximation to the FE model results.

2.6 Comparison with other homogenization approaches

In this section, the current laminate-based homogenization model is compared to standard homogenization assumptions like Taylor, as well as to that of phase-wise constant plastic deformation (EPc) considered in section 2.3. All of these are compared with the laminate model. These comparisons are carried out both for the thin-coating- or thin-film-like layered microstructure considered in the previous sections. These are carried out for the loading conditions shown in Figure 2.2. In addition, for completeness, we carry out this comparison for the "standard" homogenization case of a metal-matrix composite with spherical inclusions. As one might expect, the laminate model performs poorly in the latter context.

To begin, consider first the compression and extension of the thin-coating-like layered microstruture from Figure 2.7. Figure 2.11 shows the stress-strain curves for the different homogenization methods. In the elastic range, the Taylor model agrees quite well with the laminate model in the case of extension, whereas the EPc-model agrees with the laminate model in the case of compression. In contrast to the laminate model, the EPc model exhibits the same behavior for different loading cases in the elastic range. In addition, for the chosen material parameter combination, the Taylor and EPc models show a behavior between the extension and compression response of the laminate model in the inelastic range. In particular, the yield stress of both models lies between the extremal values of the laminate model for extension and compression. With increasing deformation the Taylor model response converges to the response of the compression case of the laminate model, whereas the EPc-model response converges to the extension case. The same behavior can also be observed for different volume fractions λ as shown in Figure 2.12. Clearly, model differences are magnified upon increase of the volume fraction of the soft phase, especially in the elastic range.

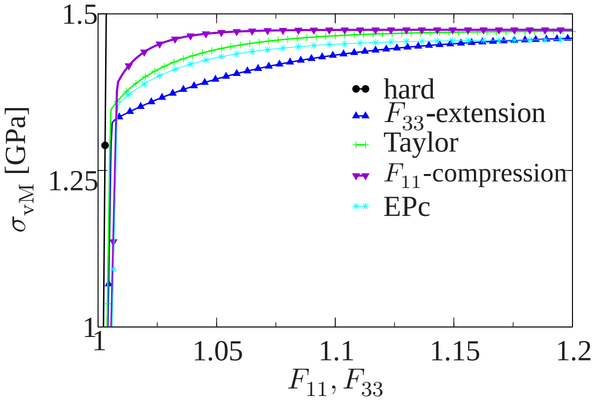

Figure 2.11: Comparison of stress-strain behavior predicted by different homogenization approaches for $\lambda = 0.5$.

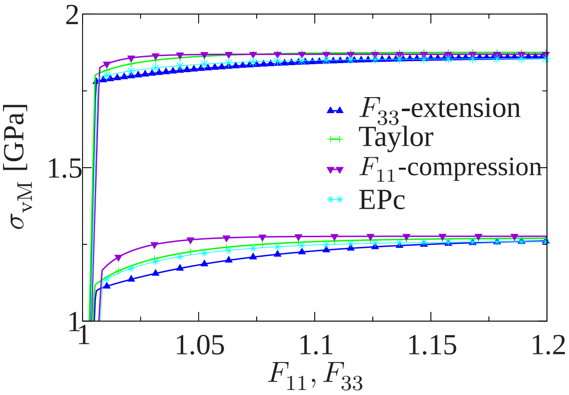

Figure 2.12: Comparison of stress-strain behavior of different homogenization models for $\lambda = 0.6$ and $\lambda = 0.3$. Different homogeneous methods show analogous results as described in Figure 2.11.

The results for shear deformation are qualitatively the same as in the normal deformation cases just considered. For F_{23}-shear, in which the interface lies in the shear plane, the predictions of the laminate model and Taylor model correspond quite well. This is to be expected since, in this case, both phases experience the same deformation state (see Figure 2.2). As before, for this case, the EPc model predicts softer behavior. As for the Taylor case, this is due to the fact that the material behavior is independent of loading direction for an isotropic material. For F_{21}-shear, the Taylor and EPc models predict the same behavior as before, in contrast to the behavior of the laminate model. In this case, the Sachs model would give the best prediction, but for all other loading conditions this model is absolutely inappropriate.

In the literature (e.g., Gross and Seelig, 2001; Molinari et al., 1997), models like the EPc and Taylor models are often shown to be too stiff. This is true for structures with homogeneously distributed spherical inclusions. For the inhomogeneous case, however, matters are more complicated. An example of such a microstructure is considered in Figure 2.13. As expected, the largest deformation takes place in the matrix between the particles near these, and the deformation field is quite heterogeneous. The stress-strain behavior of this microstructure predicted by the homogenization models under consideration is displayed in Figure 2.14 together with the corresponding FE results. It can be seen that the homogenization methods first predict stiffer behavior than the FE results. In the FE case, the soft phase can flow around the hard inclusions, resulting in less stress concentration at the inclusion-matrix interface than predicted by the homogenization models, which underestimate the amount of inelastic deformation near the inclusions. This deformation in the matrix near the inclusions also results in higher strain-rates than predicted by the laminate models and so higher stresses. With increasing deformation, this results in a higher level of hardening being predicted by the FE model and so higher stress levels than those predicted by the homogenization models. In any case, this comparison makes clear that the homogenization models presented in this work are not reasonable for composites with such microstructure.

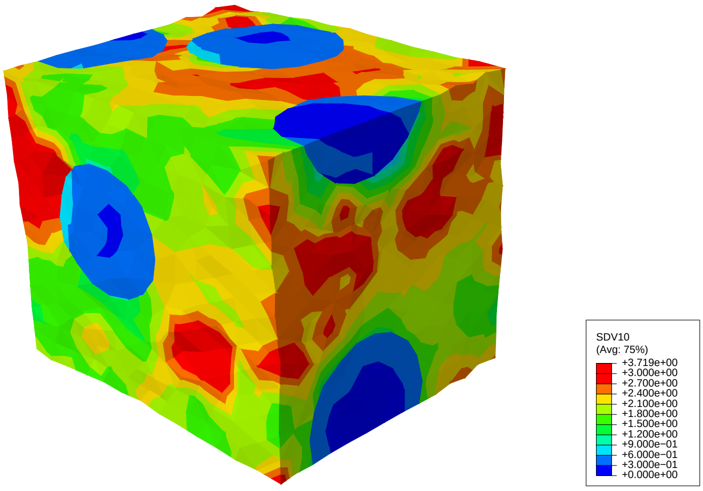

Figure 2.13: Distribution of α_{P} in an ideal composite microstructure with 30% (volume) spherical inclusions after 20% applied strain E_{11}.

2.7 The case of variable interface orientation

For simplicity, the phase interface orientation $\boldsymbol{m}$ has been kept fixed and oriented in the direction of the coating thickness. In reality, however, there is no reason to believe that it may not vary locally in the coating during loading. To have a first look at the effect this might have on the material behavior of the composite, we now allow $\boldsymbol{m}$ to vary. For simplicity, we assume to

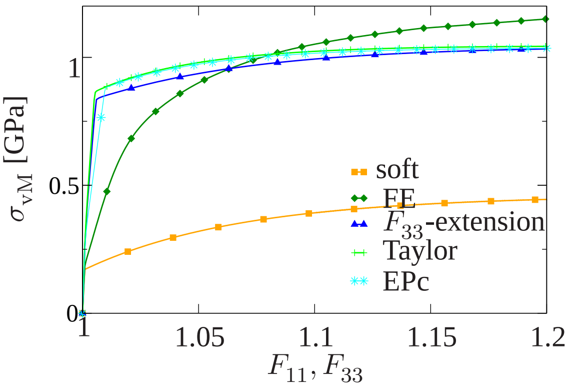

Figure 2.14: Comparison of stress-strain behavior for a metal-matrix composite with spherical inclusion ($\lambda = 0.7$) predicted by the homogenization models considered in this work. For comparison, the corresponding FE results are also shown.

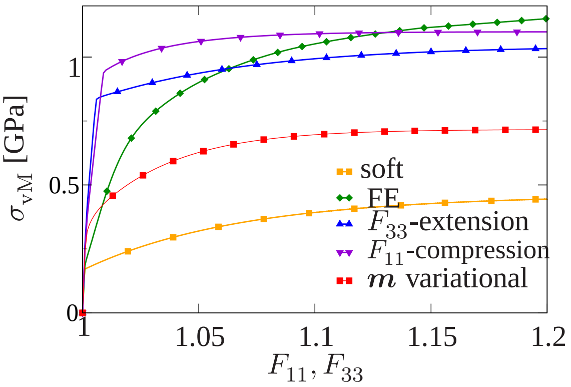

Figure 2.15: Comparison of stress-strain behavior of homogenization model for fixed $\boldsymbol{m} = \{1\,0\,0\}$ under compression and extension with model with variational $\boldsymbol{m}$ for $\lambda = 0.7$ with $\boldsymbol{m}_{\text{initial}} = \{1\,0\,0\}$. For comparison, the corresponding FE results for spherical inclusions are also shown

this end that $\boldsymbol{m}$ is purely energetic and varies only in order to satisfy angular momentum at the interface, i.e.,

$$\mathbf{0} = \partial_{\boldsymbol{m}}\psi = \lambda\,(1-\lambda)[\![\partial_{\boldsymbol{E}}\psi]\!]^{\mathrm{T}}\boldsymbol{h} \tag{2.33}$$

vanishes there in equilibrium, yielding an implicit relation for $\boldsymbol{m}$. This is of course subject to the constraint $\boldsymbol{m}\cdot\boldsymbol{m} = 1$ which is taken into account by minimizing the associated Lagrangian function

$$\ell(\boldsymbol{E}_{\mathrm{E}}, \alpha_{\mathrm{P}}, \boldsymbol{m}, \boldsymbol{h}) = \psi_{\mathrm{E}}(\boldsymbol{E}_{\mathrm{E}}, \boldsymbol{m}, \boldsymbol{h}) + \psi_{\mathrm{H}}(\alpha_{\mathrm{P}}) + \mu\,(\boldsymbol{m}\cdot\boldsymbol{m} - 1) \tag{2.34}$$

with Lagrange multiplier μ.

The values of $\boldsymbol{m}$ obtained in this fashion show that the laminate interface is reorienting to a diagonal in one plane, depending on the direction of loading as well as the initial condition. This corresponds to a reorientation of $45°$ for $\boldsymbol{m}_0 = \{1\,0\,0\}$. The corresponding stress-strain behavior is shown in Figure 2.15 and compared to the case of fixed interface orientation $\boldsymbol{m} = \{1\,0\,0\}$ as well as to the FE-result for spherical inclusion. Since the equilibrium value of $\boldsymbol{m}$ represents energetically the most favorable orientation, it results in the lowest stress levels.

On the other hand, a reorientation of $45°$ of the interface for such laminates is physically unrealistic. To prevent this, we assume that the interface has a certain stiffness in the sense that reorientation beyond a certain degree is energetically unfavorable. To this end, we add a corresponding penalty term to (2.34), i.e.,

$$\begin{aligned} \ell(\boldsymbol{E}_{\mathrm{E}}, \alpha_{\mathrm{P}}, \boldsymbol{m}, \boldsymbol{h}) &= \psi_{\mathrm{E}}(\boldsymbol{E}_{\mathrm{E}}, \boldsymbol{m}, \boldsymbol{h}) + \psi_{\mathrm{H}}(\alpha_{\mathrm{P}}) \\ &+ \tfrac{1}{2}\gamma\,(1 - \boldsymbol{m}\cdot\boldsymbol{m}_0)^2 + \mu\,(\boldsymbol{m}\cdot\boldsymbol{m} - 1)\,, \end{aligned} \tag{2.35}$$

where γ represents the interface resistance to reorientation relative to the initial orientation $\boldsymbol{m}_0$.

First results for compression are shown in Figure 2.16 for different values of the ration $\beta = \gamma/E_{\text{soft}}$ of γ to Young's modulus E_{soft} of the soft phase. The corresponding development of the reorientation angle $\alpha = \arccos(\boldsymbol{m} \cdot \boldsymbol{m}_0)$ is displayed in Figure 2.17. For large γ, the

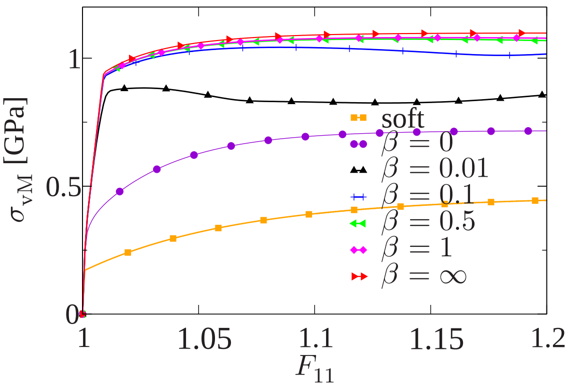

Figure 2.16: Comparison of stress-strain behavior of homogenization model for variable $\boldsymbol{m}$ for different values of the interface resistance $\gamma = \beta\, E_{\text{soft}}$ under compression with $\boldsymbol{m}_0 = \{1\,0\,0\}$ and $\lambda = 0.7$. For comparison, the corresponding results for fixed $\boldsymbol{m} = \{1\,0\,0\}$ are also shown.

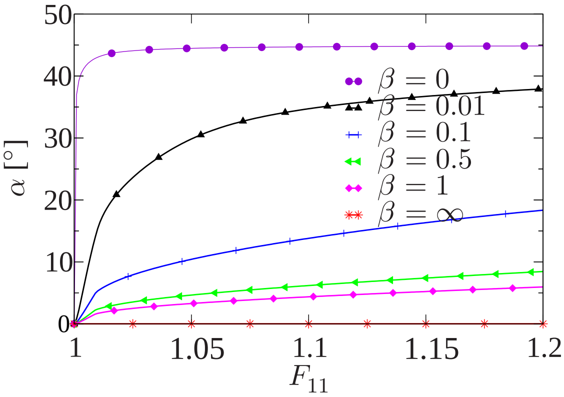

Figure 2.17: Development of the reorientation angle $\alpha = \arccos(\boldsymbol{m} \cdot \boldsymbol{m}_0)$ during compression for $\boldsymbol{m}_0 = \{1\,0\,0\}$ and various $\gamma = \beta\, E_{\text{soft}}$ with $\lambda = 0.7$.

results agree with those for fixed $\boldsymbol{m}$ as expected. As γ decreases and the interface becomes more pliable, the stress level also decreases, again as expected. Consequently, a variable $\boldsymbol{m}$ can have a significant influence on the stress level in the composite. The question arises, is the variation of $\boldsymbol{m}$ purely energetic in nature. More generally, one could expect inelastic / kinetic / dissipative processes to influence the orientation of the interface. In this case, (2.33) could be generalized to

$$\mathbf{0} = \partial_{\boldsymbol{m}}\psi + \partial_{\dot{\boldsymbol{m}}}\chi \tag{2.36}$$

in terms of a dissipation potential χ depending in particular on the rate $\dot{\boldsymbol{m}}$ of interface rotation. Detailed analysis of results for variational $\boldsymbol{m}$ under different loading conditions represent ongoing research.

2.8 Discussion and conclusions

As mentioned in previous sections, in a more realistic approach, brittle failure would have to be included in the model for the hard phase. To get a first impression how the model behaves, a computation is done according to the loading cases in Figure 2.3. To model the behavior of brittle failure and the resulting softening the material parameters are chosen as displayed in Table 2.1, but changing the parameters for the hard phase to $s_{\text{H}} = -1870\text{MPa}$ and $c_{\text{H}} = 100$. The resulting behavior is shown in Figure 2.18. The differences for the extension and compression load case are clearly visible. Due to the lower amount of deformation for the hard phase in the compression case as in the extension case (see Figure 2.4) it takes more overall deformation until the softening begins. Up to this point the soft phase was subjected to deformation which leads to an inelastic behavior with resulting hardening. Therefore the

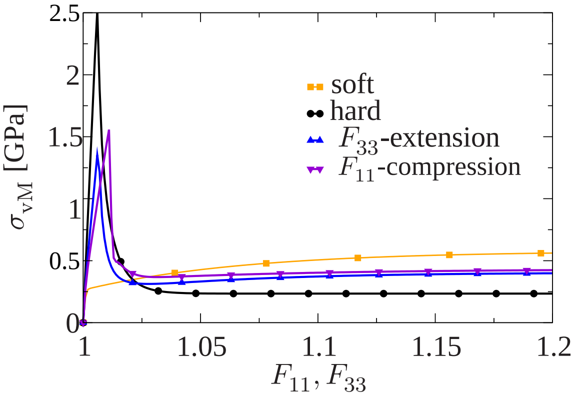

Figure 2.18: von Mises stress σ_{vM} in the composite subject to different normal deformation conditions as a function of F_{11}(compression) or F_{33} (extension) for soft-phase volume fraction of $\lambda = 0.5$. The material parameters of the hard phase are changed to $s_{\mathrm{H}} = -1870$MPa and $c_{\mathrm{H}} = 100$. Also shown for comparison is the behavior of the pure hard (solid circles), modeled with softening behavior and pure soft (solid squares) for either extension or compression.

differences in the effective yield stress as well as strain are higher for the two deformation cases in contrast to ideal viscoplasticity.

In this work, we have investigated a novel application of first-order laminate theory as a homogenization ansatz to model the inelastic behavior of thin-coating-like or thin-film-like two-phase composites whose microstructural morphology is characterized by being layered or lamellar in nature. This approach has been developed and compared with a number of existing homogenization methods as well as with a finite-element (FE) model for the microstructure. The laminate-based homogenization model showed very good agreement with the FE model for a number of different deformation conditions including extension, compression and shear. This was the case both for homogeneous and inhomogeneous deformation conditions. Additional comparisons were carried out with standard homogenization assumptions like those of Taylor, as well as with homogenization based on the assumption of phase-wise constant plastic strain (EPc). These comparisons show that the Taylor model predicts the behavior for extension quite well. On the other hand, the EPc model predicts the behavior well only for compression. The Sachs model is not appropriate in any of these cases. In the last part of the work, the homogenization models are compared with the FE model for the classical homogenization problem of a metal-matrix composite with spherical inclusions. It was shown that all homogenization methods considered predict incorrect behavior for such a microstructure, i.e., in comparison to the FE model.

For simplicity, the hard phase of the model microstructures considered in this work was treated as thermoelastic, ideal viscoplastic in nature, with elastic and yield properties significantly larger than those of the soft phase. It would be more realistic to model this phase as thermoelastic and brittle. Also for simplicity, attention has been focused in this work on a constant laminate interface normal $\boldsymbol{m}$. In particular for more realistic lamellar-like microstructures, however, this will be variable within the limits of a cone around the initial orientation as first results are shown. These generalizations of the current laminate-based approach, along with the application of the approach to the modeling and simulation of the compaction of thermally-sprayed coatings, represent work in progress, and will be reported on in the future.

Chapter 3

Crystal plastic modeling of the deformation behavior of thin sheets with large grains

Abstract– The purpose of this work is the modeling and simulation of the deformation behavior of thin sheets consisting of large grains of Fe-3%Si and comparison with experiment. To this end, an explicit finite-element-, crystal-plasticity-based model is developed for each grain, the grain morphology, and the thin sheet specimen as a whole. In particular, the crystal plasticity model is rate-dependent and accounts for (local) dissipative hardening effects. The predictions of the model are compared with experimental results of Henning and Vehoff (2005) for the deformation behavior of thin sheets of Fe-3%Si loaded incrementally in tension. To this end, attention is restricted to the two slip families $\{110\}$ and $\{112\}$. To begin, all hardening is neglected. Even for this oversimplified case, a good correlation with the experimental results is obtained. This shows the importance of predicting initially active glide systems correctly. Even better agreement is obtained with experiment when hardening is included. Finally, initial results for the development of local orientation changes are discussed.

3.1 Introduction

The relation between microstructure, material properties and mechanical response is a basic issue of research in material science and material mechanics (Groeber et al., 2007; Langer et al., 2001). From the modeling point of view, a common concept used to account for the effect of the microstructure on the material behavior is that of a representative volume element (RVE). This concept is based on the assumption of scale separation between the microstructural and macrostructural lengthscale. As the characteristic size of the microstructure (e.g., grain size) approaches that of the system (e.g., sheet thickness), however, such scale separation is no longer given and one must resort to other means of representing the effect of microstructural heterogeneity on the system behavior. One possibility in this regard is based on distribution functions (e.g., orientation distribution functions, e.g., Böhlke et al., 2009, 2010) and averaging. As the macrostructural lengthscale approaches the microstructural one, the degree of material heterogeneity increases drastically, such that the local microstructural behavior can deviate significantly from the average macrostructural behavior (e.g., Kalidindi et al., 2003; Pierard et al., 2007). In this case, the model has to account for the microstructural details such orientation details of the grain structure (e.g., Raabe et al., 2001) or pore distribution (e.g., Wiederkehr et al., 2010).

In the extreme case, the microstructural and macrostructural lengthscales are the same order of magnitude, and one must resort to numerical models of the microstructure, e.g., finite-element-based models. These are often constructed with the help of, e.g., optical and / or EBSD data on the grain morphology. In specimens with more than one grain over the thickness, the common method of projecting the two-dimensional EBSD information uniformly in the third dimension will generally lead to different behavior (e.g., Wiederkehr et al., 2010). If the specimen is one grain thick, however, such an optical- / SEM- / EBSD-based approach should be reasonable. For such a specimen, a number of size effects are expected to influence its mechanical properties. These effects have been known for years and are still subject of active research (Engel and Eckstein, 2002; Fu et al., 2001; Fülöp et al., 2006). Janssen et al. (2008) reported at least four size effects: (i) strengthening or weakening due to constrained or free boundary layers (e.g., Geers et al., 2006; Janssen et al., 2006), (ii) strengthening due to strain gradients (e.g., Bargmann et al., 2010; Bayley et al., 2006), (iii) strengthening due to dislocation annihilation (e.g., Greer et al., 2005), and (iv) size effects due to a lack of statistical microstructural averaging (e.g., Fülöp et al., 2006; Henning and Vehoff, 2007). In this work, the main focus is on the fourth size effect. One cause for the occurrence of this size effect is the change of number of grains over the thickness. The overall mechanical response is then strongly influenced by the orientation of the individual grains (Fülöp et al., 2006). In the case of thin sheets the properties in a given cross section are increasingly dominated by individual grains (Henning and Vehoff, 2005). Due to the different orientations of the grains located in the sheet plane, the deformation is no longer uniform even under homogeneous loading conditions. In order to predict the mechanical response of thin sheets correctly it is necessary to account in particular the shape of individual grains and their orientation (Fülöp et al., 2006). To understand and predict the behavior correctly simulation and experiment have to be compared locally. Therefore detailed experimental information of local details during plastic deformation are necessary (Henning and Vehoff, 2005).

The purpose of the current work is the crystal-plasticity / finite-element-based modeling and simulation of a bcc Fe-3%Si thin-sheet sample with large grains loaded incrementally in tension and comparison with experiment (Henning and Vehoff, 2005). This sample is grown in such a way that throughout the sample there is only one grain over the thickness in which the grain boundaries are perpendicular to the sample surface. The deformation of the individual grains has been measured, as well as the local orientation after each loading step. In Henning (2008), a software package has been developed to automatically construct finite-element meshes directly from different measuring devices. This software is used to construct a FE mesh from the investigated sample which is used in the crystal-plasticity-based finite-element simulations.

Crystallographic slip in body-centered cubic (BCC) metals, like Fe-3%Si, it is known to take place in close-packed $\langle 111 \rangle$ direction, but there are different opinions and experimental results regarding the operative slip planes. In Takeuchi et al. (1967), three possibilities are discussed. In the first case, it is assumed that the slip really takes place on any plane in the $\langle 111 \rangle$ zone (e.g., Takeuchi and Ikeda, 1963). Other workers (e.g., Hull, 1963) assumed that the slip takes place mainly on composite $\{110\}$ planes. A third assumption (e.g., Erickson, 1962) is that slip occurs on planes with low indices $\{110\}$ and $\{112\}$ or $\{110\}$ and $\{112\}$ and $\{123\}$. Simulations with different active sets of glide system classes will be performed to investigate which slip planes are active and dominant in the simulation.

The paper begins with a summary of the material model, its algorithmic formulation and numerical implementation. Next, the model identification and the used material parameters are given. In the following the experimental results of Henning and Vehoff (2005) are reviewed and the construction of the FE-model is discussed. On this basis, detailed and systematic comparisons between simulation and experimental results are carried out. In particular, we look at the effects of assuming different combinations of the glide-system families $\{110\}$ and $\{112\}$ on the development of deformation heterogeneity in the sample. In addition, we compare the cases of modeling the deformation behavior with and without glide-system hardening. The paper concludes with a short summary and outlook.

3.2 Model formulation for single-crystal plasticity

In the current work, a material model is formulated in the context of continuum thermodynamics for crystal plasticity. In this context, the material behavior is related to energetic and dissipative processes. For simplicity, attention is restricted to isothermal conditions. Here we are restricted to dissipative hardening alone which means that no energetic hardening occurs. As usual, the energetic part is determined by the free energy density ψ. For the case of anisotropic metals with viscoplastic behavior, the form

$$\psi(\boldsymbol{F},\boldsymbol{F}_{\mathrm{P}}) = \psi_{\mathrm{E}}(\boldsymbol{F},\boldsymbol{F}_{\mathrm{P}}) \tag{3.1}$$

holds for ψ. In particular ψ is assumed to determine the elastic relation

$$\boldsymbol{P} \;=\; \partial_{\boldsymbol{F}}\psi \tag{3.2}$$

for the first Piola-Kirchhoff stress $\boldsymbol{P}$. $\boldsymbol{F}_{\mathrm{P}}$ is assumed to be not affected by the elastic behavior, in this case, it can be modeled as a change of local reference configuration (Svendsen, 2001). In this case, the (local) intermediate configuration represents the preferred constitutive reference configuration. In the context of “small” elastic strain relevant to metals, ψ_{E} takes the form

$$\psi_{\mathrm{E}}(\boldsymbol{F},\boldsymbol{F}_{\mathrm{P}}) \approx \frac{1}{2}\,\boldsymbol{E}_{\mathrm{E}}\cdot\mathcal{C}_{\mathrm{E}\,0}\boldsymbol{E}_{\mathrm{E}} \tag{3.3}$$

for ψ_{E} pertaining to metals, with $\mathcal{C}_{\mathrm{E}\,0}$ the elastic stiffness, at constant deformation. In the context of small elastic strain, the approximation $\boldsymbol{M} \approx \boldsymbol{S}_{\mathrm{E}}$ of the Mandel stress by the elastic second Piola-Kirchhoff stress

$$\boldsymbol{S}_{\mathrm{E}} = \partial_{\boldsymbol{E}_{\mathrm{E}}}\psi_{\mathrm{E}} \tag{3.4}$$

is justified.

In the following we are discussing the single-crystal / glide-system case. As usual, the a^{th} glide system is represented by the corresponding glide direction $\boldsymbol{s}_a$, glide-plane normal $\boldsymbol{n}_a$, and direction transverse $\boldsymbol{t}_a := \boldsymbol{n}_a \times \boldsymbol{s}_a$ to $\boldsymbol{s}_a$ in the glide plane. The system $(\boldsymbol{s}_a,\boldsymbol{t}_a,\boldsymbol{n}_a)$ are assumed constant with respect to the local intermediate configuration as determined by $\boldsymbol{F}_{\mathrm{P}}$. In addition, they determine its evolution via the constitutive form

$$\boldsymbol{L}_{\mathrm{P}} = \sum\nolimits_{a=1}^{\mathfrak{a}} \dot{\gamma}_a\,\boldsymbol{s}_a \otimes \boldsymbol{n}_a \tag{3.5}$$

for $\boldsymbol{L}_\mathrm{P}$ in terms of the active glide-system shears $\gamma_1, \gamma_2, \ldots, \gamma_\mathfrak{a}$, with $\mathfrak{a} \leqslant \mathfrak{g}$ the number of active systems, and $\mathfrak{g}$ the total number of systems. Let $\sum_a := \sum_{a=1}^{\mathfrak{a}}$ represent the sum over all active glide systems. From this, we obtain in particular the form

$$-\,\partial_{\boldsymbol{F}_\mathrm{P}}\psi \cdot \dot{\boldsymbol{F}}_\mathrm{P} = \boldsymbol{M} \cdot \boldsymbol{L}_\mathrm{P} = \sum\nolimits_a \tau_a\,\dot{\gamma}_a \tag{3.6}$$

for the inelastic stress power in terms of the Schmid stress

$$\tau_a := \boldsymbol{s}_a \cdot \boldsymbol{M}\boldsymbol{n}_a\,. \tag{3.7}$$

Since γ_a is interpreted here as the glide-system shear, it can be positive or negative and increase or decrease, such that $\dot{\gamma}_a\,\boldsymbol{s}_a = |\dot{\gamma}_a|\ \mathrm{dir}(\dot{\gamma}_a)\,\boldsymbol{s}_a = \pm\,\dot{\alpha}_a\,\boldsymbol{s}_a$, where

$$\dot{\alpha}_a := |\dot{\gamma}_a| \tag{3.8}$$

represents the accumulated inelastic glide-system shear rate. Here the notation $\mathrm{dir}(a) := a/|a|$ is used. Note that $\dot{\alpha}_a \geqslant 0$, and $\alpha_a \geqslant 0$ are always positive and monotonically-increasing for all $a = 1, \ldots, \mathfrak{g}$. This situation has motivated many workers to consider both $\boldsymbol{s}_a$ and $-\boldsymbol{s}_a$ as glide directions, i.e., at the expense of doubling the number of glide systems. In this case, $\dot{\gamma}_a\,\boldsymbol{s}_a \equiv \dot{\alpha}_{a+}\,\boldsymbol{s}_a - \dot{\alpha}_{a-}\,\boldsymbol{s}_a = [\![\dot{\alpha}_a]\!]\,\boldsymbol{s}_a$. Alternatively, one works with the constitutive assumption

$$\mathrm{dir}(\dot{\gamma}_a) = \mathrm{dir}(\tau_a) \tag{3.9}$$

for the direction of the glide-system shear-rate. In turn, this implies the constitutive form

$$\dot{\gamma}_a = \mathrm{dir}(\tau_a)\,\dot{\alpha}_a \tag{3.10}$$

for the glide-system shear rates, and that

$$\boldsymbol{L}_\mathrm{P} = \sum\nolimits_a \dot{\gamma}_a\,\boldsymbol{s}_a \otimes \boldsymbol{n}_a = \sum\nolimits_a \mathrm{dir}(\tau_a)\,\boldsymbol{s}_a \otimes \boldsymbol{n}_a\,\dot{\alpha}_a \tag{3.11}$$

for $\boldsymbol{L}_\mathrm{P}$ as a function of $\dot{\boldsymbol{\alpha}}$. Lastly, the reduced form

$$-\,\partial_{\boldsymbol{F}_\mathrm{P}}\psi \cdot \dot{\boldsymbol{F}}_\mathrm{P} = \boldsymbol{M} \cdot \boldsymbol{L}_\mathrm{P} = \sum\nolimits_a |\tau_a|\,\dot{\alpha}_a \tag{3.12}$$

follows for (3.6) in terms of $\dot{\boldsymbol{\alpha}}$.

In the following we assume that no activation energy has to be overcome so that slip can directly start when a system becomes active. The viscoplastic flow rule is formulated according to Kalidindi et al. (1992)

$$\dot{\gamma}_a = \partial_{\tau_a}\phi = \dot{\gamma}_0 \left|\frac{\tau_a}{\hat{\tau}_a}\right|^m \mathrm{dir}(\tau_a) \tag{3.13}$$

where the flow potential is determined via

$$\phi(\boldsymbol{\tau_a}) = \dot{\gamma}_0 \sum\nolimits_a \frac{\hat{\tau}_a}{m+1}\left|\frac{\tau_a}{\hat{\tau}_a}\right|^{m+1}\,. \tag{3.14}$$

Here, $\dot{\gamma}_0$ represents a characteristic strain-rate associated with dislocation motion and $\hat{\tau}_a$ the energetic or athermal slip resistance is determined via (Asaro and Needleman, 1985)

$$\dot{\hat{\tau}}_a = \sum\nolimits_b q_{ab}\,h_b(\hat{\tau}_b)\,|\dot{\gamma}_a|\,. \tag{3.15}$$

q_{ab} is the hardening matrix which describes the rate of strain hardening on slip system a due to a shearing on the slip system b by

$$q_{ab} = \begin{bmatrix} 1 & q_0 & \cdots & q_0 \\ q_0 & 1 & \cdots & q_0 \\ \vdots & \vdots & \ddots & \vdots \\ q_0 & \cdots & q_0 & 1 \end{bmatrix}$$

in which $q_0 = 1.4$ represents the ratio of latent to self-hardening. Following Brown et al. (1989); Kalidindi et al. (1992), we consider the following form for the single slip hardening rate

$$h_b(\hat{\tau}_b) = h_0\,(1 - \hat{\tau}_b/\hat{\tau}_0^{\text{sat}})^{n_0} \tag{3.16}$$

Here, h_0 is the initial hardening rate, $\hat{\tau}_0^{\text{sat}}$ the saturation value of $\hat{\tau}_b$, and n_0 is the hardening exponent.

3.3 Algorithmic formulation

The introduced material model in section 3.2 is implemented based on the following algorithmic flow rules. As usual, for algorithmic purposes, we are interested in transforming these relations into algorithmic-numerical with respect to a time-interval $[t_n, t_{n+1}]$ with t_n the time at the start of the interval, $t_{n+1} \geqslant t_n$ the time at the end of the interval, and $t_{n+1,n} := t_{n+1} - t_n \geqslant 0$ its duration. In the context of large inelastic deformation, an algorithmical formulation of $\dot{\boldsymbol{F}}_{\text{P}} = \boldsymbol{L}_{\text{P}}\boldsymbol{F}_{\text{P}}$ follows via volumetric-isochoric split

$$\boldsymbol{F}_{\text{P}} = \text{vol}(\boldsymbol{F}_{\text{P}})\,\text{uni}(\boldsymbol{F}_{\text{P}}) = \det(\boldsymbol{F}_{\text{P}})^{1/3}\,\text{uni}(\boldsymbol{F}_{\text{P}})\,, \tag{3.17}$$

where $\det(\boldsymbol{A})$ describes the determinant and $\text{uni}(\boldsymbol{A})$ the unimodular part of a second order tensor $\boldsymbol{A}$. Consider next the single time derivatives

$$\begin{aligned} \dot{\overline{\det(\boldsymbol{F}_{\text{P}})}} &= \text{tr}(\boldsymbol{L}_{\text{P}})\det(\boldsymbol{F}_{\text{P}}) \\ \dot{\overline{\text{uni}(\boldsymbol{F}_{\text{P}})}} &= \text{dev}(\boldsymbol{L}_{\text{P}})\text{uni}(\boldsymbol{F}_{\text{P}})\,, \end{aligned} \tag{3.18}$$

where $\text{dev}(\boldsymbol{A})$ describes the deviatoric part of $\boldsymbol{A}$.

Algorithmically it follows for (3.18)$_1$ with forward-Euler integration that

$$\det(\boldsymbol{F}_{\text{P}\,n+1}) = (1 + t_{n+1,n}\text{tr}(\boldsymbol{L}_{\text{P}\,n}))\det(\boldsymbol{F}_{\text{P}\,n}) = \det(\boldsymbol{F}_{\text{P}\,n}) \tag{3.19}$$

holds for the case of plastic incompressibility, $\text{tr}(\boldsymbol{L}_{\text{P}}) = 0$. Here denotes $\boldsymbol{F}_{\text{P}\,n+1} \equiv \boldsymbol{F}_{\text{P}}(t_{n+1})$, relative to that $\boldsymbol{F}_{\text{P}\,n} \equiv \boldsymbol{F}_{\text{P}}(t_n)$ from the end of the previous time step. As $\boldsymbol{L}_{\text{P}}$ is full deviatoric one can algorithmically formulate the evolution of plastic deformation as

$$\boldsymbol{F}_{\text{P}\,n+1} = \text{uni}(\boldsymbol{I} + t_{n+1,n}\boldsymbol{L}_{\text{P}\,n})\,\boldsymbol{F}_{\text{P}\,n}\,. \tag{3.20}$$

In the following we are using an approximation of this equation which is based on the restriction $t_{n+1,n}\,|\boldsymbol{L}_{\mathrm{P}\,n}| \ll 1$, e.g. to “small” time steps. In this case and in the context that $\boldsymbol{F} = \boldsymbol{F}_{\mathrm{E}}\,\boldsymbol{F}_{\mathrm{P}}$, the direct algebraic approximation is

$$\boldsymbol{F}_{\mathrm{E}\,n+1} = \boldsymbol{F}^{\mathrm{tr}}_{\mathrm{E}\,n+1}\mathrm{uni}(\boldsymbol{I} - t_{n+1,n}\boldsymbol{L}_{\mathrm{P}\,n}) = \boldsymbol{F}^{\mathrm{tr}}_{\mathrm{E}\,n+1}\mathrm{uni}(\boldsymbol{\Lambda}_{\mathrm{P}\,n+1,n}) \tag{3.21}$$

for $\boldsymbol{F}_{\mathrm{E}}$ in terms of its trial value

$$\boldsymbol{F}^{\mathrm{tr}}_{\mathrm{E}\,n+1} = \boldsymbol{F}^{\mathrm{tr}}_{\mathrm{E}}(\boldsymbol{F}_{n+1}) := \boldsymbol{F}_{n+1}\boldsymbol{F}^{-1}_{\mathrm{P}\,n} = \boldsymbol{F}_{n+1,n}\boldsymbol{F}_{\mathrm{E}\,n}\ , \tag{3.22}$$

with

$$\boldsymbol{F}_{n+1,n} := \boldsymbol{F}_{n+1}\boldsymbol{F}^{-1}_{n} \tag{3.23}$$

the relative deformation gradient. Since $\boldsymbol{F}^{\mathrm{tr}}_{\mathrm{E}\,n+1}$ is an algebraic function of $\boldsymbol{F}_{n+1,n}$ and the algorithmic constant $\boldsymbol{F}_{\mathrm{E}\,n}$ via (3.22), this approach is purely algebraic. The corresponding stress algorithm is based on the Green measure

$$\boldsymbol{E}_{\mathrm{E}\,n+1}(\boldsymbol{F}_{\mathrm{E}\,n+1}) = \frac{1}{2}\,(\boldsymbol{F}^{\mathrm{T}}_{\mathrm{E}\,n+1}\boldsymbol{F}_{\mathrm{E}\,n+1} - \boldsymbol{I}) \tag{3.24}$$

of elastic strain. The corresponding stress algorithm is completed by the general relation

$$\boldsymbol{K}_{n+1} = \boldsymbol{F}_{\mathrm{E}n+1}\boldsymbol{S}_{\mathrm{E}n+1}\boldsymbol{F}^{\mathrm{T}}_{\mathrm{E}n+1} \tag{3.25}$$

for the current Kirchhoff stress $\boldsymbol{K}_{n+1}$ in terms of the corresponding elastic second Piola-Kirchhoff stress

$$\boldsymbol{S}_{\mathrm{E}n+1} = \boldsymbol{S}_{\mathrm{E}}(\boldsymbol{E}_{\mathrm{E}\,n+1}, \ldots) \tag{3.26}$$

and $\boldsymbol{F}_{\mathrm{E}\,n+1}$.

Consider next the algorithmic formulation of the crystal plasticity material model. In this case, the external variables $\boldsymbol{F}_n$ and $\boldsymbol{F}_{n+1}$ are known. Then the relative deformation gradient $\boldsymbol{F}_{n+1,n}$ is also known. Further, $\boldsymbol{F}_{\mathrm{E}\,n}$, $\dot{\gamma}_0$ and $\sigma_{\mathrm{D}\,n}$, as well as $\boldsymbol{\alpha}_n$, $\boldsymbol{\tau}_n$ and $\hat{\boldsymbol{\tau}}_n$, are known from the previous update. Consider first the explicit formulation as based on forward-Euler integration. In this case, the update of the inelastic state variables is based on that

$$\alpha_{a\,n+1,n} = t_{n+1,n}\,\dot{\gamma}_0\,\left|\frac{\tau_{a\,n}}{\hat{\tau}_{a\,n}}\right|^m \tag{3.27}$$

for the glide-system shears obtained from forward-Euler integration. In particular the update for the slip resistance is given by

$$\hat{\tau}_{a\,n+1,n} = t_{n+1,n}\,\sum\nolimits_b q_{ab}\,h_{b\,n}(\hat{\tau}_{b\,n})\,|\dot{\gamma}_{a\,n}|\,. \tag{3.28}$$

In particular, $\boldsymbol{\alpha}_{n+1,n}$ determines the updates

$$\begin{array}{rcl} \boldsymbol{\Lambda}_{\mathrm{P}\,n+1,n} & = & \boldsymbol{I} - \sum\nolimits_a \mathrm{dir}(\tau_{a\,n})\,\boldsymbol{s}_a \otimes \boldsymbol{n}_a\,\alpha_{a\,n+1,n} \\ & = & \boldsymbol{I} - \mathcal{N}_{\mathrm{P}\,n}\,\boldsymbol{\alpha}_{n+1,n}\ , \end{array} \tag{3.29}$$

from (3.21). This result then yields the “kinematic” updates

$$\begin{aligned} \boldsymbol{F}_{\mathrm{E}\,n+1} &= \boldsymbol{F}_{\mathrm{E}}(\boldsymbol{F}_{n+1}) &&= \boldsymbol{F}_{\mathrm{E}}^{\mathrm{tr}}(\boldsymbol{F}_{n+1})\,\mathrm{uni}(\boldsymbol{\Lambda}_{\mathrm{P}\,n+1,n}) \\ \boldsymbol{E}_{\mathrm{E}\,n+1} &= \boldsymbol{E}_{\mathrm{E}}(\boldsymbol{F}_{n+1}) &&= \tfrac{1}{2}\,\{\boldsymbol{F}_{\mathrm{E}}(\boldsymbol{F}_{n+1})^{\mathrm{T}}\boldsymbol{F}_{\mathrm{E}}(\boldsymbol{F}_{n+1}) - \boldsymbol{I}\} \end{aligned} \tag{3.30}$$

from (3.22) and (3.21). From these updates, we obtain those

$$\begin{aligned} \boldsymbol{M}_{n+1} &= \boldsymbol{M}(\boldsymbol{E}_{\mathrm{E}\,n+1})\,, \\ \tau_{a\,n+1} &= \tau_a(\boldsymbol{M}_{n+1}, \boldsymbol{\alpha}_{n+1})\,, \end{aligned} \tag{3.31}$$

for the constitutive stresses via (3.4) and (3.7), respectively.

As before, post-processing includes calculating the update

$$\boldsymbol{S}_{\mathrm{E}\,n+1} = \boldsymbol{S}_{\mathrm{E}}(\boldsymbol{E}_{\mathrm{E}\,n+1}) \tag{3.32}$$

for the elastic second Piola-Kirchhoff stress, and so in turn that

$$\boldsymbol{K}_{n+1} = \boldsymbol{F}_{\mathrm{E}\,n+1}\boldsymbol{S}_{\mathrm{E}\,n+1}\boldsymbol{F}_{\mathrm{E}\,n+1}^{\mathrm{T}} \tag{3.33}$$

for the Kirchhoff stress. The corresponding tangent is given by

$$\begin{aligned} \partial^{\mathrm{a}}_{\boldsymbol{\Lambda}_{n+1}}\boldsymbol{K}_{n+1} &= \boldsymbol{I}\,\square\,\boldsymbol{K}_{n+1} + \boldsymbol{K}_{n+1}\,\triangle\,\boldsymbol{I} \\ &+ (\boldsymbol{F}_{\mathrm{E}\,n+1}\,\square\,\boldsymbol{F}^{\mathrm{T}}_{\mathrm{E}\,n+1})\,\mathcal{C}_{\mathrm{E}0}\,(\boldsymbol{F}^{\mathrm{T}}_{\mathrm{E}\,n+1}\,\square\,\boldsymbol{F}_{\mathrm{E}\,n+1})\,\mathrm{sym}\,. \end{aligned} \tag{3.34}$$

In this last relation, $\mathrm{sym} = \frac{1}{2}(\boldsymbol{I}\,\square\,\boldsymbol{I} + \boldsymbol{I}\,\triangle\,\boldsymbol{I})$ represents the fourth-order tensor induced by symmetrization. Here is made use of the tensor products $(\boldsymbol{A}\,\square\,\boldsymbol{B})\boldsymbol{C} := \boldsymbol{A}\boldsymbol{C}\boldsymbol{B}$ and $(\boldsymbol{A}\,\triangle\,\boldsymbol{B})\boldsymbol{C} := \boldsymbol{A}\boldsymbol{C}^{\mathrm{T}}\boldsymbol{B}$ of any second-order tensors $\boldsymbol{A}, \boldsymbol{B}, \boldsymbol{C}$. Additionally use is made of the notation

$$\partial_{\boldsymbol{\Lambda}}\varphi(\boldsymbol{F}, \ldots) := \partial_{\boldsymbol{F}}\varphi(\boldsymbol{F}, \ldots)\,(\boldsymbol{I}\,\square\,\boldsymbol{F})$$

for the push-forward of $\partial_{\boldsymbol{F}}\varphi(\boldsymbol{F}, \ldots)$ to the current configuration as based on that $d\boldsymbol{F} = \boldsymbol{\Lambda}\boldsymbol{F}$ for the infinitesimal deformation gradient, with $\boldsymbol{\Lambda} := (d\boldsymbol{F})\,\boldsymbol{F}^{-1}$.

For the simulations, the time step is controlled via $\|\mathrm{mag}(\boldsymbol{L}_{\mathrm{P}})\|$ which value was previously identified via empirical one element tests. The simulations were performed on an Intel Core2Duo P8600 machine with 2.4GHz and 4GB memory running Ubuntu Linux 8.04 in parallel on 3 cpus. The computation time for the simulation without hardening for 20% deformation was roughly 4 weeks and for the simulation with hardening for 20% deformation roughly 3 weeks. It was observed that the value for $\|\mathrm{mag}(\boldsymbol{L}_{\mathrm{P}})\|$ has to be smaller for a stabile simulation with hardening compared to simulation without hardening. The higher computation time for simulation without hardening results from occuring deformation localization.

3.4 Model identification

It is assumed that the general mode of deformation in the silicon iron alloy is slip and that the presence of mechanical twinning is negligible. As reported in Gell and Worthington (1966), mechanical twinning occurs for fine-grained material below 180°K and for coarse grained above 320°K. Noble and Hull (1965) also did not observed any twinning and strain aging effects in tensile tests at 293°K on Fe-3%Si. The presented experimental results were obtained at room temperature and therefore mechanical twinning as well as strain aging effects are not further considered.

As mentioned in the introduction, it is well accepted that crystallographic slip in BCC metals occurs in close-packed $\langle 111 \rangle$ direction, but there is a disagreement regarding the operative slip planes in the literature. Hull (1963); Noble and Hull (1965) reported that the main dislocation movement is on $\{110\}$ slip planes at 293°K for different orientations. However, Erickson (1962); Takeuchi et al. (1967); Taoka et al. (1964) reported contradictory results where the $\{112\}$ was identified as an operative slip plane as well as the $\{110\}$ plane, depending on temperature and orientation. The average direction of the slip bands was reported to be very close to the trace of either $\{110\}$ or $\{112\}$. Similar results were reported in Ito and Vitek (2001); Šesták and Blahovec (1970); Šesták and Zárubová (1965). Some authors (e.g., Erickson, 1962) also reported slip on all planes with low indices $\{110\}$, $\{112\}$ and $\{123\}$.

In the following the glide systems $\{110\}\langle 111 \rangle$ and $\{112\}\langle 111 \rangle$ are investigated by finite element simulations using single glide system class or combinations thereof actively. The $\{123\}$ slip plane will not be considered further due to its higher Schmid factors and lower Taylor factors which results in a higher activation energy and therefore are not preferable for slip.

The values of the elastic constants for Fe-3%Si are taken from Routbort et al. (1971) and are shown in Table 3.1. The unknown inelastic parameters are identified with inverse finite-element analysis by fitting the results for tensile tests on single crystals for different orientations to corresponding experimental data extracted from Hull (1963). Due to the fact that no substantial difference stress-strain curves for different glide system classes are available in the literature and further results in the literature show nearly no difference in the yield stress at room temperature for $\{110\}$ and $\{112\}$ slip planes (e.g., Taoka et al., 1964) the hardening parameters for both glide system classes are assumed to be equal in a first step. Furthermore it is known that Fe-3%Si shows a smooth upper and lower yield point depending on grain size and sheet thickness (e.g., Henning and Vehoff, 2010; Hull, 1963). However, due to lack of information about this effect for the current grain size distribution this effect is not considered in the fitting process. Also failure phenomena, like reported in Gell and Worthington (1966), are not considered further. Due to the fact that no information about the strain rate sensitivity were available the strain rate sensitivity m is set to 20 and the reference slip rate $\dot{\gamma}_0$ is set to be $0.001 s^{-1}$ for quasi-static loading conditions

$C_{\mathrm{E},11}$ [GPa]	$C_{\mathrm{E},12}$ [GPa]	$C_{\mathrm{E},44}$ [GPa]
222	135	120

Table 3.1: Material properties of Fe-3%Si (BCC) (Routbort et al., 1971).

The determination of the remaining parameters is carried out using the program LS-OPT in conjunction with ABAQUS/Standard. The fitted hardening parameters are shown in Table 3.2. The optimization techniques used rely on response surface methodology (RSM) (Kok and

$\hat{\tau}_0$ [MPa]	$\dot{\gamma}_0$ [s^{-1}]	m [-]
161	0.001	20
h_0 [MPa]	$\hat{\tau}_0^{\mathrm{sat}}$ [MPa]	n_0 [-]
243.9	1137	0.48

Table 3.2: Material properties of hardening of Fe-3%Si (BCC) fitted to the experimental results of Hull (1963).

Stander, 1999), a mathematical method for constructing smooth approximations of functions in a design space. The approximations are based on results calculated at numerous points in the multi-dimensional design space. In this work, the hardening parameters are the design variables and the model together with the data determine the objective function of the corresponding optimization problem.

3.5 Experimental methods

The tensile test sample was laser-cut from Fe-3%Si sheets (BCC) with a thickness of 1 mm. The gauge length is about 5 mm in width and 15 mm in length. The mean grain size is about 2 mm which is of the order of the sheet thickness. In the case of the largest mean grain size of approximately 5 mm, the grains are of the order of the specimen geometry. Whereas the size effects mentioned in section 3.1 have been investigated in detail in the literature, size effects upon miniaturisation caused by the adopted processing method of microparts have done by few researchers. In Janssen et al. (2008), it is reported that machining induced damage to crystals just below a newly created surface can be neglected in macroscopic analysis but not for volumes with grain size near the geometrical size. It has to be taken care to avoid that the test sample is influenced by such processing induced size effects. By the laser-cutting it is hardly to avoid such side effect but to remove these processing induced size effects the specimen was annealed at 1200°C under vacuum for 48 h whereby a two-dimensional grain structure was achieved. Afterwards, all surfaces of the samples were polished and etched. Etching was necessary to remove the deformation layer caused by polishing. These further treatment should take care of removing all induced processing size effects if possible as well as the experiments did not show any indication of these size effects.

The experimental results (Henning and Vehoff, 2005) concerning the properties of the sample (deformation, local orientation) are determined at several stages, namely at plastic strains of $\alpha_{\mathrm{P}} \approx \{0\%, 1.5\%, 4\%, 10\%, 19.5\%\}$. To compare the experimental and simulation results concerning the deformation field only the grain boundary segments between two grain boundary triple junctions, approximated as planes perpendicular to the sample surface as displayed in Figure 3.1, are shown. The presented experimental results also show the orientation gradient, however, the focus here is on the shape changes of the sample only. For details concerning the orientation gradient see Henning and Vehoff (2005).

In Henning and Vehoff (2005), it is mentioned that the deformation results (presented in Figure 3.3) are obtained by recording the positions of the grain boundary triple junctions. Grains

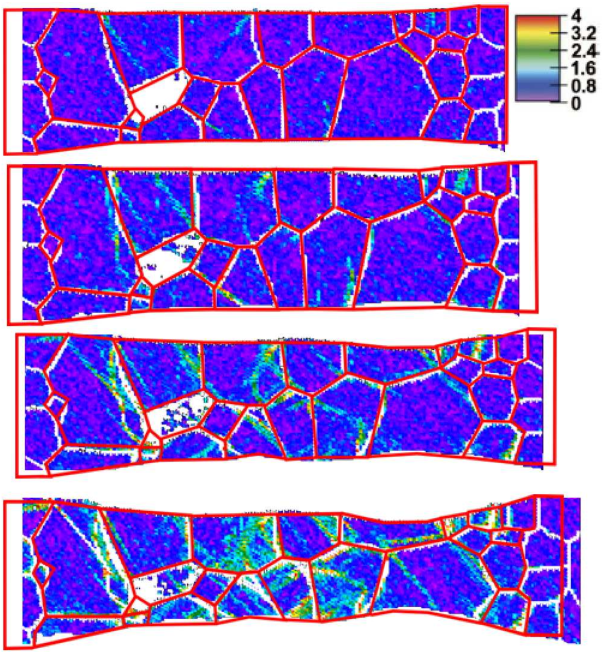

Figure 3.1: Experimental results of the deformation field and orientation gradient (Henning and Vehoff, 2005). Approximation of grain boundaries shown as red lines.

may undergo rigid-body rotation due to the plastic deformation of their neighborhood. These rigid body rotations were eliminated following the calculation of a two-dimensional per-grain average strain tensor by applying a least-square fit method as discussed in Lee et al. (1998), which is slightly corrected in Henning and Vehoff (2005). Other methods to measure two-dimensional strains are presented in Hoc et al. (2003); Tatschl and Kolednik (2003) (e.g. laser or etching), the measurement is carried out in-grain, which is done by introducing a grid on the surface which leads to unknown surface effects. Side effects like these have been avoided whenever possible.

The results obtained by experiment contain only information concerning the surface. This is assumed to be sufficient due to the fact that in the experiment the grain boundaries remain nearly perpendicular to the sample surface. At the grain boundaries, contraction perpendicular to the sample surface seems to be negligible, which agrees with the results in Stölken and Evans (1998). Therefore no investigation concerning the contraction in the third dimension will be done in the following and only results at the sample surface are presented. The orientations of the grains are obtained with electron backscatter diffraction (EBSD) using OIM. These are used as initial orientation in the finite element model.

3.6 Finite element model

The measured two-dimensional grain structure and the grain orientations were used to construct a finite-element model. The grain boundary segments between two grain boundary triple junctions were approximated as planes perpendicular to the sample surface. This task was done by using the software DEFMEASURE (Henning, 2008). The experimental sample is modeled by using the measured geometry for the creation of a finite element mesh. In order to model the experimental setup more closely at either end of the tensile specimen transition areas are introduced. These are modeled using a simple isotropic elastic material model. This reduces the boundary effects in the simulation by applying the tensile loading at the surrounding area (Zisman and Rybin, 1998). It was observed that defects such as slip lines can start from grain boundaries and edges of the sample (Polcarova et al., 1998).

The fact that neighboring grains do not share the same orientation and grain boundaries are not necessarily parallel to the local crystallographic axes in combination with the anisotropic elastic behavior may induce an inhomogeneous stress field within a single grain (Vehoff and Nykyforchyn, 2003). Therefore the model has to be setup in 3D which is done by simple extrusion of the 2D geometry. The resulting FE-mesh is shown in Figure 3.2 which consists of 18657 brick (8-node) elements. The grain orientations, found by EBSD, are accounted for via initialization of the state dependent variables (SDVs). The simulations are performed with the FE software ABAQUS using material routines introduced in section 3.3 which are implemented via the UMAT and UEL interface in ABAQUS/Standard. In what follows, the numbering shown in Fig.3.2 will be used for clarity.

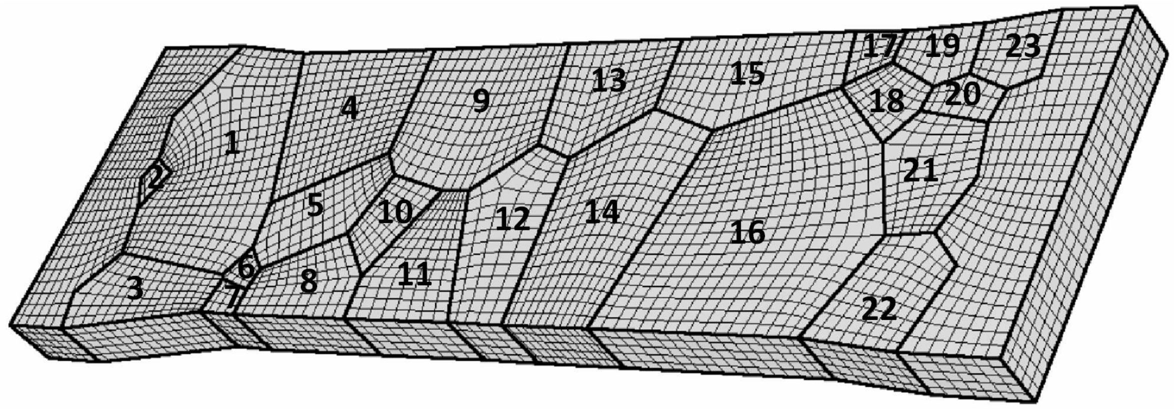

Figure 3.2: FE mesh used for simulations with grains numbered.

3.7 Results

3.7.1 Without hardening

In this section experimental results are recalled from Henning and Vehoff (2005) which are compared to simulation results for different sets of glide systems active where the simulation is preformed without hardening.

In Figure 3.3a) a micrograph obtained with a light-optical microscope displaying the length of the specimen is shown. Also small topographic details like contamination marks caused by EBSD become visible. However, the surface details visible are negligible in reality. Figure 3.3b)-e) display in the left column the experimental plastic strain component in tensile direction and in the other three columns simulations results of the accumulated crystallographic slip for all glide systems $\alpha_{\mathrm{P}} = \sum_a \alpha_a$ for different active glide systems. The experimental strain components $\alpha_{\mathrm{P},22}$ (in Figure 3.3 described by $\varepsilon_{\mathrm{pl},22}$) in tensile direction are recalled from Henning and Vehoff (2005) which were identified for a whole grain. The simulation results are done for $\{110\}\langle111\rangle$ or $\{112\}\langle111\rangle$ or $\{112\}\langle111\rangle$ and $\{110\}\langle111\rangle$ active glide systems in which α_P is displayed continuously over the structure. From this point on no exact agreement between the experiment and simulation can be expected quantitatively. For more details about obtaining the experimental results see Henning (2008); Henning and Vehoff (2005). The second column shows the simulation results for $\{110\}\langle111\rangle$ and the third for $\{112\}\langle111\rangle$ solely active. The fourth column shows the accumulated slip results for both sets of glide system classes $\{110\}\langle111\rangle$ and $\{112\}\langle111\rangle$ active simultaneously. Remarkably is that both glide systems sets show nearly the same amount of activity in the simulation which can be anticipated by analyzing the Schmid factors. Comparing experimental and simulation results for both glide system classes solely active the highest amount of slip occurs in the same region which is near grain 14 and 15. However, in the experiment the highest deformation occurs in grain 15 and 16. For the $\{112\}$ case more deformation occurs in grain 15 as for the $\{110\}$ case. The $\{110\}$ case shows a higher activity in grain 13 compared to the $\{112\}$ case. In the beginning the experimentally obtained deformation in grain 14 is higher than in grain 16 which is comparable with the simulation results. But with increasing deformation grain 15 and 16 gets more active than grain 14 which is contrary to the simulation results. Finally in the simulation a slip band becomes precisely visible in grain 14 and 15 whereas a slip band occurs in the experiment in grain 15 and 16 (see Figure 3.5). In the experiment grain 9 shows a high activity at the beginning of the tensile test but with increasing deformation the deformation rate in this grain decreases. Also the simulation results show initially a high activity in grain 9 (especially for $\{110\}$) and, as in the experiment, the amount of deformation rate compared to other grains is decreasing with increasing deformation (see Figure 3.3c) to e)). In Henning and Vehoff (2005) this effect is explained by the local differences in hardening but as can be seen from the experiment

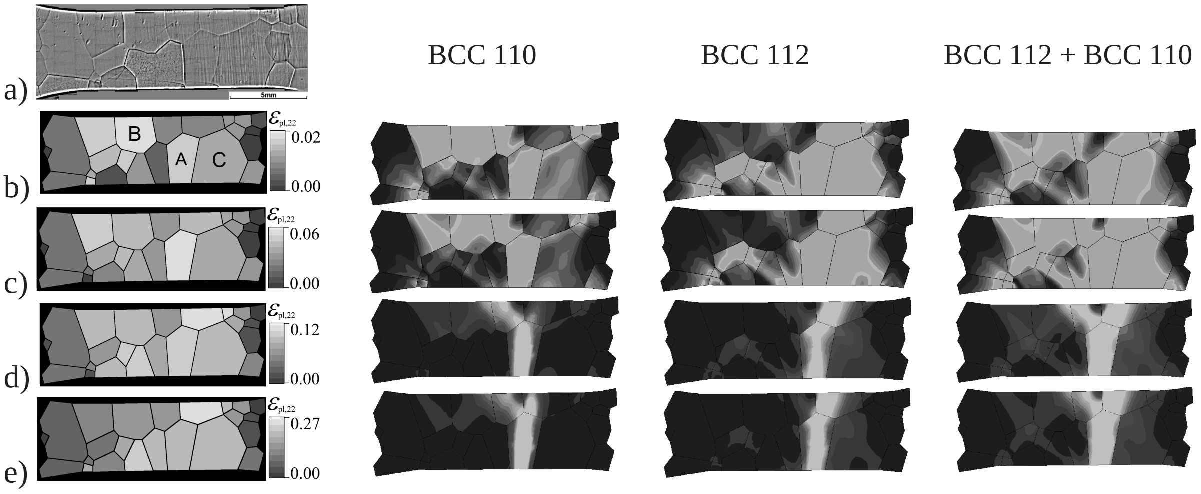

Figure 3.3: a) Light-optical micrograph of the tensile test sample. b)-e) In the left column the plastic strain component in tensile direction of the least square fit strain tensor for each grain for $\alpha_\mathrm{P} \approx \{1.5\%, 4\%, 10\%, 19.5\%\}$ Henning and Vehoff (2005) is shown. The other columns show the accumulated crystallographic slip for all glide systems in the simulation for active glide system class $\{110\}\langle111\rangle$ or $\{112\}\langle111\rangle$ or $\{112\}\langle111\rangle$ and $\{110\}\langle111\rangle$. The scale is according to the experimental ones. The shape change of the grains is not reflected.

an explanation is already given by the initial orientation and the following reorientation of the glide systems with regard to the loading direction. From this follows that some grains become more favorable for slipping just by reorientation of the grains. Finally the sample in the experiment failed in grain 16 whereas in the simulation the element distortion is getting very severe in grain 14. Due to the fact, that the simulation results in Figure 3.3 display the accumulated crystallographic slip for all glide systems, it is impossible to identify which exact glide systems are active at the analyzed deformation step after most of the systems are already active. Once a glide system is active, it will remain active for a longer period. Due to the different initial orientation every grain behaves differently under the prescribed loading condition.

The results for $\{110\}\langle 111\rangle$ and $\{112\}\langle 111\rangle$ active simultaneously show a combination of both results for solely active class. Firstly a lot of grains are active in which grain 14 gets more active with increasing deformation. From this first analysis it looks like that both glide system classes have a strong impact on the resulting behavior. This implies that neither of these set of glide systems can be neglected in the simulation to obtain more realistic results.

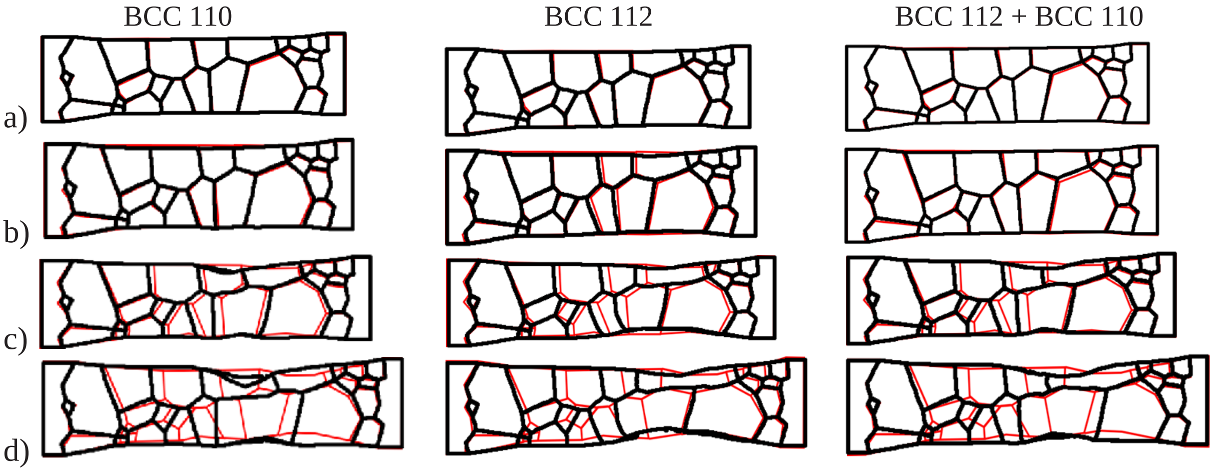

Figure 3.4: a)-d) Comparison between observed experimental deformation (red thinner lines) for $\alpha_{\mathrm{P}} \approx \{1.5\%, 4\%, 10\%, 19.5\%\}$ to simulation results (black thicker lines) for different active glide system classes ($\{110\}\langle 111\rangle$(left), $\{112\}\langle 111\rangle$(middle), $\{110\}\langle 111\rangle$ and $\{112\}\langle 111\rangle$(right)) without hardening.

Figure 3.4 shows the observed experimental deformation compared with the deformation of the grains in the simulation given by the boundary lines.

The shape changes are consistent with the previous described behavior for the plastic strain (see Fig. 3.3). In the experiment strong necking is visible near grain 15 and 16 whereas these grains undergo also a strong extension. Until $\alpha_{\mathrm{P}} \approx 20\%$ no clear shear band is visible which appear during the further deformation. Figure 3.5 shows this shear band in grain 15 and 16 at $\alpha_{\mathrm{P}} \approx 40\%$ which leads to failure of the sample.

Simulations for the case of active $\{112\}\langle 111\rangle$ glide system class shows a higher contraction than for simulations with active $\{110\}\langle 111\rangle$ glide system class only. In particular the deformation in grain 16 indicates that a deformation by active $\{112\}\langle 111\rangle$ glide systems occurs in the mesocrystal. The simulation with active $\{110\}\langle 111\rangle$ glide system class shows a very high elongation of grain 14 and 15 compared to experiment. The results for a simulation with slip

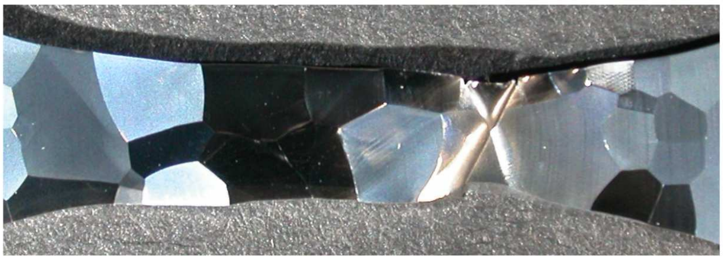

Figure 3.5: Optical photograph of the sample at $\alpha_\mathrm{P} \approx 40\%$ Henning and Vehoff (2005).

on $\{110\}$ and $\{112\}$ planes simultaneously show a slight dominance of the $\{110\}\langle 111\rangle$ glide system class. However, the results for both systems active differ significantly from the results for one single glide system class solely active, i.e., for the deformation behavior of grain 13.

In the following we want to investigate the reorientation field of the mesocrystal. The reorientation field maybe understood as a indicator where a high activity occur which may result in crystal lattice changes which are produced by dislocations (Sedláček et al., 2001). The reorientation field β_{n+1} with respect to the reference configuration can be calculated by

$$\beta_{n+1} := \min\left|\arccos\left(\frac{1}{2}\left[\mathrm{tr}(\boldsymbol{R}_{\mathrm{E}\,n+1}\,\boldsymbol{R}^{T}_{\mathrm{E}\,0}\,\boldsymbol{O}^{\mathrm{T}}_{\mathrm{C}}) - 1\right]\right)\right|, \tag{3.35}$$

where $\boldsymbol{R}_{\mathrm{E}\,n+1}$ is obtained by polar decomposition of $\boldsymbol{F}_{\mathrm{E}\,n+1}$ and $\boldsymbol{R}_{\mathrm{E}\,0}$ is given by the initial orientation. $\boldsymbol{O}_\mathrm{C}$ describes the orientation matrix for all 24 symmetry matrices of cubic symmetry. Note that the reorientation field describes the orientation difference between the actual and original orientation which is different from the concept of misorientation or orientation gradients.

Figure 3.6 shows the calculated reorientation field. It is not remarkable that the highest reorientation occurs in the region where the highest deformation occurs. Especially at the beginning of the deformation this can clearly be identified by comparing Fig. 3.3 at $\alpha_\mathrm{P} \approx 1.5\%$ with Fig. 3.6 at $\alpha_\mathrm{P} \approx 4\%$. The highest reorientation is visible in grain 14 for all different glide system sets in which the $\{112\}\langle 111\rangle$ class show a much higher reorientation in grain 16 as the $\{110\}\langle 111\rangle$ class. With both classes active the resulting reorientation is a combination of both. It may be pointed out that the reorientation can not be directly compared with the obtained orientation gradient in Figure 3.1.

By evaluation these results it has to be considered that the grains in this simulation are ideal viscoplastic and therefore no hardening occurs. Furthermore the results above $\alpha_\mathrm{P} \approx 15\%$ have to be evaluated carefully due to an occurring shear band and distorted elements. Figure 3.7 shows the mesocrystal at $\alpha_\mathrm{P} \approx 40\%$ and the resulting elements for the active $\{112\}\langle 111\rangle$ glide system class, whereas the results for the other simulations look similar. In the region of the shear band the elements have bad aspect ratios and become distorted so that the results are not reliable anymore. However, due to the explicit time integration scheme of the material routine at the integration point level the simulation is stable and does not abort. But the necessary time step for the simulation is getting very small. To keep a good element quality, remeshing techniques have to be used in future work.

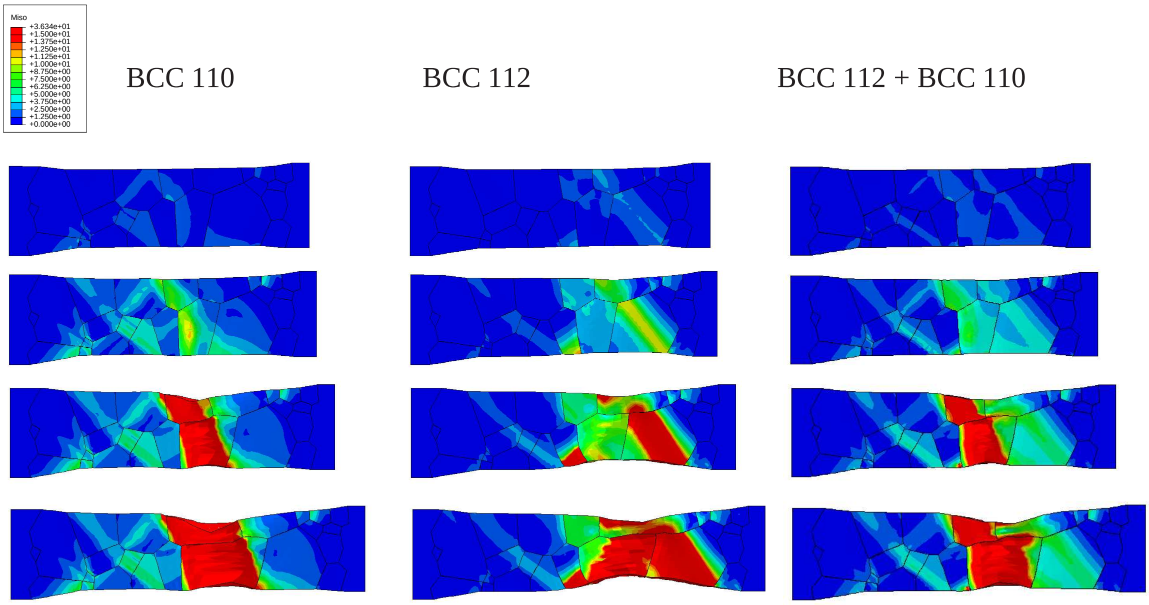

Figure 3.6: Reorientation field β for $\alpha_\text{P} \approx \{1.5\%, 4\%, 10\%, 19.5\%\}$ for active glide systems $\{112\}$+$\{110\}$(left) or $\{112\}$ (middle) alone or $\{110\}$(right) alone, respectively, without hardening.

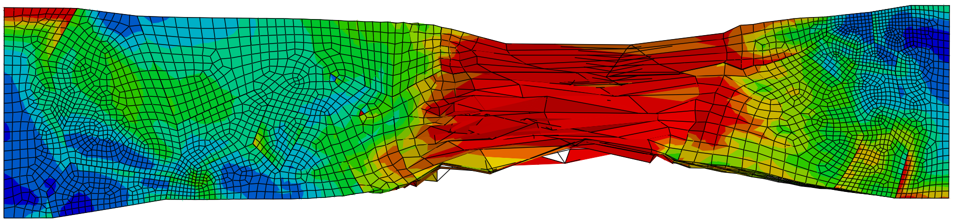

Figure 3.7: Stress distribution at $\alpha_\text{P} \approx 40\%$ with distorted finite element mesh

As input data for the simulation the measured EBSD data is used as initial orientation. The orientation in every grain is assumed to be homogeneous which is in reality not the case. As displayed by the orientation gradient in Henning and Vehoff (2005) local differences in the orientation of $1-2^\circ$ are visible inside the grains at the beginning. To investigate the influence of this distribution additional simulations are performed where the initial orientation inside the grain is randomly distributed such that it can be vary $\pm 2^\circ$ with respect to the mean value which was used in the previous simulations. The results agree with the previous presented results which indicates that the influence of the scattering can here be assumed to be negligible on the deformation behavior.

In summary, the first simulation results with ideal viscoplasticy show already a good tendency to experimental results. This indicates that the correct prediction of initially active slip systems is a very important effect. This influences the entire history of inelastic deformation in the sample substantially which is in agreement with the results in Henning and Vehoff (2005). Furthermore, these first results show that next to the $\{110\}\langle 111\rangle$ further slip systems have to be considered. Also $\{112\}\langle 111\rangle$ seem to have a significant influence. Therefore both glide system classes are included into one single simulation in which the influence on each other can be better interpreted. However, $\{110\}\langle 111\rangle$ seems to be slightly dominant.

3.7.2 With hardening

In the following the deformation behavior of the structure for an activated hardening law, as stated in section 3.3, is investigated. The material parameters identified for the used hardening law can be found in section 3.4. All simulations are carried out for the slip systems $\{110\}\langle 111\rangle$ and $\{112\}\langle 111\rangle$ active separately and simultaneously. For simplicity no coupling between these two glide system classes is assumed which is done by setting the coupling terms in the hardening matrix q_{ab} to zero.

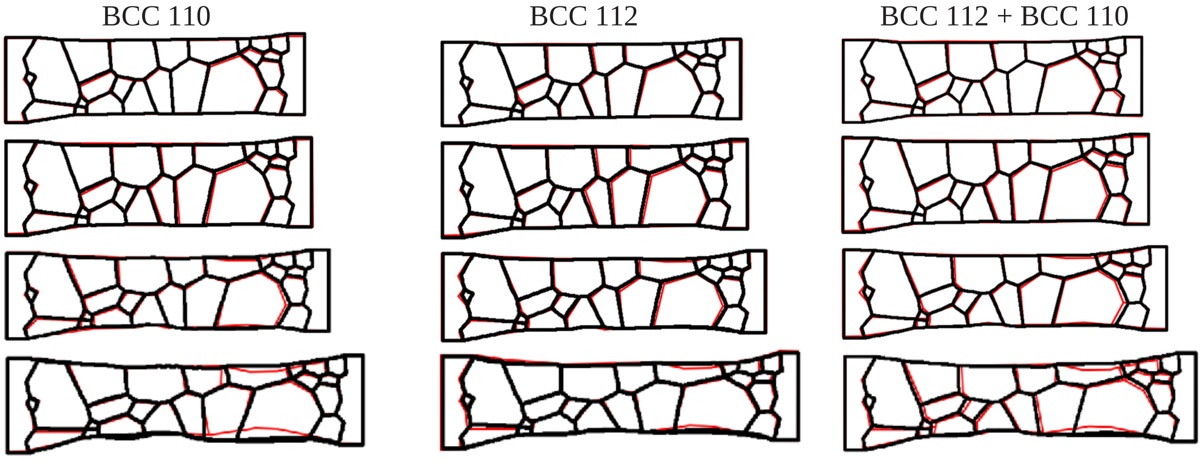

Figure 3.8: Comparison between observed experimental deformation (red thinner lines) Henning and Vehoff (2005) for $\alpha_{\mathrm{P}} \approx \{1.5\%, 4\%, 10\%, 19.5\%\}$ to simulation results (black thicker lines) for glide system classes $\{110\}\langle 111\rangle$ and $\{112\}\langle 111\rangle$ separately and simultaneously active with included hardening.

Figure 3.8 shows the obtained deformation in the simulation in comparison to the experimental results. Comparing these results to Figure 3.4 until $\alpha_{\mathrm{P}} \approx 4\%$ no deviation between the simulation with and without hardening is visible. Also the results agree very well with the experimentally observed deformation. However, for larger deformation the results between the two simulations deviate. First of all it can be observed that with increasing deformation the results without hardening show a necking behavior in the region of grains 13, 14 and 15. For the simulation with hardening nearly no necking can be observed. The results for $\{110\}$ solely active show the most contraction near grain 11 which is slightly overestimated compared to experimental results. This behavior is not seen for $\{112\}$ active alone. The simulation results show very straight boundary lines also at high deformation states. Both simulations predict the grain boundaries quite well. Nearly all boundaries in horizontal direction are consistent with the experimental ones. Especially the largest elongation of grains 15 and 16 is represented quite nicely. A few small differences between both results should be pointed out which might not be noticed immediately, however, it is difficult to say which depicts the experiment correctly: The inclination of the boundary between grain 14 and 16 is different and therefore also the shape of grain 14 is slightly different. For $\{110\}$ the grain 13 is elongated a bit more at the cost of the elongation of grain 15. Grain 5 is more compressed in the case of $\{110\}$.

The simulation results for both systems active are a combination of both previous discussed simulation results. It shows a slightly smaller contraction near grain 11 as in the $\{110\}$ case so that the shape of the deformed specimen in the experiment is well represented in this region. Compared to the case without hardening where $\{110\}$ glide system class was anticipated to be dominant, for the case with hardening this assumption can not be made due to the fact that in the investigation of the deformation behavior both systems play an active part in determining the deformation if both glide systems are active with active hardening.

In general the simulation results with hardening show a very good agreement to the experiment, leading to a very good improvement compared to the results without hardening, with the exception that the largest contraction in the experiment between grain 15 and 16 is not represented by all simulations. It is to question if the occurring shear band at $\alpha_{\mathrm{P}} \approx 40\%$ could be anticipated by this model. The distortion of the mesh at higher strains restrict a further investigation due to the fact that the results were not valid anymore. Therefore 3D remeshing techniques are on-going work and will be used in the future. However, it is generally doubtful that the shear band in grain 15 and 16 would be predicted correctly due to the smaller contraction in the simulation so far. The reason might be the overestimation of the hardening by the parameter identification which was done based on experimental data from over 40 years ago. Therefore the experimental and simulative identification of hardening parameters for Fe-3$\%$Si with nanoindentation will be on-going work. Also further methods like strain gradient plasticity to cover length-scale effects will be investigated to get an even better prediction.

Figure 3.9 shows the resulting reorientation fields for the simulations with included hardening. It can be seen that the reorientation is not localized in contrast to the simulation results without hardening. In nearly all grains a reorientation occurs in which the highest reorientation takes place in grains 10, 11 and 16 for all simulations. For the case of $\{112\}$ solely active a high reorientation occurs in grain 15. It is clear that the highest reorientation takes place in the region where the highest deformation occurs. Due to the reorientation the slip place might become more favorable for slip resulting in deformation switching to these grains. Comparing the results for $\{110\}$ and $\{112\}$ separately active certain differences can be observed but the general reorientation field is similar. The simulation results for both systems active support the previous assumption that both glide system classes are active at a similar level. As stated before the reorientation field can not directly be compared to the experimentally obtained orientation gradient and therefore no comparison to the experiment is made.

In conclusion it can be summarized that the simulation with included hardening shows a much better agreement with the experiment as without hardening. The simulation with hardening on both glide systems $\{110\}\langle 111\rangle$ and $\{112\}\langle 111\rangle$ active simultaneously shows the best agreement with the experimentally obtained deformation compared to all other simulation results. To be able to compare the results more in detail and to understand the mechanical behavior better we will investigate the evolution of dislocations and the orientation gradient during deformation in the future to include these fields in our material model to model the behavior of this mesocrystal step by step in a realistic and understandable fashion.

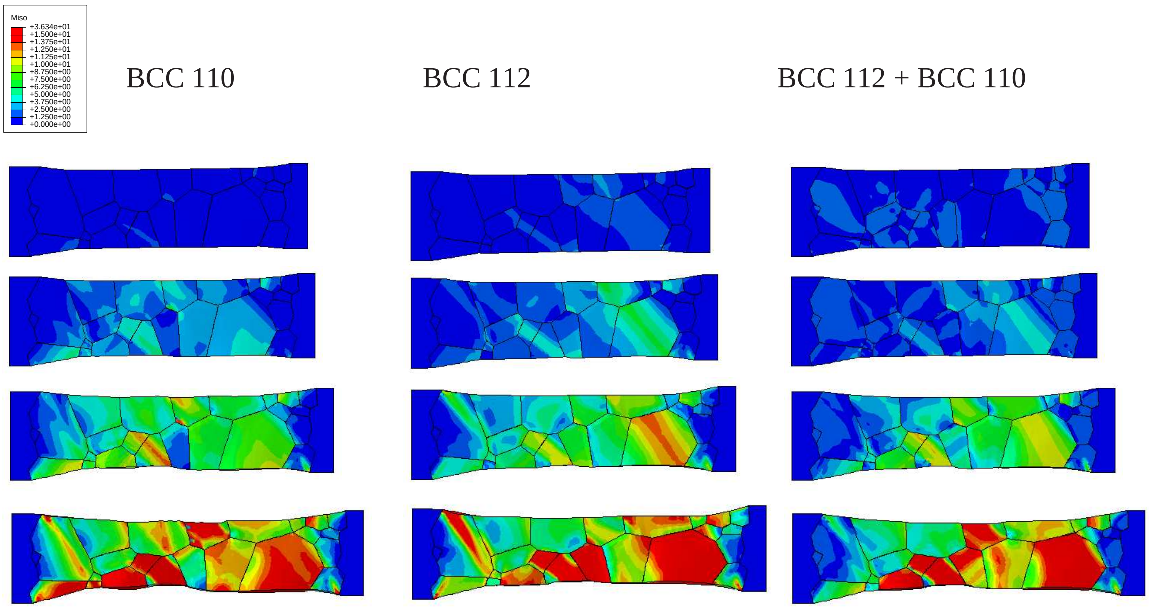

Figure 3.9: Reorientation field β for $\alpha_\mathrm{P} \approx \{1.5\%, 4\%, 10\%, 19.5\%\}$ for glide system classes $\{110\}\langle 111\rangle$ and $\{112\}\langle 111\rangle$ separately and simultaneously active with included hardening.

3.8 Conclusion

In this work the modeling and simulation of the deformation behavior of thin sheets consisting of large grains of Fe-3%Si and comparison with experiment is performed. For this an explicit finite-element-, crystal-plasticity-based model is developed for each grain, the grain morphology, and the thin sheet specimen as a whole. In particular, the crystal plasticity model is rate-dependent and accounts for (local) dissipative hardening effects. The predictions of the model are compared with experimental results of Henning and Vehoff (2005) for the deformation behavior of thin sheets of Fe-3%Si loaded incrementally in tension. To this end, attention is restricted to the two slip families $\{110\}$ and $\{112\}$. To begin, all hardening is neglected. Even for this oversimplified case, a good correlation with the experimental results is obtained which shows the importance of predicting initially active glide systems correctly. The simulation results with both glide system classes active simultaneously show that both classes have a certain influence on the deformation, however, $\{110\}\langle 111\rangle$ seems to be slightly dominant. Therefore it is concluded that both classes are necessary to simulate the experimental tensile tests. Even better agreement is obtained with experiment when hardening is included. The contraction in the region of the occurring shear band in the experiment was underestimated which indicates that the hardening might be overestimated. Finally, first results for the development of local orientation changes are discussed.

In future work the evolution of dislocations and the orientation gradient will be analyzed. Further the model formulation will be extended by hardening formalism based on GNDs. In addition remeshing techniques will be used to obtain reliable results at high deformations.

Chapter 4

Crystal plastic modeling of the development of orientation gradients and geometrically necessary dislocations in thin sheets with large grains

Abstract– The purpose of this work is the modeling and simulation of the deformation behavior of thin sheets consisting of large grains of Fe-3%Si and comparison with experiment. To this end, an explicit finite-element-, crystal-plasticity-based model is developed for each grain, the grain morphology, and the thin sheet specimen as a whole. In particular, the crystal plasticity model is rate-dependent and accounts for (local) dissipative hardening effects. The predictions of the model are compared with experimental results of Henning and Vehoff (2005) for the deformation behavior of thin sheets of Fe-3%Si loaded incrementally in tension. A detailed investigation regarding the initial activity is performed on basis of the Schmidt and Taylor factors. To this end, attention is restricted to the two slip families $\{110\}$ and $\{112\}$. To begin, all hardening is neglected. Even for this oversimplified case, a good correlation with the experimental results is obtained for the deformation behavior which shows the importance of predicting initially active glide systems correctly. However, further comparisons, e.g., with the experimentally observed orientation gradient (OGM), show no correlation between experiment and simulation. As a first improvement hardening is included which leads to better results. The deformation behavior as well as the orientation gradient show the same tendency in the simulation as in the experiment. Still certain deviations can be observed which might be related to hardening effects not accounted for. Therefore initial results for geometrically necessary dislocations as well as local orientation changes are investigated.

4.1 Introduction

A basic issue of research in material science and material mechanics is to determine the relation between microstructure, material properties and mechanical response (McPherson, 1981; Wyss et al., 2004). The modeling of the mechanical behavior for a given microstructure can be performed in different ways. A common concept is the use of statistical or averaging theories. The associated homogenization can be performed on basis of a representative volume element (RVE). This concept is based on the assumption of scale separation between the microstructural and macrostructural lengthscale. As the characteristic size of the microstructure (e.g., grain size) approaches that of the system (e.g., sheet thickness), however, such scale separation is no longer given and one must resort to other means of representing the effect of microstructural heterogeneity on the system behavior. As the macrostructural lengthscale approaches the microstructural one, the degree of material heterogeneity increases drastically, such that the local microstructural behavior can deviate significantly from the average behavior at the macroscale (e.g., Kalidindi et al., 2003; Pierard et al., 2007). In this case, the model has to account for the microstructural details such as orientation details of the grain structure (e.g., Schneider et al., 2010) or shape distribution (e.g., Arns et al., 2002). To include such details the microstructural details can be accounted for by discretizing the domain and using local single crystal plasticity models combined with finite element calculations. These models are often constructed with the help of, e.g., optical and / or EBSD data on the grain morphology. In specimens with more than one grain over the thickness, the common method of projecting the two-dimensional EBSD information uniformly in the third dimension will generally lead to different behavior (e.g., Wiederkehr et al., 2010). If the specimen is one grain thick, however, such an optical- / SEM- / EBSD-based approach should be reasonable. For such a specimen a number of size effects are expected to influence its mechanical properties. These effects have been known for years and are still subject of active research (e.g., Bargmann et al., 2010; Engel and Eckstein, 2002; Fu et al., 2001; Fülöp et al., 2006; Geers et al., 2006; Greer et al., 2005; Janssen et al., 2006, 2008).

The overall mechanical response is strongly influenced by the orientation of the individual grains if the number of grains over the thickness is fairly small (Fülöp et al., 2006). In the case of thin sheets the mechanical properties in a given cross section are increasingly dominated by each individual grain as reported in Henning and Vehoff (2005). Due to the different orientations of the grains located in the sheet plane, the deformation is no longer uniform even under homogeneous loading conditions. This heterogeneity and the size-dependence of deformation give rise to size effects (Henning and Vehoff, 2010). Different mechanisms can occur at different stages of deformation. The initial yield stress is influenced by grain size, grain orientation and elastic anisotropy (Hall, 1951; Petch, 1953; Prohászka and Dobránszky, 2003). With ongoing deformation strain hardening occurs which may be caused by geometrically necessary dislocations (GNDs) (e.g., Ashby, 1970; Evers et al., 2004a,b; Ma et al., 2006; Nye, 1953). The grain size dependent mechanical response in a polycrystal is successfully modeled by Evers et al. (2002) using a local strain gradient dependent crystal plasticity model accounting for GNDs. Various interesting viewpoints concerning the modeling and experimental concept of GNDs can be found in El-Dasher et al. (2003); Gao and Huang (2003); Kubin and Mortensen (2003).

To understand and predict the behavior correctly simulation and experiment have to be compared locally. Therefore detailed experimental information of local details during plastic deformation are necessary. The measurement of local dislocation densities and its evolution during the deformation process is very time-consuming. Thus there is a need for methods to perform local quantitative characterizations of the microstructure. Henning and Vehoff (2005) used the orientation gradient mapping (OGM) locally which is a measure of the the local strain hardening. It is known that crystallographic slip in body-centered cubic (BCC) metals, like Fe-3%Si, take place in close-packed $\langle 111 \rangle$ direction, but there are opposed experimental results regarding the operative slip planes (e.g., Erickson, 1962; Hull, 1963; Takeuchi and Ikeda, 1963). Therefore all planes with low indices will be investigated, however, for the simulation attention is restricted to the two slip families $\{110\}$ and $\{112\}$.

The goal of this study is to model and understand the experimentally obtained results of a bcc Fe-3%Si thin-sheet sample with large grains loaded incrementally in tension (Henning and

Vehoff, 2005) by a step by step procedure. To understand each mechanism in the simulation as a first step we restrict ourselves to a simple phenomenological constitutive crystal-plasticity model for ideal viscoplasticity. To get an idea how and where geometrically necessary dislocations develop inside the microstructure which may lead to strain hardening we are investigating the development of GNDs and the orientation gradient for different simulations with different active slip families. In addition to a short investigation of the deformation behavior a comparison between the experimentally and simulativly obtained orientation gradient is performed. As a next step hardening is included and comparisons to the case without hardening are made.

The paper is organized as follows. First the used material model for crystal plasticity is shortly presented. In the next section the experimental results from Henning and Vehoff (2005), the construction of the FE-model and the concepts of GNDs and OGM are discussed. Next the results from experiment and simulation without and with hardening contribution are compared and discussed in the context of their deformation behavior and the evolution of orientation gradients, GNDs and orientation changes during deformation. The paper concludes with a summary and outlook.

4.2 Model formulation for single-crystal plasticity

In the case of crystal plasticity the perfect single crystal is often used as reference state, however, it is also possible to choose any state just before deformation or any state at any time t in an incremental setting. The deformation gradient can be decomposed into an elastic $\boldsymbol{F}_\mathrm{E}$ and plastic part $\boldsymbol{F}_\mathrm{P}$ called the Kröner decomposition (Kröner, 1961)

$$\boldsymbol{F} = \boldsymbol{F}_\mathrm{E}\boldsymbol{F}_\mathrm{P} \tag{4.1}$$

which is schematic illustrated in Figure 4.1. $\boldsymbol{F}_\mathrm{E}$ is the elastic deformation component which

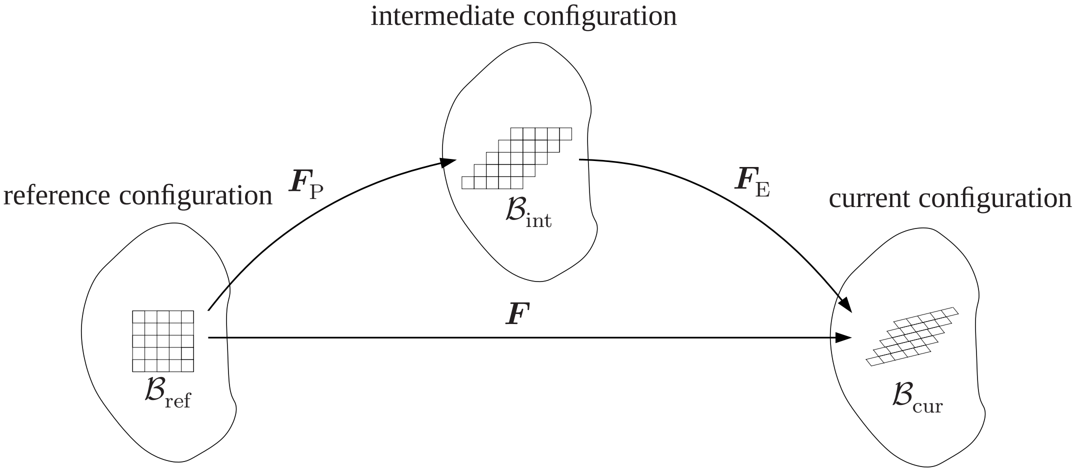
intermediate configuration
reference configuration
$\boldsymbol{F}_\mathrm{P}$
$\mathcal{B}_\mathrm{int}$
$\boldsymbol{F}_\mathrm{E}$
current configuration
$\boldsymbol{F}$
$\mathcal{B}_\mathrm{ref}$
$\mathcal{B}_\mathrm{cur}$

Figure 4.1: Decomposition of the total deformation gradient

represents the local elastic distortion of a material due to stretch and rotation of the microscopic structure. $\boldsymbol{F}_\mathrm{P}$ is the plastic distortion which represents the local deformation due to the flow of defects through the microscopic structure which is an irreversible permanent deformation.

Therefore the transformation of the reference state by $\boldsymbol{F}_{\mathrm{P}}$ leads to an intermediate configuration. Investigating the crystal lattice in the different configuration as shown in Figure 4.1, the transformation via $\boldsymbol{F}_{\mathrm{P}}$ from the reference to the intermediate configuration renders the lattice unchanged and all the deformation is produced by dislocation slip. The plastic deformation is assumed to be volume preserving which means $\det \boldsymbol{F}_{\mathrm{P}} = 1$. During the transformation from the intermediate configuration to the current one via $\boldsymbol{F}_{\mathrm{E}}$, the lattice undergoes a purely elastic shape change (Roters et al., 2010).

The corresponding stress algorithm for this model is based on the Green measure

$$\boldsymbol{E}_{\mathrm{E}}(\boldsymbol{F}_{\mathrm{E}}) = \frac{1}{2}\left(\boldsymbol{F}_{\mathrm{E}}^{\mathrm{T}}\boldsymbol{F}_{\mathrm{E}} - \boldsymbol{I}\right) \tag{4.2}$$

of elastic strain. The corresponding stress can be calculated by the general relation

$$\boldsymbol{K} = \boldsymbol{F}_{\mathrm{E}}\boldsymbol{S}_{\mathrm{E}}\boldsymbol{F}_{\mathrm{E}}^{\mathrm{T}} \tag{4.3}$$

for the current Kirchhoff stress $\boldsymbol{K}$ in terms of the corresponding elastic second Piola-Kirchhoff stress

$$\boldsymbol{S}_{\mathrm{E}} = \boldsymbol{S}_{\mathrm{E}}(\boldsymbol{E}_{\mathrm{E}}, \ldots) \tag{4.4}$$

and $\boldsymbol{F}_{\mathrm{E}}$. In terms of small elastic strains relevant for metals the approximation $\boldsymbol{M} \approx \boldsymbol{S}_{\mathrm{E}}$, i.e., of the Mandel stress by the elastic second Piola-Kirchhoff stress holds true. The Mandel stress can then be calculated by

$$\boldsymbol{M}(\boldsymbol{E}_{\mathrm{E}}) \approx \mathcal{C}_{\mathrm{E}\,0}\boldsymbol{E}_{\mathrm{E}} \tag{4.5}$$

where $\mathcal{C}_{\mathrm{E}\,0}$ is the fourth order elasticity tensor.

Basic to almost all large-deformation inelastic model formulations is the general form $\dot{\boldsymbol{F}}_{\mathrm{P}} = \boldsymbol{L}_{\mathrm{P}}\boldsymbol{F}_{\mathrm{P}}$ for the evolution of the local inelastic deformation $\boldsymbol{F}_{\mathrm{P}}$ in terms of the inelastic "velocity gradient" $\boldsymbol{L}_{\mathrm{P}}$. As usual, the a^{th} glide system is represented by the corresponding glide direction $\boldsymbol{s}_a$, glide-plane normal $\boldsymbol{n}_a$, and direction transverse $\boldsymbol{t}_a := \boldsymbol{n}_a \times \boldsymbol{s}_a$ to $\boldsymbol{s}_a$ in the glide plane. As usual, $(\boldsymbol{s}_a, \boldsymbol{t}_a, \boldsymbol{n}_a)$ represent an orthonormal system and are assumed constant with respect to the local intermediate configuration as determined by $\boldsymbol{F}_{\mathrm{P}}$. In addition, they determine its evolution the constitutive form

$$\boldsymbol{L}_{\mathrm{P}} = \sum\nolimits_{a=1}^{\mathfrak{a}} \dot{\gamma}_a\, \boldsymbol{s}_a \otimes \boldsymbol{n}_a \tag{4.6}$$

for $\boldsymbol{L}_{\mathrm{P}}$ in terms of the active glide-system shears $\gamma_1, \gamma_2, \ldots, \gamma_{\mathfrak{a}}$, with $\mathfrak{a} \leqslant \mathfrak{g}$ the number of active systems, and $\mathfrak{g}$ the total number of systems. The Schmid stress is given by

$$\tau_a := \boldsymbol{s}_a \cdot \boldsymbol{M}\boldsymbol{n}_a\,. \tag{4.7}$$

The viscoplastic flow rule is formulated according to Kalidindi et al. (1992)

$$\dot{\gamma}_a = \dot{\gamma}_0 \left|\frac{\tau_a}{\hat{\tau}_a}\right|^m \mathrm{dir}(\tau_a)\,. \tag{4.8}$$

Here the notation $\mathrm{dir}(a) := a/|a|$ is used. $\dot{\gamma}_0$ represents a characteristic strain-rate associated with dislocation motion and $\hat{\tau}_a$ the energetic or athermal slip resistance is determined via (Asaro and Needleman, 1985)

$$\dot{\hat{\tau}}_a = \sum\nolimits_{b=1}^{\mathfrak{a}} q_{ab}\, h_b(\hat{\tau}_b)\, |\dot{\gamma}_a|\,. \tag{4.9}$$

q_{ab} is the hardening matrix which describes the rate of strain hardening on slip system a due to a shearing on the slip system b by

$$q_{ab} = \begin{bmatrix} 1 & q_0 & \cdots & q_0 \\ q_0 & 1 & \cdots & q_0 \\ \vdots & \vdots & \ddots & \vdots \\ q_0 & \cdots & q_0 & 1 \end{bmatrix}$$

in which $q_0 = 1.4$ represents the ratio of latent to self-hardening. Following Brown et al. (1989); Kalidindi et al. (1992), we consider the following form for the single slip hardening rate

$$h_b(\hat{\tau}_b) = h_0 \, (1 - \hat{\tau}_b/\hat{\tau}_0^{\mathrm{sat}})^{n_0} \tag{4.10}$$

Here, h_0 is the initial hardening rate, $\hat{\tau}_0^{\mathrm{sat}}$ the saturation value of $\hat{\tau}_b$, and n_0 is the hardening exponent.

The numerical implementation is based on an explicit algorithmic formulation as based on forward-Euler integration. Details about this explicit formulation can be taken from section 3.3.

4.3 Experimental and simulation methods

4.3.1 Experimental results

The tensile test sample was laser-cut from Fe-3%Si sheets (BCC) with a thickness of 1 mm. The gauge length is about 5 mm in width and 15 mm in length. The mean grain size is about 2 mm which is of the order of the sheet thickness. In the case of the largest mean grain size of approximately 5 mm, the grains are of the order of the specimen geometry. As explained in section 3.5 all size effects due to processing were tried to be avoided as best as possible. Furthermore the experiments did not show any indication of these size effects.

The experimental results (Henning and Vehoff, 2005) concerning the properties of the sample (deformation, local orientation) are determined at several stages, namely at plastic strains of $\alpha_{\mathrm{P}} \approx \{0\%, 1.5\%, 4\%, 10\%, 19.5\%\}$. In Figure 4.2 the results of the orientation gradient measurement are displayed at the deformed shape. The calculation of the orientation gradient at points with improper orientation measurements was omitted, and the corresponding points in Figure 4.2 are represented in black. The concept of the orientation gradient will be discussed in section 4.3.5. The results obtained by experiment contain only information concerning the surface. This is assumed to be sufficient as in the experiment the grain boundaries remain nearly perpendicular to the sample surface. At the grain boundaries, contraction perpendicular to the sample surface seems to be negligible, which agrees with the results in Stölken and Evans (1998). Therefore no investigation concerning the contraction in the third dimension will be done in the following and only results obtained at the sample surface are presented. The orientations of the grains are obtained with electron backscatter diffraction (EBSD) using OIM. These are used as initial orientation in the finite element model.

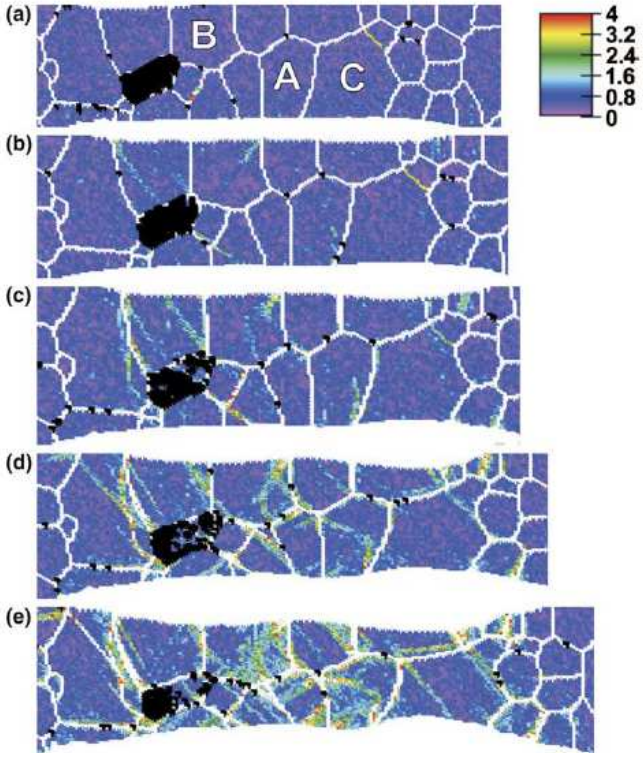

Figure 4.2: (a)(e) Orientation gradient max(θ_x,θ_y) in (°) for $\alpha_\mathrm{P} \approx \{0\%, 1.5\%, 4\%, 10\%, 19.5\%\}$. The regions in black indicate failure of automatic orientation estimation. (Henning and Vehoff, 2005).

4.3.2 Finite element model

The measured two-dimensional grain structure and the grain orientations were used to construct a finite-element model. The grain boundary segments between two grain boundary triple junctions were approximated as planes perpendicular to the sample surface. In order to model the experimental setup more closely at either end of the tensile specimen transition areas are introduced. These are modeled using a simple isotropic elastic material model. This reduces the boundary effects in the simulation by applying the tensile loading at the surrounding area (Zisman and Rybin, 1998). It was observed that defects such as slip lines can start from grain boundaries and edges of the sample (Polcarova et al., 1998). The fact that neighboring grains do not share the same orientation and grain boundaries are not necessarily parallel to the local crystallographic axes in combination with the anisotropic elastic behavior may induce an inhomogeneous stress field within a single grain (Vehoff and Nykyforchyn, 2003). Therefore the model has to be set up in 3D which is done by simple extrusion of the 2D geometry. The resulting FE-mesh is shown in Figure 4.3 which consists of 18657 brick (8-node) elements. The grain orientations found by EBSD are accounted for via initialization of the state dependent variables (SDVs). The simulations are performed with the FE software ABAQUS using material routines which are implemented via the UMAT and UEL interface in ABAQUS/Standard. In what follows the numbering shown in Fig.4.3 will be used for clarity.

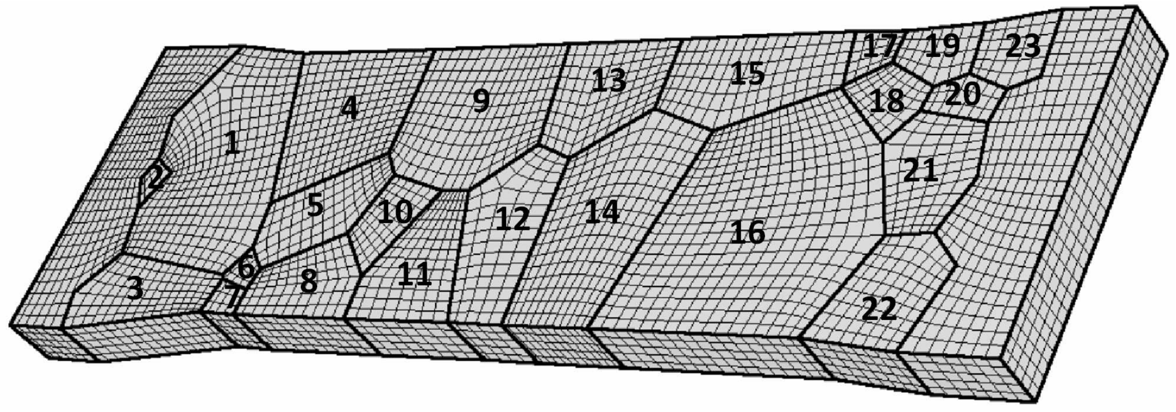

Figure 4.3: FE mesh used for simulations with grains numbered (Henning, 2008).

4.3.3 Fe-3%Si

It is assumed that the general mode of deformation in the silicon iron alloy is slip and that the presence of mechanical twinning is negligible. As reported in Gell and Worthington (1966) mechanical twinning occurs for fine-grained material below 180°K and for coarse grained above 320°K. Noble and Hull (1965) also did not observe any twinning and strain ageing effects in tensile tests at 293°K on Fe-3$\%$Si. The presented experimental results were obtained at room temperature and therefore mechanical twinning as well as strain ageing effects are not further considered. In the following the glide systems $\{110\}\langle 111\rangle$ and $\{112\}\langle 111\rangle$ are investigated by finite element simulations using single glide system class or combinations thereof actively. In section 4.4 also the $\{123\}$ slip plane will be considered regarding the Schmid factor where it is shown that their values are much lower compared to $\{110\}$ and $\{112\}$ and therefore not preferable for slip.

The used elastic constants for Fe-3%Si are taken from Routbort et al. (1971) (see Table 4.1). The hardening parameters in Table 4.2 are taken from section 3.4 which were identified based on experimental data from Hull (1963) using an inverse FE-optimization strategy.

$C_{\mathrm{E},11}$ [GPa]	$C_{\mathrm{E},12}$ [GPa]	$C_{\mathrm{E},44}$ [GPa]
222	135	120

Table 4.1: Material properties of Fe-3%Si (BCC) (Routbort et al., 1971).

$\hat{\tau}_0$ [MPa]	$\dot{\gamma}_0$ [s^{-1}]	m [-]	h_0 [MPa]	$\hat{\tau}_0^{\mathrm{sat}}$ [MPa]	n_0 [-]
161	0.001	20	243.9	1137	0.48

Table 4.2: Material properties of hardening of Fe-3%Si (BCC) fitted to the experimental results of Hull (1963).

4.3.4 *Geometrically necessary dislocations (GNDs)*

During plastic deformation, two types of dislocation occur. One type are the statistically stored dislocations (SSDs) which are accumulated by a random trapping process and are not considered here in detail. The second type of dislocations are the geometrically necessary dislocations (GNDs) which are stored due to the locally heterogeneous plastic shear. The first concepts of GNDs were introduced by Nye (1953) and Ashby (1970) to account for modes of plastic deformation, where an internal accumulation of a density of dislocations is required to accommodate the gradients of plastic strain induced by the deformation such as bending (Needleman and Sevillano, 2003), therefore GNDs are necessary to preserve lattice compatibility.

The simplest class of models for dislocation evolution is obtained for the case of self-interaction, i.e., the dislocations on each glide system interact only with themselves, not with those of other systems. Restricting to edge GNDs alone, a common self-interaction-based constitutive model is given by the evolution

$$\dot{\varrho}_a = -\bar{\boldsymbol{s}}_a \cdot \nabla \dot{\gamma}_a \tag{4.11}$$

at small deformation consistent with the model of Ashby (1970) in terms of the glide-system Burgers vector $\bar{\boldsymbol{s}}_a := b\,\boldsymbol{s}_a$. Here the dislocation density ϱ is expressed in a non-dimensional form $\varrho := b^2\,\rho$ with the help of the magnitude b of the Burgers vector. Since $\bar{\boldsymbol{s}}_a$ is by definition constant, the relation (4.11) can be integrated in time to yield the algebraic form

$$\varrho_a - \varrho_{a0} = -\bar{\boldsymbol{s}}_a \cdot \nabla \gamma_a \,, \tag{4.12}$$

assuming $\bar{\boldsymbol{s}}_a \cdot \nabla \gamma_{a0} = 0$. Generalization of this kind of relation to large deformation is often explicitly or tacitly based on the constitutive assumption of form-invariance. As shown in Gurtin (2008); Kuroda and Tvergaard (2008); Svendsen and Bargmann (2010) on this basis (4.12) generalizes to

$$\varrho_a - \varrho_{a0} = -\boldsymbol{F}_{\mathrm{P}}^{-1}\bar{\boldsymbol{s}}_a \cdot \nabla_0 \gamma_a \,, \tag{4.13}$$

which can be rewritten to

$$\varrho_a - \varrho_{a0} = -\boldsymbol{F}_{\mathrm{E}}\bar{\boldsymbol{s}}_a \cdot \nabla_c \gamma_a \,, \tag{4.14}$$

where ∇_0 or ∇_c describe the spatial gradient with respect to the reference or current configuration, respectively. Here the relation

$$\nabla_c \gamma_a = \boldsymbol{F}^{-T} \nabla_0 \gamma_a \tag{4.15}$$

between the slip gradients is used. In the following ϱ_{a0} is assumed to be zero.

4.3.5 *Orientation gradient mapping (OGM)*

Dislocations are generated by plastic deformation which may be stored or leave the specimen or annihilate. These phenomena occur inhomogeneously inside the microstructure. E.g., Kovács and Zsoldos (1973) derived strain hardening laws from interaction processes of dislocations which implies that strain hardening is connected with the increase in dislocation density. As stated before GNDs are necessary to preserve lattice compatibility. Therefore dislocations lead to local orientation changes in the crystal lattice (e.g. Sedláček et al., 2001). Roughly speaking the higher the dislocation density the higher the expected misorientation.

Henning and Vehoff (2005) introduced a method to investigate the local orientation gradient, called Orientation gradient mapping (OGM). OGM describes the orientation gradient between two neighboring measurement points in x-direction via

$$\Delta\theta_x = \min|\arccos(\frac{1}{2}\mathrm{tr}\{\boldsymbol{R}_{\mathrm{E},x}\,\boldsymbol{R}^{\mathrm{T}}_{\mathrm{E},x+1}\,\boldsymbol{O}^{\mathrm{T}}_{\mathrm{C}} - 1\})| \tag{4.16}$$

as well as for the y-direction $\Delta\theta_y$, respectively. $\boldsymbol{O}_{\mathrm{C}}$ describes the orientation matrix for all 24 symmetry matrices of cubic symmetry. In the following we use the definition

$$\Delta\theta_\infty = \max\{\Delta\theta_x, \Delta\theta_y\}. \tag{4.17}$$

The advantage of the use of OGM is the distinct quantitative representation of the local misorientations by which the result is independent from the surrounding area. For further details about the OGM see Welsch et al. (2007) and Henning and Vehoff (2010).

4.4 Determination of Schmid and Taylor factors

For the prediction which slip system is preferred to become active during deformation the Schmid and Taylor factors are valid indicators. Assuming a test loading direction $\boldsymbol{l}$ in the sample coordinate system for macroscopic uniaxial tension with which follows for the Kirchhoff stress

$$\boldsymbol{K} = K\boldsymbol{l}\otimes\boldsymbol{l}\ .$$

The Mandel stress can be written as

$$\boldsymbol{M} = \boldsymbol{R}^{\mathrm{T}}_{\mathrm{E}}\boldsymbol{K}\,\boldsymbol{R}_{\mathrm{E}} = M\boldsymbol{l}'\otimes\boldsymbol{l}'\ , \tag{4.18}$$

where

$$\boldsymbol{l}' = \boldsymbol{R}^{\mathrm{T}}_{\mathrm{E}}\boldsymbol{l}$$

describes the loading direction rotated into the crystal system. The Schmid stress can be rewritten to

$$\tau_a = S_{\mathrm{fac},a}M\ , \tag{4.19}$$

where $S_{\mathrm{fac},a}$ describes the Schmid factor for each glide system which can be calculated by

$$S_{\mathrm{fac},a} = (\boldsymbol{n}_a\cdot\boldsymbol{l}')(\boldsymbol{s}_a\cdot\boldsymbol{l}')\ . \tag{4.20}$$

To predict the behavior of one single grain all Schmid factors of one glide system class have to be averaged in some way. Here the following definition has been used

$$S_{\mathrm{fac,avg}} = \frac{\sqrt{\sum_a S^2_{\mathrm{fac},a}}}{\text{number of slip planes}} \tag{4.21}$$

as an average of all Schmid factors for the particular glide system class where the ”number of slip planes” is 12 for $\{110\}$ and $\{112\}$ and 24 for $\{123\}$.

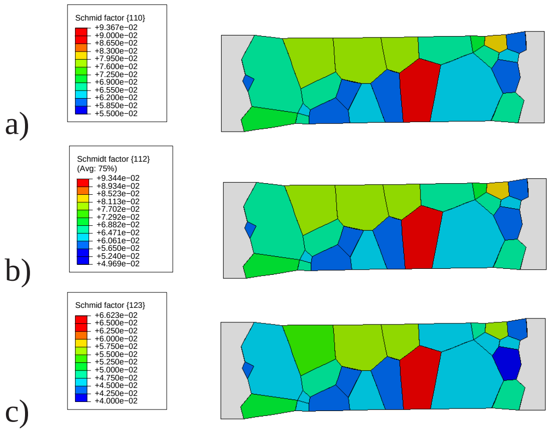

Figure 4.4: Averaged Schmid-factor $S_{\text{fac,avg}}$ in the single grains for a) $\{110\}\langle 111\rangle$ and b) $\{123\}\langle 111\rangle$ glide system for a test-loading in $[010]$ direction for the initial specimen. The same qualitative results as for $\{110\}\langle 111\rangle$ are obtained for $\{112\}\langle 111\rangle$ glide systems

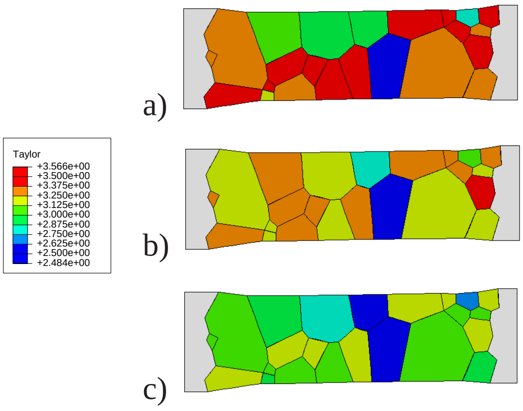

Figure 4.5: Taylor-factor T in the single grains for a) $\{110\}\langle 111\rangle$, b) $\{112\}\langle 111\rangle$ and c) $\{110\}\langle 111\rangle$ and $\{112\}\langle 111\rangle$ glide systems for a test-loading in $[010]$ direction.

In Fig. 4.4 the averaged Schmid factors are shown for single grains showing that slip on $\{110\}$ and $\{112\}$ planes is much more favorable than on $\{123\}$ due to higher Schmid factors. However, the distribution in the single grains looks quite similar for $\{110\}$, $\{112\}$ and $\{123\}$. The magnitude of the Schmid factor as well as its distribution are nearly identical between $\{110\}$ and $\{112\}$. For all cases the highest value for the averaged Schmid factor $S_{\text{fac,avg}}$ occurs in grain 14 (cf. Figure 4.3) which is 20% higher than in any other grain. Therefore the highest amount of slip at the beginning as well as the earliest slip in the structure is expected to occur in grain 14. Grain 12 direct next to it has one of the lowest Schmid factors and is therefore unfavorable for slip which could lead to a sharp gradient in stress and slip activity between both grains and to stress concentrations. The grains at the upper border (4, 9, 13, 15) all show a quite similar Schmid factor $S_{\text{fac,avg}}$. This indicates that the deformation might be more homogeneous at the beginning in this area, however, the deformation of other grains, like grain 14, influences the deformation field.

Besides the Schmid factor as an indicator for plastic slip inside the grains the Taylor factor is often used. Taylor (1938) postulates that slip systems are only active during plastic deformation which minimizes the internal work. The Taylor factor T is defined (e.g., Rosenberg and Piehler, 1971) by

$$T = \frac{\sum_i |\gamma_i|}{E} \tag{4.22}$$

where E is the applied amount of tensile or compressive strain on the sample whereas according to the assumption of Taylor each crystal undergoes the same deformation (Taylor, 1938). Details about the calculation can be found, e.g., in Bunge (1970); Chin and Mammel (1967).

Figure 4.5 shows the resulting Taylor factors for solely $\{110\}\langle 111\rangle$ or $\{112\}\langle 111\rangle$ glide systems active as well as a combination of both. The results correspond quite well with the

Schmid factors. The lowest Taylor factor is calculated in grain 14. The results for $\{110\}\langle 111\rangle$ or $\{112\}\langle 111\rangle$ differs only locally but the Taylor factors are quite similar. For simultaneously active glide systems the Taylor factors are lower than for single systems which is in agreement with reported results in the literature (e.g., Chin and Mammel, 1967; Rosenberg and Piehler, 1971). According to the evaluation of the distribution of the Taylor factors the prefered grains for slip would be grain 13 and 14. However, these are only single factors for indicating plastic slip. In order to achieve a better understanding and to check these assumptions the experimental results are compared to simulation results obtained for different sets of active glide systems.

4.5 Results

4.5.1 Without hardening

In this section experimental results are compared to simulation results for different sets of glide systems active performed for ideal viscoplasticity. Figure 4.6 shows $\|\mathrm{mag}(\boldsymbol{L}_\mathrm{P})\|$ at different values of α_P. $\boldsymbol{L}_\mathrm{P}$ describes the plastic part of the velocity gradient and therefore $\|\mathrm{mag}(\boldsymbol{L}_\mathrm{P})\|$ is a measure for the plastic flow occurring between two time steps. Thus it represents a valid indicator for activity of glide systems in the actual deformation step. In Figure 4.6 the shape changes of the grains are depicted. The actual value of $\|\mathrm{mag}(\boldsymbol{L}_\mathrm{P})\|$ is of minor importance for the interpretation, however, it controls the time step in the simulation due to the explicit integration scheme at the integration point level.

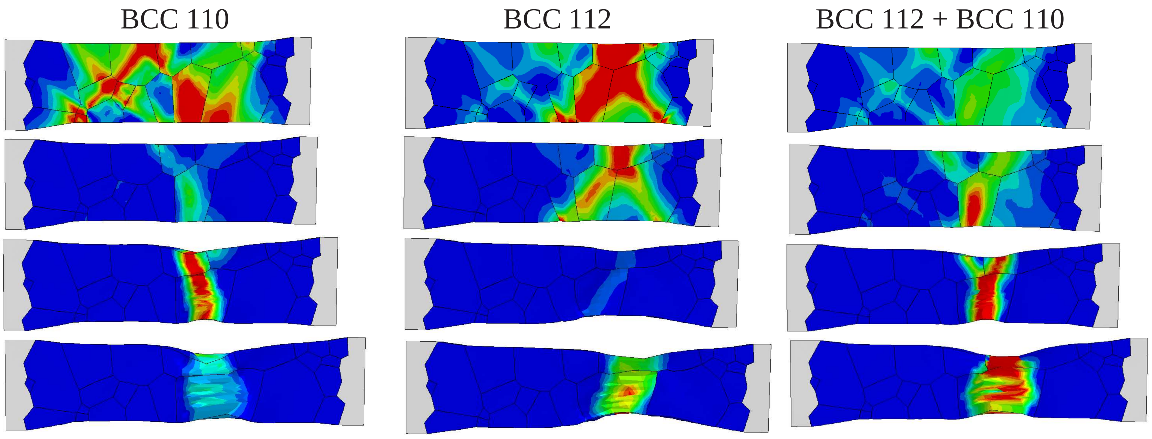

Figure 4.6: Simulation results without hardening for $\|\mathrm{mag}(\boldsymbol{L}_\mathrm{P})\|$ for $\alpha_\mathrm{P} \approx \{1.5\%, 4\%, 10\%, 19.5\%\}$ for active glide system $\{112\}$+$\{110\}$(left) or $\{112\}$(middle) alone or $\{110\}$(right) alone, respectively. The legend is constant for all deformation stages. (red=$10^{-6}s^{-1}$, blue=$0s^{-1}$)

It can be seen that in the beginning the same level of plastic flow occurs in several grains for both sets of glide system classes at the current time step. Local differences between the results of the different sets of active glide system classes are visible whereas the main deformation predicted for all simulations occurs in grain 14. However, it is impossible to identify which exact slip systems of the glide system classes are active at the analyzed deformation step after most of the systems are already active. Once a slip system is active, it will remain active for a longer period. Due to the different initial orientation every grain behaves differently under the prescribed loading condition $l = [0\,1\,0]$ which was analyzed with respect to the Schmid and Taylor factor in section 4.4. With the system active, however the amount of plastic slip will be completely different in two grains after a certain time. After a small deformation of $\alpha_\mathrm{P} \approx 4\%$ a localization zone is identifiable where the deformation is mainly concentrated. This does not change in the further deformation stages whereas a slip band becomes more precisely visible.

Simulations for the case of active $\{112\}\langle 111\rangle$ glide system class show a higher contraction than for simulations with active $\{110\}\langle 111\rangle$ glide system class. In particular the deformation in grain 15 and 16 in the beginning indicates that a deformation may occur by active $\{112\}\langle 111\rangle$ glide systems in the mesocrystal. The simulation with an active $\{110\}\langle 111\rangle$ glide system class shows a very high elongation of grain 14 compared to experiment. The results for a simulation with slip on $\{110\}$ and $\{112\}$ planes simultaneously show a slight dominance of the $\{110\}\langle 111\rangle$ glide system class. However, the results for both systems active differ significantly from the results for one single glide system class active, e.g., for the deformation behavior of grain 13. This implies that neither of these set of glide systems might be neglected in the simulation to obtain more realistic results.

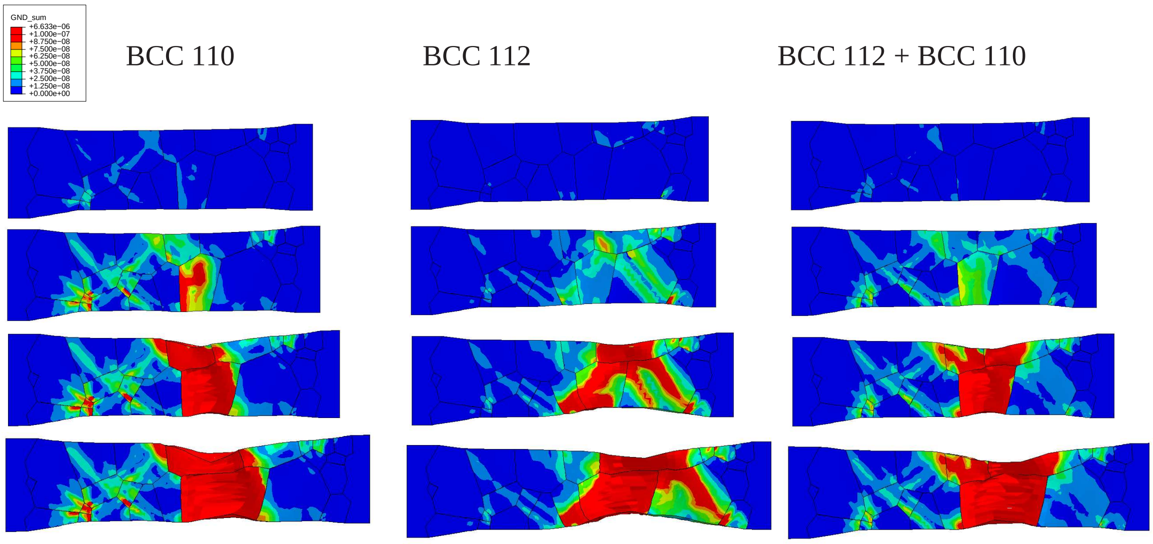

Figure 4.7: Sum of GND densities $\sum_a \varrho_a$ of all systems without hardening for $\alpha_\mathrm{P} \approx \{1.5\%, 4\%, 10\%, 19.5\%\}$ for active glide systems $\{112\}$+$\{110\}$(left) or $\{112\}$(middle) alone or $\{110\}$(right) alone, respectively.

As a first step in further understanding and modeling the material behavior of the mesocrystal the development of GNDs is analyzed in detail which could later be used as internal variables, i.e., to describe the strain hardening behavior (e.g. Ekh et al., 2007; Taylor, 1934). The sum of the GNDs densities $\sum_a \varrho_a$ over all 12 or 24 glide systems, respectively, is shown in Figure 4.7. By definition it is clear that the highest concentration of GNDs occur in the region where the main deformation occurs. Especially at the beginning of the deformation this can clearly be identified by comparing Fig. 4.6 at $\alpha_\mathrm{P} \approx 1.5\%$ with Fig. 4.7 at $\alpha_\mathrm{P} \approx 4\%$. However, this relation is more complex because the development of the GNDs depends on the gradient of the slip and not directly on the slip. GNDs are required to accommodate the gradient of plastic slip. The highest GND densities are achieved at grain boundaries where the highest slip gradients occur. With evolving slip band the GND density inside grain 13 and 14 is strongly increasing which indicates a strong strain hardening potential in this region.

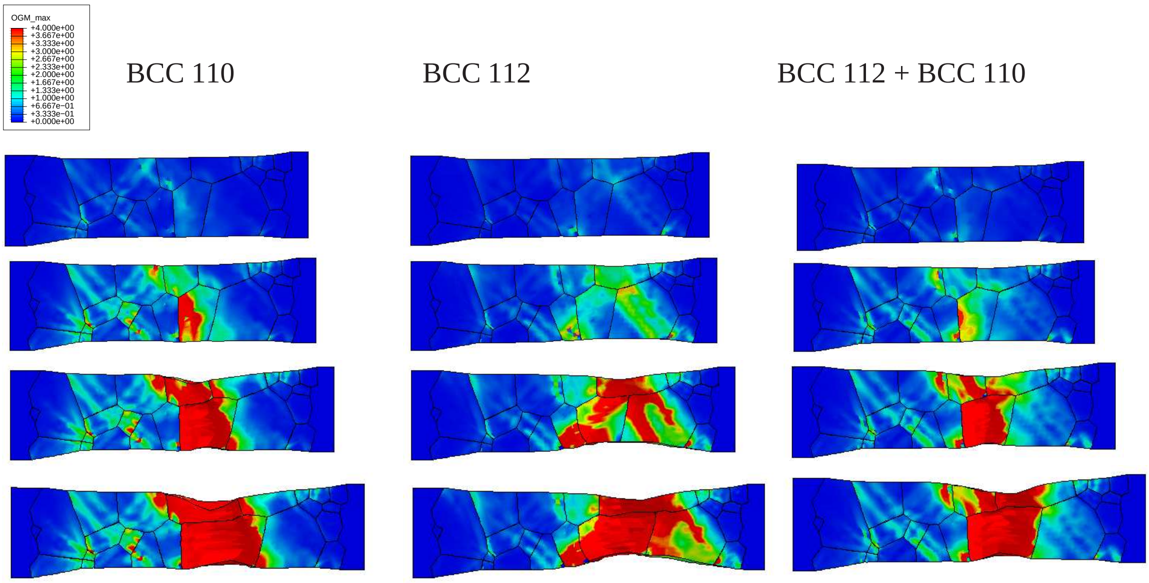

Figure 4.8: Orientation gradient for $\Delta\theta_\infty$ in ° for $\alpha_\mathrm{P} \approx \{1.5\%, 4\%, 10\% \; 19.5\%\}$ for active glide systems $\{112\}$ and $\{110\}$ without hardening.

The experimental results of the OGM were shown incorporated in Figure 4.2. Figure 4.8 shows the results for the orientation gradient mapping for the simulations without hardening which were calculated in the post-processing. As it can be seen by comparison with Figure 4.2 the simulation cannot predict the correct tendency for the OGM in the experiment. This leads to the conclusion that further effects like hardening have to be included to produce more realistic results. Further the direct correlation between the OGM and the evolution of the GND can be seen by comparing the results to Figure 4.7. As mentioned before GNDs are necessary to preserve lattice compatibility. Therefore it has to be noted that dislocations lead to local orientation changes in the crystal lattice (e.g. Sedláček et al., 2001).

The corresponding reorientation field β_{n+1} with respect to the reference configuration can be calculated by

$$\beta_{n+1} := \min \left| \arccos \left(\frac{1}{2} \left[\mathrm{tr}(\boldsymbol{R}_{\mathrm{E}\,n+1} \, \boldsymbol{R}^T_{\mathrm{E}\,0} \, \boldsymbol{O}^{\mathrm{T}}_{\mathrm{C}}) - 1 \right] \right) \right|, \tag{4.23}$$

where $\boldsymbol{R}_{\mathrm{E}\,n+1}$ is obtained by polar decomposition of $\boldsymbol{F}_{\mathrm{E}\,n+1}$ and $\boldsymbol{R}_{\mathrm{E}\,0}$ is given by the initial orientation. Figure 4.9 shows the calculated reorientation field. By comparing the results to Fig. 4.7 a dependency between the GNDs and local orientation changes could be anticipated. However, as results later will show this might not always be the case. Again, it has to be considered here that the grains in this simulation are modeled as ideally viscoplastic and therefore no hardening occurs. Furthermore the results above $\alpha_\mathrm{P} \approx 15\%$ have to be evaluated carefully due to an occurring shear band and resulting distorted elements. In the region of the shear band the elements have bad aspect ratios and become distorted so that the results are not reliable anymore. However, due to the explicit time integration scheme of the material routine at the

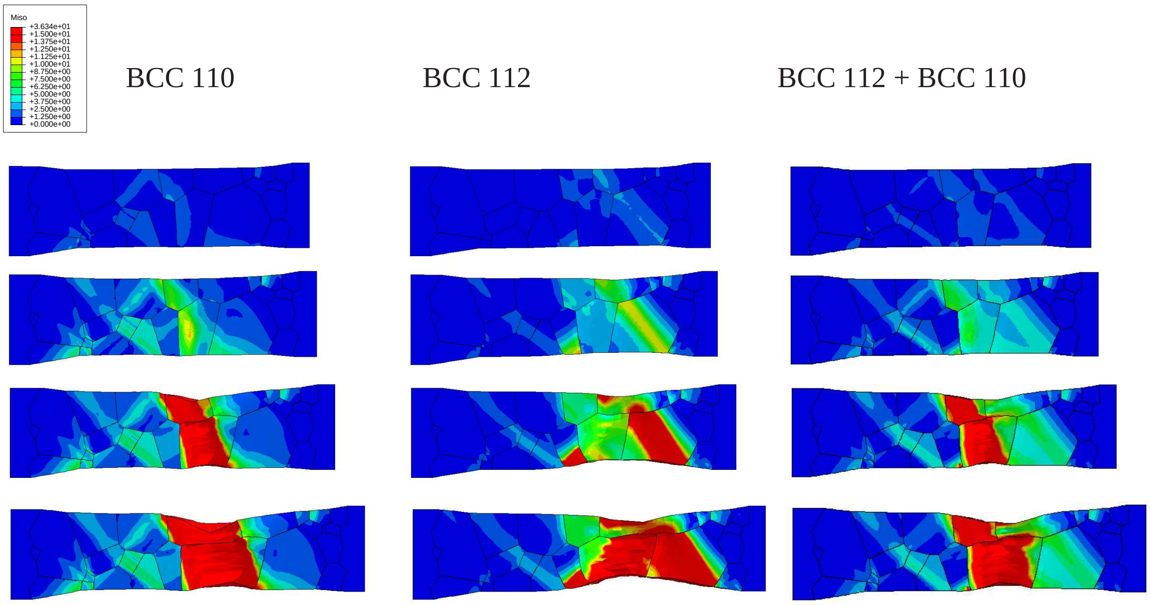

Figure 4.9: Reorientation field β in ° for $\alpha_{\mathrm{P}} \approx \{1.5\%, 4\%, 10\%, 19.5\%\}$ for active glide systems $\{112\}$+$\{110\}$(left) or $\{112\}$(middle) alone or $\{110\}$(right) alone, respectively, without hardening.

integration point level the simulation is stable and does not abort but the necessary time step for the simulation is becoming very small. To ensure a good element quality, remeshing techniques have to be used in future work.

In conclusion the first simulation results with ideal viscoplasticy already show a good tendency to experimental results. This indicates that the correct prediction of initially active slip systems is a very important effect. The previously calculated Schmid and Taylor factors predicted mainly the correct grain activity. However, further results like the orientation gradient in the experiment could not be predicted correctly in simulations without hardening.

4.5.2 With hardening

In the following the deformation behavior of the structure for an activated hardening law, as stated in section 4.2, is investigated. The material parameters identified for the used hardening law can be found in section 4.3.2. All simulations are carried out for the slip systems $\{110\}\langle 111\rangle$ and $\{112\}\langle 111\rangle$ active separately and simultaneously. For both systems active simultaneously for simplicity no coupling between these two glide system classes is assumed which is done by setting the coupling terms in the hardening matrix q_{ab} to zero.

In Figure 4.10 the distribution for $\|\mathrm{mag}(\boldsymbol{L}_{\mathrm{P}})\|$ is shown for different combinations of glide systems active on the deformed shape. Comparing the shape of the simulation results with hardening with the experimental ones in Figure 4.2 show a very good agreement to the experiment, leading to an improvement compared to the results without hardening. However, the largest contraction in the experiment between grain 15 and 16 is not represented by the simulations. The distribution for $\alpha_{\mathrm{P}} \approx 1.5\%$ is very similar to the results in the simulation without hardening as shown in Figure 4.6. Note that the value of the deformation rate is not important but rather its

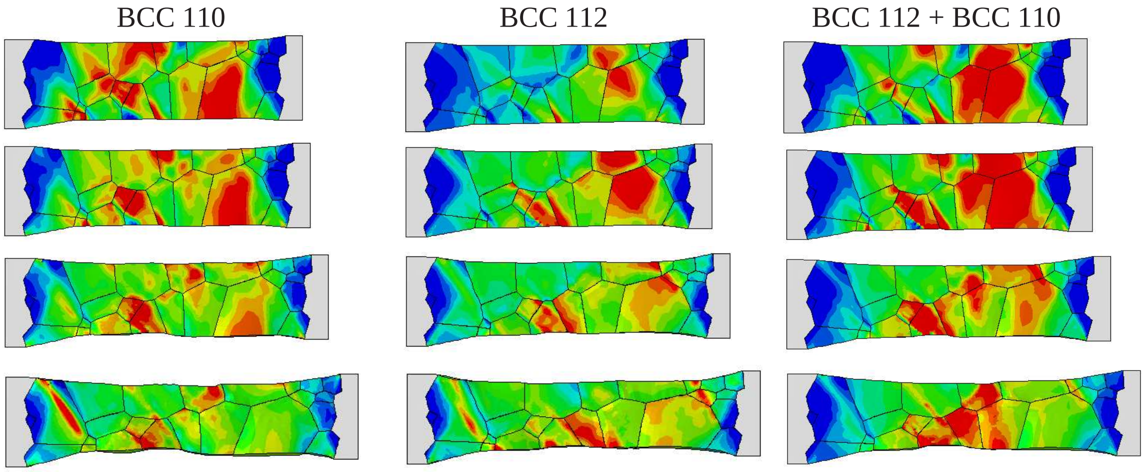

Figure 4.10: Simulation results for $\|\mathrm{mag}(\boldsymbol{L}_{\mathrm{P}})\|$ for $\alpha_{\mathrm{P}} \approx \{1.5\%, 4\%, 10\%, 19.5\%\}$ for glide systems $\{112\}$ and $\{110\}$ simultaneously and separately active with included hardening. The legend is constant for all deformation stages. (red=$10^{-6}s^{-1}$, blue=$0s^{-1}$)

distribution. For larger deformation the results between the two groups of simulations deviate. The simulations without hardening show a localization in grain 14 and 15 whereas the simulations with hardening show a high activity in many grains. In the beginning for all simulations with hardening a high activity in grain 15 and 16 can be observed which is decreasing with increasing deformation. The results for both glide systems active show neither a dominance of the $\{110\}$ nor $\{112\}$ systems. In the end the main deformation takes place in grains 11, 12, 13 and 14. However, also the surrounding grains do not stop deforming plastically for $\alpha_{\mathrm{P}} \approx 19.5\%$ which was the final investigated strain.

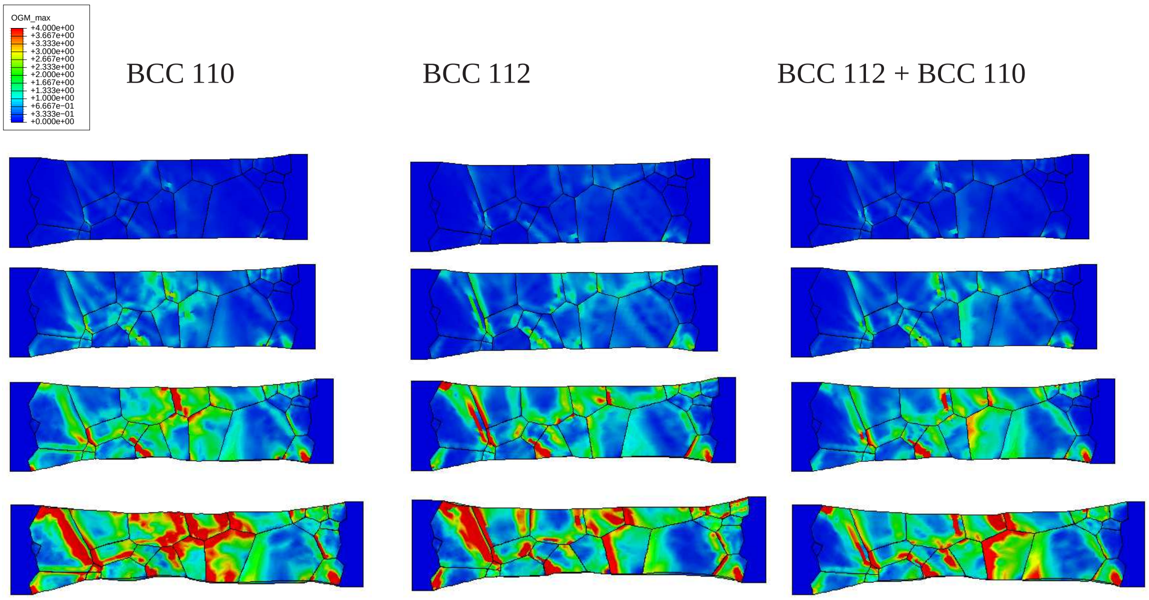

Figure 4.11: Orientation gradient for $\Delta\theta_{\infty}$ in ° for $\alpha_{\mathrm{P}} \approx \{1.5\%, 4\%, 10\%\, 19.5\%\}$ for active glide systems $\{112\}$ and $\{110\}$ with included hardening.

Figure 4.11 shows the simulatively obtained OGM results for simulation with hardening. As it can be seen by comparison to the experiment the simulation results with hardening show a much closer prediction than the simulation results without hardening. A lot of the experimental details of the OGM can also be seen in all the simulations, e.g.,

- the high gradient band at the boundary between grain 1 and 4 is predicted correctly,
- the gradient band at the boundary between grain 1 and 3 is predicted correctly in the $\{110\}$ case,
- the correct distribution in grain 9 and 14,
- the correct tendency in the grains 15 and 16 although the bands are not that fine and clear,
- correct tendency in the grains 17 and 19.

This shows that all simulations with hardening show a good tendency to the experiment, however, based on these results it is not possible to anticipate if one single glide system class is dominant or required.

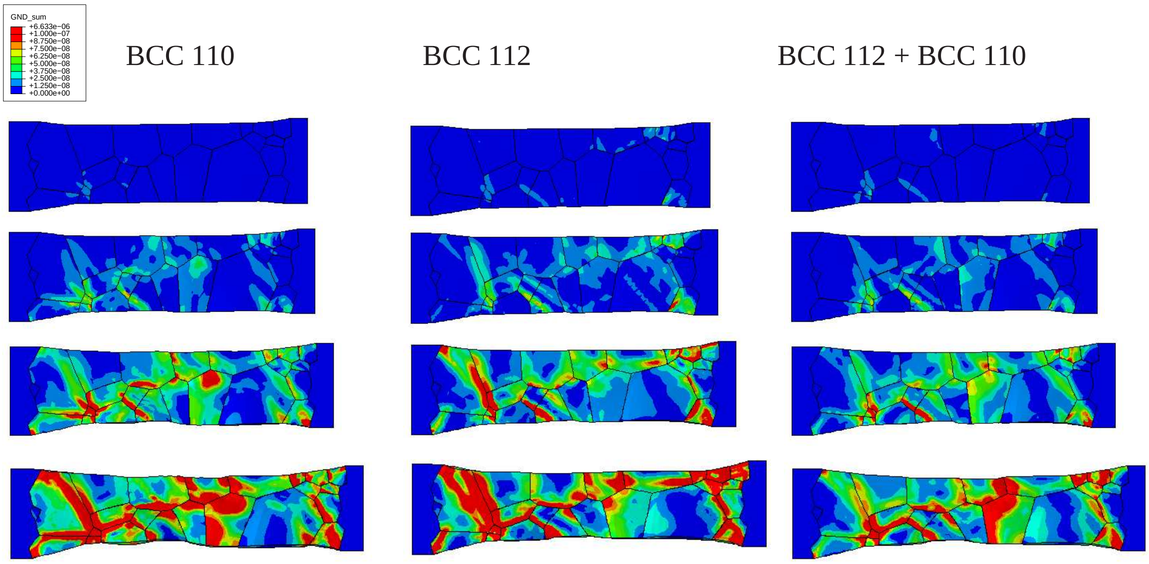

Figure 4.12: Sum of GND densities $\sum_a \varrho_a$ of all systems for $\alpha_{\mathrm{P}} \approx \{1.5\%, 4\%, 10\%\, 19.5\%\}$ for active glide systems $\{112\}$ and $\{110\}$ with included hardening.

As mentioned in the previous section GNDs are very useful to understand and model the material behavior in a more realistic way. Therefore first results concerning the GND evolution during the deformation process are given in Figure 4.12 and by comparison to Figure 4.11 the direct correlation between OGM and GND can be seen for this formulation for the GNDs. Further no direct correlation to the deformation can be made by comparing the results to Figure 4.10 which shows that GNDs calculated by the used formulation are not directly correlated to the deformation behavior. Moreover the gradient in the deformation is very important for calculating GNDs which also explains the very good correlation to the OGM results. As mentioned previously the contraction in grain 15 and 16 is underestimated in the simulations compared to the experiment. Investigating the GNDs in this region, nearly no GNDs are existent in the middle of grain 16 and also the amount is fairly small in grain 15. Averaging the GNDs over the cross-section the region through grain 15 and 16 may lead to the smallest value. This implies that this region hardens less compared to other grains whereby a higher contraction at this position might occur. This will be one of the central questions in following works.

Figure 4.13 shows the resulting reorientation fields for the simulations with included hardening. It can be seen that the reorientation is not localized as in the simulation results without hardening. In nearly all grains an reorientation occurs in which the highest reorientation takes place in grains 10, 11 and 16 for all simulations. Comparing the results for $\{110\}$ and $\{112\}$ separately active certain differences can be seen but in general the reorientation field is similar. The simulation results for both systems active support the previous assumption that both glide system classes are active at a similar level. A very interesting investigation can be made by comparing the reorientation field to the OGM or GND distribution. Partly the highest reorientation occurs at positions where nearly no GNDs or orientation gradients are developing. In general the OGM as well as the GNDs are valid indicators for hardening potential inside the microstructure. However, the behavior of the GNDs can also be influenced by the used ansatz for calculating the GNDs so that a different approach (e.g. Gurtin, 2002) can lead to slightly different results for GNDs especially compared to the reorientation which is not the case for the OGM.

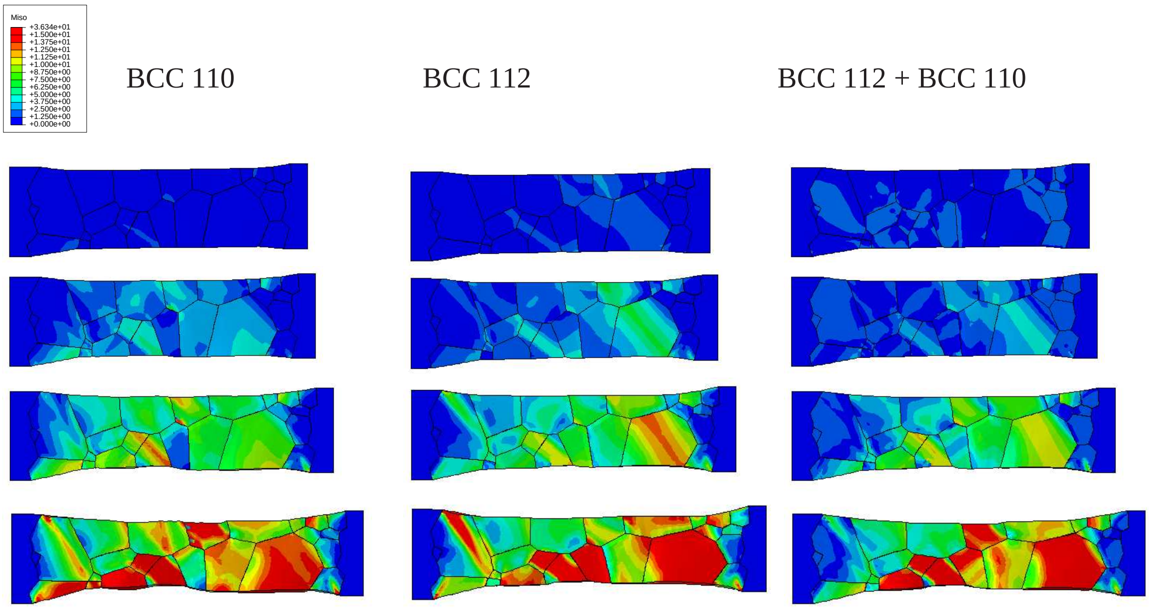

Figure 4.13: Reorientation field β in ° for $\alpha_{\mathrm{P}} \approx \{1.5\%, 4\%, 10\%, 19.5\%\}$ for glide system classes $\{110\}\langle 111\rangle$ and $\{112\}\langle 111\rangle$ separately and simultaneously active with included hardening.

In conclusion it can be summarized that the simulation with included hardening shows a much better agreement with the experiment as without hardening. The simulation with hardening predict the correct tendency in the deformation as well as for the development of the orientation gradient. At this stage it is not possible to say, if both glide systems $\{110\}$ and $\{112\}$ are necessary to predict the correct behavior in Fe-3%Si, however, the results show that both systems should be considered further.

4.6 Conclusion

A crystal-plasticity-based model formulation for anisotropic elastic ideal viscoplastic materials on the basis of an algorithmic flow rule for small elastic strain, small time steps and plastic incompressibility based on finite kinematics is presented. In particular, the crystal plasticity model is rate-dependent and accounts for (local) dissipative hardening effects. This material model is used for the FE representation of the sample of a thin sheet metal specimen with large grains. The experimental results of the tensile test obtained in Henning and Vehoff (2005) are recalled and compared to the simulation results. The simulations were carried out for two sets of glide system classes separately active, namely $\{110\}\langle 111\rangle$ and $\{112\}\langle 111\rangle$, as well as simultaneously active. To begin, all hardening is neglected. It was shown that results obtained with either system class showed a slight deviation in the deformation structure, however, the main deformation zones were predicted correctly. The simulation results with both glide system classes active simultaneously show that both classes are active at the nearly same level of deformation. However, a certain dominance of $\{110\}\langle 111\rangle$ is observable in the deformation behavior. The evolution of the GND density as well as the reorientation distribution were analyzed in detail which show the huge strain hardening potential in the material which is not included so far. Further the concept of OGM was recalled and the results were analyzed which show the direct correlation of GNDs with the OGM concept. However, the orientation gradient in the simulation show no correlation with the experimentally observed one. As an improvement hardening is included. The simulation results show an even better prediction of the experimental results. Also the correct tendency in the experimentally obtained OGM could be seen in the simulation results. For these simulations no dominance at either glide system class could be observed. Therefore it is concluded that both classes should be considered in following works. In future work the model formulation will be extended by hardening formalism based on GNDs. The presented results in this work can therefore be used as a reference to see each influence of the model extension on the simulation results. Further remeshing techniques will be used to obtain reliable results at high deformations.

Chapter 5

Identification of the macroscopic material properties for thermal sprayed coatings based on nanoindentation [*]

Abstract– The characterization of thermal sprayed coatings is often limited to microstructural analysis to evaluate the coatings morphology. Indentation is commonly used to determine the mechanical properties of different kinds of engineering materials. However, due to the complex structure of thermal sprayed coatings few results have been obtained so far. In this work experimental nanoindentation tests and simulation results are compared. The experimental indentation tests show scattering in the force-deformation data due to the complex structure of the arc-sprayed coating which is investigated by means of an indentation test simulation. Based on results for single constituent parts of the coating the Young's modulus as well as further mechanical properties are identified. A general procedure is presented to predict the effective mechanical properties based on the microstructure, porosity, chemical composition and properties of the coating after thermal spraying.

5.1 Introduction

Arc sprayed deposits are being used increasingly in a wide range of industries. In order to understand, predict and improve the reliability of coated devices, it is necessary to characterize their mechanical properties. The determination of the mechanical properties in thermal sprayed coatings is quite complicated and often contradictory mechanical properties are reported. Santana et al. (2008) reported the Young's modulus of HVOF sprayed WC-12Co to be 268 GPa. This property was determined by depth-sensing micro-indentation using the method proposed by Oliver and Pharr (1992) and Pharr et al. (1992). Ghafouri-Azar et al. (2006) also investigated a coating of WC-12Co type, deposited by HVOF spraying, regarding residual stresses. The used Young's modulus in the simulation was 669 GPa, which is 3 times higher than the value reported in Santana et al. (2008). Toparli et al. (2007) used a Young's modulus of 398 GPa for HVOF thermally sprayed WC-Co material in his simulation. This value originates from Delfosse et al. (1997), who reported elastic-plastic properties for different WC-Co composites. However, these values were determined for materials manufactured by powder metallurgical process, involving several high pressure and high temperature treatments. Also Hussainova et al. (2001) reported the mechanical properties of WC-Co composites, fabricated by conventional PM technology. The Young's modulus determined using Vickers indentation for WC-8Co and WC-15Co was

---

[*] results published in Tillmann et al. (2010a)

650 GPa and 560 GPa, respectively. These different reported values show the complexity of determination of mechanical properties of composites like WC-Co, thermal sprayed as well as powder metallurgy fabricated. It has to be accounted that the microstructural aspects of coatings are different from bulk materials which can lead to unexpected mechanical behavior as well as different mechanical properties (Brantner et al., 2003; Yin et al., 2009).

In this research work a twin wire arc spraying (TWAS) facility (Smart Arc PPT 350, Sulzer Metco, Switzerland) was employed to spray WC-FeCSiMn coatings. The work principle of the spraying process is described elsewhere (Nebel and Tillmann, 2010; Tillmann et al., 2008a). The Duramat AS 850 flux-cored wire with a diameter of 1.6 mm (Durum GmbH, Germany) was used as wire feedstock material. The wire is Fe based alloyed with 2 wt.$\%$ C, 1.4 wt.$\%$ Si and $<$1 wt.$\%$ Mn. It is filled with 50 wt.$\%$ of fused tungsten carbide (WC/ W_2C) with grain sizes of 25-125 μm. Based on the parameter optimization presented in Tillmann et al. (2010b) cleaned medium carbon steel specimens (Mat.No. 1.0503, DIN C45, AISI 1045) applying a voltage of 30V, a current of 220 A, and an atomization gas pressure of 6 bar at a spraying distance of 100 mm. For the investigated WC-FeCSiMn coating, no material properties are available in the literature. Therefore, the determination of mechanical properties either from direct measurements or parameter identifications are focused in this paper. This helps to understand the behavior during forming processes much better. In general, as a first assumption it can be anticipated that the properties are similar to WC-Co composites due to the similar mechanical properties of Co and Fe as binder. However, in WC-Co the wt.$\%$ of WC is often above 80$\%$ whereas the here investigated composite contains approximately 50$\%$ Fused Tungsten Carbide (FTC).

As reported in the literature (Hertzberg, 1995; Kim and Kweon, 1999; Okamoto et al., 2005), the material properties of thermally sprayed coatings are different in tension and compression. Conventional test procedures like bending and tensile tests are very complicated to realize on coatings (Nebel and Tillmann, 2010). To determine mechanical properties of coatings nanoindentation technique has been established. However, the strain fields under an indenter are complex and the analysis of data is non-trivial especially for complicated material systems like thermally sprayed coatings. A disadvantage of using nanoindentation for inhomogeneous materials to identify the mechanical properties is that only local properties are determined. These local properties have to be identified for each single material phase which can then be used to approximate the effective mechanical properties with the help of micrographs and different homogenization techniques as shown in the following. Another possibility is to do a number of nanoindentation tests and to average over the obtained results to receive the effective properties. However, a large number of tests are necessary to obtain reliable results.

The focus of this paper is the application of a method to identify the mechanical properties (elastic and inelastic) of an arc sprayed coating with the help of nanoindentation technique, finite element modeling and homogenization methods.

5.2 Nanoindentation

5.2.1 Experiment

The nanoindentation experiments were performed using a Nanoindenter XP with Berkovich tip (MTS Nano Instruments, Oak Ridge, TN, USA) at the Institute of Materials, Ruhr University Bochum. Two sets of experiments were performed where the indenter either penetrated the polished coating in its normal direction or a polished cross-section (see Fig. 5.1). The indentation was done at 49 points in a regular pattern for three indentation depths (100 nm, 250 nm and 500 nm). Figure 5.1 shows an overview of the indentations into a cross-section of the coating for a depth of 100 nm. Due to the fact that the chemical composition of an indented material is not known a priori the indentations were analyzed in the Scanning Electron Microscope (SEM) employing EDX afterwards, to identify which phase was indented and which points have a chemical composition with a mass percentage of one of the constituents above 80% for FTC and 80% for FeCSiMn, respectively. Only those indentations were considered where one single phase without pores and cracks was indented. Therefore a huge amount of indentations is necessary to indent in certain single phases. Investigations of the micrographs of the coating show that phases of different compositions can be identified due to the material contrast in the backscattering mode of the SEM. However it has to be mentioned that no separation, e.g., between WC and W_2C could be made. This also implies that it cannot be identified which phase combinations (i.e. FeCSiMn) are generated during the thermal spraying process. This could be one reason why deviations between the load-displacement curves were obtained at different sample points with nearly the same chemical composition. Another reason for these deviations could also be due to different residual stresses at different locations. It is anticipated that the indentation depth is small compared to the thickness of one single lamella and that the results found for one chemical composition only represent the behavior of this specific composition. This assumption is not valid for indentation into the coating surface due to the smaller thickness of the lamellas in this direction. Therefore the following procedure is based on the results of the nanoindentation test into cross sections. Figures 5.2 and 5.3 show exemplary back-scattered electron images of indentation imprints into the coating as well as the corresponding EDX results into nearly pure FTC composition (Fe<20wt.%) and FeCSiMn alloy (FTC < 20wt.%). As it can be seen from the EDX analysis different pseudoalloy combination are existent.

The Young's modulus E is one of the most important mechanical properties. It describes the relation between stresses and strains in the elastic region. Nanoindentation can be used to determine the Youngs modulus by analyzing the unloading part of the load-displacement curve (Dao et al., 2001). The analysis and determination of the Youngs modulus is done with the traditional Oliver-Pharr (OP) method (Oliver and Pharr, 1992; Pharr et al., 1992) at the corresponding unloading curves originated from an indentation into pure FTC (<20 wt.% Fe) or FeCSiMn (<20 wt.% FTC), respectively. The traditional Oliver-Pharr (OP) method yields to the contact stiffness S

$$S = \frac{2}{\sqrt{\pi}} E_{\mathrm{red}} \sqrt{\mathrm{A}} \tag{5.1}$$

and for the reduced modulus E_{red}, which combines the modulus of both indenter and specimen,

$$\frac{1}{E_{\mathrm{red}}} = \frac{1-\nu^2}{E} + \frac{1-\nu_{\mathrm{I}^2}}{E_{\mathrm{I}}} \tag{5.2}$$

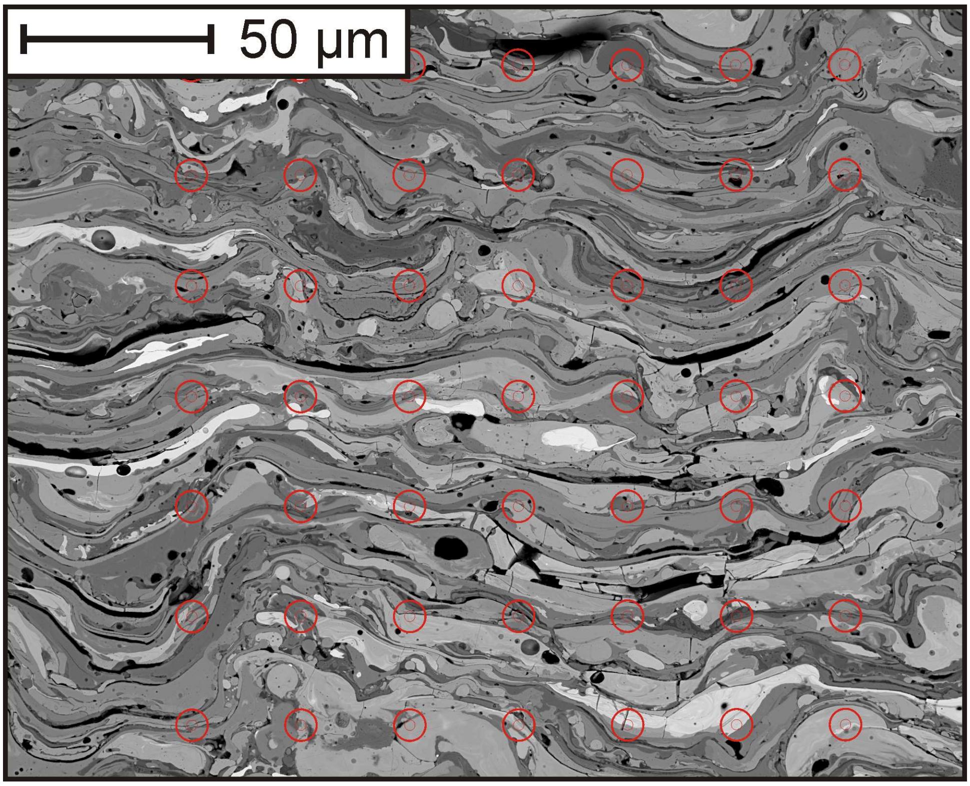

Figure 5.1: Overview of indentations for a depth of 100 nm - TWAS WC-FeCSiMn coating.

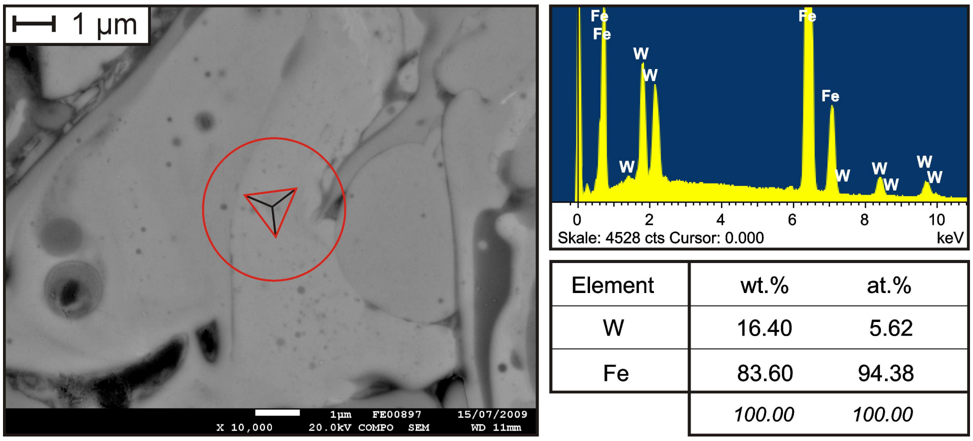

Element	wt.%	at.%
W	16.40	5.62
Fe	83.60	94.38
	100.00	*100.00*

Figure 5.2: Detail view of analyzed point of indentation into FTC for a depth of 100nm and corresponding EDX analysis.

where E and ν are Young's modulus and Poisson's ratio of the test material, and $E_{\mathrm{I}} = 1140\mathrm{GPa}$ and $\nu_{\mathrm{I}} = 0.07$ are the parameters of a diamond indenter (Shan and Sitaraman, 2003). Rewriting this equation for a Berkovich indenter leads to the following set of equations (Giannakopoulos and Suresh, 1999) for the reduced Young's modulus E_{red}

$$E_{\mathrm{red}} = \frac{1}{c\sqrt{\mathrm{A}}}\left(\frac{\mathrm{dP}}{\mathrm{dh}}\right) \tag{5.3}$$

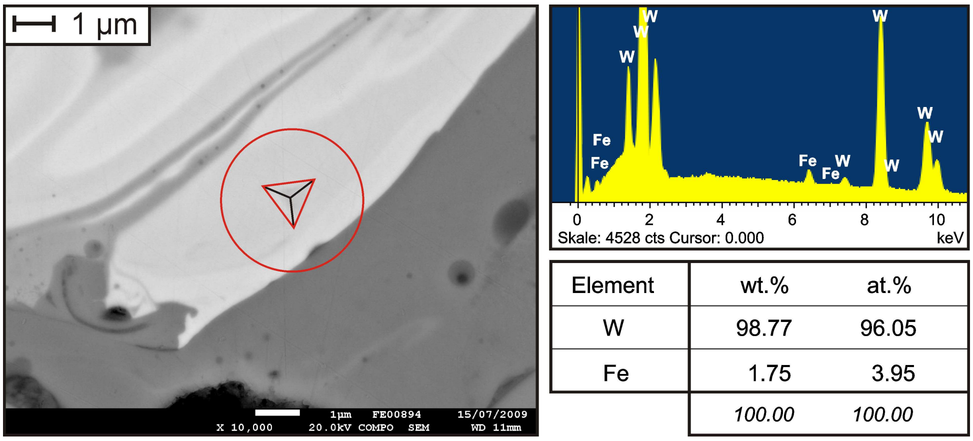
1 μm
1μm FE00894 15/07/2009
X 10,000 20.0kV COMPO SEM WD 11mm
W
W
W
W
Fe
Fe
Fe
W
Fe
W
W
W
0
2
4
6
8
10
Skale: 4528 cts Cursor: 0.000
keV

Element	wt.%	at.%
W	98.77	96.05
Fe	1.75	3.95
	100.00	*100.00*

Figure 5.3: Detail view of analyzed point of indentation into FeCSiMn for a depth of 100 nm and corresponding EDX analysis.

with $c = 1.167$ (King, 1987), $\mathrm{A} = 24.5\mathrm{h}^2$, $\frac{\mathrm{dP}}{\mathrm{dh}}$ describes the slope of the unloading curve and E the resulting effective Young's modulus of the material

$$E = \frac{(1-\nu^2)\, E_{\mathrm{red}}\, E_{\mathrm{I}}}{E_{\mathrm{I}} - (1-\nu_{\mathrm{I}}^2)\, E_{\mathrm{red}}} \,. \tag{5.4}$$

The Poisson ratio is chosen with respect to the bulk material and therefore assumed for FTC composition to be $\nu = 0.19$ and for the FeCSiMn alloy $\nu = 0.3$ (Hsieh and Tuan, 2005). The evaluated Young's modulus based on indentation into cross sections for a depth of 100nm for the FTC and FeCSiMn phase are reported in Table 5.1. The averaged Young's modulus over all 49 indents in cross sections as well as the surface for the different indentation depths are reported in Table 5.2. As shown there the Young's modulus is decreasing with increasing depth. One assumption for this is that the depth and therefore the loads are already too high and failure occurs in the coating which affects the results. Therefore mainly the results for a depth of 100nm are used where it can be assumed that no or at least a minimum of failure occurs which makes the load-displacement curves and the obtained properties more reliable.

5.2.2 Finite element modeling of nanoindentation

As mentioned in the previous section, several analytical methods are available to determine the Young's modulus. However, limited studies are available to obtain the plastic properties with the nanoindentation technique, e.g., Giannakopoulos and Suresh (1999); Venkatesh et al. (2000).

Therefore the indentation loading process is simulated by a finite element model with the software ABAQUS. The coating is modeled with continuum elements consisting of 8 nodes where the coating is modeled as consisting of one single phase. The influence of the neighboring lamella on the mechanical behavior of the indented region is assumed to be negligible, such that only the indented material (lamella) is modeled. This is assumed to be reasonable due to the small indentation depth comparing to thickness of different material layers (compare Fig. 1) which leads only to loading in one phase. Therefore the modeling of the substrate is skipped. The indenter is modeled with rigid shell elements of the type R3D4. The surface of the coating as well as the surface of the indenter is defined as contact areas. Variation of the friction coefficient did not influence the obtained results which was already mentioned by authors before e.g., Shan and Sitaraman (2003). For this reason the simulation is done frictionless. The size of the modeled region is chosen in such a way that the stresses vanish at the free faces. The Finite element model is shown in Figure 5.4.

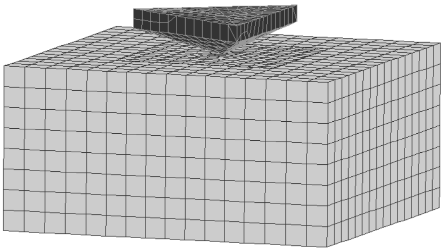

Figure 5.4: Finite element mesh of indenter and coating.

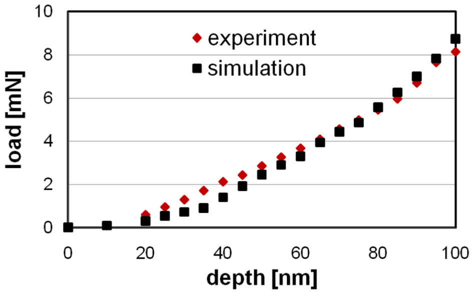

Figure 5.5: Comparison between experimental and simulation data for indentation into FTC and an indentation depth of 100nm.

In the present study the used material behavior is assumed to be of a type Voce hardening law as given by

$$\sigma = \sigma_0 + (\sigma_{\mathrm{sat}} - \sigma_0)\{1 - \exp(-\alpha_{\mathrm{p}} n_0)\} \tag{5.5}$$

where σ_0 describes the initial yield stress, σ_{sat} the saturation value of the stress and n_0 defines the rate at which the size of the yield surface changes as plastic straining develops and α_{p} is the equivalent plastic strain. The unknown material properties in (5.5) are identified with inverse Finite-element-analysis by fitting the simulation results to the experimental obtained load-displacement curves. This determination is carried out using the program LS-OPT in conjunction with ABAQUS. The optimization techniques used rely on response surface methodology (RSM) (Kok and Stander, 1999), a mathematical method for constructing smooth approximations of functions in a design space. The approximations are based on results calculated at numerous points in the multi-dimensional design space. In this work, the material parameters are the design variables and the model together with the data determine the objective function of the corresponding optimization problem. The material parameters that lead to the best fitting agreement can be considered to represent the constitutive behavior of the coating. Such a fit is shown in Figure 5.5.

To find the material parameters, first a range for the design variables has to be defined. As initial values the plastic properties of WC-Co are chosen from Hussainova et al. (2001). The simulation model and optimization method were first tested on results reported in Lee et al. (2007) for a steel coating. The identified material parameters agreed quite well with the reported one, so that the method presented as well as the simulation model seems to be justified. Based on the optimization history for one of the constituents it can be observed that after some iteration steps the LSOPT specific optimization borders are converging to one resulting value which describes the best fitting parameter for the problem. Table 5.1 displays the identified material parameters of the nanoindenter tests for the two phases. Figure 5.5 shows exemplarily the simulated load curve on top of the experimental one for indentation into FTC for an indentation depth of 100nm.

material	E [GPa]	σ_0 [MPa]
FeCSiMn ($<$ 20wt.$\%$ FTC)	190 ± 30	1900 ± 500
FTC ($<$ 20wt.$\%$ FeCSiMn)	340 ± 40	4900 ± 600
	σ_{sat} [MPa]	n_0 [-]
FeCSiMn ($<$ 20wt.$\%$ FTC)	2650 ± 700	4.8 ± 1.5
FTC ($<$ 20wt.$\%$ FeCSiMn)	6100 ± 700	60 ± 5

Table 5.1: Identified mechanical properties of single chemical composition for AS-850.

It has to be mentioned that these parameters varied, depending on the position analyzed and the associated experimental data. The values displayed in Table 5.1 are estimated from results of more than four points each for every phase. The deviation for the Young's modulus was $\approx 15\%$. The deviation for the plastic properties was $\approx 25\%$. These deviations occur from the inhomogeneities inside the coating. Therefore the measured data describes only local properties at the microscale. To achieve the macro-properties like the effective Young's modulus, homogenization techniques are used which are described in the following section.

5.3 Construction of finite element models from real micrographs

To perform analysis of real microstructures, micrographs of the thermal-sprayed coating were observed with different optical microscopes. As mentioned before, SEM micrographs served as a basis for the determination of the chemical composition of different phases. The micrograph provides the possibility to distinguish between the phases which is possible due to their different brightness in the micrograph which is coming from regions with atoms having different atomic numbers. Correlating to the huge difference in the relative atomic weight of tungsten (183.84 g/mol) and iron (55.845 g/mol) the phases of the sprayed WC-FeCSiMn feature a good contrast. In addition to these two phases many pseudoalloyed splats containing WC as well as FeCSiMn are visible which cannot be clearly identified. For WC-FeCSiMn coating it can be distinguished between the matrix material Fe, the inclusion FTC and pores. Figure 5.6a) shows an exemplary micrograph obtained from the coating.

An image processing tool is developed which now identifies the phases and generates an image consisting of Fe-, W-based alloys and pores only. The differentiation between the phases is carried out by finding optimal thresholds based on the color distribution, from which the different phases are separated. As it can be seen on the resulting image in Fig. 5.6b), much noise and small single pieces of the material-phases are included, which make this image inappropriate to perform further analyses, especially with regard to plastic behavior. Therefore these parts have to be smoothed out or removed by applying smoothing and cleanup algorithms. The resulting

	unit / method	mean Young's modulus	Young's modulus deviation
indentation in surface	GPa (NanoIndent. 500nm)	127	59
	GPa (NanoIndent. 250nm)	142	37
	GPa (NanoIndent. 100nm)	154	34
indentation in cross-section	GPa (NanoIndent. 500nm)	165	31
	GPa (NanoIndent. 250nm)	203	52
	GPa (NanoIndent. 100nm)	240	70
indentation in simulation	GPa (NanoIndent. 100nm) in cross-section	230	5
	GPa (NanoIndent. 100nm) in surface	212	4

Table 5.2: WC-FeCSiMn Youngs moduli for compression stresses.

image is shown in Fig. 5.6c).

To generate a FE-mesh from such an image the software Object Oriented Finite Element 2 (OOF2), from the United States National Institute of Standards and Technology (NIST), is used. This software was developed to investigate the behavior of microstructures. OOF2 takes a non-reductionist approach to build a data structure on the digitized image of the microstructure whereby it gets connected to the associated material properties. At the end OOF2 creates a FE-mesh which reflects the shape of the different phases in the microstructure with the associated material parameters. The mesh is generated by minimizing an energy functional which is composed of a homogeneity part E_{hom} of the mesh and a shape part E_{shape} of the elements via

$$E = \alpha E_{\mathrm{hom}} + (1-\alpha)E_{\mathrm{shape}} \tag{5.6}$$

where α is an adjustable parameter, with which the user can control if the mesh should be highly accurate to the image with bad shaped elements ($\alpha = 1$) or if the elements are well shaped but with less accuracy to the shape of the phases in the micrograph ($\alpha = 0$). A value for α between these extremes will lead to an optimal choice. For further details about the exact formulation of the energy functional and the features of the program OOF2 the readers are referred to Langer et al. (2001) and Reid et al. (2008). The resulting mesh can be seen in Fig. 5.6d). The elements representing pores are removed by which free surfaces are created on which contact elements are applied to account for closing pores in the simulation. It is assumed that the phases are perfectly bonded.

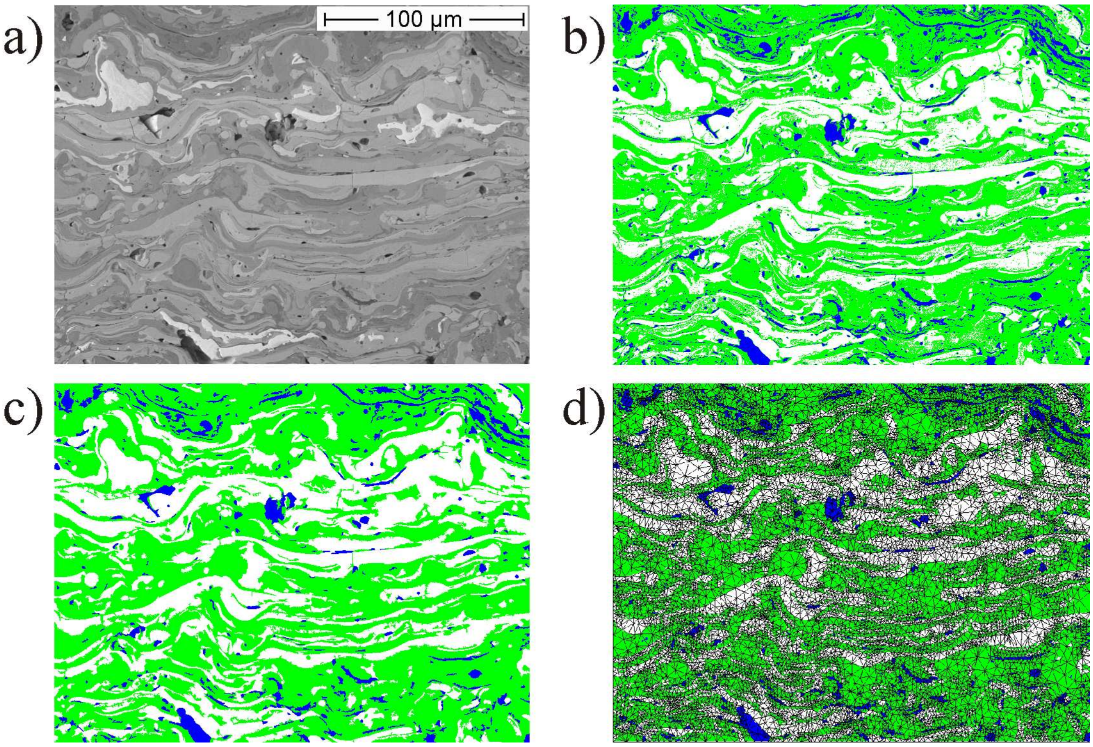

Figure 5.6: a) An exemplary micrograph obtained from a wire (AS-850) arc-sprayed coating with SEM. b) Distinguished material phases. c) Cleaned Image. d) FE-mesh on microstructure.

To obtain information about the microstructural behavior and macroscopic properties compression deformation tests are done. Due to the fact that plane strain and plane stress conditions, respectively, would either over- or underestimate the lateral contraction which would lead to a too stiff or weak behavior, respectively, a 3D-projection of the 2D-mesh is performed by simple extrusion in normal direction of the mesh. At this point it is crucial to investigate, how thick the model should be and how many layers are necessary over the thickness. Therefore convergence studies are performed. It was found that a thickness of by 6 layers gives an acceptable result.

The simple extrusion leads to columnar material phases which will still not predict the exact behavior but it is an improvement of a 2D-simulation with plane strain or stress conditions. To receive more exact impressions of the microstructure, real 3D information of the coating would be necessary which are not available at this point. As boundary conditions for compression tests typical boundary conditions are chosen: three different lateral faces, which do not oppose each other, are fixed in their respective normal direction. The compression test is displacement controlled such that the displacement is applied to one of the free lateral sides in its respective normal direction. The simulations are performed using the Finite Element software ABAQUS. First tests are restricted to linear elasticity so that a comparison of the simulated with the predicted elastic constants from homogenization methods can be made. At this point it is assumed that the micrographs fulfill the requirements for a Representative Volume Element. This is a crucial assumption in order to compare the obtained results with those from the homogenization methods. The elastic constants of the microstructure are obtained by evaluating the reaction forces at the boundaries and the displacement at the free lateral sides. The received results are presented in the next section.

5.4 Discussion

To receive macroscopic properties homogenization techniques can be used. The approximations used here are the Voigt, Reuss and Hashin-Shtrinkman methods. These methods predict maximal and minimal bounds for the effective Young's modulus with respect to the volume fraction of the two phases and pores. However, these methods do not take the morphology into account. Details to these methods can be found in Nemat-Nasser and Hori (1999). The volume fractions were identified on basis of the analyzed micrographs as mentioned in the previous section. The used volume fraction of FTC varies from 33.3 vol.$\%$ up to 36.6 vol.$\%$ and for the pores from 0.72 vol.$\%$ to 2 vol.$\%$ and the difference to 100 vol.$\%$ is used for FeCSiMn. The obtained results with these methods are compared with results from compression tests with real microstructures. Due to the lamellar structure of the coating (cf. Fig. 5.6a)) it behaves anisotropic with respect to the normal (ND, perpendicular to the lamellar structure) and horizontal direction (HD, in direction of the lamellar structure) which was previously reported for coatings in Kim and Kweon (1999); Yin et al. (2009). Therefore the microstructure has to be tested with two different load directions, parallel and perpendicular to the lamellae. This procedure discussed in the previous section is performed on seven different micrographs created from the same part at different positions. The resulting calculated effective Young's moduli are shown in Fig. 5.7. The effect of anisotropy is not accounted in the homogenization techniques due to the fact that these methods assume homogenous distributed spherical inclusion and calculate the effective Young's modulus on the basis of the volume fractions. However, these methods provide a general impression about the value for the Young's modulus. The predicted Young's moduli obtained with help of the real microstructures do not violate the Voigt and Reuss bounds which make the results valid. However, the effective Young's modulus does not lie between the Hashin-Shtrinkman bounds due to its anisotropy. It can be observed that the effective modulus calculated for the micrographs slightly differentiates. The reasons for this are the inhomogeneities of the coating. Therefore the effective Young's modulus has to be evaluated statistically over different micrographs. Here the resulting Young's moduli are calculated to be $E_{\text{HD}} = 230\,\text{GPa}$ and $E_{\text{ND}} = 212\,\text{GPa}$.

Compared with the calculated averaged values in the experiment from all indents for an indentation depth of 100nm ($E_{\text{HD}} = 240\,\text{GPa}$(indentation in cross section) and $E_{\text{ND}} = 154\,\text{GPa}$ (indentation in surface) , cf. Table 5.2), the predicted values fit for the horizontal direction. However, the averaged nanoindentation test results in normal direction do not agree with the predicted Young's modulus. One reason for this could be the local nature of nanoindentation tests. Due to the lamellar structure and relatively high aspect ratio of the lamellas and therefore small thickness in normal direction the potential to indent a pore during nanoindentation tests in the surface without noticing is much higher than in the case of nanoindentation test in the cross-section due to the high thickness in this direction. In contrast the simulation determines the macro Young's modulus by what such local phenomena do not occur.

Considering the elastic-plastic material parameters of the two phases both show a very high yield stresses. The FTC phase shows a high rate of work hardening in which the saturation value is only 20$\%$ higher than the yield strength. It is anticipated that the FTC phase would break before hardening occurs. However, the investigated phases do not contain pure FTC. It

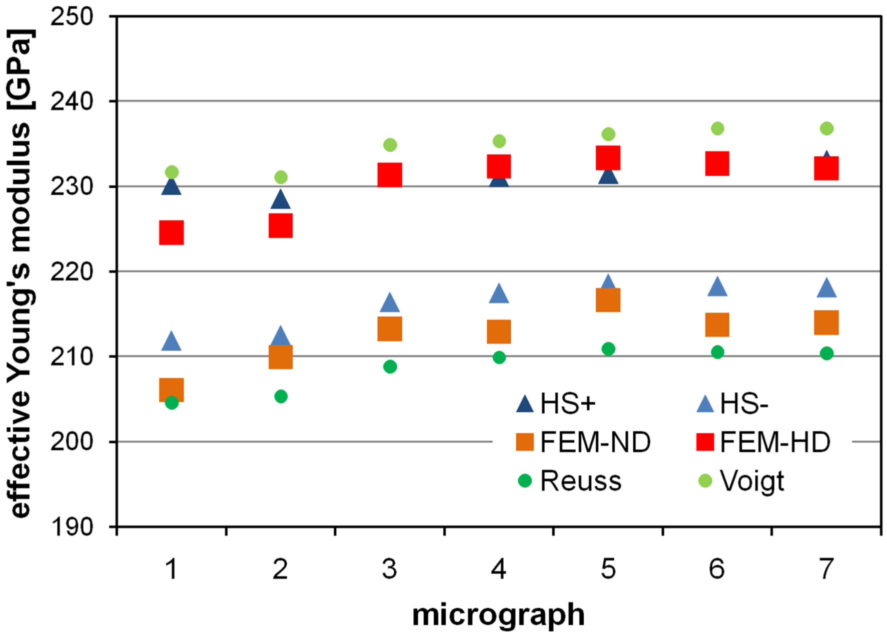

Figure 5.7: Predicted effective Young's modulus calculated from real microstructures compared (HD = parallel to lamellar structure, ND= perpendicular to lamellar structure) with results from different homogenization techniques. (HS+ = upper Hashin-Shtrinkman bound, HS- = lower Hashin-Shtrinkman bound).

is still a composite of mainly FTC but also other in the wire included elements like Fe. The FeCSiMn-phase shows a more significant hardening behavior compared to the FTC phase. The yield stress is very high for Fe compared to conventional steels which will also depend on the included FTC. In summary the single phases show very high mechanical properties although it is not possible to identify these for every chemical composition. Furthermore it is typically assumed that the mechanical properties are inferior compared to bulk material. Although no bulk material is available of this composite this assumption can be approved for the elastic region by comparing the results for the single phases with values from the literature, e.g., Okamoto et al. (2005). However, the plastic parameters are much higher which might occur due to the high temperature during the thermal spraying process which leads to a hardening in the material phases.

From experiments it is known that nearly no plastic deformation occurs in the coating. The coating fails at very low stress states, especially under tensile load (Nebel and Tillmann, 2010). This can be attributed to the weak interface between the splats which leads to significantly poor mechanical properties compared to bulk materials. This means that the phases are not perfectly bonded to each other and that the interface fails. To include these effects and to model the coating more realistically an interface model in conjunction with a failure model for the FTC phase has to be included. To do this the interface as well as failure mechanisms in FTC have to be characterized in more detail in experiments which are on-going work. Therefore we restricted the application of the calculation on basis of the real microstructure to linear elasticity, however, it can also be applied for the plastic region with help of the identified parameters in Table 5.1 for the single phases. But the computing time gets much larger as well as further effects just mentioned have to be included to get sensible results. The incorporation of an interface model is on-going work.

5.5 Summary and outlook

TWAS sprayed WC-FeCSiMn coatings have been evaluated regarding their mechanical properties. In this paper the coating was investigated with regard to nanoindentation tests in detail. The analytical Oliver-Pharr method was used to determine the Young's modulus of local points. With SEM and EDX analysis the material composites indented by the nanoindenter were identified. The elastic-plastic properties were obtained for each phase composition with simulation tools.

With help of an in-house image analysis software different chemical compositions could be identified from SEM-micrographs. A method is presented generating FE-models on the basis of these images which was successfully used to determine the global properties of the coating from the local properties of the single chemical compositions which was presented for the elastic properties. These results were compared to the averaged experimental nanoindentation results as well as to results obtained by several analytical homogenization approaches. The obtained elastic properties in the simulation agrees quite good with the averaged experimental values from all indents in direction of the lamelar structure. However the predicted values do not agree with the experimental measured Young's modulus in normal direction.

The presented method will be further developed to incorporate the interface between the single phases to model the global plastic behavior more realistically. Furthermore the failure behavior will be investigated of the coating to be able to predict cracks occuring in the coating during loading.

Appendix A

Basics of homogenization

This appendix gives a short insight into the basics of homogenization. In the following the basic results of the Eshelby solution and different standard homogenization methods are briefly discussed.

A.1 Eshelby solution

In this section we consider linear elastic composites under isothermal conditions. The main number of works on mean field descriptions used in continuum micromechanics are based on the work of Eshelby (1957). Therein the stress and strain distribution in homogeneous isotropic elastic solids embedded in a surrounding elastic material is investigated. The main result can be summarized as follows. Suppose that the inclusion ω undergoes a spontaneous change in its shape and/or size due to an ”eigenstrain” so that it no longer fits into its previous space in the surrounding material. Assuming that if the surrounding material was absent, the inclusion would undergo some prescribed homogeneous deformation according to the eigenstrain. If the inclusion is now re-embedded into the matrix which constrains the inclusion and forcing it to assume a final strain $\boldsymbol{E}(\boldsymbol{x})$. Eshelby showed that if an elastic homogeneous ellipsoidal inclusion is subjected to such uniform strain $\boldsymbol{E}^*$, uniform stresses and strains are induced in the inclusion. This uniform strain $\boldsymbol{E}$ is related linearly to the eigenstrain $\boldsymbol{E}^*$ via

$$\boldsymbol{E}(\boldsymbol{x}) = \boldsymbol{E} = \mathcal{S}^\omega\, \boldsymbol{E}^* = \text{const} \tag{A.1}$$

where the fourth order tensor $\mathcal{S}^\omega$ represents the Eshelby tensor field. Due to the uniformity of $\boldsymbol{E}^*$ inside ω the corresponding Eshelby tensor becomes constant over ω as indicated in Figure A.1. Typical examples of such eigenstrains are thermal strains, phase transformation strains or disclocation-induced residual strains.

The constant stress in the inclusion ω can be calculated by

$$\boldsymbol{T} = \mathcal{C}(\boldsymbol{E} - \boldsymbol{E}^*) = \mathcal{C}(\mathcal{S}^\omega - \mathcal{I})\boldsymbol{E}^* \tag{A.2}$$

where $\mathcal{C}$ is the elastic stiffness tensor of the material and $\mathcal{I}$ the symmetric fourth order identity tensor. In general the Eshelby tensor $\mathcal{S}$ has merely minor symmetry. Results for ellipsoidal inclusion can be found in Mura (1982). For the special case of a spherical inclusion and isotropic material the Eshelby tensor $\mathcal{S}$ can be calculated via

$$\mathcal{S}^\omega = \frac{1}{3}\alpha \boldsymbol{I} \otimes \boldsymbol{I} + \beta(\boldsymbol{I} \square \boldsymbol{I} - \frac{1}{3}\boldsymbol{I} \otimes \boldsymbol{I}) \tag{A.3}$$

with

$$\alpha = \frac{1+\nu}{3(1-\nu)} \qquad \beta = \frac{2(4-5\nu)}{15(1-\nu)}. \tag{A.4}$$

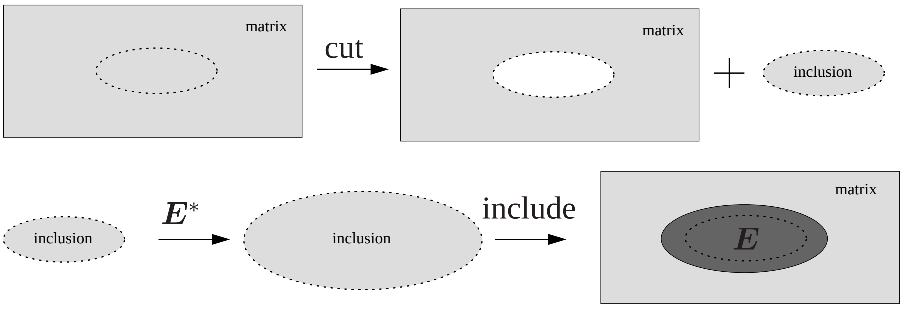

Figure A.1: The inclusion has undergone a stress-free transformation, eigenstrain $\boldsymbol{E}^*$, and has been placed back in the matrix. The matrix constrains the inclusion forcing it to assume a final strain $\boldsymbol{E}$, which can be related to $\boldsymbol{E}^*$ using the Eshelby tensor $\mathcal{S}$ (dark area represents embedded inclusion).

where ν is the Poisson's ratio of the matrix material. Here, $\boldsymbol{I}$ represents the second order identity tensor and we make use of the tensor products $(\boldsymbol{A} \otimes \boldsymbol{B})\boldsymbol{C} := (\boldsymbol{B} \cdot \boldsymbol{C})\boldsymbol{A}$ and $(\boldsymbol{A} \,\square\, \boldsymbol{B})\boldsymbol{C} := \boldsymbol{A}\boldsymbol{C}\boldsymbol{B}$ of any second-order tensors $\boldsymbol{A}, \boldsymbol{B}, \boldsymbol{C}$.

The relation (A.2) only holds, if the elasticity tensor of the matrix and the inclusion are identical. Generally this is not the case. Therefore an imaginary counter problem to the real problem has to be constructed, in which the inclusion has the same elastic stiffness as the matrix. Due to the fact that the Eshelby solution applies in this case (see Figure A.1), the size and eigenstrain for the imaginary inclusion can be assumed such that the final constrained strain and stress are equal to those of the inclusion in the real problem.

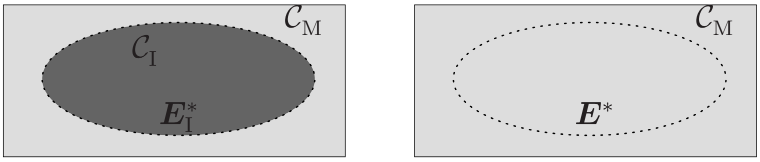

Figure A.2: The inclusion and matrix consists of two different materials. The eigenstrain can occur due to a change in temperature or a phase transformation, etc.. The equivalent imaginary problem is constructed in the way that the inclusion and matrix have identical material properties so that the Eshelby formula can be applied, as shown on the right.

Suppose the inclusion undergoes a prescribed eigenstrain $\boldsymbol{E}^{\mathrm{I}\,*}$, the residual stress in the inclusion can be calculated

$$\boldsymbol{T}^\mathrm{I} = \mathcal{C}_\mathrm{I}(\boldsymbol{E} - \boldsymbol{E}^{\mathrm{I}\,*}) \tag{A.5}$$

where $\boldsymbol{E}$ is the uniform residual strain in the inclusion. For the imaginary problem the similar relation can be obtained

$$\boldsymbol{T}^\mathrm{I} = \mathcal{C}_\mathrm{M}(\boldsymbol{E} - \boldsymbol{E}^*) \tag{A.6}$$

by assuming that the imaginary inclusion with the same elasticity tensor $\mathcal{C}_\mathrm{M}$ as the matrix undergoes a eigenstrain $\boldsymbol{E}^*$ which is imaginary construct. Therefore the Eshelby solution can be used

$$\boldsymbol{E} = \mathcal{S}\boldsymbol{E}^* \tag{A.7}$$

from which a relation between the real eigenstrain and the imaginary eigenstrain can be determined

$$\boldsymbol{E}^{*} = \left((\mathcal{C}_{\mathrm{I}} - \mathcal{C}_{\mathrm{M}})\mathcal{S} + \mathcal{C}_{\mathrm{M}}\right)^{-1} \mathcal{C}_{\mathrm{I}} \boldsymbol{E}^{\mathrm{I}\,*} \,. \tag{A.8}$$

This relation can be used with (A.2) to calculate the constant stress $\boldsymbol{T}^{\mathrm{I}}$ in the inclusion

$$\boldsymbol{T}^{\mathrm{I}} = \mathcal{C}_{\mathrm{M}}(\mathcal{S} - \mathcal{I})\boldsymbol{E}^{*} = \mathcal{C}_{\mathrm{M}}(\mathcal{S} - \mathcal{I})\left((\mathcal{C}_{\mathrm{I}} - \mathcal{C}_{\mathrm{M}})\mathcal{S} + \mathcal{C}_{\mathrm{M}}\right)^{-1} \mathcal{C}_{\mathrm{I}}\, \boldsymbol{E}^{\mathrm{I}\,*}. \tag{A.9}$$

The same concept can be applied for the case of an externally applied strain $\boldsymbol{E}^{0}$ as indicated in Figure A.3. The stress in the inclusion can be calculated by

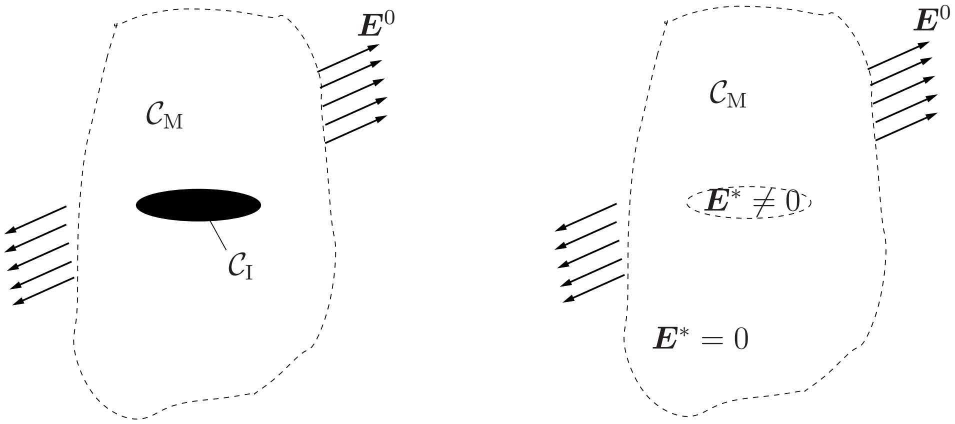
$\boldsymbol{E}^0$
$\mathcal{C}_{\mathrm{M}}$
$\mathcal{C}_{\mathrm{I}}$
$\boldsymbol{E}^0$
$\mathcal{C}_{\mathrm{M}}$
$\boldsymbol{E}^* \neq 0$
$\boldsymbol{E}^* = 0$

Figure A.3: a) Ellipsoidal inclusion embedded in a matrix. b) Homogeneous material with eigenstrain subjected to an applied external load

$$\boldsymbol{T} = \mathcal{C}_{\mathrm{I}}(\boldsymbol{E} + \boldsymbol{E}^{0}) \tag{A.10}$$

where $\boldsymbol{E}$ denotes the mismatch strain in the inclusion. Reformulate this problem to an imaginary problem where the inclusion has the same properties as the matrix yields to

$$\boldsymbol{T} = \mathcal{C}_{\mathrm{M}}(\boldsymbol{E} + \boldsymbol{E}^{0} - \boldsymbol{E}^{*}) \,. \tag{A.11}$$

Outside of the inclusion is $\boldsymbol{E}^{*} = 0$. The Eshelby solution can now be used to determine the mismatch strain

$$\boldsymbol{E} = \mathcal{S}\boldsymbol{E}^{*} \,. \tag{A.12}$$

The equivalent eigenstrain due to an externally applied strain $\boldsymbol{E}^{0}$ can then determined as

$$\boldsymbol{E}^{*} = -[\mathcal{S} + (\mathcal{C}_{\mathrm{I}} - \mathcal{C}_{\mathrm{M}})^{-1}\mathcal{C}_{\mathrm{M}}]^{-1}\boldsymbol{E}^{0} \,. \tag{A.13}$$

The total strain in the inclusion can than be calculated via

$$\begin{aligned} \boldsymbol{E}^{\mathrm{I}} &= \boldsymbol{E}^{0} + \boldsymbol{E} = \boldsymbol{E}^{0} + \mathcal{S}\boldsymbol{E}^{*} && \text{(A.14)} \\ \boldsymbol{E}^{\mathrm{I}} &= [\mathcal{I} + \mathcal{S}\mathcal{C}_{\mathrm{M}}^{-1}(\mathcal{C}_{\mathrm{I}} - \mathcal{C}_{\mathrm{M}})]^{-1}\boldsymbol{E}^{0} = const && \text{(A.15)} \end{aligned}$$

The expression $[\mathcal{I} + \mathcal{S}\mathcal{C}_{\mathrm{M}}^{-1}(\mathcal{C}_{\mathrm{I}} - \mathcal{C}_{\mathrm{M}})]^{-1}$ is also referred to as influence or concentration tensor $\mathcal{A}$ which describes the correlation between the total strain and the external load.

A.2 Review of some standard homogenization methods

Basically, a macroscopic material point at a position $\boldsymbol{X}$ in a fixed Cartesian frame is considered next. In linear elasticity the macroscopic stresses $\boldsymbol{T}^{\text{macro}}$ and strains $\boldsymbol{E}^{\text{macro}}$ are related via the macroscopic elasticity tensor $\mathcal{C}_{\text{macro}}$ with

$$\boldsymbol{T}^{\text{macro}} = \mathcal{C}_{\text{macro}} \boldsymbol{E}^{\text{macro}}. \tag{A.16}$$

Homogenization procedures are mainly based on the definition of a local surrounding of a macroscopic material point with microscopic volume V and the boundary ∂V. This volume V represents a characteristic part of the material in terms of its structure and behavior, respectively. This implies that the size of heterogeneities at the microlevel is at least one order of magnitude smaller than the size of the volume V of the macropoint. As it is shown by Nemat-Nasser and Hori (1999) and Gross and Seelig (2001) the Hill-Mandel condition is fulfilled by applying linear displacement, periodic or uniform traction or mixed boundary conditions (Pahr and Zysset, 2008) on ∂V. This section focuses on the detailed discussion of different homogenization methods.

The basic concept of homogenization is shown in Figure A.4. At the macro-scale the material is considered as homogeneous continuum where the microscale describes an infinitesimal surrounding of a material point at the macroscale. The microscale is generally heterogeneous, e.g., the morphology consists of different particles, inclusions, etc.. The microscopic length d of an RVE has to be much larger than the dimensions of the single particles l. In the context of the principle of separation of scales, the characteristic length L at the macroscale has also to be much larger than the size of the RVE. This characteristic length L is not determined by the size of the macroscopic domain but rather by the spatial variation of the kinematic fields and stress fields within that domain (Kouznetsova et al., 2010). Therefore the following relation has to hold

$$l \ll d \ll L \tag{A.17}$$

in order that homogenization methods can be applied.

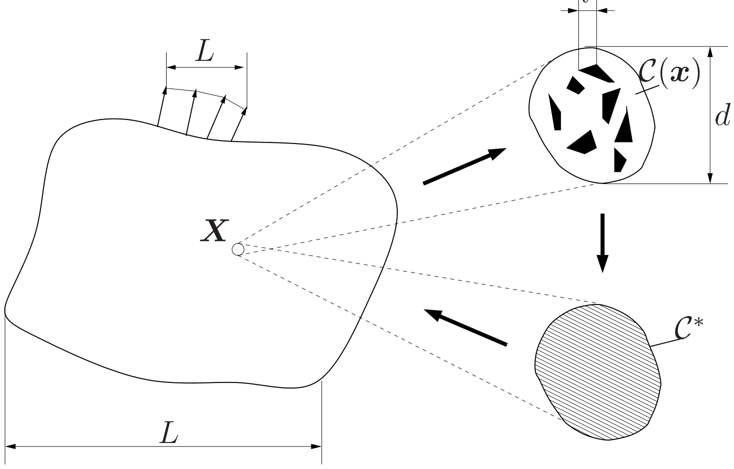

Figure A.4: Principle of homogenization and different length scales

A material point at the macroscale is related over an RVE to the volume V of the microscale. The microscale is subjected to fluctuated stress-strain fields as shown in Figure A.5. The mechanical state at the macroscale can be calculated over volume averaging the microscopic quantities

$$\boldsymbol{T}^{\text{macro}} = \langle \boldsymbol{T} \rangle = \frac{1}{V} \int_V \boldsymbol{T}(\boldsymbol{x}) \, \mathrm{d}V \qquad \boldsymbol{E}^{\text{macro}} = \langle \boldsymbol{E} \rangle = \frac{1}{V} \int_V \boldsymbol{E}(\boldsymbol{x}) \, \mathrm{d}V \tag{A.18}$$

where $\langle \bullet \rangle$ describes the average over the volume.

The constitutive law from the microlevel

$$\boldsymbol{T}(\boldsymbol{x}) = \mathcal{C}(\boldsymbol{x}) \, \boldsymbol{E}(\boldsymbol{x}) \tag{A.19}$$

can be rewritten to the macroscale

$$\langle \boldsymbol{T} \rangle = \mathcal{C}^* \, \langle \boldsymbol{E} \rangle \tag{A.20}$$

with the effective elasticity tensor $\mathcal{C}^* = \mathcal{C}_{\text{macro}}$. This relation is only valid if the average distortion energy of the microscale is equal to the one at the macroscale exemplified by

$$\langle \psi \rangle = \left\langle \frac{1}{2} \boldsymbol{E}(\boldsymbol{x}) \cdot \mathcal{C}(\boldsymbol{x}) \, \boldsymbol{E}(\boldsymbol{x}) \right\rangle = \frac{1}{2} \langle \boldsymbol{E} \rangle \cdot \mathcal{C}^* \, \langle \boldsymbol{E} \rangle \tag{A.21}$$

which is captured by the Hill-Mandel-condition

$$\langle \boldsymbol{T}(\boldsymbol{x}) \cdot \boldsymbol{E}(\boldsymbol{x}) \rangle = \langle \boldsymbol{T} \rangle \cdot \langle \boldsymbol{E} \rangle \ . \tag{A.22}$$

This condition general means, that the fluctuation fields have to be energetically equivalent to their averages as shown in Figure A.5. To calculate the stress and strain fields at the microlevel in a volume V next to the balance of linear momentum and the governing equation additional boundary conditions have to be added at the boundary ∂V. Due to the fact that the behavior of the heterogeneous volume at the microlevel is represented only by a point at the macrolevel homogeneous boundary conditions should be chosen as boundary conditions for the microlevel. In principle there are four types of boundary conditions which fulfill the Hill-Mandel lemma:

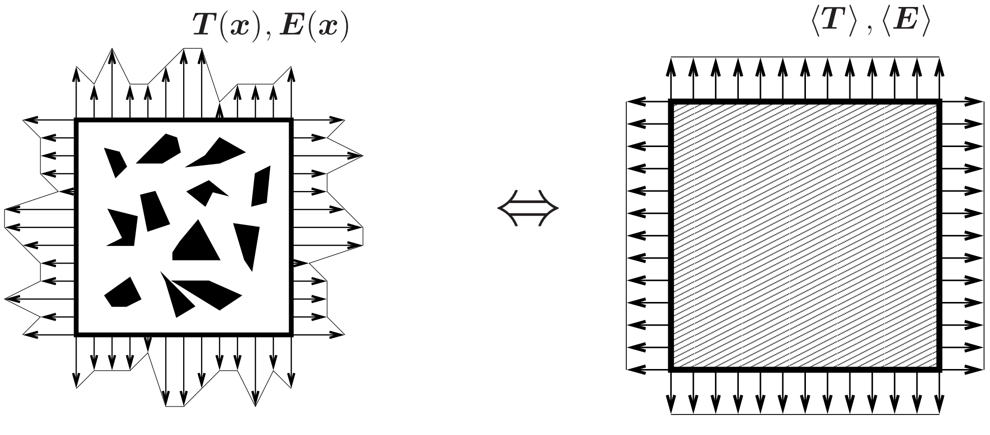
$\boldsymbol{T}(\boldsymbol{x}), \boldsymbol{E}(\boldsymbol{x})$
$\Leftrightarrow$
$\langle \boldsymbol{T} \rangle , \langle \boldsymbol{E} \rangle$

Figure A.5: Micro fluctuation fields on the RVE boundary and their average.

- linear displacements at ∂V
- uniform tractions at the boundary ∂V
- periodic boundary conditions at the boundary ∂V
- mixed boundary conditions (Pahr and Zysset, 2008) at the boundary ∂V

We restrict the composite to the matrix-inclusion type with perfect interfacial bonds between inclusions and their immediate surrounding matrix. The matrix phase is labeled by M and the inclusion is assumed to be of type-i and therefore labeled by i or I for one single inclusion. For a multiphase composite consisting of n phases, $c_\alpha = V_\alpha / V$ denotes the volume fraction of each phase α with respect to the total volume V of the RVE, which are subjected to the restriction $\sum_{\alpha=1}^{n} c_\alpha = 1$. The volume V at the microlevel is subjected to linear boundary displacements which corresponds to a macroscopic strain $\boldsymbol{E}^0$. The microscopic strain within the RVE depends upon an initially unknown fourth-order tensor $\mathcal{A}(\boldsymbol{x})$ with

$$\boldsymbol{E}(\boldsymbol{x}) = \mathcal{A}(\boldsymbol{x})\boldsymbol{E}^0 \tag{A.23}$$

referred to as concentration tensor. In the following, $\mathcal{A}$ describes the volume average of $\mathcal{A}(x)$. As the averaging procedure is done phase-wise, this results in phase-wise constant concentration tensors $\mathcal{A}_\alpha$. Hence, the effective elasticity tensor can be calculated via

$$\mathcal{C}^* = \sum_{\alpha=1}^{\mathrm{n}} c_\alpha \mathcal{C}_\alpha \mathcal{A}_\alpha . \tag{A.24}$$

For the special case of an ellipsoidal inclusion in an infinite matrix, the Eshelby solution can be used to determine the so far unknown concentration tensors $\mathcal{A}_\alpha$. As shown by many authors (e.q Gross and Seelig, 2001; Nemat-Nasser and Hori, 1999) and in the previous section (see (A.15)), the strain in the inclusion can be calculated by

$$\boldsymbol{E}^{\mathrm{I}} = \mathcal{A}_{\mathrm{I}}^0 \boldsymbol{E}^0 = \left[\mathcal{I} + \mathcal{S}\mathcal{C}_{\mathrm{M}}^{-1}(\mathcal{C}_{\mathrm{I}} - \mathcal{C}_{\mathrm{M}})\right]^{-1} \boldsymbol{E}^0 = const \tag{A.25}$$

where $\mathcal{I}$ denotes the fourth-order symmetric identity tensor, $\mathcal{C}_{\mathrm{M}}$ the elasticity tensor of the matrix, $\mathcal{C}_{\mathrm{I}}$ the elasticity tensor of the inclusion and $\mathcal{S}$ the Eshelby tensor.

Similar results can be obtained by applying uniform tractions at the boundary of the volume V which correspond to a macroscopic stress $\boldsymbol{T}^0$. The microscopic stress is related to the macroscopic one via an unknown fourth-order tensor $\mathcal{B}$ according to

$$\boldsymbol{T}(x) = \mathcal{B}(\boldsymbol{x})\boldsymbol{T}^0 \tag{A.26}$$

where $\mathcal{B}(\boldsymbol{x})$ is a concentration tensor. In the following $\mathcal{B}$ describes the volume average of $\mathcal{B}(x)$, where this results in phase wise constant concentration tensors $\mathcal{B}_\alpha$. Therefore the effective elasticity tensor can be calculated via

$$\mathcal{C}^* = \left(\sum_{\alpha=1}^{\mathrm{n}} c_\alpha \mathcal{C}_\alpha^{-1} \mathcal{B}_\alpha\right)^{-1} . \tag{A.27}$$

A.2.1 Voigt- and Reuss-bounds

A homogeneous material loaded by homogeneous boundary conditions undergoes homogeneous state fields. For heterogeneous material this generally does not hold true but it is the most primitive assumption to suppose constant microfields. Voigt (1889) assumed the strain to be constant in the volume V and therefore follows $\mathcal{A} = \mathcal{I}$. This assumption can be understood as a parallel connection of the different materials. According to this the effective elasticity tensor can be calculated by averaging the stiffnesses of the single materials.

$$\mathcal{C}^*_{(\mathrm{Voigt})} = \langle \mathcal{C}(\boldsymbol{x}) \rangle = \sum_{\alpha=1}^{\mathrm{n}} c_\alpha \mathcal{C}_\alpha \tag{A.28}$$

Reuss (1929) assumed the stress to be constant in the volume V and analogously to Voigt follows that $\mathcal{B} = \mathcal{I}$. This assumption can be understood as a serial connection of the different materials. This leads to the result that the effective compliance tensor can be calculated by averaging the compliance of the single materials.

$$\mathcal{C}^{*-1}_{(\mathrm{Reuss})} = \left\langle \mathcal{C}(\boldsymbol{x})^{-1} \right\rangle = \sum_{\alpha=1}^{\mathrm{n}} c_\alpha \mathcal{C}_\alpha^{-1} \tag{A.29}$$

With the minimum of stored energy potential and dual (conjugated) potential it can be shown that

$$\mathcal{C}^*_{(\mathrm{Voigt})} \;\geq\; \mathcal{C}^* \;\geq\; \mathcal{C}^*_{(\mathrm{Reuss})} \tag{A.30}$$

where it is emphasized that the inequality implies that the eigenvalues of the tensors $\mathcal{C}^* - \mathcal{C}^*_{(\mathrm{Reuss})}$ and $\mathcal{C}^*_{(\mathrm{Voigt})} - \mathcal{C}^*$ are non-negative (Zohdi and Wriggers, 2005). These bonds are the limits which can occur for the effective elasticity tensor if the investigated microstructure meets the RVE requirements mentioned before.

A.2.2 Mori-Tanaka method

The Mori-Tanaka method approximates the interaction between the phases by assuming that each inclusion i is embedded, in turn, in an infinite matrix that is remotely loaded by the average matrix strain $\boldsymbol{E}^{\mathrm{M}}$ or average matrix stress $\boldsymbol{T}^{\mathrm{M}}$, respectively. Therefore the strain in the single inclusion can be calculated by

$$\boldsymbol{E}_i^{\mathrm{I}} = \mathcal{A}^0_{\mathrm{I},i} \boldsymbol{E}^{\mathrm{M}}, \tag{A.31}$$

where the influence tensor $\mathcal{A}^0_{\mathrm{I},i}$ is given by

$$\mathcal{A}^0_{\mathrm{I},i} = \left[\mathcal{I} + \mathcal{S}_{\mathrm{M}} \mathcal{C}_{\mathrm{M}}^{-1} (\mathcal{C}_{\mathrm{I},i} - \mathcal{C}_{\mathrm{M}}) \right]^{-1}. \tag{A.32}$$

In the case of ellipsoidal inclusions the Mori-Tanaka homogenization approach leads to $\boldsymbol{E}_{\mathrm{I},i} = \mathcal{A}^0_{\mathrm{I(MT)},i} \boldsymbol{E}^0$, where $\mathcal{A}_{\mathrm{I(MT)},i}$ is obtained by

$$\mathcal{A}_{\mathrm{I(MT)},i} = \left[c_i \mathcal{I} + c_{\mathrm{M}} (\mathcal{A}^0_{\mathrm{I},i})^{-1} + \sum_j c_j \mathcal{A}^0_{\mathrm{I},j} (\mathcal{A}^0_{\mathrm{I},i})^{-1} \right]^{-1}. \tag{A.33}$$

With this result we can calculate the effective elasticity tensor

$$\mathcal{C}^*_{(\mathrm{MT})} = \mathcal{C}_\mathrm{M} + \sum_i c_i(\mathcal{C}_{\mathrm{I},i} - \mathcal{C}_\mathrm{M})\mathcal{A}_{\mathrm{I(MT)},i}. \tag{A.34}$$

In Benveniste (1987) the method is interpreted in the sense that ”each inclusion behaves like an isolated inclusion in the matrix seeing $\boldsymbol{E}^\mathrm{M}$ as a far-field strain”.

A.2.3 Hashin-Shtrikman bounds

Following the approach of Hashin and Shtrikman (1963) leads to the equation for the upper and lower bound of the elasticity tensor for a two-phase material:

$$\begin{aligned} \mathcal{C}^*_{(\mathrm{HS}+)} &= \mathcal{C}_\mathrm{I} + c_\mathrm{M}\left[(\mathcal{C}_\mathrm{M} - \mathcal{C}_\mathrm{I})^{-1} + c_\mathrm{I}\mathcal{S}_\mathrm{I}\mathcal{C}_\mathrm{I}^{-1}\right]^{-1} \\ \mathcal{C}^*_{(\mathrm{HS}-)} &= \mathcal{C}_\mathrm{M} + c_\mathrm{I}\left[(\mathcal{C}_\mathrm{I} - \mathcal{C}_\mathrm{M})^{-1} + c_\mathrm{M}\mathcal{S}_\mathrm{M}\mathcal{C}_\mathrm{M}^{-1}\right]^{-1}. \end{aligned} \tag{A.35}$$

As can be seen the upper Hashin-Shtrikman bound corresponds to the Mori-Tanaka result. The upper bound can also be obtained with the Mori-Tanaka method just by interchanging matrix and inclusion material.

A.2.4 Interpolative Double Inclusion model (IDIM)

In Pierard et al. (2004) the following interpolative homogenization model for a two-phase material was introduced:

$$\mathcal{C}^*_{(\mathrm{IDIM})} = \left[\left(1 - \frac{c_\mathrm{I} + c_\mathrm{I}^2}{2}\right)\mathcal{C}^{*-1}_{(\mathrm{MT}^{-1})} + \frac{c_\mathrm{I} + c_\mathrm{I}^2}{2}\mathcal{C}^{*-1}_{(\mathrm{MT})}\right]^{-1}, \tag{A.36}$$

in which $\mathcal{C}_{(\mathrm{MT})}$ is the estimation for the effective elasticity from the Mori-Tanaka method. $\mathcal{C}_{(\mathrm{MT}^{-1})}$ is the effective elasticity tensor following from the inverse Mori-Tanaka approximation in which, for a two-phase material, the smaller volume part becomes the matrix material and vice versa. Therefore the interpolative double inclusion model can be seen as a properly chosen interpolation between the Mori-Tanaka and inverse Mori-Tanaka method and between the Hashin-Shtrikman bounds, respectively. This model was first developed by Lielens (1999).

A.2.5 Self-consistent scheme

The self-consistent scheme approximates the interaction between the phases by assuming that each phase is embedded in an infinite volume of an effective medium with elastic properties $\mathcal{C}^*$ of the composite. Therefore the effective elasticity stiffness of the material passes into the matrix stiffness ($\mathcal{C}_\mathrm{M} = \mathcal{C}^*$) and we obtain the influence tensor

$$\mathcal{A}_{\mathrm{I(SCS)},i} = \left[\mathcal{I} + \mathcal{S}^*\,\mathcal{C}^{*-1}\left(\mathcal{C}_{\mathrm{I},i} - \mathcal{C}^*\right)\right]^{-1}. \tag{A.37}$$

Due to the fact that the influence tensor $\mathcal{A}_{\mathrm{I(SCS)},i}$ depends on the effective elasticity tensor $\mathcal{C}^*_\mathrm{E}$, the equation is implicit and nonlinear.

$$\mathcal{C}^*_{(\mathrm{SCS})} = \mathcal{C}_\mathrm{M} + \sum_i c_i\left(\mathcal{C}_{\mathrm{I},i} - \mathcal{C}_\mathrm{M}\right)\mathcal{A}_{\mathrm{I(SCS)},i} \tag{A.38}$$

Algorithmically, the method requires an additional iterative loop to calculate $\mathcal{C}^*_{(\mathrm{SCS})}$. In general, the self-consistent method gives a sufficient prediction of the behavior of polycrystals but it is less accurate in the case of two-phase composites as the IDIM as shown by Pierard et al. (2004).

Appendix B

Crystalline Structure

B.1 Lattice structures of metals

Every metal consists of a crystalline structure that is regular and repetitive. The simplest possible choice to serve as a representative structural unit is called a unit cell. A real crystal mainly consists of a multiplicity of unit cells. Therefore the structure can be described by one single unit cell. All metals form their unit cell as close-packed as possible. In metal structures the three most important unit cells are the body-centered cubic (bcc), face-centered cubic (fcc) and hexagonal close-packed structure (hcp) shown in Figure B.1.

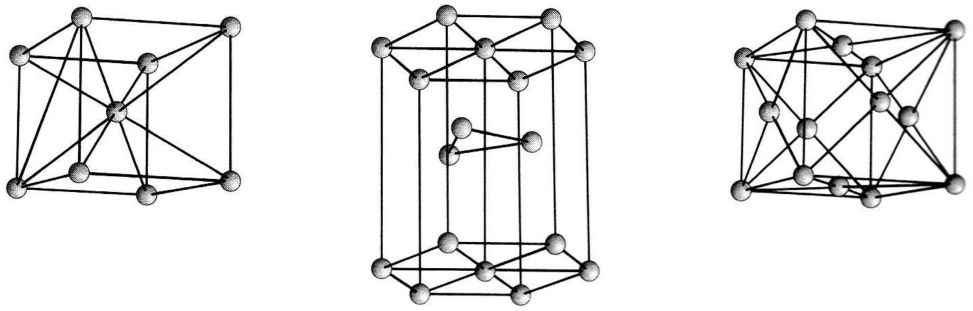

Figure B.1: The most important lattice structures of metals (bcc, hcp, fcc) (Bauser et al., 2001).

The bcc crystal consists of a simple cubic lattice structure which has one atom in every corner and one atom in the center. The atoms at the corners are shared by eight adjacent unit cells. The atomic packing factor is 68%. Typical metals with this structure are chromium, vanadium, molybdenum, tungsten, α-iron and δ-iron. The fcc structure has an atom at each corner and at the center of every face. It belongs to the crystal structure with an atomic packing factor of 74%, the highest value possible. Aluminum, nickel, copper, silver, platinum, gold and γ-iron appear in this structure. The hcp structure is more complicated than the cubic structures. The unit cell consists of three layers of atoms. The top and bottom layers contain six atoms at the corners of a hexagon and one atom at the center of each hexagon. The middle layer contains three atoms positioned in the gaps between the atoms of the top and bottom layers. As the name already implies, hcp belongs to the structures that are close-packed with an atomic packing factor of 74%. Hcp structures are found in beryllium, magnesium, α-titanium, zinc and zirconium (Bargel and Schulze, 2000).

To describe the geometry around and inside a unit cell the Miller indices are used. The following explanation applies only to cubic crystal structures. A description for hcp-crystals can be found in the literature, e.g., Shackelford and Sullivan (2005). For describing lattice planes a set of integers, usually called h, k and l, represent the inverse of axial intercepts. That means if the lines ma, nb and pc describe the intersection between the lattice plane and the coordinate axis (through the point of origin), the Miller indices result in the reciprocal value:

$$h : k : l = \frac{1}{m} : \frac{1}{n} : \frac{1}{p} \, .$$

The indices of planes are written in ( )-brackets and for negative indices a minus is placed above the number (e.g.,$\bar{1}$). The lattice directions are expressed as a set of integers, which are obtained by identifying the smallest integer positions intercepted by the line from the origin and are written in [ ]-brackets. Due to this definition the direction orthogonal to the plane is described by the same set of integers. $\{\}$-brackets describe all planes which are crystallographically equivalent due to the symmetry of the unit cell like (111), ($\bar{1}$11), ($\bar{1}\bar{1}$1) and ($\bar{1}\bar{1}\bar{1}$) in the cubic case. $\langle\,\rangle$-brackets describe the group of all equivalent directions.

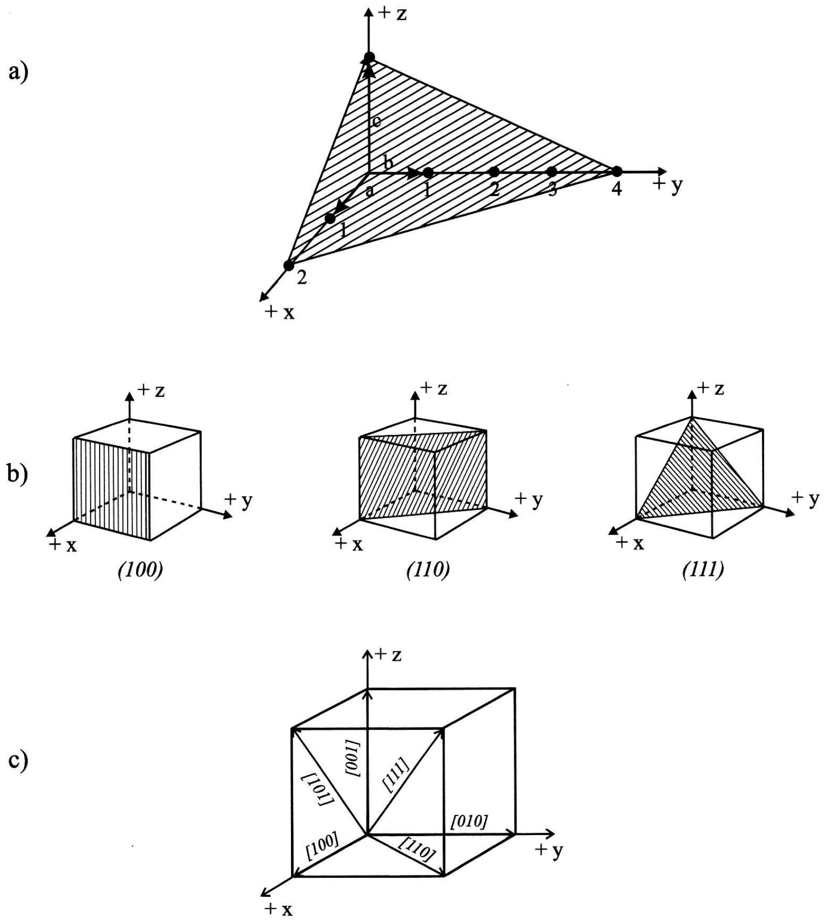

Figure B.2: Miller indices (Bauser et al., 2001).

B.2 Crystal defects

As described, a metal consists of repetitive unit cells but with the restriction that there are structural flaws in the metal due to the fact that no material consists of a perfect repeating crystal structure. These defects have an important effect on the mechanical properties of the metal, e.g., plasticity, diffusion and conductivity are based on these mechanisms of defects.

The simplest type of flaw is the point defect which is associated with the crystalline point lattice. The three common types of point defects are vacancy, interstitial and substitution atom (see Figure B.3). Vacancy means an unoccupied atom site in the crystal structure. In interstitial defects an atom takes a position in the crystal structure which is normally not occupied by an atom in the perfect structure. Substitution atom means that a foreign atom (impurity) replaces an atom in the crystal structure. This can only happen when the atoms are based on the same lattice type and the atom diameters are nearly the same. Point defects are especially dependent on the temperature. With increasing temperature the thermal vibration gets higher and with it the energy of the atoms vacancies and interstitials can occur easier.

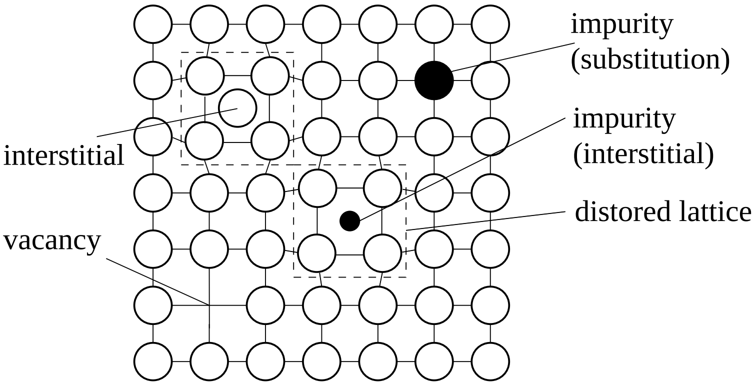

Figure B.3: Different types of point defects

In comparison with point defects, which result from thermal agitation, dislocations are associated with mechanical deformation. The two common types of dislocations are edge and screw dislocation shown in Figure B.4. The edge dislocation bears this name because the dislocation line runs along the edge of an extra row of atoms. The dislocation line is movable in this plane, the so called sliding plane. The screw dislocation derives its name from the spiral stacking of crystal planes around the dislocation line.

Besides point and line flaws in crystalline materials it is also important to consider that the material is contained within some boundary surfaces which are a distribution of the atomic-stacking arrangement of the crystal. One special form is the twin boundary, which separates two crystalline regions that are structurally mirror images of each other. If the orientations of two single crystals in the metal are different, the crystals are called grains and the contact line is called grain boundary. Many properties of metals are highly sensitive to such grain structures (Shackelford and Sullivan, 2005). The influence depends on the relative orientation of the adjacent grains. If the adjacent grains are only tilted by a few degrees relative to each other, also called the misorientation, the boundary is called low angle boundary. This can occur through a few isolated edge dislocations (see Figure B.5). The misorientation angle for this

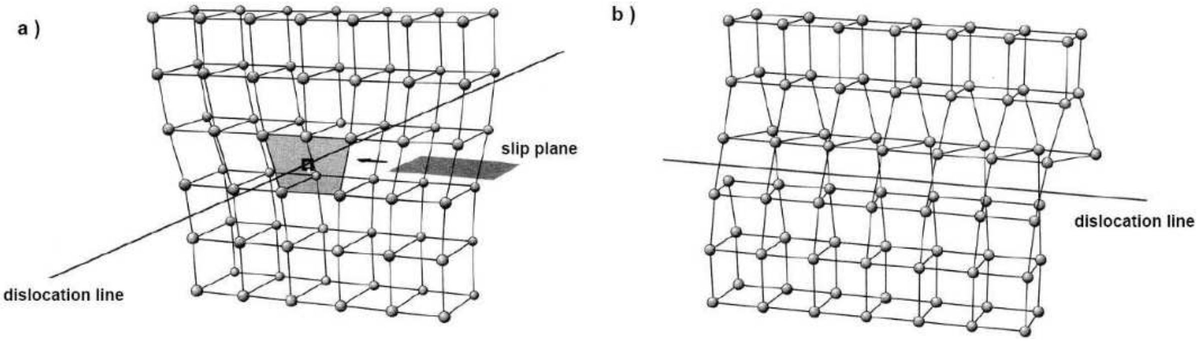

Figure B.4: Different types of line defects: a) edge dislocation b) screw dislocation (Bauser et al., 2001).

case is usually defined to be smaller than $15°$. All grains belonging to such a boundary are not separated in single grains but in so-called subgrains. The boundary structure involving adjacent grains which are tilted by a large misorientation angle is more complex than for small misorientation angles (see Figure B.5). The boundary is a strongly disturbed region containing a multitude of different defect mechanisms.

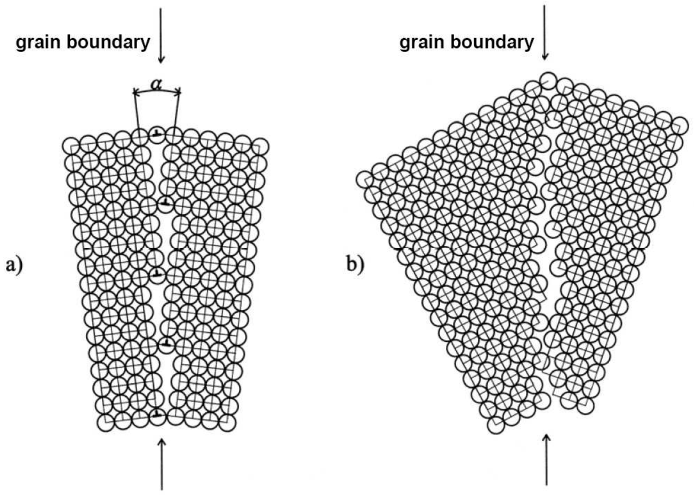

Figure B.5: Different types of grain boundaries: a) low angle grain boundary ($\alpha < 15°$) b) high angle grain boundary (Bauser et al., 2001).

Plastic deformation is the distortion and reformation of atomic bonds. In perfect crystals the plastic deformation would occur by sliding one plane of atoms over an adjacent plane. The necessary shear stress to deform the material would be hundreds to thousands times bigger than it is in reality. This is based on the sliding of dislocations which needs a relatively small shearing stress to slide through the metal. It is obvious that this slip mechanism would tend to be more difficult as the atomic slip distance increases, which means that the dislocation motion will always occur first in high-atomic-density-planes and directions. The motion of the dislocation will start when the shear stress on the plane exceeds a critical value. This shear stress is called Peierls-stress τ_p which can approximately be calculated from

$$\tau_p = \frac{2\mu}{1-\nu}\exp\left(-\frac{2\pi}{(1-\nu)}\frac{d}{b}\right) \tag{B.1}$$

where μ is the shear modulus and ν the Poisson ratio of the material. d describes the distance between the gliding planes and b the Burgers vector. This exponential dependence on $\frac{d}{b}$ explains why high-atomic-density-directions are favorable due to the small occurring Burgers vector. For cubic systems (lattice parameter a) high indexed planes are favorable through the maximum distance d between the planes with Miller indizes $\{hkl\}$ given by

$$d = \frac{a}{\sqrt{h^2+k^2+l^2}}\,. \tag{B.2}$$

These preferred planes and directions combined are called slip systems and can be found in different types of unit cells. The number of different high-density plane-directions is essential for the characteristical deformability of a metal. Due to the fact that fcc has twelve of them, determined through the 4 octahedron $\{111\}$ slip planes with the 3 associated $\langle 110\rangle$ directions, fcc is relatively ductile compared to hcp which has only three high-density plane-directions. For bcc slip is possible on more than one family of planes ($\{110\}$,$\{112\}$ and $\{123\}$) in the 2 associated $\langle 111\rangle$ directions. This results in a maximum of 48 possible slip systems. However, some of these slip systems are often only operable in certain temperature ranges.

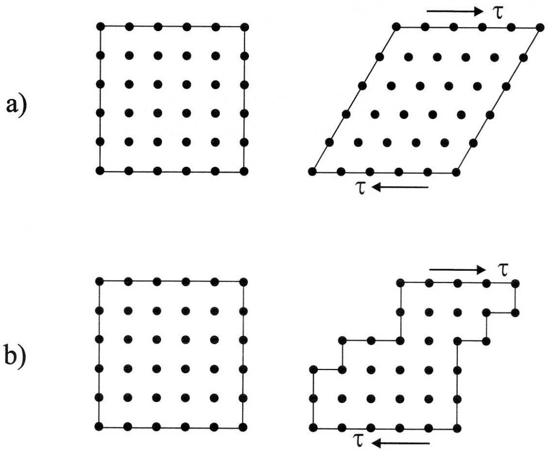

Figure B.6: Different deformation behavior when applying shear stress: a) elastic deformation b) plastic deformation (Bauser et al., 2001).

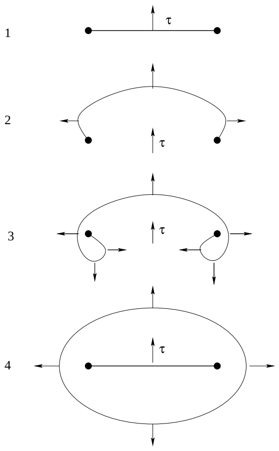

Figure B.7: Frank-Read mechanism (Bauser et al., 2001).

The dislocation motion is also obstructed by different lattice defects so that the necessary shear stress becomes higher. For example, foreign atoms in form of a substitution or interstitial atoms serve as obstacles for dislocation. This phenomenon is called solution hardening which is of major importance for aluminum alloys. In that case the foreign atoms create bracing. The dislocation motion can also be hindered by other dislocations. During deformation the material can harden through the accumulation of dislocations at obstacles like grain boundaries. Beyond these phenomena the motion of dislocation can also create new dislocations which become an obstacle. Figure B.7 exemplarily shows the Frank-Read mechanism in which the overcoming of the defects generates new dislocations.

B.3 Critical resolved shear stress

The yield stress which characterizes the start of plastic deformation varies for specimen consisting of one single crystal. Deforming the single crystal under different orientations in a tensile test results in different yield stresses. The orientation dependence can be explained by the Peach-Koehler equation. As mentioned in the previous section plastic flow is related to dislocation motion. A dislocation moves when it becomes subjected to a force parallel to the slip plane in slip direction. Hence, it is not the completely applied stress, rather the resolved shear stress in the slip system that causes dislocation motion. The resolved shear stress, also called Schmid stress, τ is related to the applied tensile stress σ by

$$\tau = \sigma \, \cos(\phi) \, \cos(\lambda) = M \, \sigma \, , \tag{B.3}$$

where ϕ is the angle between the tensile direction and the slip plane normal and λ is the angle between tensile direction and the slip direction. This principle relation is shown in Figure B.8. The factor $M = \cos(\phi) \, \cos(\lambda)$ is called Schmid factor and assumes values $0 \leq |M| \leq 0.5$ for tensile deformation. Therefore the force acting on the dislocations depends on the orientation of the slip system relative to the tensile axis. For more possible slip systems, the Schmid-factors are different for each system, meaning that the system with the highest Schmid-factor experiences the highest resolved shear stress. Dislocations start to move if the force acting on the dislocation, which is equivalent to the resolved shear stress, exceeds a critical value σ_{A} (Gottstein, 2004).

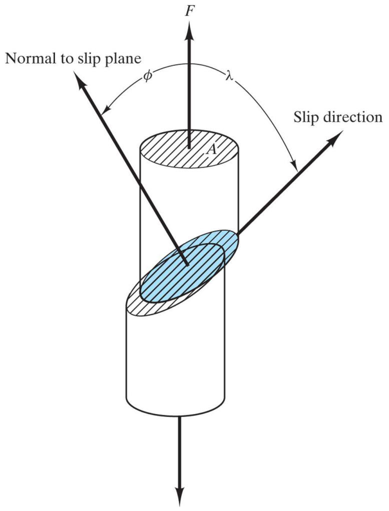

Figure B.8: Determining the Schmid-factor (Shackelford and Sullivan, 2005).

Appendix C

Basics of continuum mechanics

This appendix gives a short insight into the basics of continuum mechanics and makes no claim of completeness. The underlying kinematics are introduced for the general nonlinear case. In the following the mechanical balance equations are given which represent the fundamental relations of continuum mechanics. Finally, the fundamental ideas of material modeling are introduced, i.e. the principles of constitutive theory of materials.

C.1 Flow kinematics

The following kinematics are given in terms of finite deformation measures from which the small deformation case can always be derived. If the motion is characterized with respect to the material coordinates $\boldsymbol{X}$, this is called material, referential or Lagrangian description. In the material description one follows the movement of a particle of body B in time. Another possibility is the use of the spatial coordinates $\boldsymbol{x}$ when the motion of body B has to be described, which is called spatial or Eulerian description. In this formulation, attention is paid to a point in space and the change of the motion with time t at this point. This description is called current, spatial or Eulerian description of motion. Let $\boldsymbol{X}$ denote the fixed position of a material point in the body B in the undeformed and stress free reference (material) configuration $\mathcal{B}_{\text{ref}}$.

During deformation or motion the configuration changes with time which is described by the time-dependent vector field of the nonlinear spatial deformation map

$$\varphi : \mathcal{B}_{\text{ref}} \rightarrow \mathcal{B}_{\text{cur}} \quad \text{with} \quad \varphi(\boldsymbol{X}, t) := \boldsymbol{x}, \tag{C.1}$$

where $\boldsymbol{x}$ denotes the spatial position of the particle $\boldsymbol{X}$ in the current deformed (spatial) configuration $\mathcal{B}_{\text{cur}}$ at time t. This mapping has to be unique and continously differentiable. In complete analogy to this spatial motion problem, the inverse material motion problem can be formulated. This is described by the material deformation map Φ which is given by

$$\Phi : \mathcal{B}_{\text{cur}} \rightarrow \mathcal{B}_{\text{ref}} \quad \text{with} \quad \Phi(\boldsymbol{x}, t) := \boldsymbol{X}\,. \tag{C.2}$$

where physical particles are observed at fixed spatial coordinates $\boldsymbol{x}$.

The motion of a body B is characterized by the displacement vector $\boldsymbol{u}$, defined by

$$\boldsymbol{u}(\boldsymbol{X}, t) := \varphi(\boldsymbol{X}, t) - \boldsymbol{X}\,. \tag{C.3}$$

To introduce the deformation gradient $\boldsymbol{F}$ we describe the distance between two neighboring material points in the reference configuration by the vector $\mathrm{d}\boldsymbol{X}$. Due to the deformation this

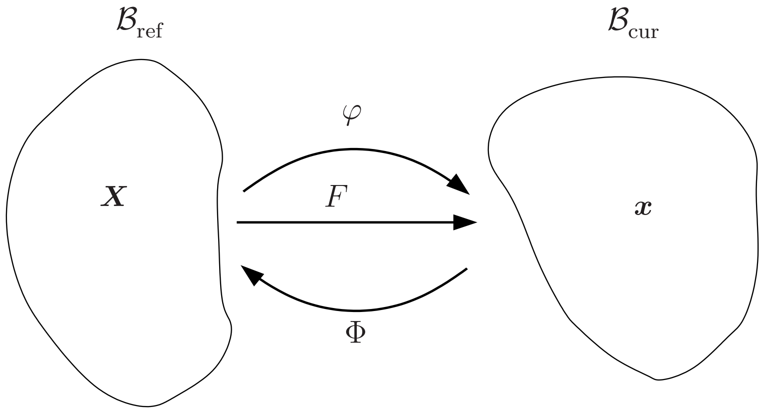

Figure C.1: Kinematics: Deformation map ϕ maps the reference configuration $\mathcal{B}_{\text{ref}}$ to the current configuration $\mathcal{B}_{\text{cur}}$ and the deformation map Φ maps vice versa.

vector is mapped into its image in the current configuration given by $\mathrm{d}\boldsymbol{x} = \mathrm{d}\boldsymbol{X} + \mathrm{d}\boldsymbol{u}$ where $\mathrm{d}\boldsymbol{u}$ is the differential total displacement vector. These vectors are connected by the deformation gradient $\boldsymbol{F}$ via

$$\mathrm{d}\boldsymbol{x} = \frac{\partial \boldsymbol{x}}{\partial \boldsymbol{X}}\mathrm{d}\boldsymbol{X} = \left(\boldsymbol{I} + \frac{\partial \boldsymbol{u}}{\partial \boldsymbol{X}}\right)\mathrm{d}\boldsymbol{X} := \boldsymbol{F}\mathrm{d}\boldsymbol{X}\,, \tag{C.4}$$

where $\boldsymbol{H} := \frac{\partial \boldsymbol{u}}{\partial \boldsymbol{X}}$ is also known as the displacement gradient or shape distortion tensor and $\boldsymbol{I}$ denotes the second rank identity tensor and. The deformation gradient can therefore also be written as

$$\boldsymbol{F} = \nabla_r \varphi(\boldsymbol{X}, t)\,, \tag{C.5}$$

where ∇_r denotes the derivative with respect to the reference configuration. $\boldsymbol{F}$ is a second order two-field tensor which is in general non-symmetric. Since the deformation gradient is a linear operator, the local transformation in (C.4) is also linear. To maintain the connection of B during the deformation process, the mapping has to be one-to-one which excludes a singularity of $\boldsymbol{F}$ which is formally guarantied by a condition for the determinant of the deformation gradient, called Jacobian

$$J = \det\boldsymbol{F} \neq 0. \tag{C.6}$$

To exclude a self penetration of the body, the Jacobian has to be positive: $J > 0$. Due to this requirements $\boldsymbol{F}$ is invertible. (C.4) provides the transformation between line elements from the initial to the current configuration. The transformation relations for area and volume elements are given for completeness:

$$\begin{aligned} &\text{area element :} & \mathrm{d}\boldsymbol{a} &= \boldsymbol{n}\mathrm{da} = J\boldsymbol{F}^{-T}\boldsymbol{N}\mathrm{dA} = J\boldsymbol{F}^{-T}\mathrm{d}\boldsymbol{A}\,. \\ &\text{volume element :} & \mathrm{d}v &= J\mathrm{d}V\,. \end{aligned} \tag{C.7}$$

The deformation gradient $\boldsymbol{F}$ can be expressed as the product of a proper orthogonal rotation tensor $\boldsymbol{R}$ with $\boldsymbol{R}^{-1} = \boldsymbol{R}^T$ and one of two symmetrical tensors $\boldsymbol{U}$ and $\boldsymbol{V}$ which are a measure for pure stretching. Two representations are possible

$$\boldsymbol{F} = \boldsymbol{R}\boldsymbol{U} = \boldsymbol{V}\boldsymbol{R} \tag{C.8}$$

where $\boldsymbol{U}$ and $\boldsymbol{V}$ are the right and left stretch tensor, respectively (Ogden, 1984).

In continuum mechanics $\boldsymbol{F}$ is the most important measure of deformation and basis for strain measures. One strain measure used in this work is the Green-Lagrange strain tensor

$$\boldsymbol{E} = \frac{1}{2}(\boldsymbol{F}^T\boldsymbol{F} - \boldsymbol{I}) \tag{C.9}$$

where $\boldsymbol{C} := \boldsymbol{F}^T\boldsymbol{F}$ is the right Cauchy-Green tensor.

In the context of crystal plasticity three different coordinate systems are used (Roters et al., 2010).

- shape coordinate system: This is a curvilinear system based on the physical shape of the body during deformation.
- lattice coordinate system: The coordinate axes are fixed locally parallel to the crystallographic directions. The distinction between shape and lattice distortion is crucial for calculating internal stresses (Bilby et al., 1958). The reason for this is that the shape deformation does not necessarily follow the deformation of the lattice. They only coincide when no motion of crystal defects occurs (Roters et al., 2010).
- laboratory coordinate system: Often the deformation of the body B and its associated lattice is described in a coordinate system that does not deform with the body.

In the case of crystal plasticity the perfect single crystal is often used as reference state, however, it is also possible to choose any state just before deformation or any state at any time t in an incremental setting. The deformation gradient can be decomposed into an elastic part $\boldsymbol{F}_\mathrm{E}$ and a plastic part $\boldsymbol{F}_\mathrm{P}$ called the Kröner decomposition (Kröner, 1961)

$$\boldsymbol{F} = \boldsymbol{F}_\mathrm{E}\boldsymbol{F}_\mathrm{P} \tag{C.10}$$

which is schematically illustrated in Figure C.2.

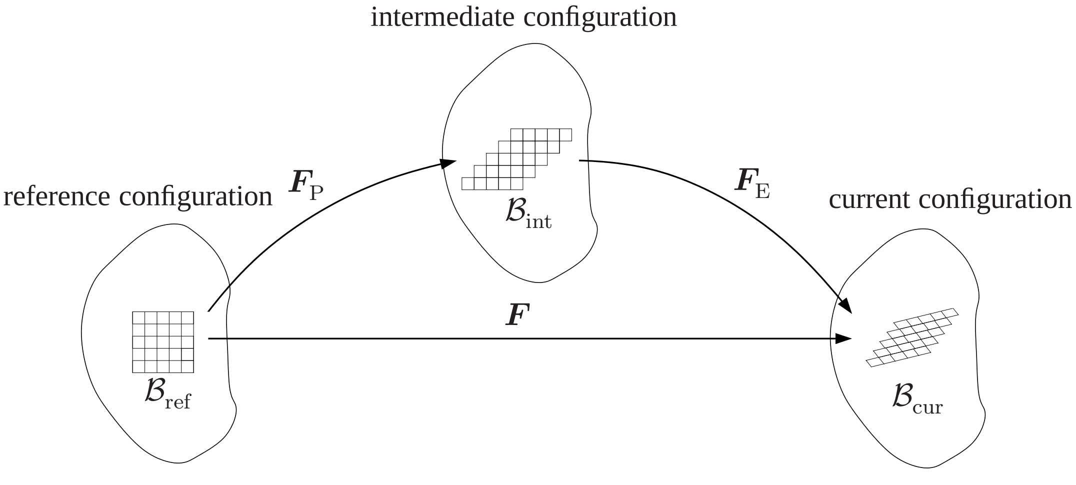
intermediate configuration
reference configuration
$\boldsymbol{F}_\mathrm{P}$
$\mathcal{B}_\mathrm{int}$
$\boldsymbol{F}_\mathrm{E}$
current configuration
$\boldsymbol{F}$
$\mathcal{B}_\mathrm{ref}$
$\mathcal{B}_\mathrm{cur}$

Figure C.2: Decomposition of the total deformation gradient.

$\boldsymbol{F}_{\mathrm{E}}$ is the elastic deformation component which represents the local elastic distortion of a material due to stretch and rotation of the microscopic structure. Therefore $\boldsymbol{F}_{\mathrm{E}}$ occurs due to reversible response of the lattice to external loads and displacements. $\boldsymbol{F}_{\mathrm{P}}$ is the plastic distortion which represents the local deformation due to the flow of defects through the microscopic structure. Therefore $\boldsymbol{F}_{\mathrm{P}}$ is an irreversible permanent deformation. The transformation of the reference state by $\boldsymbol{F}_{\mathrm{P}}$ leads to an intermediate configuration. Investigating the crystal lattice in the different configuration as shown in Figure 4.1, the transformation via $\boldsymbol{F}_{\mathrm{P}}$ from the reference to the intermediate configuration renders the lattice unchanged and all the deformation is produced by dislocation slip. The plastic deformation is assumed to be volume preserving which means $\det \boldsymbol{F}_{\mathrm{P}} = 1$. During the transformation from the intermediate configuration to the current one via $\boldsymbol{F}_{\mathrm{E}}$, the lattice undergoes a purely elastic shape change. This means the external force has to be maintained in order to preserve the shape changes (Roters et al., 2010).

The dependence of the deformation $\varphi(\boldsymbol{X}, t)$ on time t has to be considered in nonlinear problems in case that the constitutive behavior is history dependent. The spatial velocity $\boldsymbol{v}$ is introduced as the material time derivative of the spatial motion map

$$\boldsymbol{v} := \mathrm{D}_t \varphi(\boldsymbol{X}, t) = \frac{\partial \varphi(\boldsymbol{X}, t)}{\partial t} = \dot{\varphi}(\boldsymbol{X}, t). \tag{C.11}$$

From this the time derivative for the deformation gradient $\boldsymbol{F}$ follows from (C.5) to be

$$\dot{\boldsymbol{F}} = \nabla_r \varphi(\dot{\boldsymbol{X}}, t) = \nabla_c \hat{\boldsymbol{v}} \boldsymbol{F} \tag{C.12}$$

where ∇_c is the derivative with respect to the current configuration. $\hat{\boldsymbol{v}}$ describes the velocity of a particle at point $\boldsymbol{x}$ at time t in the current configuration given by $\hat{\boldsymbol{v}}(\boldsymbol{x}, t) = \hat{\boldsymbol{v}}(\varphi(\boldsymbol{X}, t), t) = \boldsymbol{v}(\boldsymbol{X}, t)$. The spatial velocity gradient is defined as

$$\boldsymbol{L} := \nabla_c \hat{\boldsymbol{v}} = \dot{\boldsymbol{F}} \boldsymbol{F}^{-1}. \tag{C.13}$$

The relationship of $\boldsymbol{L}$ to $\boldsymbol{L}_{\mathrm{E}}$ and $\boldsymbol{L}_{\mathrm{E}}$ can be obtained by taking the derivate of (C.10) and apply the product rule of differentiation

$$\dot{\boldsymbol{F}} = \dot{\boldsymbol{F}}_{\mathrm{E}} \boldsymbol{F}_{\mathrm{P}} + \boldsymbol{F}_{\mathrm{E}} \dot{\boldsymbol{F}}_{\mathrm{P}} \tag{C.14}$$

which yields in combination with (C.13) to

$$\boldsymbol{L} = \dot{\boldsymbol{F}}_{\mathrm{E}} \boldsymbol{F}_{\mathrm{E}}^{-1} + \boldsymbol{F}_{\mathrm{E}} \dot{\boldsymbol{F}}_{\mathrm{P}} \boldsymbol{F}_{\mathrm{P}}^{-1} \boldsymbol{F}_{\mathrm{E}}^{-1} = \boldsymbol{L}_{\mathrm{E}} + \boldsymbol{F}_{\mathrm{E}} \boldsymbol{L}_{\mathrm{P}} \boldsymbol{F}_{\mathrm{E}}^{-1}. \tag{C.15}$$

Due to the fact that the spatial velocity gradient is calculated in the deformed configuration and the plastic velocity gradient $\boldsymbol{L}_{\mathrm{P}}$ is evaluated in the intermediate configuration, $\boldsymbol{L}_{\mathrm{P}}$ has to be mapped into the deformed configuration by $\boldsymbol{F}_{\mathrm{E}}$.

C.2 Mechanical balance equation

Balance laws describe the universally valid physical principles which are independent of the specific material properties. In the following the differential equations which describe the local balance equations such as balance of mass, balance of linear and angular momentum as well as balance of energy and balance of entropy are derived from a general balance law introduced next (see, e.g., Liu (2002)). These equations represent the fundamental relations of continuum mechanics. A balance law is called conservation law if it has vanishing sources.

Let us start with a general balance equation in integral form for a closed system describing the evolution of a physical quantity Λ in a body B in a spatial motion problem. The actual state of a body B can mathematically be described by volume integrals over the specific density of the physical quantity $\boldsymbol{\Lambda}$. The impact of the surroundings has to be described by area or volume integrals over the corresponding volume or area densities of the applied loadings. A general balance equation can then be written as

$$\mathrm{D}_t \int_{\mathcal{B}_{\mathrm{ref}}} \boldsymbol{\Lambda}\, \mathrm{d}V = - \int_{\partial \mathcal{B}_{\mathrm{ref}}} \boldsymbol{\phi}_n\, \mathrm{d}A + \int_{\mathcal{B}_{\mathrm{ref}}} \boldsymbol{\zeta}\, \mathrm{d}V + \int_{\mathcal{B}_{\mathrm{ref}}} \boldsymbol{\xi}\, \mathrm{d}V \tag{C.16}$$

where $\boldsymbol{\phi}_n$ denotes the non-convective flux density vector, $\boldsymbol{\zeta}$ the corresponding source density and $\boldsymbol{\xi}$ the production in the body. Assuming $\boldsymbol{\phi}_n(\boldsymbol{x}, \boldsymbol{n}, t)$ depending on the position $\boldsymbol{x}$ and the outward unit normal vector $\boldsymbol{n}$ and time t leads to the Cauchy lemma which states that there exists a unique tensor $\boldsymbol{\Phi}$ such that

$$\boldsymbol{\phi}_n(\boldsymbol{x}, \boldsymbol{n}, t) = \boldsymbol{\Phi}(\boldsymbol{x}, t)\, \boldsymbol{n}. \tag{C.17}$$

Using this the balance equation can be rewritten

$$\mathrm{D}_t \int_{\mathcal{B}_{\mathrm{ref}}} \boldsymbol{\Lambda}\, \mathrm{d}V = - \int_{\partial \mathcal{B}_{\mathrm{ref}}} \boldsymbol{\Phi}\, \boldsymbol{n}\, \mathrm{d}A + \int_{\mathcal{B}_{\mathrm{ref}}} \boldsymbol{\zeta}\, \mathrm{d}V + \int_{\mathcal{B}_{\mathrm{ref}}} \boldsymbol{\xi}\, \mathrm{d}V. \tag{C.18}$$

Applying the Gauss theorem to reformulate the area integral into a volume integral and with the knowledge that the integral has to hold for all volume elements let $\mathrm{d}V \to 0$ lead to the local form of the balance equation

$$\mathrm{D}_t \boldsymbol{\Lambda} = -\mathrm{Div} \boldsymbol{\Phi} + \boldsymbol{\zeta} + \boldsymbol{\xi}. \tag{C.19}$$

Further details with respect to material and spatial motion problem can be found, e.g., in Gurtin et al. (2009).

C.2.1 Balance of mass

Only processes are considered in which the mass of a system is conserved. This implies that no change in mass occurs and that the mass in the initial and current configuration has to be equal. This leads to

$$\rho_0 \mathrm{d}V = \rho \mathrm{d}v \tag{C.20}$$

where ρ_0 and ρ describe the densities in the initial and current configuration. The balance of mass can also be derived from (C.19) by substituting $\boldsymbol{\Lambda}$ by ρ_0 and setting the flux $\boldsymbol{\Phi}$, the production $\boldsymbol{\zeta}$ and source densities $\boldsymbol{\xi}$ equal to zero which leads to

$$\mathrm{D}_t \rho_0 = 0 \tag{C.21}$$

C.2.2 Balance of linear momentum

The balance of linear momentum can be understood as the continuum version of Newton's second law. The change of linear momentum $\rho_0\, \boldsymbol{v}$ in time is equal to the sum of all external forces acting on the body $\mathcal{B}$. With the application of Cauchy's stress theorem and use of the divergence theorem one derives

$$\mathrm{D}_t \rho_0\, \boldsymbol{v} = \mathrm{Div} \boldsymbol{P}^T + \rho_0 \boldsymbol{b} \tag{C.22}$$

where $\boldsymbol{P}$ denotes the unsymmetric first Piola-Kirchhoff stress relating spatial forces to material area elements and $\boldsymbol{b}$ denotes the volume forces. The Piola-Kirchhoff stress is related to the the Cauchy stress $\boldsymbol{T}$ via a push forward to the spatial configuration with

$$\boldsymbol{P} = J\, \boldsymbol{T} \boldsymbol{F}^{-T}. \tag{C.23}$$

C.2.3 Balance of angular momentum

The change of angular momentum in time with respect to a point A is equal to the sum of all moments stemming from external volume and surface forces $\boldsymbol{b}$ and $\boldsymbol{t}$ with respect to point A. Writing the balance of angular momentum in a spatial integral form leads to

$$\mathrm{d}_t \int_{\mathcal{B}_{\mathrm{cur}}} (\boldsymbol{x} - \boldsymbol{x}_A) \times (\rho\, \boldsymbol{v}) \mathrm{d}v = \int_{\mathcal{B}_{\mathrm{cur}}} (\boldsymbol{x} - \boldsymbol{x}_A) \times \boldsymbol{t}\, \mathrm{d}a + \int_{\mathcal{B}_{\mathrm{cur}}} (\boldsymbol{x} - \boldsymbol{x}_A) \times \boldsymbol{b}\, \mathrm{d}v. \tag{C.24}$$

This equation yields after some manipulations to the symmetry of the Cauchy stress tensor

$$\boldsymbol{T} = \boldsymbol{T}^T \tag{C.25}$$

and the unsymmetry of the first Piola-Kirchhoff stress tensor

$$\boldsymbol{P}\, \boldsymbol{F}^T = (\boldsymbol{P}\, \boldsymbol{F}^T)^T. \tag{C.26}$$

C.2.4 Balance of energy

The balance of energy postulates the conservation of energy in a thermodynamical process which is also known as first law of thermodynamics. The change of the total energy in time is equal to the sum of the mechanical power of all external loads P_{ext} and the heat supply Q_{ext}

$$\mathrm{D}_t E = P_{\mathrm{ext}} + Q_{\mathrm{ext}} \tag{C.27}$$

where the total energy can be split into internal U and kinetic energy K. The balance of energy does not provide any information about the direction of a thermodynamic process. The local form of the first law of thermodynamics can be obtained by inserting relations for E,P_{ext} and Q_{ext} and some manipulation (e.g., Greve, 2003)

$$\rho_0\, \mathrm{D}_t u = -\mathrm{Div} \boldsymbol{Q} + \frac{1}{2} \boldsymbol{S} \cdot \dot{\boldsymbol{C}} + \rho_0\, r \tag{C.28}$$

where u denotes the internal energy density, $\boldsymbol{Q}$ the material heat flux vector and r the external heat supply per unit mass. $\frac{1}{2}\boldsymbol{S} \cdot \dot{\boldsymbol{C}}$ is named specific stress power. $\boldsymbol{S}$ describes the symmetric second PiolaKirchhoff stress tensor which is related to the first PiolaKirchhoff stress tensor $\boldsymbol{P}$ via

$$\boldsymbol{S} = \boldsymbol{F}^{-1} \boldsymbol{P}. \tag{C.29}$$

C.2.5 Balance of entropy

The direction of a thermodynamical process is given by the second law of thermodynamics which states that the internal entropy production per unit mass ξ is non-negative

$$\xi \geq 0. \tag{C.30}$$

The balance of entropy states that rate of entropy η is equal to the divergence of the entropy flux $\boldsymbol{H}$ plus the source and the production terms s and ξ

$$\rho_0 \, \mathrm{D}_t \eta = -\mathrm{Div} \boldsymbol{H} + \rho_0 (s + \xi). \tag{C.31}$$

C.3 Concepts in material modeling

The fundamental concepts of material modeling are introduced in the following. The previously described kinematics and balance equations are a general basis for formulating the thermomechanical behavior of a continuum body. For the distinction of different materials constitutive equations are necessary to complete the framework. The constitutive equations have to fulfill principles of the constitutive theory of materials in order to not contradict general physical observations. These principles are summarized (see, e.g., Holzapfel (2000); Truesdell and Noll (1965)) as follows: The principle of equipresence demands a priori the same set of variables for all constitutive equations. The principle of determinism describes the fact that the present state of a particle is only determined by the history of the body and not its future. The principle of local action states that the material functions are restricted to pointwise dependences and the state of particles outside of an arbitrary neighborhood can be disregarded. The principle of material frame-indifference states that the response of a material is independent of the observer. The constitutive equations must be invariant with respect to frame changes (Truesdell and Noll, 1965). That constitutive equations are consistent with forms of symmetry that can exist in materials. This requirement is named the principle of material symmetry (Gurtin et al., 2009). The principle of Isomorphism states that the elastic properties, if properly identified, are not effected by yielding (Bertram, 2003). The used constitutive equations for modeling different material behavior which fulfill these concepts can be found in the various chapters.

References

Arns, C., Knackstedt, M., Pinczewski, W., Garboczi, E., Computation of linear elastic properties from microtomographic images: Methodology and agreement between theory and experiment, Geophysics, Volume 67, pp. 1396–1405, 2002.

Asaro, R., Needleman, A., Overview no. 42 Texture development and strain hardening in rate dependent polycrystals, Acta Metallurgica, Volume 33, pp. 923–953, 1985.

Ashby, M. F., The deformation of plastically non-homogeneous materials, Philosophical Magazine, Volume 21, pp. 399 – 424, 1970.

Bargel, H.-J., Schulze, G., Werkstoffkunde, 7th edition, Springer Verlag, Berlin, 2000.

Bargmann, S., Ekh, M., Runesson, K., Svendsen, B., Modeling of polycrystals with gradient crystal plasticity: A comparison of strategies, Philosophical Magazine, Volume 90, pp. 1263 – 1288, 2010.

Bartel, T., Multiskalenmodellierung martensitischer Phasentransformationen in Formgedächtnislegierungen unter Verwendung relaxierter Energiepotenziale, Ph.D. thesis, Mitteilungen aus dem Institut für Mechanik Nr. 150, Ruhr-Universität Bochum, Germany, 2009.

Bauser, M., Sauer, G., Siegert, K., Strangpressen, 2nd edition, Aluminium-Verlag, Düsseldorf, 2001.

Bayley, C., Brekelmans, W., Geers, M., A comparison of dislocation induced back stress formulations in strain gradient crystal plasticity, International Journal of Solids and Structures, Volume 43, pp. 7268–7286, 2006.

Benveniste, Y., A new approach to the application of Mori-Tanaka's theory in composite materials, Mechanics of Materials, Volume 6, pp. 147–157, 1987.

Bertram, A., Finite thermoplasticity based on isomorphisms, International Journal of Plasticity, Volume 19, pp. 2027–2050, 2003.

Bilby, B., Gardner, L., Smith, E., The relation between dislocation density and stress, Acta Metallurgica, Volume 6, pp. 29–33, 1958.

Böhlke, T., Fritzen, F., Jöchen, K., Tsotsova, R., Numerical methods for the quantification of the mechanical properties of crystal aggregateswith morphologic and crystallographic texture, International Journal of Material Forming, Volume 2, pp. 915–917, 2009.

Böhlke, T., Jöchen, K., Kraft, O., Löhe, D., Schulze, V., Elastic properties of polycrystalline microcomponents, Mechanics of Materials, Volume 42, pp. 11–23, 2010.

Böhlke, T., Risy, G., Bertram, A., A micro-mechanically based quadratic yield condition for textured polycrystals, ZAMM Zeitschrift fur Angewandte Mathematik und Mechanik, Volume 88, pp. 379–387, 2008.

Brantner, H., Pippan, R., Prantl, W., Local and global fracture toughness of a flame sprayed molybdenum coating, Journal of Thermal Spray Technology, Volume 12, pp. 560–571, 2003.

Brown, S. B., Kim, K. H., Anand, L., An internal variable constitutive model for hot working of metals, International Journal of Plasticity, Volume 5, pp. 95–130, 1989.

Bunge, H. J., Some applications of the Taylor theory of polycrystal plasticity, Kristall und Technik, Volume 5, pp. 145–175, 1970.

Castaneda, P. P., Willis, J. R., The effect of spatial distribution on the effective behavior of composite materials and cracked media, Journal of the Mechanics and Physics of Solids, Volume 43, pp. 1919–1951, 1995.

Chin, G. Y., Mammel, W. L., Computer solutions of the Taylor analysis for axisymmetric flow, Transactions of the Metallurgical Society of AIME, Volume 239, pp. 1400–1405, 1967.

Christensen, R. M., A critical evaluation for a class of micro-mechanics models, Journal of the Mechanics and Physics of Solids, Volume 38, pp. 379–404, 1990.

Dao, M., Chollacoop, N., Vliet, K. J. V., Venkatesh, T. A., Suresh, S., Computational modeling of the forward and reverse problems in instrumented sharp indentation, Acta Materialia, Volume 49, pp. 3899–3918, 2001.

Delfosse, D., Cherradi, N., Ilschner, B., Numerical and experimental determination of residual stresses in graded materials, Composites Part B: Engineering, Volume 28, pp. 127–141, 1997.

Du, D., Zheng, Q., A further exploration of the interaction direct derivative (IDD) estimate for the effective properties of multiphase composites taking into account inclusion distribution, Acta Mechanica, Volume 157, pp. 61–80, 2002.

Duschlbauer, D., Computational Simulation of the Thermal Conductivity of MMCs under Consideration of the Inclusion-Matrix Interface, Ph.D. thesis, ILSB, Vienna University of Technology, Austria, 2004.

Dvorak, G., Transformation field analysis of inelastic composite materials, Proceedings of the Royal Society of London, Volume A 437, pp. 311–326, 1992.

Ekh, M., Grymer, M., Runesson, K., Svedberg, T., Gradient crystal plasticity as part of the computational modelling of polycrystals, International Journal for Numerical Methods in Engineering, Volume 72, pp. 197–220, 2007.

El-Dasher, B. S., Adams, B. L., Rollett, A. D., Viewpoint: experimental recovery of geometrically necessary dislocation density in polycrystals, Scripta Materialia, Volume 48, pp. 141–145, 2003.

Engel, U., Eckstein, R., Microforming–from basic research to its realization, Journal of Materials Processing Technology, Volume 125-126, pp. 35–44, 2002.

Erickson, J., Mobility of edge dislocations on 112 slip planes in 3.25 silicon iron, Journal of Applied Physics, Volume 33, pp. 2499–2506, 1962.

Eshelby, J. D., The determination of the elastic field of an ellipsoidal inclusion, and related problems, Proceedings of the Royal Society of London, Volume 241, pp. 376–396, 1957.

Evers, L. P., Brekelmans, W. A. M., Geers, M. G. D., Non-local crystal plasticity model with intrinsic SSD and GND effects, Journal of the Mechanics and Physics of Solids, Volume 52, pp. 2379–2401, 2004a.

Evers, L. P., Brekelmans, W. A. M., Geers, M. G. D., Scale dependent crystal plasticity framework with dislocation density and grain boundary effects, International Journal of Solids and Structures, Volume 41, pp. 5209–5230, 2004b.

Evers, L. P., Parks, D. M., Brekelmans, W. A. M., Geers, M. G. D., Crystal plasticity model with enhanced hardening by geometrically necessary dislocation accumulation, Journal of the Mechanics and Physics of Solids, Volume 50, pp. 2403–2424, 2002.

Forest, S., Some links between Cosserat, strain gradient crystal plasticity and the statistical theory of dislocations, Philosophical Magazine, Volume 88, pp. 3549–3563, 2008.

Fu, H. H., Benson, D. J., Meyers, M. A., Analytical and computational description of effect of grain size on yield stress of metals, Acta Materialia, Volume 49, pp. 2567–2582, 2001.

Fülöp, T., Brekelmans, W., Geers, M., Size effects from grain statistics in ultra-thin metal sheets, Journal of Materials Processing Technology, Volume 174, pp. 233–238, 2006.

Gao, H., Huang, Y., Geometrically necessary dislocation and size-dependent plasticity, Scripta Materialia, Volume 48, pp. 113–118, 2003.

Gavazzi, A. C., Lagoudas, D. C., On the numerical evaluation of Eshelby's tensor and its application to elastoplastic fibrous composites, Computational Mechanics, Volume 7, pp. 13–19, 1990.

Geers, M., Brekelmans, W., Janssen, P., Size effects in miniaturized polycrystalline FCC samples: Strengthening versus weakening, International Journal of Solids and Structures, Volume 43, pp. 7304–7321, 2006.

Geers, M., Kouznetsova, V., Brekelmans, W., Multi-scale computational homogenization: Trends and challenges, Journal of Computational and Applied Mathematics, Volume 234, pp. 2175–2182, 2010.

Gell, M., Worthington, P., The plastic deformation and fracture of Iron-3% Silicon in the temperature range 295K-473K, Acta Metallurgica, Volume 14, pp. 1265–1271, 1966.

Ghafouri-Azar, R., Mostaghimi, J., Chandra, S., Modeling development of residual stresses in thermal spray coatings, Computational Materials Science, Volume 35, pp. 13–26, 2006.

Giannakopoulos, A. E., Suresh, S., Determination of elastoplastic properties by instrumented sharp indentation, Scripta Materialia, Volume 40, pp. 1191–1198, 1999.

Gottstein, G., Physical Foundations of Materials Science, 1th edition, Springer-Verlag, Berlin, 2004.

Greer, J. R., Oliver, W. C., Nix, W. D., Size dependence of mechanical properties of gold at the micron scale in the absence of strain gradients, Acta Materialia, Volume 53, pp. 1821–1830, 2005.

Greve, R., Kontinuumsmechanik: Ein Grundkurs fü Ingenieure und Physiker, 1th edition, Springer-Verlag, Berlin, 2003.

Groeber, M., Gosh, S., Uchic, M. D., Dimiduk, D. M., Developing a robust 3-D characterization-representation framework for modeling polycrystalline materials, JOM Journal of the Minerals, Metals and Materials Society, Volume 59, pp. 32–36, 2007.

Gross, D., Seelig, T., Bruchmechanik, mit einer Einführung in die Mikromechanik, 4th edition, Springer, Berlin, Heidelberg, 2001.

Guinovart-Díaz, R., Rodríguez-Ramos, R., Bravo-Castillero, J., Sabina, F. J., Otero-Hernández, J. A., Maugin, G. A., A recursive asymptotic homogenization scheme for multi-phase fibrous elastic composites, Mechanics of Materials, Volume 37, pp. 1119–1131, 2005.

Gurtin, M., A finite-deformation, gradient theory of single-crystal plasticity with free energy dependent on densities of geometrically necessary dislocations, International Journal of Plasticity, Volume 24, pp. 702–725, 2008.

Gurtin, M., Fried, E., Anand, L., The Mechanics and Thermodynamics of Continua, 1th edition, Cambridge University Press, Cambridge, 2009.

Gurtin, M. E., A gradient theory of single-crystal viscoplasticity that accounts for geometrically necessary dislocations, Journal of the Mechanics and Physics of Solids, Volume 50, pp. 5–32, 2002.

Hall, E., The deformation and ageing of mild steel: III Discussion of results, Proceedings of the Physical Society. Section B, Volume 64, pp. 747–753, 1951.

Han, D., Jr, J. J. M., Strength and Toughness Degradation of Tungsten Carbide-Cobalt Due to Thermal Shock, Journal of the American Ceramic Society, Volume 73, pp. 3692–3695, 1990.

Hashin, Z., Shtrikman, S., A variational approach to the theory of the elastic behaviour of multiphase materials, Journal of the Mechanics and Physics of Solids, Volume 11, pp. 127–140, 1963.

Henning, M., Größeneffekte auf die mechanischen Eigenschaften - Experiment und Simulation, Vol. 10 of Saarbrücker Reihe Materialwissenschaft und Werkstofftehcnik, 4th edition, Shaker Verlag, Aachen (Germany), 2008.

Henning, M., Vehoff, H., Local mechanical behavior and slip band formation within grains of thin sheets, Acta Materialia, Volume 53, pp. 1285–1292, 2005.

Henning, M., Vehoff, H., Statistical size effects based on grain size and texture in thin sheets, Materials Science and Engineering: A, Volume 452-453, pp. 602–613, 2007.

Henning, M., Vehoff, H., Size effects resulting from local strain hardening; microstructural evaluation of Fe-3% Si and Cu deformed in tension and deep drawing using orientation gradient mapping (OGM), International Journal of Materials Research, Volume 2010, pp. 715–728, 2010.

Henrici, P., Applied and computational complex analysis, Volume Power series, integration, conformal mapping, location of zeros, Wiley, New York, 1974.

Hertzberg, R. W., Deformation and fracture mechanics of engineering materials, 4th edition, John Wiley & Sons, Chichester, 1995.

Hill, R., A self-consistent mechanics of composite materials, Journal of the Mechanics and Physics of Solids, Volume 13, pp. 213–222, 1965.

Hoc, T., Crépin, J., Gélébart, L., Zaoui, A., A procedure for identifying the plastic behavior of single crystals from the local response of polycrystals, Acta Materialia, Volume 51, pp. 5477–5488, 2003.

Holzapfel, G., Nonlinear Solid Mechanics: A Continuum Approach for Engineering, 1st edition, John Wiley & Sons, Chichester, 2000.

Hsieh, C., Tuan, W., Poisson's ratio of two-phase composites, Materials Science and Engineering A, Volume 396, pp. 202–205, 2005.

Hull, D., Orientation and Temperature Dependence of Plastic Deformation Processes in 325% Silicon Iron, Proceedings of the Royal Society of London. Series A, Mathematical and Physical Sciences, Volume 274, pp. 5–20, 1963.

Hussainova, I., Kubarsepp, J., Pirso, J., Mechanical properties and features of erosion of cermets, Wear, Volume 250, pp. 818–825, 2001.

Ito, K., Vitek, V., Atomistic study of non-schmid effects in the plastic yielding of bcc metals, Philosophical Magazine A: Physics of Condensed Matter, Structure, Defects and Mechanical Properties, Volume 81, pp. 1387–1407, 2001.

Jänicke, R., Diebels, S., Sehlhorst, H., Düster, A., Two-scale modelling of micromorphic continua : A numerical homogenization scheme, Continuum Mechanics and Thermodynamics, Volume 21, pp. 297–315, 2009.

Janssen, P., de Keijser, T., Geers, M., An experimental assessment of grain size effects in the uniaxial straining of thin Al sheet with a few grains across the thickness, Materials Science and Engineering: A, Volume 419, pp. 238–248, 2006.

Janssen, P., Hoefnagels, J., de Keijser, T., Geers, M., Processing induced size effects in plastic yielding upon miniaturisation, Journal of the Mechanics and Physics of Solids, Volume 56, pp. 2687–2706, 2008.

Kachanov, M., Tsukrov, I., Shafiro, B., Effective moduli of solids with cavities of various shapes, Appl. Mech. Rev., Volume 47, pp. 151–174, 1994.

Kalidindi, S., Bhattacharyya, A., Doherty, R., How Do Polycrystalline Materials Deform Plastically?, Advanced Materials, Volume 15, pp. 1345–1348, 2003.

Kalidindi, S., Bronkhorst, C., Anand, L., Crystallographic texture evolution in bulk deformation processing of FCC metals, Journal of the Mechanics and Physics of Solids, Volume 40, pp. 537–569, 1992.

Kang, H., Milton, G., Solutions to the PlyaSzeg Conjecture and the Weak Eshelby Conjecture, Archive for Rational Mechanics and Analysis, Volume 188, pp. 93–116, 2008.

Kawashita, M., Nozaki, H., Eshelby Tensor of a Polygonal Inclusion and its Special Properties, Journal of Elasticity, Volume 64, pp. 71–84, 2001.

Kim, H., Kweon, Y., Elastic modulus of plasma-sprayed coatings determined by indentation and bend tests, Thin Solid Films, Volume 342, pp. 201–206, 1999.

King, R., Elastic analysis of some punch problems for a layered medium, International Journal of Solids and Structures, Volume 23, pp. 1657–1664, 1987.

Klusemann, B., Hortig, C., Svendsen, B., Modeling and simulation of the microstructural behaviour in thermal sprayed coatings, PAMM, Volume 9, pp. 421–422, 2009a.

Klusemann, B., Hortig, C., Svendsen, B., Modellierung und Simulation des heterogenen Materialverhaltens in thermisch gespritzten Schichten, in SFB708 - 3. öffentliches Kolloquium: Praxiswissen (3D-Surface Engineering für Werkzeugsysteme der Blechformteilefertigung, 3), 107 – 115, Tillmann, W., Dortmund, 2009b.

Klusemann, B., Svendsen, B., Homogenization methods for multi-phase elastic composites: Comparisons and Benchmarks, Technische Mechanik, Volume 30, pp. 374–386, 2010.

Kok, S., Stander, N., Optimization of a sheet metal forming process using successive multipoint approximations, Structural Optimization, Volume 18, pp. 277–295, 1999.

Kouznetsova, V., Balmachnov, A., Geers, M., A multi-scale model for structure-property relations of materials exhibiting martensite transformation plasticity, International Journal of Material Forming, Volume 2, pp. 491–494, 2009.

Kouznetsova, V., Geers, M., Brekelmans, W., Multi-scale second-order computational homogenization of multi-phase materials: a nested finite element solution strategy, Computer Methods in Applied Mechanics and Engineering, Volume 193, pp. 5525–5550, 2004.

Kouznetsova, V., Geers, M., Brekelmans, W., multiscale Modeling in Solid Mechanics: Computational Approaches, chapter Computational Homogenisation for Non-Linear Heterogeneous Solids, 1–42, 1st ed. edition, Imperial College London, London, 2010.

Kovács, I., Zsoldos, L., Dislocations and plastic deformation, International series of monographs in natural philosophy ; v. 60, Pergamon Press, Oxford, ; New York, :, 1973.

Kröner, E., Zur plastischen verformung des vielkristalls (On the plastic deformation of polycrystals), Acta Metallurgica, Volume 9, pp. 155–161, 1961.

Kubin, L. P., Mortensen, A., Geometrically necessary dislocations and strain-gradient plasticity: a few critical issues, Scripta Materialia, Volume 48, pp. 119–125, 2003.

Kuroda, M., Tvergaard, V., A finite deformation theory of higher-order gradient crystal plasticity, Journal of the Mechanics and Physics of Solids, Volume 56, pp. 2573–2584, 2008.

Langer, S. A., Fuller, E. R., Carter, W. C., OOF: An Image-based Finite-Element Analysis of Material Microstructures, Computing in Science and Engineering, Volume 3, p. 1523, 2001.

Lebensohn, R., Tome, C., A self-consistent anisotropic approach for the simulation of plastic deformation and texture development of polycrystals: Application to zirconium alloys, Acta Metallurgica et Materialia, Volume 41, pp. 2611–2624, 1993.

Lee, J., Angelier, J., Chu, H., Yu, S., Hu, J., Plate-boundary strain partitioning along the sinistral collision suture of the Philippine and Eurasian plates: Analysis of geodetic data and geological observation in southeastern Taiwan, Tectonics, Volume 17, pp. 859–871, 1998.

Lee, J., Ko, D., Lee, K., Kim, B., Identification of the bulk behavior of coatings by nanoindentation test and FE-analysis and its application to forming analysis of the coated steel sheet, Journal of Materials Processing Technology, Volume 187-188, pp. 309–313, 2007.

Lielens, G., Micro-Macro Modeling of structured materials, PhD thesis, 1999.

Liu, I., Continuum Mechanics, 1st edition, Springer Verlag, Berlin, 2002.

Liu, L., Solutions to the Eshelby conjectures, Proceedings of the Royal Society A: Mathematical, Physical and Engineering Science, Volume 464, pp. 573–594, 2008.

Ma, A., Roters, F., Raabe, D., A dislocation density based constitutive model for crystal plasticity FEM including geometrically necessary dislocations, Acta Materialia, Volume 54, pp. 2169–2179, 2006.

Markenscoff, X., On the Shape of the Eshelby Inclusions, Journal of Elasticity, Volume 49, pp. 163–166, 1997.

McPherson, R., The relationship between the mechanism of formation, microstructure and properties of plasma-sprayed coatings, Thin Solid Films, Volume 83, pp. 297–310, 1981.

Mercier, S., Molinari, A., Homogenization of elastic-viscoplastic heterogeneous materials: Self-consistent and Mori-Tanaka schemes, International Journal of Plasticity, Volume 25, pp. 1024–1048, 2009.

Molinari, A., Ahzi, S., Kouddane, R., On the self-consistent modeling of elastic-plastic behavior of polycrystals, Mechanics of Materials, Volume 26, pp. 43–62, 1997.

Molinari, A., Canova, G., Ahzi, S., A self consistent approach of the large deformation polycrystal viscoplasticity, Acta Metallurgica, Volume 35, pp. 2983–2994, 1987.

Mori, T., Tanaka, K., Average stress in matrix and average elastic energy of materials with misfitting inclusions, Acta Metallurgica, Volume 21, pp. 571–574, 1973.

Mura, T., Micromechanics of Defects in Solids, 2nd edition, Martinus Nijhoff, The Hague, The Netherlands, 1982.

Nebel, J., Tillmann, W., Arc spraying of WC-FeCSiMn cored wires. Part 1: Bending, compression, and tension behavior, in Proceedings of the International Thermal Spray Conference, pp. 607–615, Singapore, 2010.

Needleman, A., Sevillano, J. G., Preface to the viewpoint set on: geometrically necessary dislocations and size dependent plasticity, Scripta Materialia, Volume 48, pp. 109–111, 2003.

Nemat-Nasser, S., Hori, M., Bounds and estimates of overall moduli of composites with periodic microstructure, Mechanics of materials, Volume 15, pp. 163–181, 1993.

Nemat-Nasser, S., Hori, M., Micromechanics: overall properties of heterogeneous materials, 2nd edition, Elsevier, Amsterdam, 1999.

Noble, F. W., Hull, D., Deformation of single crystals of iron 3% Silicon, Philosophical Magazine, Volume 12, pp. 777 – 796, 1965.

Nogales, S., Böhm, H. J., Modeling of the thermal conductivity and thermomechanical behavior of diamond reinforced composites, International Journal of Engineering Science, Volume 46, pp. 606–619, 2008.

Nozaki, H., Taya, M., Elastic Fields in a Polygon-Shaped Inclusion With Uniform Eigenstrains, Journal of Applied Mechanics, Volume 64, pp. 495–502, 1997.

Nozaki, H., Taya, M., Elastic Fields in a Polyhedral Inclusion With Uniform Eigenstrains and Related Problems, Journal of Applied Mechanics, Volume 68, pp. 441–452, 2001.

Nye, J., Some geometrical relations in dislocated crystals, Acta Metallurgica, Volume 1, pp. 153–162, 1953.

Ogden, R., Non-linear Elastic Deformations, 1th edition, Dover Publications Inc., New York, 1984.

Okamoto, S., Nakazono, Y., Otsuka, K., Shimoitani, Y., Takada, J., Mechanical properties of WC/Co cemented carbide with larger WC grain size, Materials Characterization, Volume 55, pp. 281–287, 2005.

Oliver, W., Pharr, G., Improved technique for determining hardness and elastic modulus using load and displacement sensing indentation experiments, Journal of Materials Research, Volume 7, pp. 1564–1580, 1992.

Pahr, D., Zysset, P., Influence of boundary conditions on computed apparent elastic properties of cancellous bone, Biomechanics and Modeling in Mechanobiology, Volume 7, pp. 463–476, 2008.

Petch, N., The cleavage strength of polycrystals, Journal of the Iron and Steel Institute, Volume 174, pp. 25–28, 1953.

Pharr, G., Oliver, W., Brotzen, F., On the generality of the relationship among contact stiffness, contact area, and elastic modulus during indentation, Journal of Materials Research, Volume 7, pp. 613–617, 1992.

Pierard, O., Friebel, C., Doghri, I., Mean-field homogenization of multi-phase thermo-elastic composites: a general framework and its validation, Composites Science and Technology, Volume 64, pp. 1587–1603, 2004.

Pierard, O., LLorca, J., Segurado, J., Doghri, I., Micromechanics of particle-reinforced elasto-viscoplastic composites: Finite element simulations versus affine homogenization, International Journal of Plasticity, Volume 23, pp. 1041–1060, 2007.

Polcarova, M., Gemperlova, J., Bradler, J., Jacques, A., George, A., Priester, L., In-situ observation of plastic deformation of Fe-Si bicrystals by white-beam synchrotron radiation topography, Philosophical Magazine A, Volume 78, pp. 105 – 130, 1998.

Ponte Castaneda, P., Suquet, P., Nonlinear Composites, Advances in Applied Mechanics, Volume 34, pp. 107–301, 1998.

Prohászka, J., Dobránszky, J., The role of an anisotropy of the elastic moduli in the determination of the elastic limit value, Materials Science Forum, Volume 414-415, 2003.

Raabe, D., Sachtleber, M., Zhao, Z., Roters, F., Zaefferer, S., Micromechanical and macromechanical effects in grain scale polycrystal plasticity experimentation and simulation, Acta Materialia, Volume 49, pp. 3433–3441, 2001.

Reid, A. C., Langer, S. A., Lua, R. C., Coffman, V. R., Haan, S., Garcia, R. E., Image-based finite element mesh construction for material microstructures, Computational Materials Science, Volume 43, pp. 989–999, 2008.

Reuss, A., Berechnung der Fließgrenze von Mischkristallen auf Grund der Plastizitätsbedingung für Einkristalle ., ZAMM - Zeitschrift für Angewandte Mathematik und Mechanik, Volume 9, p. 4958, 1929.

Riemann, G. F. B., Grundlagen für eine allgemeine Theorie der Functionen einer veränderlichen complexen Grösse, Ph.D. thesis, Göttingen, Germany, 1851.

Rodin, G. J., Eshelby's inclusion problem for polygons and polyhedra, Journal of the Mechanics and Physics of Solids, Volume 44, pp. 1977–1995, 1996.

Rosenberg, J., Piehler, H., Calculation of the taylor factor and lattice rotations for bcc metals deforming by pencil glide, Metallurgical and Materials Transactions B, Volume 2, pp. 257–259, 1971.

Roters, F., Eisenlohr, P., Hantcherli, L., Tjahjanto, D., Bieler, T., Raabe, D., Overview of constitutive laws, kinematics, homogenization and multiscale methods in crystal plasticity finite-element modeling: Theory, experiments, applications, Acta Materialia, Volume 58, pp. 1152–1211, 2010.

Routbort, J., Reid, C., Fisher, E., Dever, D., High-temperature elastic constants and the phase stability of silicon-iron, Acta Metallurgica, Volume 19, pp. 1307–1316, 1971.

Ru, C. Q., Analytic Solution for Eshelby's Problem of an Inclusion of Arbitrary Shape in a Plane or Half-Plane, Journal of Applied Mechanics, Volume 66, pp. 315–322, 1999.

Sachs, G., Plasticity problems in metals, Z. Ver. Dent. Ing., Volume 72, pp. 734–736, 1928.

Santana, Y., Renault, P., Sebastiani, M., Barbera, J. L., Lesage, J., Bemporad, E., Bourhis, E. L., Puchi-Cabrera, E., Staia, M., Characterization and residual stresses of WC-Co thermally sprayed coatings, Surface and Coatings Technology, Volume 202, pp. 4560–4565, 2008.

Schneider, Y., Bertram, A., Böhlke, T., Hartig, C., Plastic deformation behaviour of Fe-Cu composites predicted by 3D finite element simulations, Computational Materials Science, Volume 48, pp. 456–465, 2010.

Sedláček, R., Kratochvíl, J., Blum, W., Deformation Induced Misorientations: Initial Stage of Subgrain Formation as a Plastic Instability, physica status solidi (a), Volume 186, pp. 1–16, 2001.

Šesták, B., Blahovec, J., The Temperature Dependence of Slip Planes in Fe-3.4% Si Single Crystals, physica status solidi (b), Volume 40, pp. 599–607, 1970.

Šesták, B., Zárubová, N., Asymmetry of Slip in Fe-Si Alloy Single Crystals, physica status solidi (b), Volume 10, pp. 239–250, 1965.

Sevostianov, I., Kachanov, M., Zohdi, T., On computation of the compliance and stiffness contribution tensors of non ellipsoidal inhomogeneities, International Journal of Solids and Structures, Volume 45, pp. 4375–4383, 2008.

Shackelford, J., Sullivan, M., Introduction to Materials Science for engineers, 6th edition, Pearson Education, London, 2005.

Shan, Z., Sitaraman, S. K., Elastic-plastic characterization of thin films using nanoindentation technique, Thin Solid Films, Volume 437, pp. 176–181, 2003.

Silhavy, M., The Mechanics and Thermodynamics of Continuous Media, 1st edition, Springer Verlag, Berlin, 1997.

Stölken, J. S., Evans, A. G., A microbend test method for measuring the plasticity length scale, Acta Materialia, Volume 46, pp. 5109–5115, 1998.

Svendsen, B., On the modelling of anisotropic elastic and inelastic material behaviour at large deformation, International Journal of Solids and Structures, Volume 38, pp. 9579–9599, 2001.

Svendsen, B., Bargmann, S., On the continuum thermodynamic rate variational formulation of models for extended crystal plasticity at large deformation, Journal of the Mechanics and Physics of Solids, Volume 58, pp. 1253–1271, 2010.

Takeuchi, S., Furubayashi, E., Taoka, T., Orientation dependence of yield stress in 4.4% silicon iron single crystals, Acta Metallurgica, Volume 15, pp. 1179–1191, 1967.

Takeuchi, T., Ikeda, S., Low Temperature Creeps and Delay Times in Iron of Very Low Carbon Content, Journal of the Physical Society of Japan, Volume 18, pp. 767–772, 1963.

Taoka, T., Takeuchi, S., Furubayashi, E., Slip systems and their critical shear stress in 3% silicon iron, Journal of the Physical Society of Japan, Volume 19, pp. 701–711, 1964.

Tatschl, A., Kolednik, O., On the experimental characterization of crystal plasticity in polycrystals, Materials Science and Engineering A, Volume 342, pp. 152–168, 2003.

Taylor, G., Plastic strains in metals, Journal of the Institute of Metals, Volume 62, pp. 307–324, 1938.

Taylor, G. I., The Mechanism of Plastic Deformation of Crystals. Part I. Theoretical, Proceedings of the royal society London A, Volume 145, pp. 362–387, 1934.

Temizer, I., Wriggers, P., An adaptive method for homogenization in orthotropic nonlinear elasticity, Computer Methods in Applied Mechanics and Engineering, Volume 196, pp. 3409–3423, 2007.

Temizer, I., Zohdi, T., A numerical method for homogenization in non-linear elasticity, Computational Mechanics, Volume 40, pp. 281–298, 2007.

Tillmann, W., Klusemann, B., Nebel, J., Svendsen, B., Analysis of the Mechanical Properties of an Arc-Sprayed WC-FeCSiMn Coating, Journal of Thermal Spray Technology, accepted for publication, 2010a.

Tillmann, W., Vogli, E., Baumann, I., Krebs, B., Nebel, J., Thermally sprayed wear-protective cermet coatings for forming tools, in Proceedings of the International Thermal Spray Conference, pp. 924–932, Bremen, Germany, 2008a.

Tillmann, W., Vogli, E., Baumann, I., Krebs, B., Nebel, J., Wear-protective cermet coatings for forming toolsCermet-Schichten für den Verschleißschutz von Umformwerkzeugen, Materialwissenschaft und Werkstofftechnik, Volume 41, pp. 597–607, 2010b.

Tillmann, W., Vogli, E., Baumann, I., Matthaeus, G., Ostrowski, T., Influence of the HVOF Gas Composition on the Thermal Spraying of WC-Co Submicron Powders (8 + 1 m) to Produce Superfine Structured Cermet Coatings, Journal of Thermal Spray Technology, Volume 17, pp. 924–932, 2008b.

Toparli, M., Sen, F., Culha, O., Celik, E., Thermal stress analysis of HVOF sprayed WC-Co/NiAl multilayer coatings on stainless steel substrate using finite element methods, Journal of Materials Processing Technology, Volume 190, pp. 26–32, 2007.

Truesdell, C., Noll, W., The non-linear field theories of mechanics, 1st edition, Springer Verlag, Berlin, 1965.

Tsukrov, I., Novak, J., Evaluation of the Contribution of Irregularly Shaped Holes into the Effective Elastic Moduli by Numerical Conformal Mapping, International Journal of Fracture, Volume 107, pp. 21–28, 2001.

Tsukrov, I., Novak, J., Effective elastic properties of solids with two-dimensional inclusions of irregular shapes, International Journal of Solids and Structures, Volume 41, pp. 6905–6924, 2004.

Vehoff, H., Nykyforchyn, A., Fatigue crack nucleation at grain boundaries - Experiment and simulation, Zeitschrift fuer Metallkunde/Materials Research and Advanced Techniques, Volume 94, pp. 682–686, 2003.

Venkatesh, T. A., Vliet, K. J. V., Giannakopoulos, A. E., Suresh, S., Determination of elasto-plastic properties by instrumented sharp indentation: guidelines for property extraction, Scripta Materialia, Volume 42, pp. 833–839, 2000.

Voigt, W., Über die Beziehung zwischen den beiden Elastizitätskonstanten isotroper Körper, Wied. Ann., Volume 38, pp. 573–587, 1889.

Welsch, M., Henning, M., Marx, M., Vehoff, H., Measuring the plastic zone size by Orientation Gradient Mapping (OGM) and Electron Channeling Contrast Imaging (ECCI), Advanced Engineering Materials, Volume 9, pp. 31–37, 2007.

Wiederkehr, T., Klusemann, B., Gies, D., Müller, H., Svendsen, B., An Image Morphing Method for 3d Reconstruction and FE-Analysis of Pore Networks in Thermal Spray Coatings, Computational Materials Science, Volume 47, pp. 881–889, 2010.

Wyss, H., Tervoort, E., Meier, L., Müller, M., Gauckler, L., Relation between microstructure and mechanical behavior of concentrated silica gels, Journal of Colloid and Interface Science, Volume 273, pp. 455–462, 2004.

Yin, Z., Tao, S., Zhou, X., Ding, C., Evaluating Bending Strength of Plasma Sprayed Al2O3 Coatings, Journal of Thermal Spray Technology, Volume 18, pp. 292–296, 2009.

Zheng, Q., Zhao, Z., Du, D., Irreducible structure, symmetry and average of Eshelby's tensor fields in isotropic elasticity, Journal of the Mechanics and Physics of Solids, Volume 54, pp.

368–383, 2006.

Zheng, Q. S., Du, D. X., An explicit and universally applicable estimate for the effective properties of multiphase composites which accounts for inclusion distribution, Journal of the Mechanics and Physics of Solids, Volume 49, pp. 2765–2788, 2001.

Zisman, A. A., Rybin, V. V., Mesoscopic stress field arising from the grain interaction in plastically deformed polycrystals, Acta Materialia, Volume 46, pp. 457–464, 1998.

Zohdi, T., Wriggers, P., Introduction to Computational Micromechanics, 1st edition, Springer Verlag, Berlin, 2005.

Zou, W., He, Q., Huang, M., Zheng, Q., Eshelby's problem of non-elliptical inclusions, Journal of the Mechanics and Physics of Solids, Volume 58, pp. 346–372, 2010.

Acknowledgements

The work presented in this thesis was carried out between 2008 and 2010 during my time as a research assistant at the Institute of Mechanics, TU Dortmund. The financial support of the DFG (Deutsche Forschungsgemeinschaft) within the special research project SFB 708 (TP B6) and under contract Sv 8/8-2 is gratefully acknowledged.

Having come to the end, I would like to express my thanks to all the people here who gave me tremendous support and help in the last two years.

First of all, I would like to express my heartfelt thanks to my academic advisor Professor Bob Svendsen for his support and for providing me with inspiring advice through all these years. Without his knowledge in the fields of material modeling and computational mechanics this thesis could not have been achieved.

Further, I would like to thank Professor Thomas Böhlke for his interest in my work and willingness to act as reviewer of this thesis. Furthermore I thank Jun.-Professor Swantje Bargmann for willingness to act as examiner of this thesis. Also I am very grateful to Professor Andreas Menzel for taking the chairmanship of the examination committee.

Moreover, I would like to express my gratitude to my fellow colleagues at the Institute of Mechanics. The discussions I have had with them have been fruitful, inspirational and have facilitated my research. In particular, I would like to express my gratitude to Mr. Till Clausmeyer for his great support, help and the many discussions we had on various scientific issues. Furthermore, I would like to thank Mr. Tobias Kayser and Mr. Matthias Weiss for their continuous support in the area of computational hardware and software facilities.

My special thanks also go to Dr.-Ing. Thorsten Bartel, Mr. Tobias Waffenschmidt, Mr. Christian Hortig and Mr. Farhad Parvizian for their help with all aspects of the work, willingness to answer my questions and for their friendship.

Special thanks would go to Mrs. Kerstin Walter for her years warm help for my research, contract and business travelling issues. Thanks to Mrs. Christine Vu and Mrs. Daria Walenczyk for their excellent language correction of the thesis and papers.

I want to thank all colleagues in the project SFB 708, especially Mr. Thomas Wiederkehr and Mr. Jan Nebel for the very productive cooperations across different scientific fields.

Last but not least, I would like to thank my parents, my brother, Mrs. Ann-Kristin Dirksmöller and all those who have contributed in one way or another in their very personal ways.

Dortmund, November 2010 Benjamin Klusemann

Curriculum Vitae

Personal

Name: Benjamin Klusemann

Date of Birth: February 22, 1984

Place of Birth: Hamm/Westfalen, Germany

Nationality: German

Education

2003-2008	TU Dortmund, Diploma studies in mechanical engineering
08/2007-12/2007	University of Idaho, USA, Studies of mechanical engineering
2000-2003	Freiherr-vom-Stein Gymnasium, Hamm/Westfalen
1994-2000	Marienschule, Hamm/Westfalen
1990-1994	Maximilianschule, Hamm/Westfalen

Profession

09/2008-onwards	Research Assistant, TU Dortmund Institute of Mechanics (Prof. Dr. rer. nat. B. Svendsen)